



HAL
open science

Analyzing and exploiting the natural dynamics of underactuated robots

Ziad Zamzami

► **To cite this version:**

Ziad Zamzami. Analyzing and exploiting the natural dynamics of underactuated robots. Robotics [cs.RO]. Sorbonne Université, 2018. English. NNT : 2018SORUS408 . tel-02918222

HAL Id: tel-02918222

<https://theses.hal.science/tel-02918222>

Submitted on 20 Aug 2020

HAL is a multi-disciplinary open access archive for the deposit and dissemination of scientific research documents, whether they are published or not. The documents may come from teaching and research institutions in France or abroad, or from public or private research centers.

L'archive ouverte pluridisciplinaire **HAL**, est destinée au dépôt et à la diffusion de documents scientifiques de niveau recherche, publiés ou non, émanant des établissements d'enseignement et de recherche français ou étrangers, des laboratoires publics ou privés.

THÈSE DE DOCTORAT

présentée à

SORBONNE UNIVERSITÉ

par

Ziad ZAMZAMI

Pour obtenir le grade de
DOCTEUR de SORBONNE UNIVERSITÉ

Spécialité
MÉCANIQUE - ROBOTIQUE

École doctorale de Sciences mécaniques, acoustique, électronique et robotique de
Paris

Analyse et exploitation de la dynamique naturelle des robots sous-actionnés

Soutenance prévue le 27 Juin 2018

devant le jury composé de :

M. Pierre BLAZEVIC	Professeur à l'UVSQ	<i>Rapporteur</i>
M. Nazih MECHBAL	Maître de conférences HDR à l'ENSAM	<i>Rapporteur</i>
M. Saïd ZEGHLOUL	Professeur à l'Université de Poitiers	<i>Examineur</i>
M. Vincent PADOIS	Maître de conférences HDR à Sorbonne Université	<i>Examineur</i>
M. Faïz BEN AMAR	Professeur à Sorbonne Université	<i>Directeur de thèse</i>
M. Anis SAHBANI	Maître de conférences à Sorbonne Université	<i>Encadrant</i>

Ziad ZAMZAMI: *Analyzing And Exploiting Natural Dynamics Of Underactuated Robots*, Phd Thesis, Sorbonne Université - ISIR, 4 place Jussieu, 75005, Paris, June 2018

Dedicated to the loving memory of my grand mother, Hoda .

1936–2011

ABSTRACT

Humans and animals are capable of overcoming complex terrain challenges with graceful and agile movements. One of the key ingredients for such complex behaviors is motion coordination to exploit their natural dynamics. Sports performers coordinate their muscles actions to achieve a synergistic motion that surpasses their physical limits. Lizards and Cheetahs coordinate their tail swing to rapidly accelerate and maneuver during the pursuit of their prey. Understanding and emulating these motions is one of the long-standing grand challenges in robotics and biomechanics, with possible applications in rehabilitation, sport, search-and-rescue, environmental monitoring, and defense.

In striking contrast, the traditional research in robotics has either ignored or purposely suppressed the inherent dynamics of the robotic systems. Interlimb dynamic coupling and nonlinear dynamics has been long viewed as a source of perturbation that needs to be avoided either by means of mechanical design (e.g., link design to decouple motion, reduced mass appendages to neglect inertial coupling) or via a decoupling controller to compensate for the coupling effects (e.g., feedback linearization). This control philosophy is the reminiscence of the control schemes developed for industrial manipulators with the aim of achieving highly accurate and robust and repetitive motions. In this work, we focus our attention on a particular class of robotic systems called underactuated robots. Underactuation imposes a second-order nonholonomic constraints on their dynamics that restrict the family of trajectories their accelerations can follow. This is one of the reasons that has compelled us to treat underactuated robots with torque limits. The fact that it is not feedback-linearizable, the non-negligible dynamic coupling and the severe torque limits remove the full control authority that one enjoyed in the fully-actuated robots, thus the class of underactuated robots forces you to handle the inherent nonlinear dynamics in an unconventional way.

Despite the existence of powerful tools such as nonlinear trajectory optimization, they are usually treated as black boxes that provide local optimal trajectories. We introduce the Dynamical Coupling Map (DCM), a novel graphical analysis technique, to help gain insight into the output trajectory of the optimization and analyze the capability of underactuated robots. The key insight is to manipulate the Euler-Lagrange differential equations of motion to approximate the acceleration capabilities of the passive system as an ellipsoid coined as the

Dynamic Coupling Ellipsoid (DCE). The volume of this ellipsoid represents the capability of the robot to transmit the torque of the active subsystem to the passive subsystem while the origin of the ellipsoid in the acceleration space represents the bias term which comes from the contribution of gravity and nonlinear velocity dependent forces on the set of allowed accelerations of the passive subsystem. We introduce three novel performance indexes aptly named Natural Dynamics Indexes (NDI) which allow to quantify the role of the natural dynamics during a dynamic motion and its significance with respect to the input control its physical bounds. Furthermore, the benefits of the DCM analysis is demonstrated on several highly dynamic maneuvers such as the swing-up motion of a simplified model of a gymnast on high bar. The formulation of DCM is extended to floating base systems with contact forces while demonstrating its merits on the analysis of dynamic maneuver such as standing high jump for a high-dimensional humanoid robot showing the beneficial use of dynamic coupling of arms swings on jumping height. The motion is generated first using direct trajectory optimization method based direct collocation trajectory optimization technique. The generated trajectory is subsequently analyzed using the DCM tool. The DCM shows graphically and intuitively the pivotal role of exploiting the natural dynamics in order to exceed their physical capacity which is dictated by the input torques limits. We also extend the current utilization of DCM from a posteriori analysis tool to a fundamental heuristic for guiding motion generation of highly dynamic maneuvers by leveraging random based motion planning approaches with a new natural dynamic based heuristic. We introduce the Natural Dynamics based Tree (NDT), a novel kinodynamic planning algorithm which plans a dynamic motion based on the natural dynamics of the system which results in a more efficient kinodynamic motion planning.

Keywords: Underactuated robots, Natural dynamics, Inter-segmental Dynamic coupling, Acceleration analysis, Motion planning

CONTENTS

1	INTRODUCTION	1
1.1	Motivation & Context	1
1.1.1	Interlimb Dynamic Coordination	2
1.1.2	Natural Dynamics	8
1.1.3	Underactuated robotics	10
1.2	Thesis Goals	12
1.3	Thesis Outline	14
2	A REVIEW ON PERFORMANCE MEASURES	17
2.1	kinetostatic performance measures	17
2.1.1	kinetostatic manipulability	18
2.1.2	Kinematic Isotropy	22
2.1.3	Singular Values and Their Combinations	22
2.1.4	Task Compatibility Index	23
2.2	Dynamic Performance Measures	24
2.2.1	Generalized Inertia Ellipsoid (GIE)	24
2.2.2	Dynamic Manipulability Ellipsoid (DME)	25
2.2.3	Inertia Matching Ellipsoid (IME)	27
2.2.4	Acceleration Radius	29
2.2.5	Dynamic Capability Equation	30
2.2.6	Dynamic Coupling Measure of Space Robot Systems	32
2.2.7	Dynamic Coupling Index for Underactuated Manipulators	32
2.3	Conclusion	32
3	DYNAMIC COUPLING MAP IN THE JOINT SPACE	33
3.1	Dynamic Coupling Map for Underactuated Manipulators	33
3.1.1	Underactuated Manipulator Lagrangian Dynamics	33
3.1.2	Dynamic Coupling in the Passive Joint Acceleration Space	36
3.1.3	Dynamic Coupling Ellipsoid in the Passive Joint Acceleration Space	39
3.1.3.1	Visualizing the relation between torque space and the passive acceleration space	41
3.1.3.2	Interpretation of the Dynamic Coupling Ellipsoid	41
3.1.4	Natural Dynamic Index in the Passive Acceleration Space	45
3.2	Dynamic Coupling for Floating-Base Articulated Systems	46

3.2.1	Lagrangian Dynamics of floating base articulated system	47	
3.2.2	Dynamic Coupling for floating base articulated systems	48	
3.2.3	Dynamic Coupling Ellipsoid	50	
3.3	Case Study: Humanoid's Vertical Jump with Arm Swing		51
3.3.1	Vertical Jump as a Dynamic Maneuver	52	
3.3.2	Motion Synthesis of Dynamic Motions	53	
3.4	Experiment Results	55	
3.4.1	Model Description: Atlas Humanoid Robot		55
3.4.2	Results	56	
3.5	Conclusion	58	
4	DYNAMIC COUPLING MAP IN THE TASK SPACE	61	
4.1	Dynamic Coupling Map In The Task Space	61	
4.1.1	Dynamic Coupling Ellipsoid in the Task Acceleration Space	62	
4.1.2	Natural Dynamic Index in the Task Acceleration Space	66	
4.1.3	Effect of Actuation Distribution on the DCE	67	
4.1.4	Effect of Inertia Distribution on the DCE	70	
4.1.5	Effect of Torque Limits on the DCE	73	
4.1.6	Effect of Gravity on the DCE	75	
4.2	Case Study: Gymnast Swing-up Dynamic Maneuver		80
4.2.1	Model Description	82	
4.2.2	Approach	84	
4.2.3	Results	88	
4.2.4	Discussion	100	
4.3	Conclusion	105	
5	MOTION PLANNING WITH NATURAL DYNAMICS	107	
5.1	A Review on Kinodynamic Sampling Based Motion Planning	107	
5.1.1	Kinodynamic Planning Problem Formulation	108	
5.1.2	Taxonomoy Of Kinodynamic Planners	109	
5.2	The Proposed Dynamic Coupling Based Algorithm	110	
5.2.1	Natural Dynamics based Control Policy	112	
5.2.1.1	Natural Dynamics Based Control Inputs	113	
5.2.1.2	Operational space control	114	
5.2.1.3	Demonstration of the natrual dynamics-based policy on the Acrobot	115	
5.2.2	Natural Dynamics based Motion Planning Algorithm	119	
5.3	Experiment Results	127	
5.3.1	Model Description	127	
5.3.2	Results	127	
5.3.3	Discussion	129	

5.4	Conclusion	136
6	CONCLUSIONS & PERSPECTIVES	137
6.1	Conclusion	137
6.2	Perspectives	139
I	APPENDIX	145
A	UNDERACTUATED ROBOTS DYNAMIC MODELLING	147
A.1	Underactuated Manipulator Dynamics	147
A.1.1	Manipulator's Kinetic energy	148
A.1.2	Manipulator's Kinematics using adjoint maps	148
A.1.3	Joint Space Inertia Matrix (JSIM)	149
A.1.4	Potential energy	150
A.1.5	Lagrangian Dynamics	151
A.2	Floating-base Rigid Body Dynamics	151
A.2.1	Floating-base System's Configuration Space	152
A.2.2	Floating-base System Kinematics	154
A.2.3	Kinetic energy	156
A.2.3.1	Articulating links kinetic energy	156
A.2.3.2	floating-base kinetic energy	157
A.2.3.3	Total Kinetic energy	157
A.2.4	Free-floating base Dynamics	157
A.2.5	Contact dynamics as complementarity problem	158
B	TRAJECTORY OPTIMIZATION BASED CONTROL	161
B.1	Background	161
B.2	Optimal Control Overview	161
B.2.1	Dynamic Programming	162
B.2.2	Indirect Methods	163
B.2.3	Direct Methods	163
B.3	Trajectory Optimization by Direct Collocation	164
B.3.1	NLP Solvers	166
C	SAMPLING-BASED KINODYNAMIC PLANNERS	169
C.1	Rapidl-exploring Random Trees (RRT)	169
C.2	Expansive Space Tree (EST)	172
	BIBLIOGRAPHY	175

LIST OF FIGURES

Figure 1	Mapping between the input actuator space and the passive acceleration space	41	
Figure 2	Illustration of the Joint Space Dynamic Coupling Map (JS-DCM)	44	
Figure 3	The Boston Dynamics Atlas humanoid robot		56
Figure 4	Dynamic Coupling Map between the first nine consecutive instants during a vertical jump.		57
Figure 5	Comparison of the evolution of the CoM in the vertical direction between vertical jump with arms swing and with locked arms	57	
Figure 6	Dynamic Coupling ellipsoids between two consecutive instants during a vertical jump with arm swing.	58	
Figure 7	Illustration of the Task Space Dynamic Coupling Map (TS-DCM)	65	
Figure 8	Effect of actuation distribution on the Dynamic Coupling Ellipsoid in the task space for 2-DoF underactuated manipulator	68	
Figure 9	Effect of actuation distribution on the Dynamic Coupling Ellipsoid in the task space for a 3-DoF underactuated manipulator	71	
Figure 10	Effect of actuation distribution on the Dynamic Coupling Ellipsoid in the task space for a 4-DoF underactuated manipulator	72	
Figure 11	Effect of inertia distribution on the Dynamic Coupling Ellipsoid in the task space for a 3-DoF underactuated manipulator	74	
Figure 12	Effect of torque limits on the Dynamic Coupling Ellipsoid in the task space for a 4-DoF AAPP-type underactuated manipulator	76	
Figure 13	Effect of Gravity on DCE	78	
Figure 14	Decomposition of task acceleration bias due to gravity into its components	79	
Figure 15	Relationship between torque limits and task acceleration bias due to gravity	80	
Figure 16	Dynamic singularity demonstration using DCE		81
Figure 17	Gymnast model	82	
Figure 18	Swing-up stages	87	
Figure 19	Local-optimal motion results for the gymnast-robot swing-up dynamic manoeuvre for both low torque and high-torque constraints	90	

Figure 20	Nonlinear trajectory optimization results for the dynamic swingup manoeuver of the gymnast-robot swing-up with low torque capacity	91
Figure 21	Nonlinear trajectory optimization results for the dynamic swingup manoeuver of the gymnast-robot swing-up with high torque capacity	96
Figure 22	Comparison of the Natural Dynamic Index (NDI) during the swing-up dynamic manoeuvre for the gymnast robot between both cases: low-torque capacity and high-torque capacity	101
Figure 23	Taxonomy of kinodynamic planners	109
Figure 24	Illustration of DCM-based control policy	112
Figure 25	Block diagram of DCE-based control	116
Figure 26	Feedback control policies for the acrobot based on \ddot{X}_0 and \ddot{X}_π	120
Figure 27	Feedback control policies for the acrobot based on \ddot{X}_ϕ and $\ddot{X}_{\phi+\pi}$	121
Figure 28	Resulting motion for the acrobot upon applying the four DCE based control policies	122
Figure 29	Configuration and velocity trajectories for the acrobot upon applying the four DCE control policies	123
Figure 30	Model of the Acrobot robot	128
Figure 31	Comparison of calculation time between NDT and RRT motion planning algorithms	130
Figure 32	Comparison of number of nodes to reach a motion solution of the acrobot's swing-up by the NDT and RRT motion planning algorithms	130
Figure 33	Comparison of number of iterations to reach a motion solution of the acrobot's swing-up by the NDT and RRT motion planning algorithms	131
Figure 34	Comparison of energy consumption during the final motion solution of the acrobot's swing-up by the NDT and RRT motion planning algorithms	131
Figure 35	Comparison of the acrobot's swing-up motion duration given by the NDT and RRT motion planning algorithms	132
Figure 36	Output motion solution from the RRT kinodynamic algorithm for the acrobot swing-up manoeuvre with a torque limit of 5 N.m	133
Figure 37	Output motion solution from the NDT motion planning algorithm for the acrobot swing-up manoeuvre with a torque limit of 5 N.m	134

Figure 38	Output motion solution from the NDT motion planning algorithm for the acrobot swing-up manoeuvre with a torque limit of 5 N.m	135
Figure 39	Illustration of a general floating-base system	152
Figure 40	Overview of numerical methods for optimal control	162
Figure 41	Illustration of direct methods for trajectory optimization	164
Figure 42	Illustration of the state trajectory discretization occurring in direct collocation optimization. System dynamics $f(t_c)$ are enforced to match the slope of the cubic \dot{x}_c at the collocation point x_c .	165

LIST OF TABLES

Table 1	Comparative overview on the state of the art of performance measures	31
Table 2	Snapshots of the vertical jump with arms swing trajectory: Instants are ordered from top left to bottom right	59
Table 3	Physical parameters of the Gymnast robot model	85
Table 4	DCM analysis for the dynamic swing-up manoeuvre of the gymnast robot with low torque capacity	92
Table 5	Table 3 Continued: DCM analysis for the dynamic swing-up manoeuvre of the gymnast robot with low torque capacity	93
Table 6	Table 4 Continued: DCM analysis for the dynamic swing-up manoeuvre of the gymnast robot with low torque capacity	94
Table 7	Table 5 Continued: DCM analysis for the dynamic swing-up manoeuvre of the gymnast robot with low torque capacity	95
Table 8	DCM analysis for the dynamic swing-up manoeuvre of the gymnast robot with high torque capacity	97
Table 9	table 7 continued: DCM analysis for the dynamic swing-up manoeuvre of the gymnast robot with high torque capacity	98
Table 10	table 8 continued: DCM analysis for the dynamic swing-up manoeuvre of the gymnast robot with High torque capacity	99

Table 11	Acrobot model parameters	128
Table 12	Comparison of motion planning results	129
Table 13	Continued: Comparison of motion planning results	129

INTRODUCTION

1.1 MOTIVATION & CONTEXT

As we are witnessing the dawn of the fourth industrial revolution, robotic systems play an increasing role in our economic and personal ecosystem. Robots have transitioned from industrial manipulators, locked inside a steel cage, executing a pre-designed repetitive task, to more complex and versatile mobile manipulators conquering other spaces beyond the steel cage. Nowadays, robotic systems are ubiquitous everywhere starting from advanced aerial manipulators in the sky to the underwater scuba diver robotic mobile manipulator, needless to mention the ongoing efforts for autonomous humanoids. Robots are increasingly employed across all sectors and for a broad range of tasks from personal entertainment to search and rescue operations. Consequently, there is a strong demand for increasing the capabilities, efficiency, and reliability of different robotic systems.

Despite all recent technological advances and efforts to take cues from nature to biomimic the biological systems, the performance of robotic systems is still far from their natural counterparts from the animal kingdom on many levels including agility, maneuverability, energy performance, motion smoothness, etc. Humans and animals are capable of overcoming complex terrain challenges with graceful and agile movements. Sports performers coordinate their muscles actions to achieve a synergistic motion that surpasses their physical limits. Lizards and Cheetahs coordinate their tail swing to rapidly accelerate and maneuver during the pursuit of their prey [Lib+12; PB14].

One of the fundamental reasons behind this gap of performance is due to our limited understanding of how the brain represents, controls, and coordinates the numerous Degrees of Freedom (DoF) of the musculoskeletal system. The complexity rises partly from the fact that the central nervous system (CNS) generates motor commands to many muscles, each comprising thousands of motor units, which are simultaneously activated and coordinated. Selecting the appropriate DoF patterns to achieve a purposeful movement is extremely demanding task given the huge dimensionality of the search space and its inherent nonlinearities. This led to the most influential and controversial [TJ09] seminal idea of the Russian physiologist Nikolai Bernstein (1896-1966) of "motor synergy"[Ber67]. Broadly speaking, *motor synergy* refers to the correlated activation of multiple muscles in

Bernstein did his research behind the iron curtain of the USSR, his ideas only became known to Western scientists in 1967, when his seminal book, The Co-ordination and Regulation of Movements, was translated to English.

a coordinative structure which is used by the central nervous system (CNS) as building blocks to represent and control actions, thus alleviating the problem of controlling a large number of muscles. In other words, motor synergy causes multiple degrees of freedom to interact and coordinate more efficiently than possible with standard robot control techniques that decouple the control of individual joints.

However, after almost half a century the concept of synergy is still debated and not well-defined despite the numerous observations made on tasks ranging from walking and running to reaching and grasping [FH85; Iva05; Cl06; Ber+09]. While these studies focus on physiological aspects of the muscle synergy hypothesis, very few research addresses the theoretical foundation of the proposed modular controller. How to compose a motor synergy? Which synergies should be employed to execute the desired motor tasks? How many synergies are needed? How does the dynamics of the system to be controlled affect the synergy-set? This uncertainty led researchers to propose a proliferation of definitions and conceptualizations of motor synergy ranging from kinematic synergy to postural synergy. However, the fundamental nature of motor synergy remains an open question.

Beyond the question of solving the problem of kinematic redundancy, Bernstein [Ber67] also stressed the need for studying the contributions of the passive forces and moments to the final expression of movement, arguing that skilled movements exploited these passive forces to control movements simply and efficiently. It is almost a tautology of locomotion research that the motions of the various body segments 'co-operate' to facilitate a specific gait, minimize forces and/or energy expenditure, or ensure adequate stability, or some combination of these. However, Synergy and coordination in highly-dynamic and agile motions are still beyond the realm of human knowledge. By coordination we refer to efficient motor skills that exploit, rather than cancel, the natural dynamics of the mechanism. The work in this thesis attempts to take a step forward in that direction.

1.1.1 Interlimb Dynamic Coordination

In the literature of sports biomechanics [Chao0], one of the most cited reasons for an increase in performance is an improved coordination among the muscles involved in the task. However, there is not yet a well-established theory on motor coordination.

*Dynamic
Coordination in
Bioscience*

A dictionary defines "Coordination" as "bringing different elements (parts, movements, etc.) into a harmonious or efficient relationship." This definition can be applied to all different motions of human and ani-

mals as a motion coordination problem in which coupled motor units have to cooperate in order to achieve a particular task. The most influential thinker and a pioneer of the study of coordinated movements, Bernstein (1967) [Ber67] defined coordination as *a problem of mastering the redundant degrees of freedom involved in a particular movement*. Bernstein proposed a number of appealing ideas such as "regularity without regulation" and "patterned outputs from unpatterned inputs" however they remain largely vague and doesn't provide a rigorous theory or a satisfactory explanation of motor coordination [BPS95; Tur90]. Nevertheless, his work initiated an extensive research effort across many scientific domains including, neuroscience, behavioral science, kinesiology, biomechanics, and dynamics; all strive for a better understanding of how the human or animal's control system manages to organize the cooperation among the limbs. However, since each field of science employs its unique techniques and methodology and due to the compositional complexity (e.g., vascular, neural, muscular, skeletal) operating at different time and space scale, the problem of movement coordination is extremely difficult to resolve in a scientifically satisfactory way. This led to a disparity and sometimes an inconsistent explanation of the interlimb dynamic coordination. Reader is referred to [Swi+94] for a comprehensive review.

For example, the difference between the meaning of the term dynamics in dynamical system theory and mechanics has been a persistent source of confusion. Most of the work in interlimb dynamical coordination employ the term dynamics based on the broad definition of from dynamical system theory as the time evolution of a system at any level of description (e.g., cell, brain or behavior). In mechanics, in contrast, the term is used as a synonym of kinetics, i.e., the realm of force- inertia- acceleration the causes of motion (kinematics). The confusion is amplified when terms like energy, dissipation, stiffness, and difference in eigenfrequencies are used in the abstract sense of dynamics system theory which refers to the space-time behaviour of the system as a whole.

Coordination can take many forms as well. Studies on interlimb dynamic coordination extend over a wide range of systems; starting from the mechanically decoupled system of two persons walking side-by-side [Ulz+08] to the interlimb dynamic coordination of a highly-coupled mechanical system of an athlete performing a vertical jump [AH02] or a gymnastic maneuver [OT15; HY16]. However, most of the investigations focused on the interlimb dynamic coordination of rhythmic activities such as locomotion (walking, running, swimming) [Dico0; Iva05; Cl06; Wan+01]. These experiments show that voluntary rhythmic movements are either in phase or out of phase. This indicates a common internal pace or a Central Pattern Generator (CPG)

that coordinates movements. In this sense, coordination is argued to be a consequence of evolving processes of self-organization or pattern formation.

Conversely, the traditional research in robotics has either ignored or purposely suppressed the inherent dynamics of the robotic systems. Interlimb dynamic coupling has been long viewed as a source of perturbation that needs to be avoided either by means of mechanical design (e.g., link design to decouple the dynamics, or high mass ratio to neglect the inertial coupling) or via a decoupling controller to compensate for the coupling effect. Furthermore, the robot's nonlinear dynamics itself is usually regarded as an undesirable disturbance that must be suppressed by means of control. The main reason behind this control paradigm can be attributed to set of mature control tools that have been designed principally for industrial manipulators. For example, a widely adopted control scheme is the inverse dynamics or computed torque (a form of feedback linearization [Kre89]) which is essentially employed as a feedback loop to compensate for the coupled, nonlinear dynamics of the manipulator. Thus, rendering the robot into a linear decoupled system in the canonical form, which can then be controlled by an outer loop designed using standard linear control techniques. The advantage of linear control theory is that it is much more mature than its nonlinear counterpart that can easily provide guarantees on convergence, robustness, and stability. However, the resulting motion is usually very stiff, overly conservative and energetically inefficient.

Another control paradigm that results in emerging coordination of body parts is the regulation of the robot's linear and angular momentum about its Center Of Mass (COM). Kajita [Kaj+03] pioneered this approach by proposing the resolved momentum controller which he demonstrated a robust and coordinated motion of a humanoid while walking and balancing while kicking. The key insight behind this approach is to regulate the robot's angular momentum about the COM, also know as the Centroidal Angular Momentum (CAM), to zero. This strategy will lead to a coordinated inter-segmental momentum cancellation. This insight was also verified in biomechanical studies [PHH04] which showed that CAM is a privileged quantity during steady-state human walking; subjects had a high non-zero angular momentum for individual bodies in their limbs, yet the CNS coordinate their movements in such to regulate their CAM to near zero. Later, the centroidal momentum regulation approach has attracted the attention of many follow-ups works in biomechanics, computer animation [MZS09; LMH10; Zor10], and robotics [LG07; OGL13; WO16; Her+16] . However, the main critique of this approach is that it requires a reference trajectory for the linear and angular centroidal

momentum, yet it is not clear how to design these trajectories in a principled manner. Although it is convenient to derive the centroidal linear momentum based on the prescribed trajectory of the center of mass, the angular momentum cannot be integrated to yield any meaningful orientation of the humanoid as a function of its configuration. In other words, the average linear position and velocity of any multi-body system are accepted to be the position and velocity of its COM. However, neither an average angular position nor an average angular velocity exists for a multibody system. This is the reason why most of the work regulate the CAM around zero. However, this restricts the resultant motions to just a rotational stabilization where the inter-limb dynamic coordination emerges as a reactive strategy to increase the rotational stability in situations such as tipping and tumbling. A recent work [WO16] enforces a non-zero CAM to induce a pitching rotation angle of humanoid while kicking a ball. However, it remains an ad-hoc solution, and a more rigorous way to design a non-zero CAM reference for rich and proactive motor skills remains an open research topic.

More recently, impressive results for highly dynamic and agile motions (e.g., running, jumping, pronking, etc..) with substantial aerial phase for a range of robotics systems were shown using motion planning and control techniques remotely based on optimal control theory such as trajectory optimization [DVT14; Bel+18; Win+18], differential dynamic programming [TET12], reinforcement learning [TBS10] or even deep learning [Lil+15; Hee+17]. Although the foundation of these approaches were known for more than half a century, nowadays they leverage the current progress in computational power and the readily available mature mathematical libraries (e.g., numerical optimization, automatic differentiation, etc..). Nevertheless, our main critique of those approaches beside their known limitation of excessive computational time (can take up to several hours or few days depending on the method and the complexity of motion) is that they are often treated as black-box that result in a locally optimal solution, and it is difficult to understand the underlying mechanism behind the given motion plan. A popular example is the work [Hee+17] of Google DeepMind’s on using a reinforcement learning method to generate a set of rich, dynamic locomotion behaviours for a range of systems (quadruped, humanoid, planar walker) in an environment rich with obstacles and floor gaps. A remarkable observation from the associated video is that the resulting motion of the humanoid uses a dramatic oscillation and nonintuitive motion of the humanoid’s arms although they are never used to contact any surface. One might think that the arm’s dynamic motion is an artifact of the algorithm. However, a recent study [BTB] has confirmed that the arm’s dynamic motion is not a random exploration of the robot’s redundancies but it

has a physical function, and it actually helps in the stabilization of the humanoid’s motion. Research in biomechanics has also provided evidence on the importance of the dynamic coupling between the different body limbs on general locomotion.

Another problem with the optimization-based methods or reinforcement learning is that it is not always obvious what should be the proper optimality criteria or reward function. This problem has spurred research lines such as inverse optimal control [MTL10] or inverse reinforcement learning [KAN08; ACN10] with the goal to find the optimal criterion given a dynamic process and an observed solution. However, this is a mathematically difficult problem since it requires to solve a parameter identification problem inside an optimal control problem. Moreover, the solution of the inverse optimal control problem is sensitive to the choice of the base function. Thus, the data fitting can only get as good as its base functions permit. Also, several studies show that many widely used ideas for objective functions studied in the robotics and biomechanical communities such as jerk, velocity or kinetic energy related terms are not plausible objective functions to explain the locomotion trajectories entirely. It is generally agreed upon that acceleration is an important quantity for human motion if studied from a global perspective, and that sensing of acceleration is with the vestibular organ is crucial for all human movement.

As emphasized by Schaal [SS05], questions in motor control often parallel questions in robotics, and a fruitful interaction has emerged between neuroscience and engineering. This is particularly true for the control of rhythmic tasks where the idea of CPG has seen numerous successes in the robotics community [FKC03; RI06; Ijs08]. CPGs are neural networks (a system of coupled oscillators controlling each joint) capable of producing coordinated patterns of rhythmic activity without any rhythmic inputs from sensory feedback, or from higher control centers. Models of CPGs have been used to control a variety of different types of robots and different modes of locomotion. Perhaps the most notable result is that of Ijspeert [Ijs+07] concerning his work on the salamander locomotion—a unique amphibian with a bi-locomotion mode; swimming and walking—where he demonstrated the transition between swimming and walking using just few input parameters modulating the frequencies, phases, and amplitudes of the system of coupled oscillators. This result highlights the most interesting feature of the CPG-based approach as it provides a reduction in the dimensionality of the control problem.

However, there are several critiques /disadvantages to the CPG-based approach. Even though CPG is the most cited method in robotics

in the context of interlimb dynamic coordination, it still lacks a solid theoretical foundation and methodology for designing the CPG as most implementations depend on learning or optimization techniques to identify the adequate parameters of the system of coupled oscillators [Ijs08]. More importantly, most CPG-based studies disregard the actual mechanical dynamics and energetics of the robot's body and are only applicable for steady-state locomotion. It is worth noting, however, that there are few studies which investigated the idea of exploiting the passive dynamics to minimizing energy consumption [BII06; VKH09; Wil99]. The basic idea behind this approach relies on the fact that most robots have several resonant frequencies due to pendulum and/or spring-mass phenomena (e.g., due to robot's structure compliance). Therefore, it is possible to synchronize the intrinsic frequency of CPG with the resonant frequency of the robot, thus achieving an energy efficient and robust control of a rhythmic limb movement. However, the problem of how to design controllers capable of producing rich motor skills not limited to steady state rhythmic while exploiting the natural dynamics remains an open research question [Ijs08].

On the other hand, it is obvious that interlimb dynamic coordination plays a significant role in many non-rhythmic animal and athletes dynamic maneuvers while exploiting the natural dynamics of the body such as a brachiating gibbon swinging their body from a tree limb to a tree limb [GR05] or a gymnast performing acrobatic maneuvers on a high bar [OT15; HY16]. Understanding and exploiting these dynamical effects is thus crucial to reduce the necessary active contribution to the motion. In this thesis, we start from Bernstein's qualitative definition of dynamic coordination

"...the secret of co-ordination lies not only in not wasting superfluous force in extinguishing reactive phenomena but, on the contrary, in employing the latter in such a way as to employ active muscle forces only in the capacity of complementary force." [Ber67]

If such philosophy can be transferred to the domain of design and control of robots, this may lead to a new generation of hyper-performance robots that can exceed the capability of its motor system.

In consideration of the foregoing discussion, the work in this thesis explores a new avenue of research which concentrates on demonstrating, explaining and understanding the behavior of underactuated robots performing a dynamic non-rhythmic maneuver such as the swing-up of a gymnast on a high-bar while highlighting the role of coordinating the motion with the natural dynamics.

1.1.2 *Natural Dynamics*

Natural dynamics refers to the set of motions that a robot or animal exhibits without using their actuators

The concept of natural dynamics can be found in virtually any scientific domain that is dealing with dynamical processes. Be it the regeneration of tropical dry forests in biology, the development of an informal employment sector in economics, or the transformation of a coastline in civil engineering, in all these examples, the term *natural dynamics* refers to the behavior that a system follows without external intervention.

Applying this definition to robotics systems implies that the natural dynamics describes a set of motions that a robot or animal exhibits without using their actuators. Of course, these dynamics can be initiated and excited through muscle activity or other forms of actuation, but they are shaped and maintained as a result of inertia, gravity, and elastic oscillations. Natural dynamics exist for any system, whether premeditated or not, whether favorable or detrimental to the task at hand. For highly dynamic behaviors, with large accelerations, impacts, and energy transfers, natural dynamics significantly affect the performance, energy economy, stability, and task bandwidth. Applied control must work in complementarity with the passive dynamics, and not by forcing the robot's motion against its natural dynamics. In this context, the terms natural dynamics and passive dynamics are often used interchangeably, not to be confused with zero dynamics which is a property of feedback control of nonlinear systems. However, in this thesis we will abstain from employing the term passive dynamics to not confuse the reader with the dynamics of passive subsystem of an underactuated robot.

For industrial robots, natural dynamics have long been considered an undesired side-effect that degrades kinematic precision. To reduce its impact, traditional robots are built as stiff as possible: mechanically rigid structures in combination with strong motors, large transmission ratios, and high-gain position controllers ensure that the robots are moving in kinematically exact ways. The underlying goal is to build systems that precisely follow predefined trajectories, independent of the shape of the motion that they execute or the payload they are carrying. The same traditional approach has been applied on legged robots such as Asimo which is characterized by high impedance actuators and control systems that resist any unplanned variation to movement or acceleration caused by the outside world or more critically the natural dynamics of the system that act against the prescribed trajectory for the robot to follow. The result is a quasi-static motion and unnatural motion. A more dynamical motion is typically seen in Boston Dynamics hydraulic machines which are characterized by very high bandwidth, high power actuators. These robots are

sometimes capable of overcoming unfavorable natural dynamics and exhibiting highly dynamic behavior, but they do so at the cost of extremely high power requirements. Designing systems with appropriate passive dynamics can simplify the active control system, permit low-bandwidth actuation, and minimize energy costs [Colo5].

Nature, on the other hand, shows us that it can be actually quite beneficial to enable natural dynamics in a system. Especially in periodic movements, such as walking or running, large fluctuations in kinetic and potential energy arise, and instead of creating the entire motion (and thus the energetic fluctuations) actively, the mechanical structure of animals and humans is built in such a way that a substantial part of the motion emerges passively. Energy is stored elastically in muscles and tendons, and motions are shaped by the pendulum dynamics of the leg segments. By exploiting these dynamical effects, the necessary active contribution to the motion can be reduced greatly.

Many Motions are shaped by the pendulum dynamics for example the swing leg motion in all legged animals locomotion are approximated by the dynamics of a pendulum or a multi-pendulum system with relatively high accuracy [Aleo3; DDKo5]. *Swinging* is a primordial movement primitive which is ubiquitous in the dynamic behavior of many living organisms. Brachiation [GRo5], or body swinging, is a principal movement element in arboreal locomotion in which primates, such as gibbons, swing from tree limb to tree limb by swinging their body while at least one hand is grasping a support at all times. This locomotion mode is also known as a continuous contact brachiating gait which can be regarded as an upside down walking. Understanding and exploiting these dynamical effects is thus crucial to reduce the necessary active contribution to the motion.

From the robotics perspective, natural dynamics was not always seen as an adversary that needs to be suppressed by means of input control. The recognition of the importance of natural dynamics has witnessed several waves of interest in the robotics community. Most of the work in robotics citing natural dynamic or passive dynamics are actually referring principally to the dynamics of the compliant actuators in the robot. The interest in compliant actuators —as opposed to the traditionally rigid and high impedance motors —can be traced back to the observation that many dynamic motions of animals and humans can be approximated as a mass-spring behavior [Ale90; Aleo3], later on, formalized as the Spring Loaded Inverted Pendulum (SLIP) model. In the late 80s, Raibert hoppers [Rai86] were among the earliest to demonstrate mechanical compliance by using pneumatic actuators which gave his running robots a springy bouncing behavior and then used three simple controllers to modify the

speed, height and pitch stability of the bouncing motion. This approach yielded robots which could run fast as well as do gymnastic maneuvers with a degree of agility that is still impressive to this day [Pla95]. However, the motion planning and control depend on a set of intuitive heuristics which cannot be easily transferred to a more general anthropomorphic bipedal robot.

The second wave of interest in natural dynamics raised with the introduction of passive dynamic walkers. Counterintuitively, one way to improve maneuverability and efficiency is to strategically remove actuators from a robot. McGeer [McG90] introduced an alternative paradigm of robot design of completely passive bipedal robot that exploits gravitational forces which can be considered as a system which is completely powered and stabilized by the natural dynamics of the system. However, these systems are characterized by narrow stability regions and weak robustness and can only walk at a specific speed and can neither jog, nor walk up stairs or stand still.

More recently, a third wave of interest in natural dynamics grew with the advent of more advanced actuators such as Serial Elastic Actuators (SEA) [Pra00] or Variable Stiffness Actuators (VSA) [WH08]. Several studies showed that it is possible not only to exploit natural dynamics in hardware [Pra00; AHH15] but also in control [Wil99; Ren+15; Ugu+12; Van+06; Rem11; BII06]. However, all these studies concentrate on the compliance inhibited in the robot's structure as the source of natural or passive dynamics. From their perspective, this is sufficient because the vast majority of these studies build on a mass-spring model while assuming negligible limbs masses (legs or arms), therefore inertial coupling is neglected with respect to the dominant behavior of a mass-spring system. In this thesis, we focus on the natural dynamics inhibited in the dynamic coupling of multi-link underactuated systems.

1.1.3 *Underactuated robotics*

In the control of fully-actuated robots, desired control forces and/or torques may be applied to each joint by actuators. These are actuated joints or active joints. There are however robots that have a fewer number of joints actuators than the number of its total joints is so-called an underactuated robots. It is a well-known fact that an articulated underactuated manipulator with passive joints satisfies a second-order nonholonomic constraint which is a non-integrable constraint on the acceleration.

Examples of nonholonomic underactuated systems are acrobots, cart-pole systems, mobile-based robots with no base actuators, a car

with n-trailers with passive joints, robot manipulators with failed actuators, free-flying manipulators without jets or momentum wheels where the base can be considered as a virtual passive linkage in inertial space, underactuated spacecrafts, underactuated surface vessels, hyper-redundant (snake-like) robots with passive joints, underwater vehicles with no base actuators, legged robots with passive joints.

The advantages of using such underactuated systems reside in the fact that they weigh less and consume less energy than their fully-actuated counterparts, and allow a more compact design and simpler communication scheme all at the expense of a more complicated control scheme than their fully-actuated counterpart. The underactuated robot concept is also useful for the reliability or fault-tolerant design of fully actuated manipulators working with dangerous materials or in remote or hazardous areas such as space, underwater, nuclear power plants, etc.

Moreover underactuation imposes constraints on the dynamics that restrict the family of trajectories that configurations, velocities and accelerations can follow. These constraints are classified as second-order nonholonomic constraints [ON91]. Though, control of mechanical systems with nonholonomic first-order (or velocity) constraints is very well-studied, the control of underactuated systems with nonholonomic second-order (or acceleration) constraints still remain on the frontier of our knowledge and remains a major open problem.

These challenges for the underactuated systems has a profound impact on the ability to plan a trajectory and design a controller. For example, underactuated systems are known to be cannot be fully feedback linearized [Sp098], which is a common control method that uses high gain feedback control to suppress the nonlinearity in the system and renders the closed loop system linear. On the other hand, underactuated systems can only be partially linearized under certain conditions. Underactuated mechanical systems can only be controlled indirectly either through contact forces with the environment or through inertial forces which rise from the nonlinear inertial coupling of the articulated system. The dynamics of a nonlinear system are much richer than the dynamics of a linear system. In this thesis we advocate to embrace the nonlinearity that originates from the dynamic coupling and to exploit these forces to achieve a high performance behaviour that cannot be achieved from a linearized system.

Mature Nonlinear optimization algorithms such as Sequential Quadratic Program (SQP) and interior point are available [Bet10] and were successfully applied on many robotic application. However, these nonlinear programs are limited to local search which often struggle to

converge to high quality solutions for particularly high dimensional problems or long trajectories. More importantly, Nonlinear optimization tools are often treated as black boxes that are very sensitive to the initial guess solution.

These challenges has motivated us to develop a novel trajectory analysis tool that can peek into the output solution and evaluate its performance. The *Dynamic Coupling Map (DCM)* help in gaining insight into the motion of the system. Our ultimate goal for studying such systems is to understand problems of dynamic locomotion in both biological systems and in robotic systems.

1.2 THESIS GOALS

The philosophical motivation of this thesis is driven by the performance gap between the motion of humans and animals and the state of art of motion control and synthesis of robotic systems. Alternatively, to put it in simpler words; why is it easy to tell animal movement from machine movements? Despite the simplicity of this question, it is very subtle and remains an open question. The complexity of the question reflects the richness of human and animal behavior which encompasses a broad range of fundamental interdisciplinary problems that still need to be understood. In the previous section, we've highlighted some of these aspects which range from understanding the principles of how the brain represents and control the high-dimensional, nonlinear, and highly-coupled DoFs to the complexity of their biological bodies as dynamical systems. But the motion richness does not just come from biological complexity, a large body of research and observations in biomechanics and sports sciences suggest that the richness of human and animals motion stems from the inter-segmental coordination and their ability to execute dynamically synergistic motions that exploit —gravity, inertia, joint coupling, elasticity, contact wrenches, and so on —as a regular part of skillful, coordinated movements

On the robotics side, in striking contrast, the prevailing philosophy of robotic motion synthesis and control relies heavily upon cancellation of the nonlinear dynamics by means of feedback linearization technique or by ignoring the dynamic coupling effects by virtue of mechanical design and decoupling controller. Clearly, the advantage of this approach is to linearize the dynamical system and be able to apply the well-founded theories for linear control and stability analysis tools. However, this approach risks the design of forced and uncoordinated behavior. This is one of the reasons that has compelled us to treat underactuated robots with torque limits. The fact that it is not feedback linearizable, the non-negligible dynamic coupling, and

the severe torque limits remove the full control authority that one enjoyed in the fully-actuated robots, thus the class of underactuated robots forces you to handle the inherent nonlinear dynamics in an unconventional way.

The philosophy behind the work in this thesis is to embrace the inherent nonlinear dynamics of the system rather than avoid them. Moreover, this work departs from the recent trending approaches such as trajectory optimization, dynamic programming, random sampling-based motion planning, reinforcement learning, and evolution strategy. All of which has remarkable success in synthesizing dynamic motions for a wide array of robotic systems. However, they do not address the fundamental principles of natural dynamic motions as they are often treated as a black-box which provide a local-optimal solution with little insight into the mechanism of the output motion. This work takes a new approach by going back to the fundamentals; first by generating dynamic motions using state of the art non-linear trajectory optimization tool and analyzing thoroughly from a dynamical perspective the pivotal role of the natural dynamics and dynamic coupling, thus abstracting the principles of natural dynamics. Subsequently, this approach enables us to synthesize natural dynamics based motion by applying directly those principles. Although this work does not provide a complete theory of natural dynamic motion, it is a stepping stone towards that ambitious goal. The contributions of this thesis can be outlined as follows:

- The introduction of the Joint Space Dynamic Coupling Ellipsoid (JS-DCE) of the passive subsystem acceleration, which describes the set of admissible accelerations of the passive subsystem while taking into consideration the second-order nonholonomic constraint imposed by the underactuation, torque bounds on the active subsystem, inertial distribution over the manipulator, gravity effect, nonlinear velocity-dependent forces, and external wrenches.
- The introduction of the "Joint Space Dynamic Coupling Map (JS-DCM)," a novel analysis technique in the joint acceleration space based on JS-DCE, to help gain insight into a dynamic trajectory and analyze the dynamic coupling between the passive and active subsystems of an underactuated robot. More importantly, it allows analyzing the pivotal role of the natural dynamics of the system on the passive joints during a dynamic motion.
- The introduction of three novel performance indexes aptly named Natural Dynamics Indexes (NDI) which allow to quantify the role of the natural dynamics during a dynamic motion and its significance with respect to the input control its physical bounds.

- Extending the formulation of the aforementioned analysis technique for floating-base systems and demonstrating its merits by applying it on a high-dimensional humanoid robot performing a vertical jump with the aid of arm swing.
- Extending the formulation of the aforementioned analysis technique for task-space acceleration analysis, thus, TS-DCE and TS-DCM allow to study the set of admissible accelerations of a particular operational point in the task space while taking into consideration different dynamic constraints and parameters (i.e. the second-order nonholonomic constraint imposed by the underactuation, torque bounds on the active subsystem, inertial distribution over the manipulator, gravity effect, nonlinear velocity-dependent forces, and external wrenches). Hence, it is possible to find the direction and magnitude of influence of each force on the task acceleration space in a graphical and intuitive manner.
- In addition, the merits of the TS-DCM analysis tool is demonstrated by applying it to the dynamic swing-up maneuver of the gymnast-robot on a high bar. The dynamic motion is formulated as a nonlinear optimal control problem which is solved using the direct collocation method. The TS-DCM along with the associated natural dynamic indexes are employed to help gain insight into the dynamic motion of the underactuated system and the associated control strategy and highlight the pivotal role of exploiting the natural dynamics to achieve the dynamic motion.
- The introduction of the Natural Dynamics based Tree (NDT), a novel kinodynamic planning algorithm which plans a dynamic motion based on the natural dynamics of the system. Moreover, the effectiveness of the proposed NDT algorithm is demonstrated on planning the motion and control of the swing-up of the Acrobot, a canonical underactuated robot which is typically used as a benchmark for control of underactuated robots. In addition, a statistical comparison between the proposed NDT algorithm and RRT—a classical kinodynamic motion planning algorithm—show that the proposed NDT algorithm is superior in terms of computation time and motion solution quality.

1.3 THESIS OUTLINE

The rest of the thesis can be outlined as follows:

- **Chapter 2** provides a complete panorama of performance metrics while highlighting the difference with the contribution in this thesis.

- **Chapter 3** introduces the JS-DCE and the JS-DCM as a novel analysis technique in the joint acceleration space analysis as well as three novel performance measures based on the aforementioned analysis while highlighting its interpretation of the natural dynamics of the system. In addition, chapter 3 extends the analysis to floating-base systems and demonstrates its merits on a high-dimensional humanoid robot performing a vertical jump with the aid of arm swing. The motion planning and control of the vertical jump are generated using the state-of-the-art trajectory optimization tool, and the JS-DCM is used as a posteriori analysis tool of the resultant motion.
- **Chapter 4** extends the formulation of the aforementioned analysis technique for task-space acceleration analysis while highlighting the interpretation of TS-DCE and the TS-DCM of the robot dynamics by applying it on a variety of underactuated manipulators with different kinematic and dynamic parameters to demonstrate clearly the mechanism of the analysis technique. Finally, chapter 4 demonstrates the merits of the TS-DCM analysis tool is demonstrated by applying it to the dynamic swing-up maneuver of the gymnast-robot on a high bar. The dynamic motion is first generated using direct collocation trajectory optimization loosely based on the actual motion of a gymnast on a high-bar. However, since trajectory optimization is often treated as a black-box providing a local-optimal trajectory without any insight into the mechanism of the motion, the TS-DCM along with the associated natural dynamic indexes are employed to help gain insight into the dynamic motion of the underactuated system and the associated control strategy and highlight the pivotal role of exploiting the natural dynamics to achieve the dynamic motion.
- **Chapter 5** introduces a novel kinodynamic motion planning algorithm based on the natural dynamics of the system. First, an overview and a taxonomy of the different kinodynamic motion planning algorithms is given while highlighting the merits of our novel algorithm. In addition, the effectiveness of the proposed NDT algorithm is demonstrated on planning the motion and control of the swing-up of the Acrobot along with a statistical comparison with RRT in terms of computation time and motion solution quality.
- **Chapter 6** concludes the thesis with discussion and suggestions for future work.

Performance measures are quintessential to the design, synthesis, study and application of robotic systems. Numerous performance measures have been defined to study the performance and behavior since the early days of robotics. We briefly review some of the relevant measures and discuss their scope and limitations. For extensive survey the reader should refer to [PS15].

[DP96] defined performance measures as a field defined on the configuration manifold, i.e. the space of all postures of the manipulator, that measures some general property of the manipulator. In other words, the theory of performance tries to answer the question "which robot configuration is optimal for a certain task? carry a heavy object? to hammer a nail?". However, this definition is more suited for fully actuated robots with quasi-static motion (low velocity) as it attempts to grasp the dynamics based on the configuration only while assuming that the velocity-dependent forces are negligible. In this thesis we show the importance of these forces in the context of highly dynamic maneuverers.

Historically, performance measures were developed for fully actuated manipulators due to the importance of their industrial applications. The need for such measures became more evident as industrial manipulators grew more complicated regarding the mechanical design and increase in DoFs. Consequently, the dynamics emerging from the coupling among multiple joints, nonlinear effects such as Coriolis and centrifugal forces, and varying inertia depending on the arm configuration made it difficult to have a good grasp of the dynamics and the overall behavior of the system. Moreover, as the bar of expected performance in terms of speed and accuracy keeps increasing these complicated dynamics become more prominent and cannot be neglected.

Performance measures can be categorized into two groups: kinematic or kinetostatic measures, and dynamic measures.

2.1 KINETOSTATIC PERFORMANCE MEASURES

Kinetostatic measures focus on studying the differential kinematics relationship, together with the statics relationship from the duality principle. The purpose of these measures is to provide a performance index that characterizes the twist/ wrench capabilities of the end ef-

factor in terms of the performance of the velocity/torque capabilities of the robot actuators. Despite the plenitude of the proposed kinetostatic performance measures, most of them depend on the forward kinematic map between joint space and task space, and in particular its Jacobian.

2.1.1 *kinetostatic manipulability*

kinetostatic manipulability [Yos85b; CBVP97] ellipsoids can be defined for each configuration of the arm. The velocity ellipsoid gives an index of the ability of performing end-effector velocities along each task space direction for a given set of joint velocities. Dually, the force ellipsoid gives an index of the ability of performing end-effector forces along each task space direction for a given set of joint torques. It can be shown that the principal axes of the two ellipsoids coincide, whereas the lengths of the axes are in inverse proportion.

The motivation to study the kinetostatic manipulability of robots comes from the fact that, in order to perform an end-effector twist or to withstand a wrench acting on the end-effector, the velocities and the efforts at the actuators are, in general, greater at configurations close to singularities. At singular configuration, some twists cannot be executed and some wrenches can only be passively resisted by the manipulator. Therefore, maintaining a manipulator away from singularities is convenient to general task execution.

The kinetostatic manipulability can have several interpretation:

- Manipulability can be interpreted as how closely the forward kinematic map of a manipulator approximates an isometry. Or in other words, as the ease of arbitrarily changing the position and orientation of the end effector at the tip manipulator.
- Manipulability can also be interpreted as the efficiency of the velocity and force transmission between the joint space and task space as certain configuration of the manipulator.

VELOCITY ELLIPSOID :

Consider a manipulator with n degrees of freedom. The joint variables are denoted by an n -dimensional vector, q . An m -dimensional vector $r = [r_1, r_2, \dots, r_m]^T$ ($m \leq n$) describes the position and/or orientation of the end effector. The kinematic relation between q and r is assumed to be

$$r = f_r(q) \quad (1)$$

The relation between the velocity vector v corresponding to r and the joint velocity \dot{q} is

$$v = J(q)\dot{q} \quad (2)$$

where $J(q)$ is the Jacobian matrix. For the sake of brevity $J(q)$ may also be written as J hereafter. Now we consider the set of all end-effector velocities v which are realizable by joint velocities contained in the unit sphere of the joint velocity space. This constraint can be defined as

$$\dot{q}^T \dot{q} \leq 1 \quad (3)$$

Or alternatively we can express the Euclidean norm of \dot{q}

$$\|\dot{q}\|^2 = (\dot{q}_1^2 + \dot{q}_2^2 + \dots + \dot{q}_n^2) \quad (4)$$

satisfies $\|\dot{q}\|^2 \leq 1$

It can be shown that the corresponding velocities in the task space are defined by

$$v^T (J^+)^T J^+ v \leq 1, \quad v \in \mathcal{R}(J) \quad (5)$$

where J^+ is the right pseudo-inverse matrix of J and $\mathcal{R}(J)$ denotes the range of J . The right pseudo-inverse matrix is given by

$$J^+ = J^T (JJ^T)^{-1} \quad (6)$$

If the manipulator is not in a singular configuration (that is, if $\text{rank } J = m$), then, since $v \in \mathcal{R}(J)$ for any v , the manipulability ellipsoid is given by

$$v^T (J^+)^T J^+ v \leq 1 \quad (7)$$

Equation (7) can be further simplified by accounting for the expression of the pseudo-inverse of J in Eq (6) to represent the velocity manipulability in its final form as

$$v^T (JJ^T)^{-1} v \leq 1 \quad (8)$$

The principal axes of the manipulability ellipsoid can be found by employing To analyze the linear mapping, the Singular Value Decomposition (SVD) of the Jacobian matrix can be written in the form

$$JJ^T = U \Sigma V^T = \sum_{i=1}^M \sigma_i u_i v_i^t \quad (9)$$

where U is the $M \times M$ orthonormal matrix of the output singular vectors u_i , V is the $N \times N$ orthonormal matrix of the input singular vectors v_i , and $\Sigma = (S0)$ is the $M \times N$ matrix whose $M \times M$ diagonal submatrix S contains the singular values σ_i of the matrix JJ^T .

It is worth noticing that the SVD is a continuous and well-behaved function of its matrix argument; therefore, the input and output singular vectors as well as the singular values do not change much in the neighbourhood of the current configuration.

The velocity ellipsoid is useful for analyzing the velocity transmission performance of the robot. The principle axes of the ellipsoid are given by the vector of U_i , which are the eigenvectors of JJ^T . The length of the principle axes are determined by the singular value $\sqrt{\sigma_i}$ of JJ^T which is equal to λ_i where $(\lambda_i, i = 1, 2, \dots, n)$ are the eigenvalues of J .

The principle axis of the velocity manipulability ellipsoid can provide several useful analytical indications of the robot's current configuration. For example, the optimum direction to generate velocity is along the major axis where the transmission ratio is maximized. Conversely, the minimum velocity in the task space for the given configuration is along the ellipsoid's minor axis. However, velocity is most accurately controlled along the minor axis. Further, the closer the ellipsoid is to a sphere i.e., unit eccentricity, the better the end-effector can move isotropically along all directions of the operational space.

FORCE ELLIPSOID :

Analogous to the velocity ellipsoid, we can also define a force ellipsoid for describing the force transmission characteristics of a manipulator at a given posture. According to the duality principle, forces in the joint space and task space are mapped via the same Jacobian through the relation

$$\tau = J^T f \quad (10)$$

where f is the force vector in the task space and τ is the joint torque vector. Hence, the set of achievable force in \mathbb{R}^m subject to the constraint $\|\tau\|^2 \leq 1$ is the ellipsoid defined by

$$f^T (JJ^T) f \leq 1 \quad (11)$$

DUALITY OF VELOCITY AND FORCE :

From Eqs. (8) and (11), the velocity ellipsoid is defined by the matrix $(JJ^T)^{-1}$, and the force ellipsoid is defined by the matrix (JJ^T) . It can be shown that both matrices share the same eigenvectors while the eigenvalues of $(JJ^T)^{-1}$ are the reciprocals of the eigenvalues of (JJ^T) . Consequently, The principal axes of the force ellipsoid coincide with the eigenvectors of the velocity ellipsoid while the length of a principle axis of the force ellipsoid is reciprocal of that of the velocity ellipsoid in the same direction. This means the optimal direction for

effecting velocity (maximum velocity transmission ratio) is also the optimal direction for controlling force (minimum force transmission ratio). Similarly, the optimal direction for effecting force is also the optimal direction for controlling velocity.

This inverse force-velocity behaviour is a direct consequence of the conservation of energy principle, which dictates that amplification in velocity transmission must invariably be accompanied by reduction in force transmission, and vice versa. This can also be explained from the control perspective, the velocity is most accurately controlled in the direction where the manipulator can resist large disturbance forces, while force is most accurately controlled in the direction where the manipulator can quickly adapt its motion.

Yoshikawa, however, has focused on an index to indicate the distance from a configuration of singularity so he proposed the manipulability index as proportional to the volume of the ellipsoid which is given by

$$w(q) = \sqrt{\det[J(q)J^T(q)]} \quad (12)$$

In case of non-redundant manipulator where $m = n$, the measure reduces to a regular determinant of the Jacobian matrix J as

$$w(q) = |\det(J(q))| \quad (13)$$

This measure is viewed as a generalized concept of the determinant, because of the followings:

- The manipulability reduces to the regular determinant in the nonredundant case.
- The manipulability becomes zero, when the workspace rank reduces at singularity, just as the regular determinant of a square Jacobian matrix does.
- since the singular values of JJ^T have the square values of those of J , the determinant of JJ^T may be regarded as if it were the square of the regular determinant of a square Jacobian matrix.
- The manipulability cannot indicate the degree of singularity when it approaches zero, just as the absolute value of the determinant of the jacobian matrix.

In linear algebra, the determinant of a matrix has been an important measure used to test the invertibility of the matrix and its nearness to singularity. Accordingly the determinant of the Jacobian matrix has been tried for the dexterity measure for both nonredundant

The driving motivation for most kinematic performance measures is to avoid Singularity to guarantee dexterity

and redundant manipulators. For nonredundant manipulators, for instance, the determinant has been used as a measure of degeneracy for the analysis of the wrist configurations. However [ALC92] noted the limitation of relying on the absolute value of the determinant to determine the invertibility of the Jacobian matrix and recommended the condition number of a matrix as a measure of the relative roundoff error amplification upon solving a linear system of equations.

2.1.2 Kinematic Isotropy

Salisbury and Craig [SC82] introduced the concept of dexterity while working on the design of articulated hands. In the pursuit of isotropic points, Salisbury et al proposed the minimization of condition number of $c(J^T)$ as an optimization criterion for link design. The author defined isotropic points as configurations with a condition number of unity by virtue of having all their singular values identical. Thus a manipulator in these configuration minimizes the error propagation from the input torque to the output force - equivalently, the velocity error propagation from joint space to workspace - for nonredundant manipulator.

$$\frac{\|\delta F\|}{\|F\|} \leq c(J^T) \frac{\|\delta \tau\|}{\|\tau\|} \quad (14)$$

This can be understood as demonstrated by the velocity/force ellipsoid, the Jacobian matrix distorts the velocity/force inputs that are uniformly applied towards all the directions joint space into an ellipsoidal outputs in the end-effector space. The condition number is used to describe the distortion in the velocity and force transmission. Along the direction of major semi-axis of the ellipsoid, disturbance in the joint space will result in larger error of end-effector in the task space. Therefore, the condition number also measures the ability of error propagation of a mechanism at some kinematical configuration

The condition can be computed in more than one ways. One of the computation defined the condition number as the ratio of the largest singular value σ_{Max} to the smallest singular value σ_{min} of the Jacobian.

$$k(J) = \frac{\sigma_{Max}}{\sigma_{min}} \quad (15)$$

2.1.3 Singular Values and Their Combinations

The determinant and the condition number of the Jacobian matrix can be expressed in terms of the singular values of the matrix: the determinant is the product of all the singular values, while the condition

number is the ratio of the largest to the smallest singular value. Thus, several variations were proposed.

Angeles [ALC92] defined kinematic isotropy as the reciprocal of the condition number $k(J)$, which denotes the singular values of the Jacobian matrix are all identical and non zero at certain

Since the minimum singular value becomes zero when the matrix is singular, and approximately determines the worst limits of the two measures, the value itself was suggested as a new measure [Klein85]. In addition to its simple expression, the measure has a relatively clear physical meaning: it may be interpreted as the minimum responsiveness in end effector velocity due to a unit change in joint velocity

Moreover, the geometric mean and harmonic mean of singular values have been proposed for the dexterity measures (yoshikawa), which may be viewed essentially as variations of the aforementioned measures.

2.1.4 Task Compatibility Index

Chiu [Chi88] had a different perspective on the utility of the velocity/force ellipsoid; he viewed the manipulator as a mechanical transformer, with joint space velocity and torques as input and task space velocity and forces as output. Chiu noted that manipulation tasks could be described as a sequence of actions in the cartesian task coordinates and for a given posture of a manipulator there are preferred directions for motion and force exertion in task coordinates. Hence, he proposed the task compatibility index to exploit the manipulator's redundancy to adjust its posture to optimize the performance of a given task.

The manipulator can be viewed as a mechanical transformer, with joint space velocity and torques as input and task space velocity and forces as output.

By varying the posture of a manipulator, we can change the shape and orientation of the velocity and force ellipsoids, and hence change the optimal directions for effecting or controlling velocity and force. The effective capability of a manipulator can be increased by adopting postures that align the optimal directions with the task directions.

The transmission ratio along a particular direction is equal to the distance from the center to the surface of the ellipsoid along the directional vector. Then if \mathbf{u} is a unit vector in the direction of interest, and the scalar α is the force transmission ratio in the direction \mathbf{u} , then $\alpha\mathbf{u}$ is a point on the ellipsoid and must satisfy equation (11)

$$(\alpha\mathbf{u})^T(\mathbf{J}\mathbf{J}^T)(\alpha\mathbf{u}) = 1 \quad (16)$$

Therefore, the force transmission ratio α is given by

$$\alpha = [\mathbf{u}^T(\mathbf{J}\mathbf{J}^T)\mathbf{u}]^{-1/2} \quad (17)$$

Conversely the velocity transmission ratio β in the direction of \mathbf{u} can be obtained as

$$\beta = [\mathbf{u}^T (\mathbf{J}\mathbf{J}^T)^{-1} \mathbf{u}]^{-1/2} \quad (18)$$

Chiu continued by defining the task compatibility index as the weighted sum of the square of both ratios.

$$c = \sum_{i=1}^l w_i \alpha_i^{\pm 2} + \sum_{j=1}^m w_j \beta_j^{\pm 2} \quad (19)$$

where the + sign is used for the directions in which the magnitude is of interest, and the – sign is used for the directions in which accuracy is of interest; w_i and w_j are weighting factors that indicate the relative magnitude or accuracy

2.2 DYNAMIC PERFORMANCE MEASURES

2.2.1 Generalized Inertia Ellipsoid (GIE)

Asada [Asa83] was one of the earliest to seek a geometrical representation of robotic manipulator dynamics. He realized that although we have efficient algorithms in recursive Lagrangian formulations and Newton-Euler formulation to calculate the dynamics, we still need an efficient and more intuitive means to analyze the behaviour of the multi-DoF motion for control and design purposes. He proposed the Generalized Inertia Ellipsoid (GIE) which gives a geometric representation of the manipulator's effective inertia seen at the end effector.

$$\text{GIE} = \mathbf{J}^{-T} \mathbf{M} \mathbf{J}^{-1} \quad (20)$$

where \mathbf{M} denotes the joint space inertia matrix of the manipulator, and \mathbf{J} is the Jacobian to the manipulator's end effector or any point of interest.

The GIE can also be seen as the generalization of the inertia ellipsoid associated with the inertia tensor \mathbf{I} of a single body. However, unlike the inertia ellipsoid of a single body, the GIE changes its orientation and size depending on the manipulator's configuration. Therefore, the GIE would measure the resistance of the robot if a human operator were holding the end effector and attempting to move it.

It is noteworthy to mention that Asada's original motivation for developing the GIE is to design a manipulator by modifying the link lengths and the distribution of mass so that the GIE is uniform in any

direction over a wide range of the reachable region. The reason for this is that when the GIE is a pure circle a better control performance is expected. This is mainly due to two main reasons:

- First, In case of circular GIE the manipulator responds accurately and uniformly in all directions while large difference in axial lengths between the major and minor axes shows that generalized moment of inertia at the tip of the arm varies significantly depending on the direction of motion.
- Second, Asada showed that dynamic nonlinear forces vanish in the case of circular GIE and they are reduced if the GIE doesn't change much in orientation and shape over the course of its movement.

LIMITATIONS: The main limitation of the GIE is that it doesn't take explicitly into account the velocity dependent forces such as Coriolis and centripetal forces nor gravity nor torque limits.

2.2.2 Dynamic Manipulability Ellipsoid (DME)

Yoshikawa [Yos85a] has extended his kinetostatic manipulability measure to a dynamic version. This measure describe the ease of accelerating arbitrarily the the manipulator's end effector while taking into consideration the dynamics of the manipulator and the torque limits. However, we will show that he has not correctly took into consideration all the robot's nonlinear dynamics except for the robot's inertia as shown by [Chi+91]. Moreover, Yoshikwa has not studied the full dynamics because in his paper he assumed that the robot's velocity is zero to neglect the nonlinear dynamic terms.

For a fully actuated manipulator, we can write the equations of motion in the following form

$$M(q)\ddot{q} + h(q, \dot{q}) + g(q) = \tau \quad (21)$$

where q is the generalized coordinates, \ddot{q} is second time derivative of q given by $\ddot{q} = \frac{d^2q}{dt^2}$, $M(q) \in \mathbb{R}^{n \times n}$ is the positive definite joint space inertia matrix, $h(q, \dot{q}) \in \mathbb{R}^n$ represents the velocity dependent torques such as centrifugal and Coriolis forces, and $g(q) \in \mathbb{R}^n$ represent the gravity induced torques.

Moreover to find the relation between joints accelerations and the acceleration of the end effector we can differentiate Eq.(2) with respect to time to get the following equation

$$\dot{v} = J\ddot{q} + a_r(q, \dot{q}) \quad (22)$$

$$a_r(q, \dot{q}) = \dot{J}\dot{q} \quad (23)$$

where a_r can be interpreted as the virtual acceleration caused by the non-linear relation between the two coordinate frames q and r , which are the joint space and the task space, respectively.

In Yoshikawa's original derivation he introduced two new variables $\tilde{\tau} \in \mathbb{R}^n$ and $\dot{\hat{v}} \in \mathbb{R}^m$

$$\tilde{\tau} = \tau - h(q, \dot{q}) - g(q) \quad (24)$$

$$\dot{\hat{v}} = \dot{v} - J\ddot{q} - a_r(q, \dot{q}) \quad (25)$$

Finally, using Eqs. (21), (22), (24) and (25) we can get a relationship between the two new variables

$$\dot{\hat{v}} = JM^{-1}\tilde{\tau} \quad (26)$$

therefore JM^{-1} can be considered as the transmission factor between $\tilde{\tau}$ and $\dot{\hat{v}}$ which can be interpreted as the joint torque space and the end effector acceleration space, respectively.

Furthermore, the Dynamic manipulability ellipsoid can be defined as the set of all $\dot{\hat{v}}$ which is realizable by the joint torque space such that

$$\|\tilde{\tau}\| \leq 1 \quad (27)$$

From Eqs. (26) and (27) this set is given by the following equation of an ellipsoid

$$\dot{\hat{v}}^T (MJ^+)^T MJ^+ \dot{\hat{v}} \leq 1, \quad \dot{\hat{v}} \in \mathcal{R}(J) \quad (28)$$

Analogous to the kientostatic manipulability we can find the Dynamic manipulability ellipsoid's orientation and size by calculating the eigenvectors and eigenvalues of the matrix $J(M^T M)^{-1} J^T$ or simply JM^{-1} principal axes by finding the singular value decomposition

$$JM^{-1} = U\Sigma V^T \quad (29)$$

the principal axes are $\sigma_1 u_1, \sigma_2 u_2, \dots, \sigma_m u_m$, where $u_i \in \mathbb{R}^m$ is the i -th column vector of U and $\sigma_i \in \mathbb{R}^m$ are the singular values.

THE RELATION BETWEEN DME AND GIE: Although both concepts were developed in a fundamentally different manner, we can show the relation between them through an intuitive example. Imagine a manipulator with a moving end-effector. Then, the GIE expresses the resistance to changing the position and orientation of the end effector

in various direction for a human operator who holds the end-effector and applies a force with a fixed magnitude. On the other hand, the DME expresses the easiness of changing the position and orientation of the end effector *via the set of actuators* which drives the manipulator joints by applying joint torques with a fixed magnitude.

the dynamic manipulability measure is proportional to the volume of the dynamic manipulability ellipsoid which gives an indication on the uniformity of the torque acceleration gain.

$$W_d = \sqrt{\det [J(M^T M)^{-1} J^T]} \quad (30)$$

The measure w_d can also be expressed as the product of the singular values

$$W_d = \sigma_1 \sigma_2 \dots \sigma_m \quad (31)$$

In case of nonredundant manipulators, i.e. when $m = n$ the dynamic manipulability measure w_d reduces to

$$W_d = \frac{|\det J|}{|\det M|} \quad (32)$$

IMPORTANT NOTES: Yoshikawa's DME does not explicitly relate the control input torques τ to the end effector's acceleration \dot{v} but rather $\tilde{\tau}$ to \tilde{v} . Recall that $\tilde{\tau}$ represents all torques acting on the joints including gravity and velocity dependent forces in addition to the control input torques.

2.2.3 Inertia Matching Ellipsoid (IME)

Kurazume et al. [KH06] introduced a new index for fully actuated serial link manipulators which indicates the torque-force transmission efficiency from the joint torques to the forces and moments (wrench) received by the load at the end-effector. This index is inspired by the impedance matching concept found in electric circuit design or mechanical gear design with the objective of maximizing the power transfer from source to load. In addition, Kurazume showed that by taking into consideration the load dynamics at the end effector which has a mass M_p , the IME index behaves as continuum between both dynamic manipulability ellipsoid and static force manipulability as the two ends of the spectrum related to the weight of the load. In other words, if the load weight is relatively very large $M_p \rightarrow \infty$ IME behaves as the static force manipulability since the manipulator dynamics can be neglected. Conversely, if the load weight is relatively very small $M_p \rightarrow 0$ then the manipulator dynamics will be dominant, thus IME will behave as the DME.

This can be shown by expressing the equation of motion of a fully actuated serial manipulator with n links and n joints and an external force applied to the end effector $F_e \in \mathbb{R}^m$

$$M(q)\ddot{q} + C(q, \dot{q}) + G(q) + J(q)^T F_e = \tau \quad (33)$$

while the motion equation for the load held at the end-effector is given as

$$F_e = M_p \ddot{x} + M_p \mathbf{g} \quad (34)$$

where $M_p \in \mathbb{R}^{m \times m}$ is the inertia matrix of the load, $\ddot{x} \in \mathbb{R}^m$ is the acceleration of the end-effector, and $\mathbf{g} \in \mathbb{R}^m$ is the gravity acceleration vector. The acceleration of the end-effector can also be defined as

$$\ddot{x} = J(q)\ddot{q} + \dot{J}(q)\dot{q} \quad (35)$$

The relation between the input torques and the external force(wrench) on the payload can be found by substituting Eqs. (34) and (35) into Eq. (33)

$$\tau = M(q)J(q)^+ M_p^{-1} [F_e - M_p \mathbf{g} - M_p \dot{J}(q)\dot{q}] + C(q, \dot{q}) + G(q) + J(q)^T F_e \quad (36)$$

Which can be simplified as

$$\tau = Q(f_e - f_{bias}) \quad (37)$$

where

$$F_{bias} = W(J(q)^T + M(q)J(q)^+ M_p^{-1})^+ [M(q)J(q)^+ (\mathbf{g} + \dot{J}(q)\dot{q}) + C(q, \dot{q}) + G(q)] \quad (38)$$

$$Q(q) = J(q)^T + M(q)J(q)^+ M_p^{-1} \quad (39)$$

W is a weighting matrix and $J(q)^+ \in \mathbb{R}^{n \times m}$ is the pseudo inverse of the Jacobian matrix $J(q)$, which is calculated in case of redundant manipulator as

$$J(q)^+ = W^{-1} J^T (JW^{-1} J^T)^{-1} \quad (40)$$

Finally, we proceed by following the derivation of the ellipsoid as in the manipulability ellipsoid by taking the norm of the torques or

the normalized torques to obtain the equation of the inertia matching ellipsoid

$$(f_e - f_{bias})^T Q^T L^{-2} Q (f_e - f_{bias}) \leq 1 \quad (41)$$

Eq. (41) describes the wrench transmitted from the joints to the load. Q which is defined in Eq. (39) can be regarded as the transmission factor. Q is the sum of two terms; the first term depend only on the Jacobian matrix $J(q)$ while the second term depends on the joint space inertia matrix $M(q)$, the Jacobian matrix $J(q)$ and the inverse of load inertia M_p . The bias force F_{bias} can be regarded as the manipulator dynamics projected at load plus the load dynamics itself.

Kurzame follows the same line of thought of yoshikawa by defining the inertia matching index as the volume of the ellipsoid which can be obtained by calculating the singular value decomposition of $Q(q)$

$$Q(q) = U \Sigma V^T \quad (42)$$

where $\Sigma = \text{diag}(\sigma_1, \sigma_2, \dots, \sigma_m) \in \mathbb{R}^{m \times n}$ is the matrix containing the singular values, while $U \in \mathbb{R}^{m \times m}$, and $V \in \mathbb{R}^{n \times n}$ are orthogonal matrices containing the singular vectors. Therefore, the measure w_{IME} can be expressed as the product of the singular values

$$w_{IME} = \sigma_1^{-1} \sigma_2^{-1} \dots \sigma_m^{-1} \quad (43)$$

2.2.4 Acceleration Radius

Unlike other performance measures which depend on a particular state, hence categorized as a local measure, the acceleration radius is considered as a global measure which indicates the maximal lower bound on the magnitude of the acceleration that can be achieved at the end effector over the entire operating region. The acceleration radius is initially proposed to measure the minimum acceleration capability of the end-effector in arbitrary directions, for given torque bounds on the actuators. the acceleration radius is defined as the largest sphere centered at the origin that is constrained in this polytope; the radius reflects the minimum guaranteed end-effector acceleration in arbitrary directions. This concept is applied to measure the end-effector acceleration radius. Although this might seems to be a conservative measure for the purpose of motion planning, it was originally developed by [GK88] to compare the dynamic performance of two or several manipulator design in terms of the maximal lower bound on the acceleration capabilities of its end-effector. The acceleration radius is obtained by solving a particular type of nonlinear

optimization called semi-infinite program (SIP), which is, a mathematical program with a finite number of decision variables and an infinite number of constraints. The infinite number of constraints arise from the fact that joint torques bounds and manipulator dynamic constraints must be satisfied over a continuum of positions, velocities and accelerations.

2.2.5 *Dynamic Capability Equation*

In [BK05] the concept of acceleration radius is generalized to capture both the force, acceleration, and velocity capabilities of the end-effector, with a view to quantifying the worst-case dynamic performance capability of a manipulator. In a series of work [BK95; BK98; BK00; BK03; Bow05], Bowling and Khatib proposed to adopt the operational space formulation of the equations of motion to analyze the tradeoffs between different capabilities, acceleration, force and velocity given torque bounds in a common framework. The driving motivation behind this type of analysis is to analyze a fully actuated manipulator's dynamic performance for tasks which require specific force and velocity such as the task of polishing the surface of a cylinder.

Another particularity of this method is that it addresses the problem of units homogeneity between the linear and angular components by treating them separately and mapping them to the torque space instead of scaling both components in the same vector.

The end result of this type of analysis is what the author defines as the *Dynamic Capability Hypersurface (DCH)* and the associated worst-case directions, which show the limitations on the force, acceleration and velocity capabilities of the robot's end-effector. The DCH is generally a six-dimensional hypersurface. The six dimensions of this space are the norm of the following capabilities of the end effector: linear velocity, linear acceleration, linear force, angular velocity, angular acceleration and the moment on the end effector. This hypersurface guarantees the isotropic performance of any of the mentioned quantity before saturating any of the actuators. Therefore, this kind of analysis is mostly adapted for the actuator design phase as it can show which actuator is oversized or undersized.

Table 1: Comparative overview on the state of the art of performance measures

	Kinetostatic Manipulability Ellipsoid [Yos85b]	Kinetostatic Manipulability Measure [Yos85b]	Dynamic Manipulability Ellipsoid [Yos85a]	Dynamic Manipulability Measure [Yos85a]	Acceleration Radius [GK88]	Dynamic Coupling Index [BLX95]	Force Polytope [CBVP97]	Inertia Matching Ellipsoid (IME) [KH06]	Dynamic Capability Hypersurface (DCH) [BK05]	Force Capacity Index (FCI) [BB18]	Thesis Contribution	
											Dynamic Coupling Map	Natural Dynamics Index
Output type	Single velocity/force ellipsoid in the task space	Scalar	Single ellipsoid in the task acceleration space	Scalar	Scalar	Scalar	Polytope in the task space	Single ellipsoid in the task space	Hypersurface in the N-D velocity-acceleration space	Scalar	Accumulate Ellipsoids in the task/joint acceleration space	Scalar
Applicable to fully-actuated manipulator	✓	✓	✓	✓	✓	✗	✓	✓	✓	✓	✗	✓
Applicable to under-actuated manipulator	✗	✗	✗	✗	✗	✓	✗	✗	✗	✗	✓	✓
Handles Inertia distribution	✗	✗	✓	✓	✓	✓	✗	✓	✓	✓	✓	✓
Handles bias forces (natural dynamics)	✗	✗	✗*	✗	✓*	✗	✗	✓*	✓*	✗	✓	✓

2.2.6 *Dynamic Coupling Measure of Space Robot Systems*

[Xu93] introduced the concept of dynamic coupling factor for space robots that represents the inertial coupling between the base motion and the end-effector motion. Due to the absence of gravity in space and by assuming no external forces the analysis is simply based on conservation of momentum. The measure is function of the manipulator configuration, geometric and inertia parameters of the manipulator and the free-floating base. Eigenvalue analysis of the coupling factor results in the direction and relative magnitude of the maximum base (or end-effector) motion produced by end-effector (or base) motion.

The driving motivation in this work is to minimize the dynamic coupling between the free-floating base and the manipulator to minimize motion disturbance and to reduce fuel consumption used in attitude control to compensate for this disturbance.

2.2.7 *Dynamic Coupling Index for Underactuated Manipulators*

Bergerman et al. [BLX95] attempted to quantify the coupling between the passive and the active joints to ensure that the controller could transmit the torques to the passive joints in order to drive them. The author proposed the dynamic coupling index based solely on the eigenvalue analysis of the inertial coupling matrix between the passive and active subsystems. The author defines the dynamic coupling index as the product of the singular values of the inertial coupling matrix, thereby the index can be regarded as the degree of invertibility and thus the capacity to transmit the torque from the active to the passive joints. However, a serious limitation of the proposed index is that it doesn't take into account the influence of gravity or the velocity-dependent forces such as Coriolis and centrifugal forces which may drastically affect the capacity of the active joints to generate acceleration at the passive joints.

2.3 CONCLUSION

We have presented a brief panorama of the different performance measures along with their original motivation, advantages, and limitations. Table 1 summarizes the state of art while highlighting the main difference with the proposed contribution in this thesis. In particular, the proposed Dynamic Coupling Map (DCM) and the associated Natural Dynamic Index (NDI) are the first analytical techniques that aim to investigate the influence of natural dynamic and its relationship with the input torques during a highly dynamic manoeuvre in both graphical and quantitative manner as demonstrated in the subsequent sections.

DYNAMIC COUPLING MAP IN THE JOINT SPACE

3.1 DYNAMIC COUPLING MAP FOR UNDERACTUATED MANIPULATORS

3.1.1 Underactuated Manipulator Lagrangian Dynamics

Consider a dynamic system defined on a configuration manifold \mathcal{Q} . let $(q, \dot{q}) = (q^1, \dots, q^n, \dot{q}^1, \dots, \dot{q}^n)$ denote local coordinates on the tangent bundle $\mathcal{T}\mathcal{Q}$. We refer to q, \dot{q} , and \ddot{q} as the vectors of generalized coordinates, generalized velocities, and generalized accelerations, respectively. Let the system possess a control input space of dimension $a < n$, where $u \in \mathbb{R}^a$ denote the vector of the control variables. Thus, we have $\dim(q_a) = a$ degrees of freedom which the control input act upon and $\dim(q_p) = n - a$ are the passive degrees of freedom with no direct control. Without loss of generality, we decompose the set of generalized coordinates $q = (q^1, \dots, q^n) \in \mathbb{R}^n$ into $q = (q_p, q_a)$ where $q_p \in \mathbb{R}^p$, $q_a \in \mathbb{R}^a$ denote the passive generalized coordinate vector and the actuated generalized coordinate vector, respectively. The generalized coordinates vector can be written as

$$q = \begin{bmatrix} q_p((n-a) \times 1) \\ q_a(a \times 1) \end{bmatrix} \in \mathfrak{X}^n \quad (44)$$

Accordingly, we can express the decomposed Euler-Lagrange equation of motion for the serial underactuated manipulator in its canonical form as

$$\begin{pmatrix} M_{pp}(q) & M_{pa}(q) \\ M_{pa}^T(q) & M_{aa}(q) \end{pmatrix} \begin{pmatrix} \ddot{q}_p \\ \ddot{q}_a \end{pmatrix} + \begin{pmatrix} C_{pp}(q, \dot{q}) & C_{pa}(q, \dot{q}) \\ C_{ap}(q, \dot{q}) & C_{aa}(q, \dot{q}) \end{pmatrix} \begin{pmatrix} \dot{q}_p \\ \dot{q}_a \end{pmatrix} + \begin{pmatrix} G_p(q) \\ G_a(q) \end{pmatrix} + \begin{pmatrix} B_p(\dot{q}) \\ B_a(\dot{q}) \end{pmatrix} - \begin{pmatrix} J_p^T(q)F \\ J_a^T(q)F \end{pmatrix} = \begin{pmatrix} \mathbf{0}_{n_p \times 1} \\ \tau_{n_a \times 1} \end{pmatrix} \quad (45)$$

Equation (45) describe the dynamics of the underactuated serial manipulator as two subsystems, namely, the active subsystem and the passive subsystem, thus coupling between the two subsystems appears explicitly. Equation (45) accounts for inertial forces, gyroscopic forces, gravity, damping forces and external wrench. For the detailed derivation, reader is referred to chapter (2). However, the physical interpretation of each term can be given as following:

- $M_{pp}(q)$: represents the joint space inertia matrix for the system seen at the passive articulating subsystem with a dimension of $n_p \times n_p$. The dependence of the passive inertia matrix of the generalized coordinates depend on the distribution of actuators over the manipulator's DoF. For example, a special case where the passive inertia matrix can depend only on the passive generalized coordinates $M_{pp}(q_p)$ is when the passive links are grouped at the end of the serial manipulator w.r.t the frame of reference at the fixed base. Otherwise, the inertia matrix of the manipulator seen at the passive subsystem can generally be expressed as $M_p + M_{p/a}$ which is the sum of the inertia of the passive subsystem and the part of the manipulator affecting the passive subsystem, respectively.
- $M_{aa}(q)$: represents the inertia matrix of the active articulating subsystem. The same argument regarding the dependence of the active inertia matrix on the generalized coordinates can be given as for the passive inertia matrix.
- $M_{pa}(q)$: denotes the $p \times a$ inertial coupling matrix between the passive and the active articulating subsystems. If M_{pa} is a null matrix, then no coupling exist between the passive and active subsystems, consequently the motion of the passive subsystem is independent of the motion of the active subsystem. Conversely, If M_{pa} has a full rank or its rank is at equal to the number of Dof of the passive subsystem $\text{rank}(M_{pa}) = n - a = p$ then the system is called *strongly coupled*. Also note that due to the symmetry of in the joint-space inertia matrix of the manipulator then $M_{ap}(q) = M_{pa}^T(q)$.
- \ddot{q}_p, \ddot{q}_a : are the $p \times 1$ generalized acceleration vector of the passive subsystem and the $p \times 1$ active generalized acceleration vector, respectively.
- $\tau \in \mathbb{R}^{n_a \times 1}$ vector of joint torques acting on the active subsystem, assuming that the active subsystem system is fully actuated.
- $C_{pp}(q, \dot{q})$: the velocity dependent gyroscopic torques containing the Coriolis and centrifugal terms $C(q, \dot{q})$ can be decomposed in the same manner as with the manipulator's joint space inertia matrix. Hence, $C_{pp}(q, \dot{q}) \in \mathbb{R}^{n_p \times n_p}$ denotes the velocity dependent gyroscopic torques on the passive subsystem as if it was isolated.
- $C_{aa}(q, \dot{q}) \in \mathbb{R}^{n_a \times n_a}$ denotes the the velocity dependent gyroscopic (Coriolis/centrifugal) torques on the active subsystem as if it was isolated.

- $C_{pa}(q, \dot{q}) \in \mathbb{R}^{n_p \times n_a}$ denotes the the velocity dependent gyroscopic (Coriolis/centrifugal) torques from the active subsystem acting on the passive subsystem.
- $C_{ap}(q, \dot{q}) \in \mathbb{R}^{n_a \times n_p}$ denotes the the velocity dependent gyroscopic (Coriolis/centrifugal) torques from the passive subsystem acting on the active subsystem.
- $G_p(q) \in \mathbb{R}^{n_p \times 1}$ denotes the generalized gravitational torque vector acting on the passive subsystem.
- $G_a(q) \in \mathbb{R}^{n_a \times 1}$ denotes the generalized gravitational torque vector acting on the active subsystem.
- $B_p(\dot{q}) \in \mathbb{R}^{n_p \times 1}$ denotes the generalized damping torque vector acting on the passive subsystem.
- $B_a(\dot{q}) \in \mathbb{R}^{n_a \times 1}$ denotes the generalized damping torque vector acting on the active subsystem.
- $J_p^T(q)F \in \mathbb{R}^{n_p \times 1}$ denotes the external wrench projected on the passive generalized coordiantes.
- $J_a^T(q)F \in \mathbb{R}^{n_a \times 1}$ denotes the external wrench projected on the active generalized coordiantes.

For the sake of clarity of demonstration and without loss of generality Eq (45) can be simplified as

$$\begin{pmatrix} M_{pp} & M_{pa} \\ M_{pa}^T & M_{aa} \end{pmatrix} \begin{pmatrix} \ddot{q}_p \\ \ddot{q}_a \end{pmatrix} + \begin{pmatrix} \mathcal{N}_p(q, \dot{q}) \\ \mathcal{N}_a(q, \dot{q}) \end{pmatrix} = \begin{pmatrix} 0 \\ \tau \end{pmatrix} \quad (46)$$

where

$$\mathcal{N}_p(q, \dot{q}) = C_p(q, \dot{q}) + G_p(q) + B_p(\dot{q}) - J_p^T(q)F \quad (47)$$

$$\mathcal{N}_a(q, \dot{q}) = C_a(q, \dot{q}) + G_a(q) + B_a(\dot{q}) - J_a^T(q)F \quad (48)$$

- $\mathcal{N}_a(q, \dot{q})$: is the generalized bias force, it follows that it is the value that τ would have to take in order to produce zero joint acceleration, assuming that all the other joint accelerations are zero. Generalized bias force is a vector of force terms that account for Coriolis and centrifugal forces, gravity.
- $\mathcal{N}_p(q, \dot{q})$: is the generalized bias force acting on the passive subsystem.

3.1.2 Dynamic Coupling in the Passive Joint Acceleration Space

Kinematic and dynamic coupling between the active articulated system and the passive subsystem is usually regarded as unwanted perturbation that degrades positioning accuracy and operational dexterity. In this work we attempt to exploit the dynamic coupling between the unactuated subsystem and its associated active articulated subsystem. We will start first by exploring the relationship between the acceleration space of the unactuated subsystem and the torque space of the active articulating subsystem.

The dynamic equations of the system (46) can be decomposed into two main equations; one describing the dynamics of the passive free-floating base.

$$M_p \ddot{q}_p + M_{pa} \ddot{q}_a + \mathcal{N}_p = 0 \quad (49)$$

and the second equation describing the dynamics of the articulated system

$$M_a \ddot{q}_a + M_{pa}^T \ddot{q}_p + \mathcal{N}_a = \tau \quad (50)$$

For the sake of clarity, we dropped the dependence of the force bias terms $\mathcal{N}_{a,p}$ on q, \dot{q} .

Definition 3.1.1. *The underactuated mechanical system (45) is locally Strongly Inertially Coupled if and only if*

$$\text{rank}(M_{pa}(q)) = n - a = p \quad \text{for all } q \in \mathcal{B}$$

where \mathcal{B} is a neighborhood of the origin. The Strong Inertial Coupling is global if the rank condition holds for all $q \in \mathcal{Q}$

the strong inertial coupling condition [Spo98] requires that the number of active degrees of freedom be at least as great as the number of passive degrees of freedom. This condition can be thought of as an analogue of controllability. Note that that this condition is configuration dependent, therefore it is defined locally. A system is can have the property of *Global Strong Inertial Coupling* if the rank condition is valid for every configuration

Under the assumption of Strong Inertial Coupling we may compute the pseudo-inverse M_{pa}^\dagger for M_{pa} as

$$M_{pa}^\dagger = M_{pa}^T (M_{pa} M_{pa}^T)^{-1} \quad (51)$$

Then active joints generalized accelerations \ddot{q} in (49) can be expressed as

$$\ddot{q}_a = -M_{pa}^\dagger M_p \ddot{q}_p - M_{pa}^\dagger \mathcal{N}_p \quad (52)$$

By substituting (52) in (50), we can find a relation between the acceleration of the passive subsystem and its *acting surrounding*, which include; joint torques, nonlinear inertial forces, gravity and wrench acting on the end points of the articulated system, if exists.

$$\ddot{q}_p \left(M_{pa}^T - M_a M_{pa}^\dagger M_p \right) - M_a M_{pa}^\dagger \mathcal{N}_p + \mathcal{N}_a = \tau \quad (53)$$

we finally express equation (53) as

$$\ddot{q}_p = \mathcal{Z}^\dagger \left(\tau + \tilde{\mathcal{N}} \right) = \ddot{q}_{p\tau} + \ddot{q}_{p\text{bias}} \quad (54)$$

where we introduce the *dynamic coupling factor* \mathcal{Z}^\dagger as

$$\mathcal{Z}^\dagger = \left(M_{pa}^T - M_a M_{pa}^\dagger M_p \right)^\dagger \quad (55)$$

\mathcal{Z} is the Schur complement [KBo8] of the inertia coupling M_{pa} between the passive subsystem and the active articulating system We denote, as well, the bias term.

$$\tilde{\mathcal{N}} = M_a M_{pa}^\dagger \mathcal{N}_p - \mathcal{N}_a \quad (56)$$

Equation (54) provides an intuitive comprehension of the influence of different forces on the motion of the passive subsystem. The acceleration of the passive subsystem can be viewed as the sum of two sources of motion:

- $\ddot{q}_{p\tau}$ is the acceleration caused by the torque τ , which is transmitted from the active subsystem to the passive subsystem through the transmission factor or the dynamic coupling factor \mathcal{Z}^\dagger . Note that from Eq. (55), the dynamic coupling factor \mathcal{Z}^\dagger depends on the inertial coupling M_{pa} , therefore if $M_{pa}(q)$ is a null matrix then it wouldn't be possible to control the passive subsystem via the control input τ . Conversely, the dynamic coupling factor is maximized by maximizing $M_{pa}(q)$.
- $\ddot{q}_{p\text{bias}}$ is the bias acceleration due to gravity, non-linear velocity dependent forces (Coriolis, centrifugal, damping), and wrenches -if exist- acting on the passive subsystem which include part of these forces coming from the active subsystem as well. This term can also be considered as the acceleration due to the natural dynamics of the passive subsystem, because this acceleration persist even if the control input vector is null.

Furthermore, we note that the inverse of the dynamic coupling factor \mathcal{Z}^\dagger act as transmission factor between the control input space τ and the acceleration space of the passive subsystem. \mathcal{Z}^\dagger is configuration-dependent matrix. Thereby, it is possible to search for the configuration that maximizes the dynamic coupling factor which will result in

a decrease in the effort expenditure. However, in dynamic manoeuvres with high velocities the motion planning approach should be state based rather than configuration based. In addition, in such scenarios, the natural dynamics, represented by the bias term $\ddot{q}_{p_{bias}}$, becomes dominant. Therefore, planning highly dynamic motion while exploiting these forces can result in highly efficient and graceful motion.

This formulation of the dynamic equation helps in analyzing the effects of these three sets of variables on the achievable set of passive subsystem acceleration.

Note that the previous derivation of Eq. (54) is valid if and only if M_{pa} is non singular and that the inverse of the Schur complement M_{pa}^T of M_{pa} . An alternative and equivalent formulation of Eq. (54) but more robust to singularity is to consider the inverse of the 2×2 block matrix of the joint space inertia matrix.

According to [LS02], there are four different but equivalent inverse matrices of the 2×2 matrix. If $n_a \geq n_p$ then the Schur complement $M_{aa} - M_{pa}^T M_{pp}^{-1} M_{pa}$ is invertible assuming M_{pp}^{-1} is nonsingular. We can express the inverse of the 2×2 joint space inertia block matrix as

$$\begin{aligned} \begin{pmatrix} M_{pp} & M_{pa} \\ M_{pa}^T & M_{aa} \end{pmatrix}^{-1} &= \begin{bmatrix} \zeta_{pp} & \zeta_{pa} \\ \zeta_{ap} & \zeta_{aa} \end{bmatrix} \\ &= \begin{bmatrix} M_{pp}^{-1} + M_{pp}^{-1} M_{pa} \zeta_{pp}^{-1} M_{pa}^T M_{pp}^{-1} & -M_{pp}^{-1} M_{pa} \zeta_{pp}^{-1} \\ -\zeta_{pp}^{-1} M_{pa}^T M_{pp}^{-1} & \zeta_{pp}^{-1} \end{bmatrix} \end{aligned} \quad (57)$$

where ζ_{pp} is the Schur complement of M_{aa}

$$\zeta_{pp} = M_{aa} - M_{pa}^T M_{pp}^{-1} M_{pa} \quad (58)$$

If $n_p \geq n_a$ then the Schur complement $M_{pp} - M_{pa} M_{aa}^{-1} M_{pa}^T$ is invertible assuming M_{aa}^{-1} is nonsingular. We can express the inverse of the 2×2 joint space inertia block matrix as

$$\begin{aligned} \begin{pmatrix} M_{pp} & M_{pa} \\ M_{pa}^T & M_{aa} \end{pmatrix}^{-1} &= \begin{bmatrix} \zeta_{pp} & \zeta_{pa} \\ \zeta_{ap} & \zeta_{aa} \end{bmatrix} \\ &= \begin{bmatrix} \zeta_{aa}^{-1} & -\zeta_{aa}^{-1} M_{pa} M_{aa}^{-1} \\ -M_{aa} M_{pa}^T \zeta_{aa}^{-1} & M_{aa}^{-1} + M_{aa}^{-1} M_{pa}^T \zeta_{aa}^{-1} M_{pa} M_{aa}^{-1} \end{bmatrix} \end{aligned} \quad (59)$$

where ζ_{aa} is the Schur complement of M_{aa}

$$\zeta_{aa} = M_{pp} - M_{pa} M_{aa}^{-1} M_{pa}^T \quad (60)$$

We can then reformulate Eq.(46) as

$$\begin{pmatrix} \ddot{q}_p \\ \ddot{q}_a \end{pmatrix} = \begin{pmatrix} \zeta_{pp} & \zeta_{pa} \\ \zeta_{ap} & \zeta_{aa} \end{pmatrix} \begin{pmatrix} -\mathcal{N}_p \\ \tau - \mathcal{N}_a \end{pmatrix} \quad (61)$$

Hence, the passive subsystem acceleration from Eq.(54) can be reformulated as

$$\ddot{q}_p = \ddot{q}_{p\tau} + \ddot{q}_{p\text{bias}} \quad (62)$$

where

$$\ddot{q}_{p\tau} = \zeta_{pa}\tau \quad (63)$$

$$\ddot{q}_{p\text{bias}} = -\zeta_{pa}\mathcal{N}_a - \zeta_{pp}\mathcal{N}_p \quad (64)$$

We can see from Eq.(63) and Eq.(64) that all forces originating from the active subsystem including the control input τ are modulated or transmitted via the factor ζ_{pa} which depends on the inertial coupling M_{pa} . Therefore, the action of ζ_{pa} can be regarded as *projecting and modulating* all forces from the active subsystem to the acceleration of the passive subsystem.

3.1.3 Dynamic Coupling Ellipsoid in the Passive Joint Acceleration Space

The goal of the dynamic coupling ellipsoid is to represent geometrically, in the acceleration space, the ensemble of the accelerations achievable by the unactuated subsystem while taking into consideration the torque limits on the active subsystem and the natural dynamics affecting the acceleration limits such as gravity and gyroscopic forces.

The torque limits at each actuator in the active subsystem are assumed to be symmetrical, that is,

$$-\tau_{i,\max} \leq \tau_i \leq \tau_{i,\max}, \quad i = 1, \dots, n_a \quad (65)$$

Each actuator may have unique bounding torque. As such, Eq. (65) may be normalized via the introduction of the diagonal matrix L whose diagonal terms are $L_{ii} = \frac{1}{\tau_{i,\max}}$. The normalized joint torque vector $\tilde{\tau}$ can be expressed as

$$\tilde{\tau} = L^{-1}\tau \quad (66)$$

where the scaling matrix L is given by

$$L = \text{diag}(\tau_{1,\max}, \tau_{2,\max}, \dots, \tau_{n,\max}) \quad (67)$$

Each inequality constraint in Eq. (65) defines a closed half-space in the torque space. The set of admissible torques can then be represented as a unit hypercube defined by $2n_a$ inequalities written in the following compact form

$$\|\tilde{\tau}\|_{\infty} \leq 1 \quad (68)$$

Substituting $L\tilde{\tau}$ for τ in Eq. (62) yields

$$\ddot{q}_p = \zeta_{p\alpha} L \tilde{\tau} + \ddot{q}_{p\text{bias}} \quad (69)$$

where $\ddot{q}_{p\text{bias}}$ from Eq.(64) represents the acceleration of the passive subsystem due to natural dynamics, i.e., when the joint actuators are quiescent, $\tilde{\tau} = 0$.

Eq. (69) and Eq. (68) maps the n_a -dimensional hypercube to a polytope of dimension n_p in the passive acceleration space that delimits the set of feasible accelerations. Alternatively, the feasible torque represented by hypercube in the torque space can be approximated as a n_a -dimensional sphere defined by l2 norm of the torque $\|\tilde{\tau}\| \leq 1$ as

$$\tilde{\tau}^T \tilde{\tau} \leq 1 \quad (70)$$

Substituting Eq.(62) in Eq.(104) yields the equation of a n_p -dimensional ellipsoid in the acceleration space of the passive subsystem. Note that this ellipsoid is the approximation of the acceleration polytope defined in Eq.(69)

$$(\ddot{q}_p - \ddot{q}_{p\text{bias}})^T (\zeta_{p\alpha} L)^{-T} (\zeta_{p\alpha} L)^{-1} (\ddot{q}_p - \ddot{q}_{p\text{bias}}) \leq 1 \quad (71)$$

Since L is a symmetric matrix, the previous result simplifies to

$$(\ddot{q}_p - \ddot{q}_{p\text{bias}})^T \tilde{\mathcal{Z}}^{-1} (\ddot{q}_p - \ddot{q}_{p\text{bias}})^T \leq 1 \quad (72)$$

where

$$\tilde{\mathcal{Z}} = \zeta_{p\alpha}^T L^2 \zeta_{p\alpha} \quad (73)$$

We denote by Eq. (72) the *Dynamic Coupling Ellipsoid in the joint space*. Note that this ellipsoid is the approximation of the achievable passive acceleration whose convex envelope is bounded by the polytope defined in Eq.(69). $\ddot{q}_{p\text{bias}}$ represents the offset of the center of the ellipsoid from the origin of the acceleration space, while the matrix $\tilde{\mathcal{Z}} \in \mathbb{R}^{n_p \times n_p}$, which depends on the torque limits L and the inertial coupling $M_{p\alpha}$, determines the size and the orientation of the ellipsoid. More insights are explored in details in [Section 3.1.3.2](#).

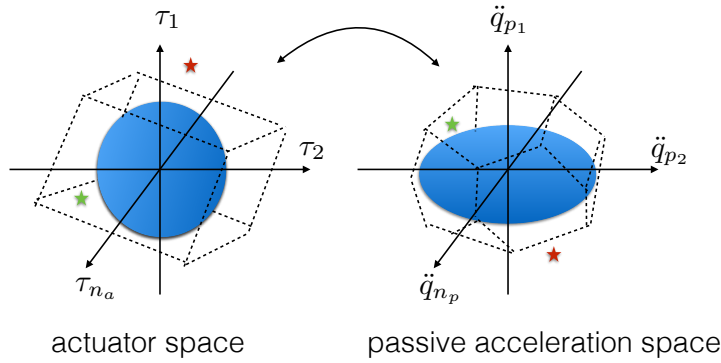


Figure 1: Mapping between the input actuator space and the passive acceleration space

3.1.3.1 Visualizing the relation between torque space and the passive acceleration space

The goal of these analyses, particularly in Eq. (68)-Eq.(72), is to explore the mapping between passive subsystem n_p acceleration space and the n_a actuator torque space, using different representations of the available torque and attainable acceleration. Figure 1 illustrates the various representations and highlights their differences.

The physical capacity of the control input is represented by the torque limits in Eq. (65). The set of inequality constraints in Eq. (65) defines an n_a -orthope (hyper-rectangle) in the n_a torque space. Mapping these torque bounds to the acceleration space of the passive subsystem using Eq. (62) yields a polyhedron with a pair of n_a parallel faces in the n_p -dimensional passive acceleration space, as shown in Figure 1. The l2-norm of normalized torques in Eq. (104) defines a unit n_a -hypersphere in the n_a -torque space. This sphere is inscribed in the n_a -hypercube defined in Eq. (68) and can be considered as an approximation. It follows from Eq.(72), that the n_a hypersphere torque bounds in the n_a -dimensional torque space is mapped to an n_p -dimensional ellipsoid in the n_p -dimensional passive acceleration space.

3.1.3.2 Interpretation of the Dynamic Coupling Ellipsoid

The major advantage of approximating the n_p polyhedron to an n_p -dimensional ellipsoid is to simplify the analysis of the achievable ac-

celerations of the passive system. In particular, it is sufficient to know the position of the center of the ellipsoid in the acceleration space, its orientation and the lengths of its semi-axes to have a complete knowledge of the attainable acceleration of the passive subsystem at a certain robot's state.

The Dynamic Coupling Ellipsoid (DCE) of the passive subsystem acceleration –which describes the set of admissible passive accelerations given the manipulator's state (generalized configuration and velocities) while taking into consideration the torque bounds on the active subsystem, inertial distribution over the manipulator, gravity effect, nonlinear velocity-dependent forces, and external wrenches (if it exist), is given by the equation of an ellipsoid in center form

Definition 3.1.2. *The Dynamic Coupling Ellipsoid (DCE) of the passive subsystem of an underactuated manipulator is*

$$\mathcal{E}_{\ddot{q}_p} = \{ \ddot{q}_p \in \mathbb{R}^{n_p} \mid (\ddot{q}_p - \ddot{q}_{p_{\text{bias}}})^T \tilde{\zeta}^{-1} (\ddot{q}_p - \ddot{q}_{p_{\text{bias}}})^T \leq 1 \} \quad (74)$$

where $\ddot{q}_{p_{\text{bias}}} \in \mathbb{R}^{n_p}$ is the center of the ellipsoid $\mathcal{E}_{\ddot{q}_p}$ while the dynamic coupling factor $\tilde{\zeta} \in \mathbb{S}_{++}^{n_p}$ determines the size and orientation of $\mathcal{E}_{\ddot{q}_p}$

Note that from Eq.(73), $\tilde{\zeta}$ depends on the diagonal torque bounds matrix L and the inertia distribution of the manipulator ζ_{p_a} which, in turn, crucially depends on the inertial coupling M_{p_a} as shown in Eq.(57) or Eq. (59). As noted earlier, all inertia submatrices are configuration dependent, thus, $\tilde{\zeta}$ is configuration dependent as well. $\tilde{\zeta}$ matrix is a real, symmetric, positive-definite matrix. Consequently, it has orthogonal eigenvectors and real, positive eigenvalues. Let the singular-value decomposition of the dynamic coupling factor, $\tilde{\zeta}$, be

$$\tilde{\zeta} = U \Sigma V^T \quad (75)$$

$$= \underbrace{\begin{pmatrix} \mathbf{u}_1 & \dots & \mathbf{u}_{r+1} & \dots & \mathbf{u}_p \\ \left| \right. & & \left| \right. & & \left| \right. \\ \left(\begin{array}{c} \vdots \\ \vdots \\ \vdots \end{array} \right) & & \left(\begin{array}{c} \vdots \\ \vdots \\ \vdots \end{array} \right) & & \left(\begin{array}{c} \vdots \\ \vdots \\ \vdots \end{array} \right) \\ \left. \right) & & \left. \right) & & \left. \right) \\ \text{col}(A) & & \text{null}(A) & & \end{pmatrix} \begin{pmatrix} \sigma_1 & & & & \\ & \ddots & & & \\ & & \mathbf{O} & & \\ & & & \sigma_r & \\ & & & & 0 \\ \mathbf{O} & & & & \ddots \\ & & & & & 0 \end{pmatrix} \underbrace{\begin{pmatrix} \text{---} \\ \vdots \\ \text{---} \\ \vdots \\ \text{---} \\ \vdots \\ \text{---} \end{pmatrix}}_{\begin{matrix} \left. \begin{matrix} \vdots \\ \vdots \\ \vdots \end{matrix} \right\} \text{row}(A) \\ \left. \begin{matrix} \vdots \\ \vdots \\ \vdots \end{matrix} \right\} \text{null}(A) \end{matrix}} \begin{matrix} \left. \begin{matrix} \vdots \\ \vdots \\ \vdots \end{matrix} \right\} v_1^T \\ \left. \begin{matrix} \vdots \\ \vdots \\ \vdots \end{matrix} \right\} v_r^T \\ \left. \begin{matrix} \vdots \\ \vdots \\ \vdots \end{matrix} \right\} v_{r+1}^T \\ \left. \begin{matrix} \vdots \\ \vdots \\ \vdots \end{matrix} \right\} v_n^T \end{matrix} \quad (76)$$

where $\tilde{\mathcal{Z}}$ is a rank r matrix, $U \in \mathbb{R}^{n_p \times n_p}$ and $V \in \mathbb{R}^{n_a \times n_a}$ are orthogonal matrices. The principal axes of the n_r -dimensional ellipsoid is determined by the eigenvectors u_1, u_2, \dots, u_r . While the corresponding lengths of the semi-axes are given by $\sqrt{\sigma_1}, \sqrt{\sigma_2}, \dots, \sqrt{\sigma_r}$ where $\sqrt{\sigma_1} \geq \sqrt{\sigma_2} \geq \dots \geq \sqrt{\sigma_r}$. Thus, the principal axes of the DCE $\mathcal{E}_{\ddot{q}_p}$ are

$$\sqrt{\sigma_1}u_1, \sqrt{\sigma_2}u_2, \dots, \sqrt{\sigma_r}u_r$$

Similar to the dynamic manipulability ellipsoid, the volume of the ellipsoid dynamic coupling ellipsoid $\mathcal{E}_{\ddot{q}_p}$ is proportional to the determinant of the dynamic coupling factor $\det(\tilde{\mathcal{Z}})$, or equivalently, the product of its singular values $\sigma_1 \sigma_2 \dots \sigma_r$.

However, unlike the dynamic manipulability ellipsoid which is defined only for fully actuated manipulators, as shown in Eq.(28), the dynamic coupling ellipsoid correctly accounts for the underactuation constraint. In addition, the interpretation of the ellipsoid is different in this case, the volume of the ellipsoid determines the manipulator's ability to transmit the joint torques indirectly through the inertial coupling. Therefore, the volume of the ellipsoid $\mathcal{E}_{\ddot{q}_p}$ is directly proportional to the ability of the underactuated manipulator to indirectly control the passive subsystem. If all the singular values of the ellipsoid are zero, then this indicates that the underactuated manipulator has no authority to influence the acceleration the passive subsystem by means of the control input torques at the given configuration q . Moreover, If one of the singular values is zero, then the manipulator is dynamically degenerate in the direction of the corresponding singular vector in the passive acceleration space, and no torque can be transmitted in that direction.

On the other hand, the term \ddot{q}_{bias} is responsible for translating the ellipsoid center from its origin. This term has been overlooked or neglected in all previous work except for few studies which studied special cases on a fully actuated manipulator. We introduce *the Joint Space Dynamic Coupling Map (JS-DCM)*, which helps in analyzing the relationship between the joint space DCE $\mathcal{E}_{\ddot{q}}$, its principal axis, and the vector \ddot{q}_{bias} in the passive joint acceleration space, as shown in [Figure 2](#). More importantly, it has a pivotal role in providing graphical and intuitive manner to analyze the evolution this relationship in a dynamic trajectory. The term \ddot{q}_{bias} groups all forces on the passive subsystem except the input control torque. Therefore, it represents the natural dynamics of the passive subsystem as previously defined in [Chapter 1](#). The term \ddot{q}_{bias} have strong implications on the behaviour of the underactuated manipulator which have not been considered in previous studies. For example, if the origin is not included in the

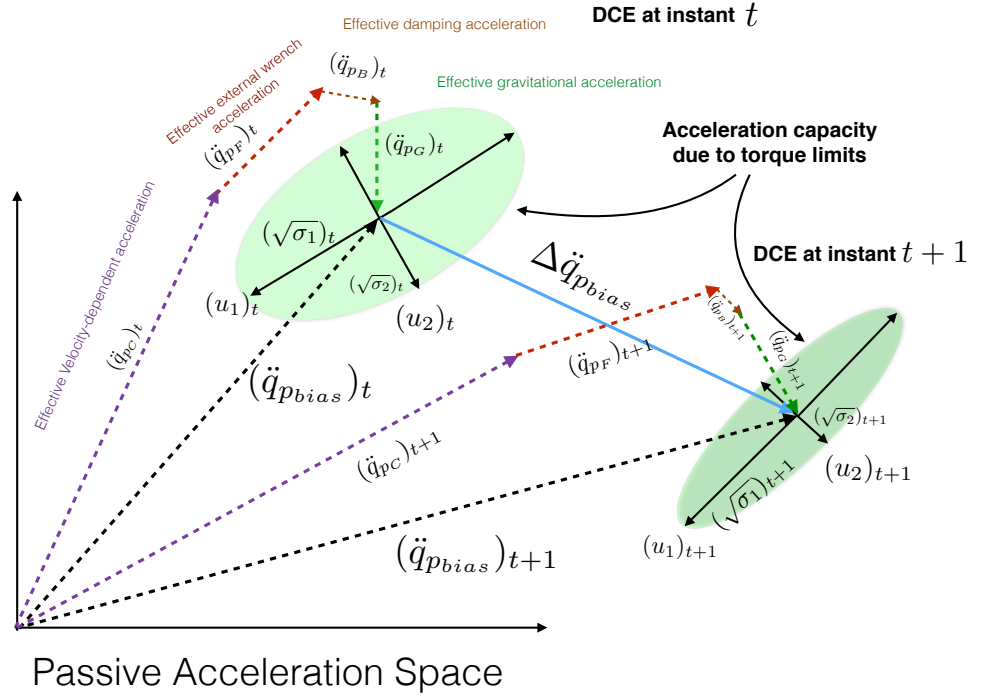


Figure 2: Illustration of the Joint Space Dynamic Coupling Map (JS-DCM)

ellipsoid this means that that passive subsystem has a considerable drift acceleration due to the natural dynamics and that the physical capacity of the actuators cannot bring the passive subsystem to a halt. Moreover, the ellipsoid's center displacement due to the term \ddot{q}_{pbias} is a \mathbb{R}^{n_p} vector in the passive acceleration space which can be decomposed to its original constituents. Eq. (64) describes an affine relation between the natural dynamics of the active subsystem \mathcal{N}_a projected to space of the passive subsystem through the dynamic coupling ζ_{pa} , in addition to the natural dynamics of the passive subsystem itself \mathcal{N}_p . Recall that from Eqs.(47) and (48), \mathcal{N}_p and \mathcal{N}_a depend on gravity, velocity dependent forces, damping and external wrench, if exist. Hence, it is possible to find the direction and magnitude of influence of each force on the passive subsystem acceleration in a graphical and intuitive manner.

$$\ddot{q}_{pbias} = \ddot{q}_{pG} + \ddot{q}_{pC} + \ddot{q}_{pB} + \ddot{q}_{pF} \quad (77)$$

Where the gravitational effect on the acceleration of the passive subsystem on \ddot{q}_p is represented by the displacement vector $\ddot{q}_{pG} \in \mathbb{R}^{n_p}$ of the center of the ellipsoid $\mathcal{E}_{\ddot{q}_p}$. From Eqs. (64), (48), and (47) it can be expressed as

$$\ddot{q}_{p_G} = -\zeta_{p_a} G_a - \zeta_{p_p} G_p \quad (78)$$

Accordingly, the effect of the nonlinear velocity dependent forces, damping, and external wrenches can be expressed as

$$\ddot{q}_{p_C} = -\zeta_{p_a} C_a - \zeta_{p_p} C_p \quad (79)$$

$$\ddot{q}_{p_B} = -\zeta_{p_a} B_a - \zeta_{p_p} B_p \quad (80)$$

$$\ddot{q}_{p_F} = -\zeta_{p_a} F_a - \zeta_{p_p} F_p \quad (81)$$

3.1.4 Natural Dynamic Index in the Passive Acceleration Space

We propose three performance indices derived from the DCM analysis tool. These performance indices describe the relationship between the influence of the natural dynamics and the input torque along with its limits on the acceleration of a particular body part or a subsystem. Thus, the performance measure is aptly named as *Natural Dynamic Index (NDI)*, or in this particular case the passive acceleration space Natural Dynamic Index.

The first index of the three variants is named *NDI-1*, and it describes the scalar ratio of the natural dynamics influence represented by the norm of $\|\vec{q}_{p_{bias}}\|$ to the norm of the eigenvalues of DCE, $\|\sigma\|$, which is an approximation the maximum torque influence on the passive acceleration space.

$$NDI-1 = \frac{\|\vec{q}_{p_{bias}}\|}{\|\sigma\|} \quad (82)$$

NDI-1 is important to understand the significance of the natural dynamics in a particular dynamic motion e.g. if $NDI-1 \gg 1$ then it would signify that the torque capacity of the underactuated robot cannot override the natural dynamics and vice versa.

The second natural dynamic index *NDI-2* describes the absolute value of cosine the angle between the vector of the effective acceleration due to the natural dynamics on the passive acceleration, $\vec{q}_{p_{bias}}$, and the major axis of the DCE, \vec{u}_1 , which represents the direction of the maximum torque transmission in the passive acceleration space.

$$NDI2 = \left| \frac{(\vec{u}_1 \cdot \vec{q}_{p_{bias}})}{(\|\vec{u}_1\| \cdot \|\vec{q}_{p_{bias}}\|)} \right| \quad (83)$$

NDI-2 attempts to grasp the relationship between the natural dynamics and the ability of the system to exploit these forces. *NDI-2* is a scalar value bounded between 0 and 1. $NDI-2 = 1$ signifies that the DCE's major axis is aligned with the effective natural dynamics, meaning that the direction corresponding to maximum torque transmission in the passive acceleration space is aligned with the direction of the effective natural dynamics in the same space.

The third natural dynamic index *NDI-3* describes the value of cosine the angle between the vector of the actual torque transmission to the passive acceleration space $\vec{q}_{p\tau}$ and the vector of the effective acceleration due to the natural dynamics on the passive acceleration, \vec{q}_{pbias}

$$NDI3 = \frac{(\vec{q}_{p\tau} \cdot \vec{q}_{pbias})}{(\|\vec{q}_{p\tau}\| \cdot \|\vec{q}_{pbias}\|)} \quad (84)$$

NDI-3 is a performance measure crucial to understand the relationship between the actual input torques and the natural dynamics acting on the passive subsystem. *NDI-3* is a signed scalar value bounded between -1 and 1 . $NDI-3 = 1$ signifies that the effective acceleration due the actual torque input vector is aligned and acting in the same direction of the effective natural dynamics acting on the acceleration of the passive subsystem, whereas $NDI-3 = -1$ signifies that the actual input torque acts against the influence of the natural dynamics on the passive subsystem.

3.2 DYNAMIC COUPLING FOR FLOATING-BASE ARTICULATED SYSTEMS

Humans usually employ and coordinate their full body dynamics even in locomotion modes that seemingly doesn't depend on all appendages such as walking or running where arms don't directly contribute to the forward motion. Studies in biomechanics [CAK09; MBD13] show evidence that arm swing help in reducing ground reaction moment angular momentum leading to a decrease in overall energy expenditure. The effect of arm swings on jump performance has been studied for a few decades. It is well established that if the arms are swung upwards when jumping maximally for height, jump height improves by 10% or more compared with when the arms are held in position. However, the high dimensionality and the complexity of the human's motion hinder the understanding of the mechanisms that enable the arms to increase jump height, despite the numerous proposed conjecture[Che+08; AH02; Bv88] .

Unlike previous studies on capabilities and manipulability analysis[CFM10; NLo6; ABM17]. To our knowledge, no one has studied the

acceleration capacity of high-dimensional floating base system during highly dynamic motions. We show in particular the importance of dynamic coupling between articulated body and the floating base which could outweigh the physical actuation capacity of the robot. We extend our work on DCM to floating-base systems which interact with the environment through contact forces. We chose the vertical jump with arm swing as a dynamic motion where we first generate its motion using nonlinear optimization building on the work of [DVT14].

3.2.1 Lagrangian Dynamics of floating base articulated system

Consider an underactuated dynamic system defined on a configuration manifold \mathcal{Q} . let $(q, \dot{q}) = (q^1, \dots, q^n, \dot{q}^1, \dots, \dot{q}^n)$ denote local coordinates on the tangent bundle \mathcal{TQ} . We refer to q, \dot{q} , and \ddot{q} as the vectors of generalized coordinates, generalized velocities, and generalized accelerations, respectively. Let the system possess a control input space of dimension $m < n$, where $u \in \mathbb{R}^m$ denote the vector of the control variables. Without loss of generality, we decompose the set of generalized coordinates $q = (q^1, \dots, q^n) \in \mathbb{R}^n$ into $q = (q_p, q_a)$ where $q_p \in \mathbb{R}^{n-m}$, $q_a \in \mathbb{R}^m$ denote the passive degrees of freedom and the actuated degrees of freedom. Adopting the floating base formulation of a humanoid we can describe it as a class of underactuated system where $q_p = q_f \in \mathbb{R}^6$ which corresponds to the translation and rotation motion of the floating-base in the space. For the sake of clarity of the presentation, we assume Euler description of rotations as well as the full actuation of the all degrees of freedom of the articulating body. Hence we can write the generalised coordinates of a humanoid as

$$q = \begin{bmatrix} q_{f(6 \times 1)} \\ q_{a(m \times 1)} \end{bmatrix} \in \mathfrak{R}^n \quad (85)$$

We can then write the Euler-Lagrange equation of motion in the canonical form as

$$M(q) \ddot{q} + C(q, \dot{q}) \dot{q} + G(q) = S\tau + \sum_{i=1}^{N_c} J_i^T w_i \quad (86)$$

where $M(q) \in \mathfrak{R}^{n \times n}$ is the joint space positive definite inertia matrix, $C(q, \dot{q}) \in \mathfrak{R}^{n \times n}$ is the Coriolis matrix and $G(q) \in \mathfrak{R}^n$ is the vector of gravity torques in the joint space. $J_i^T(q)$ is the wrench jacobian that maps the corresponding wrench $w_i \in \mathfrak{R}^6$ to the generalized forces of the system. The selection matrix S maps the torques $\tau \in \mathfrak{R}^m$ of the active degrees of freedom to the generalized forces of the system.

The previous formulation can be developed further in order to highlight the dynamic coupling between the unactuated floating-base and the active articulating system. Other unactuated degrees of free-

doms can be easily considered as well but for the sake of clarity we limit our study on fully actuated articulating body.

$$\begin{pmatrix} M_{ff} & M_{fa} \\ M_{fa}^T & M_{aa} \end{pmatrix} \begin{pmatrix} \ddot{q}_f \\ \ddot{q}_a \end{pmatrix} + \begin{pmatrix} \mathcal{N}_f(q, \dot{q}) \\ \mathcal{N}_a(q, \dot{q}) \end{pmatrix} = \begin{pmatrix} 0 \\ \tau \end{pmatrix} + \begin{pmatrix} J_f^T(q) \\ J_a^T(q) \end{pmatrix} \lambda \quad (87)$$

where the joint space inertia matrix is decomposed into:

- M_{ff} : represents The inertia matrix for the system seen at the passive floating base.
- M_{aa} : represents The inertia matrix of the active articulating subsystem.
- M_{fa} : The inertial coupling term between the active articulated subsystem and the passive floating-base.
- \ddot{q}_f is the second derivative of the floating base's pose (position and orientation) w.r.t time. While \ddot{q}_a is the m-actuated joints acceleration.
- τ : The vector of the joint torques of the articulated system, assuming that articulated system is fully actuated.
- $\mathcal{N}_a(q, \dot{q})$: is the generalized bias force, it follows that it is the value that τ would have to take in order to produce zero joint acceleration, assuming that all the other joint accelerations are zero and in the absence of external wrenches. Generalized bias force is a vector of force terms that account for Coriolis, centrifugal forces, and gravity.
- $\mathcal{N}_f(q, \dot{q})$: is the generalized bias force acting on the floating base.
- $J_f^T(q), J_a^T(q)$: is the jacobian that maps external wrenches to the generalized forces on the floating base and the generalized torques on the articulating body, respectively.
- λ : is the vector that groups contact forces acting at N_c contact points where $\lambda = \begin{bmatrix} \mathbf{w}_1^T & \dots & \mathbf{w}_{N_c}^T \end{bmatrix}^T$

3.2.2 Dynamic Coupling for floating base articulated systems

Kinematic and dynamic coupling between the articulated system and the floating base is usually regarded as unwanted perturbation that degrades positioning accuracy and operational dexterity. In this work we attempt to exploit the dynamic coupling between the unactuated

floating-base and the active articulating body. We start first by exploring the relationship between the acceleration space of the floating-base and the torque space of the active articulating subsystem.

The dynamic equations of the system (87) can be rewritten as (for the sake of clarity, we dropped the dependence on q, \dot{q})

$$\begin{bmatrix} \ddot{q}_f \\ \ddot{q}_a \end{bmatrix} = \begin{bmatrix} \zeta_{ff} & \zeta_{fa} \\ \zeta_{af} & \zeta_{aa} \end{bmatrix} \begin{bmatrix} \tilde{\tau}_f \\ \tilde{\tau}_a \end{bmatrix} \quad (88)$$

Where ζ is the explicit block inverse for the 2×2 inertia block matrix given by the formulae :

$$\zeta_{ff} = (M_{ff} - M_{fa}M_{aa}^{-1}M_{fa}^T)^{-1} \quad (89)$$

$$\zeta_{fa} = -(M_{ff} - M_{fa}M_{aa}^{-1}M_{fa}^T)^{-1}M_{aa}^{-1}M_{fa}^T \quad (90)$$

$$\zeta_{af} = -M_{aa}M_{fa}^T(M_{ff} - M_{fa}M_{aa}^{-1}M_{fa}^T)^{-1} \quad (91)$$

$$\zeta_{aa} = M_{aa}^{-1} + M_{aa}^{-1}M_{fa}^T(M_{ff} - M_{fa}M_{aa}^{-1}M_{fa}^T)^{-1}M_{fa}M_{aa}^{-1} \quad (92)$$

The inverse of the inertia matrix exists assuming that M_{aa} is non-singular and that the Schur complement $M_{pp} - M_{pa}M_{aa}^{-1}M_{pa}^T$ of M_{aa} is invertible.

The effective generalized torques are given by

$$\tilde{\tau}_f = J_f^T \lambda - \mathcal{N}_f \quad (93)$$

$$\tilde{\tau}_a = \tau + J_a^T \lambda - \mathcal{N}_a \quad (94)$$

We can now proceed by writing the dynamics of the floating-base as

$$\ddot{q}_f = \zeta_{ff}(J_f^T \lambda - \mathcal{N}_f) + \zeta_{fa}(\tau + J_a^T \lambda - \mathcal{N}_a) \quad (95)$$

We are interested in exploring the coupling between the passive floating base and the active articulating system. Thus we can regroup equation (95) as

$$\ddot{q}_f = \ddot{q}_{f_{bias}} + \ddot{q}_{f_\tau} \ddot{q}_{f_\tau} = \zeta_{fa} \tau \quad (96)$$

Where

$$\ddot{q}_{f_\tau} = \zeta_{fa} \tau \quad (97)$$

And we denote as well the bias term as

$$\ddot{q}_{f_{bias}} = \zeta_{ff}(J_f^T \lambda - \mathcal{N}_f) + \zeta_{fa}(J_a^T \lambda - \mathcal{N}_a) \quad (98)$$

Equation (96) gives a relation between the acceleration of the floating base and its *acting surrounding* : \ddot{q}_{f_τ} is the acceleration of the floating base due to the torques of the active articulated system modulated by ζ_{fa} , $\ddot{q}_{f_{bias}}$ is the acceleration due to gravity, velocity-dependent inertial forces, and wrenches acting on the contact points of the articulated system, if they exist.

We finally express equation (96) as

$$\boldsymbol{\tau} = \mathcal{Z} (\ddot{\mathbf{q}}_f - \ddot{\mathbf{q}}_{f\text{-bias}}) \quad (99)$$

Where we introduce the dynamic coupling factor \mathcal{Z} as

$$\mathcal{Z} = (\zeta_{fa})^\dagger = -(M_{ff} - M_{fa}M_{aa}^{-1}M_{fa}^\top)^{-1}M_{aa}^{-1}M_{fa}^\top)^\dagger \quad (100)$$

The existence of the dynamic coupling factor is closely related to Spong's strong inertial coupling condition[Spo98].

Theorem 1. *The underactuated mechanical system (87) is locally Strongly Inertially Coupled if and only if*

$$\text{rank}(M_{bm}(q)) = n - m \quad \text{for all } q \in \mathcal{B}$$

where \mathcal{B} is a neighborhood of the origin. The Strong Inertial Coupling is global if the rank condition holds for all $q \in Q$

Furthermore, we note that the the dynamic coupling factor \mathcal{Z} act as transmission factor between the control input space $\boldsymbol{\tau}$ and the acceleration space of the passive subsystem. \mathcal{Z} is a configuration-dependent matrix. Thereby, it is possible to search for the configuration that maximizes the dynamic coupling factor which will result in a decrease in the effort expenditure. This formulation of the dynamic equation helps in analyzing the effects of these three sets of variables on the achievable set of free floating base acceleration.

3.2.3 Dynamic Coupling Ellipsoid

The goal of the Floating base dynamic coupling ellipsoid is to represent geometrically, in the acceleration space, the ensemble of the accelerations achievable by the floating base. The torque limits at each actuator in the articulated system are assumed to be symmetrical, that is,

$$-\tau_{i,\max} \leq \tau_i \leq \tau_{i,\max} \quad (101)$$

The normalized joint torque vector $\tilde{\boldsymbol{\tau}}$ can be expressed as

$$\tilde{\boldsymbol{\tau}} = \mathbf{L}^{-1} \boldsymbol{\tau} \quad (102)$$

where the scaling matrix \mathbf{L} is given by

$$\mathbf{L} = \text{diag}(\tau_{1,\max}, \tau_{2,\max}, \dots, \tau_{n,\max}) \quad (103)$$

The control input space can then be represented as m -dimensional sphere defined by

$$\tilde{\boldsymbol{\tau}}^\top \tilde{\boldsymbol{\tau}} \leq 1 \quad (104)$$

By solving Eq.(99) and substituting in Eq.(104) we get the equation of an ellipsoid in the acceleration space of the passive floating base.

$$(\ddot{\mathbf{q}}_f - \ddot{\mathbf{q}}_{f\text{bias}})^\top (\mathbf{L}^{-1} \mathcal{Z})^\top (\mathbf{L}^{-1} \mathcal{Z}) (\ddot{\mathbf{q}}_f - \ddot{\mathbf{q}}_{f\text{bias}}) \leq 1 \quad (105)$$

which simplifies to

$$(\ddot{q}_f - \ddot{q}_{f_{\text{bias}}})^T \tilde{\mathcal{Z}} (\ddot{q}_f - \ddot{q}_{f_{\text{bias}}})^T \leq 1 \quad (106)$$

where

$$\tilde{\mathcal{Z}} = \mathcal{Z}^T \mathbf{L}^{-T} \mathbf{L}^{-1} \mathcal{Z} \quad (107)$$

By applying singular value decomposition, $\tilde{\mathcal{Z}}$ can be decomposed into

$$\tilde{\mathcal{Z}} = \mathbf{U} \Sigma \mathbf{V}^T \quad (108)$$

where $\mathbf{U} \in \mathbb{R}^{m \times m}$ and $\mathbf{V} \in \mathbb{R}^{n \times n}$ are orthogonal matrices. The principal axis of the $n - m$ -dimensional ellipsoid is determined by the eigenvectors \mathbf{u}_i , while its length is specified by the corresponding eigenvalue $1/\sqrt{\sigma_i}$. Furthermore, the term $\ddot{q}_{f_{\text{bias}}}$ is responsible for translating the ellipsoid center from its origin.

3.3 CASE STUDY: HUMANOID'S VERTICAL JUMP WITH ARM SWING

Humans and animals are distinguished from their robotic counterpart with their graceful and agile movements. Literature [Zaj93; Ber67; Todo4; PB15; Dico0] suggests that a key ingredient to highly dynamic motions is multiple joint coordination and synchronization across the body in order to exploit dynamic coupling between the moving parts of the body as well as the inherent natural dynamics of the body.

Humans usually employ and coordinate their full body dynamics even in locomotion modes that seemingly doesn't depend on all appendages such as walking or running where arms don't directly contribute to the forward motion. Studies in biomechanics [CAK09; MBD13] show evidence that arm swing help in reducing ground reaction moment angular momentum leading to a decrease in overall energy expenditure. The effect of arm swings on jump performance has been studied for a few decades. It is well established that if the arms are swung upwards when jumping maximally for height, jump height improves by 10% or more compared with when the arms are held in position. However, the high dimensionality and the complexity of the human's motion hinder the understanding of the mechanisms that enable the arms to increase jump height, despite the numerous proposed conjectures [Che+08; AH02; Bv88].

In this work, we focus on the full body dynamics and to exploit the dynamic coupling between body parts and to coordinate their motions to achieve a particular task. We choose the vertical jumping of a humanoid as a dynamic task and study the effect of the dynamic coupling across all degrees of freedom of the system while jumping with and without arm swings.

3.3.1 Vertical Jump as a Dynamic Maneuver

Vertical jump is an important motor skill for both robotic systems and athletics that has attracted researchers attention in both fields. From the technological perspective, hopping robots has better mobility in a natural environment [Arm+07]. It can move with great speed and maneuverability even on rough terrain which is suitable for applications like search and rescue and reconnaissance tasks. While in sports biomechanics, the study and analysis of vertical jump are primordial. Vertical jump agility contributes to successful athletic performance, particularly in sports such as basketball, volleyball, and football.

High power demand and high-dimensionality render the jumping motion of more general walking and running legged robots very complex thus researchers focused on designing jumping-specialized robots [Hal+16; Kov+08; SSD07]. These robots have few degrees of freedom and most of them rely on the catapult mechanism; the principle of slow energy storage in elastic elements, and a quick release of the stored energy translating it into the initial leap speed that propels the robot into the air. Other non-conventional mechanisms such as chemical energy [Tol+14] or shape memory alloy spring actuators were also demonstrated.

Dynamic maneuvers such as hopping and somersaults were first demonstrated first on a monopod and later on 3D biped in the seminal work of Raibert and his team which remains impressive till nowadays [Rai86]. Raibert's machine was tethered to a hydraulic, a pneumatic, and an electrical power supply. It was a low-dimensional system with hydraulically actuated telescopic leg and a hip joint with negligible dynamic coupling. The motion planning and control depend on a set of intuitive heuristics which cannot be easily transferred to a more general anthropomorphic bipedal robot.

Legged robots such as Raibert's machine [Rai86], HyQ and MIT cheetah neglected inertial coupling by assuming massless legs and installing the hip actuators near the center of mass. By having the center of mass coincident with the hip, the ground impulse is transmitted directly through the center of mass, as the SLIP model assumes. This allows controllers to neglect inertial coupling and implement SLIP-based trajectory with few modifications.

[DVT14] presents a direct collocation nonlinear optimization framework to jointly optimize the robot's joint angles, the center of mass and angular momentum trajectories as well as the forces between the robot and the environment. This framework has been able to gener-

ate a broad range of behaviors including running, jumping, as well as traversing multi-contact scenarios such as monkey bars and salmon ladder. However, the author has not focused on generating and analyzing the contribution of arm swing on the jump's performance. Other studies [NNG06; AF13] focus on bipedal jumping without dynamic coupling that arises from arm swings.

Arm swing has been studied in the context of walking [Hub+16; Kob+15]. However, few work [SY05; Nis+12] report the utilization of arm swing in humanoid jumping and is still not well studied. [SY05] employs full body dynamics trajectory optimization while enforcing Ground Reaction Forces (GRF) obtained from human jumping as a task constraint.

3.3.2 *Motion Synthesis of Dynamic Motions*

Synthesis of highly dynamic maneuvers such as jumping and acrobatic somersaults for humans and humanoids is a challenging task mainly due to the high dimensionality and nonlinearity. Besides, the hybrid nature of these motions that have multiple phases, or modes of locomotion, with implicit switching functions and discontinuities at impact with the environment. Nevertheless, this problem gained the interest of sports science, computer graphics, and robotics communities. Each offered different solutions with an emphasis on its own interests.

Sports science as a field of biomechanics is interested in analyzing human motion and identifying optimum parameters that maximize performance. The principal method for such studies relies on acquiring kinematic data of the motion using a motion capture system and ground force measurements using force plates. However, relying only on a direct measurement of experimental quantities to understand the motion dynamics has its fundamental limits. First, it is difficult to establish cause-effect relationships in complex dynamic systems by relying only on experimental data. Secondly, it is currently impossible to measure important variables such as neuro-muscular activities during motion due to technical and ethical reasons. Moreover, the accuracy of the motion analysis using inverse dynamics technique highly depends on the accuracy of the underlying model, which varies from a 2-D simplification to a musculoskeletal model for a subset of the human body.

Computer graphics community has addressed the synthesis of the dynamic and acrobatic behavior of human motion more aggressively than the robotics community due to the physical constraints of agility and power of the available hardware. However, their research shifts

away from physical realism and focuses more on natural-looking and interactive control of animations. Early approaches relied on ad-hoc locomotion controllers applied using PD servos and coordinated by a high-level state machine. Despite its capability of producing a variety of motions including running and athletic motions the combination of high gain tracking and discrete state machines frequently leads to stiff motions that are difficult to tune to get a physically realistic full-body behavior. To facilitate the synthesis of more natural motion the graphics community relies heavily on motion capture data or trajectory optimization using physically simple models or a combination of both. However, physical realism is usually relaxed by formulating the problem as an unconstrained nonlinear optimization with the physical dynamics as an objective to optimize. Moreover, contact impulses are usually approximated by smooth functions to make the problem tractable but produce artifact forces; allowing contact forces at a distance.

In robotics, motion generation approaches can be categorized over a wide spectrum depending on the level of description of the dynamic model. At one end of the spectrum are optimizations that reason about the full hybrid dynamics of the floating-base systems. Unfortunately, progress on full-body trajectory optimization has been limited to systems with low DoF and remains an open problem for systems like Atlas. Nonlinear optimization reaches a bottleneck for high-dimensional and highly nonlinear problems as they lead optimization procedures into poor local minima. At the other end of the spectrum are methods based on reduced dynamical models, where assumptions such as the absence of angular momentum simplify the dynamics but limit the range of possible motions. Recent work proposes a tractable nonlinear optimization by focusing on centroidal dynamics while taking into account full kinematics of the robot ensuring proper treatment of contact dynamics using wrench cones [DVT14]. The term centroidal momentum has been recently proposed as the sum of the individual link momenta expressed at the robot's instantaneous Center of Mass (CoM) position and aligned with the world frame [OG08; OGL13], and the dynamics expressed at the CoM has been introduced as centroidal dynamics. This is a particularly important concept since the dynamic motion of humanoid robots typically involves large angular momenta. The main limitation is that it relies on a predefined contact sequence and the inability to handle joints torque limits. Nevertheless, it is suitable to our scope of study as it offers a sufficient level of abstraction that captures the dynamic coupling between body parts of a humanoid during a vertical jump. Moreover, centroidal momentum has been previously employed [YGS09; Gos+14] as a technique for inertia shaping to generate angular momentum to divert the robot away from obstacles while falling. The success of this ap-

proach along with the optimization framework presented in [DVT14] that enables the incorporation of kinematic constraints has compelled us to use it to investigate the dynamic motion of a humanoid's vertical jump with arm swing.

The general framework of the optimization can be described as following, refer to [DVT14] and Appendix B for more details.

$$\begin{aligned}
& \underset{\Gamma}{\text{minimize}} && \sum_{k=1}^M L(\mathbf{q}[k], \mathbf{v}[k], \dot{\mathbf{r}}[k], \boldsymbol{\lambda}[k], dt[k]) \\
& \text{subject to} && m\dot{\mathbf{r}}[k] = m\mathbf{g} + \sum_{j=1}^{N_c} \boldsymbol{\lambda}_j[k] \\
& && \text{(linear momentum rate)} \\
& && \dot{\mathbf{k}}[k] = \sum_{j=1}^{N_c} (\mathbf{c}_j[k] - \mathbf{r}[k]) \times \boldsymbol{\lambda}_j \\
& && \text{(angular momentum rate)} \\
& && \mathbf{h}_G[k] = \mathbf{A}^k_G(\mathbf{q}[k])\mathbf{v}[k] \\
& && \text{(centroidal momentum)} \\
& && \forall_j \boldsymbol{\lambda}_j[k] = \sum_{i=1}^{N_d} \beta_{ij}[k] \mathbf{w}_{ij} \\
& && \forall_{i,j} \beta_{ij} \geq 0 \tag{109} \\
& && \text{friction cone approximation} \\
& && \mathbf{r}[k] = \text{COM}(\mathbf{q}[k]) \\
& && \text{COM location} \\
& && \mathbf{q}_{\text{ref}}[k] - \delta \leq \mathbf{q}[k] \leq \mathbf{q}_{\text{ref}}[k] + \delta \\
& && \text{Kinematic constraints} \\
& && dt[k]\mathbf{v}[k] = \mathbf{q}[k] - \mathbf{q}[k-1] \\
& && dt[k]\dot{\mathbf{k}}[k] = \mathbf{k}[k] - \mathbf{k}[k-1] \\
& && dt[k]\dot{\mathbf{r}}[k] = \dot{\mathbf{r}}[k] - \dot{\mathbf{r}}[k-1] \\
& && \frac{dt[k]}{2}\dot{\mathbf{r}}[k] + \dot{\mathbf{r}}[k-1] = \mathbf{r}[k] - \mathbf{r}[k-1] \\
& && \text{Time integration constraints}
\end{aligned}$$

3.4 EXPERIMENT RESULTS

In order to illustrate the importance of dynamic coupling in highly dynamic motions, we generate a vertical jump with and without arm swing for a humanoid robot using direct collocation nonlinear optimization. We then proceed by analyzing the trajectories using the DCM analysis technique.

3.4.1 Model Description: Atlas Humanoid Robot

The Humanoid robot used in this experiment is Atlas, a full-scale, hydraulically-actuated humanoid robot manufactured by Boston Dy-

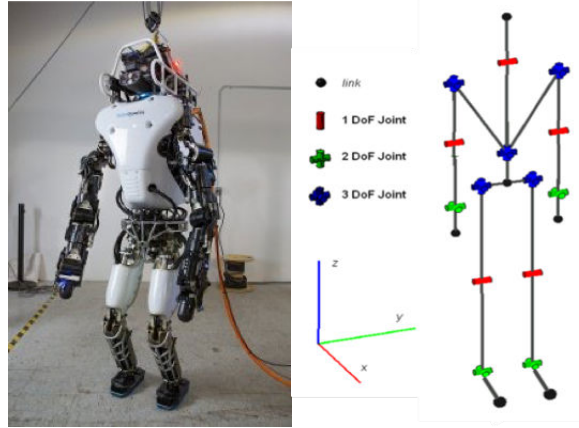


Figure 3: The Boston Dynamics Atlas humanoid robot (photo credits: Boston Dynamics)

namics, Inc. The robot stands approximately 1.88 m tall with a chest depth of 0.56 m and shoulder width of 0.76 m and having a total mass of 175 kg. Atlas has 30 actuated revolute joints (shown in Figure 3: six in each leg, six in each arm (plus an extra DoF in the hand), three in the back, and a neck joint).

The robot is modeled using MIT toolbox Drake [Ted16] in a Matlab environment. The optimization problem is solved using a non-linear optimization solver SNOPT based on Sequential Quadratic Program (SQP) algorithm.

3.4.2 Results

Table (2) shows a compilation of the vertical jump motion with arms swing. Figure (5) compares the evolution of the CoM of the robot during the vertical jump. Using Arms swing increase the jump height by more than 20%. However CoM's height is not a good performance measure as it fluctuates with the motion of the arms. That is why we focus our study on the floating base of the humanoid. The DCM shows the capacity of the robot to accelerate its floating base. The DCM decouples the capacity of the active articulated system, which is dependant on the torque limits and the configuration and placement of actuators, from the generalized bias force which includes the velocity-dependent nonlinear inertial forces and the gravitational force on all body parts projected at the floating base as well as the effect of contact wrenches on the acceleration of the floating base. Figure (6) shows the dynamic coupling ellipsoid and the generalized bias between two consecutive motion instants during the vertical jump with arm swing. It is clear that dynamic coupling ellipsoid is degenerated in the sagittal plane with limited capacity in the vertical direction despite the high torque capabilities of the robot. However

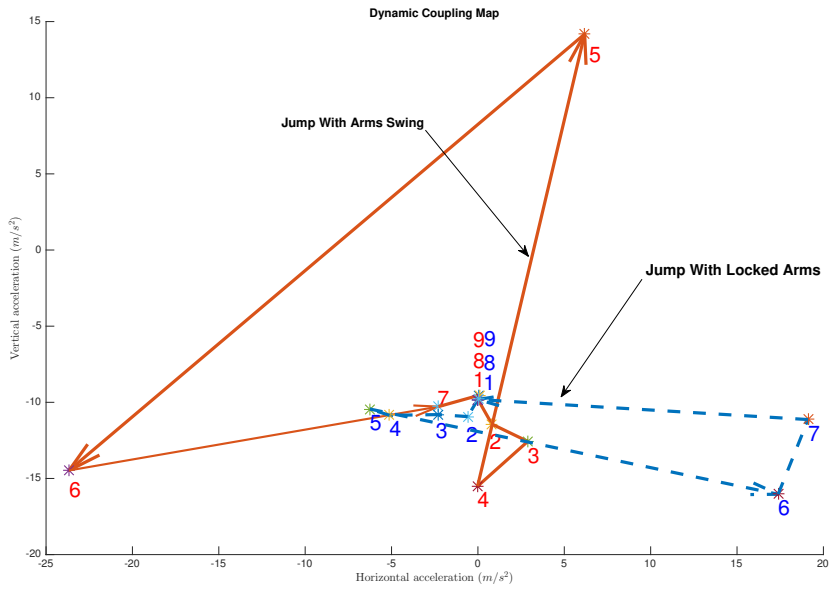


Figure 4: Dynamic Coupling Map between the first nine consecutive instants during a vertical jump.

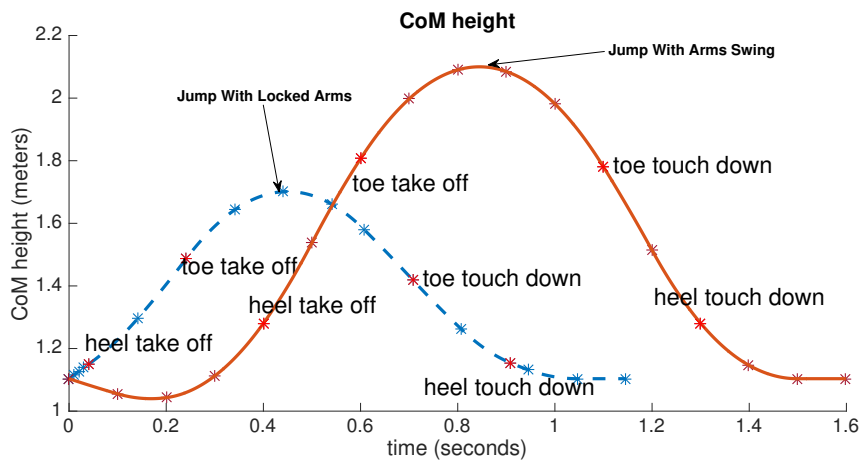


Figure 5: Comparison of the evolution of the CoM in the vertical direction between vertical jump with arms swing and with locked arms

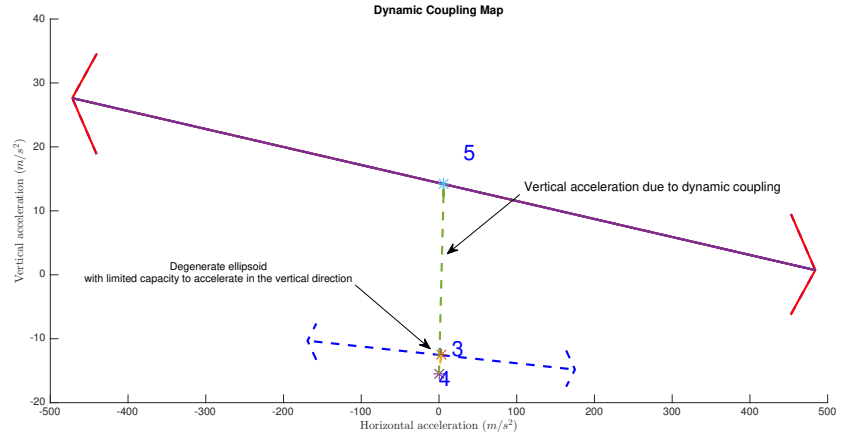


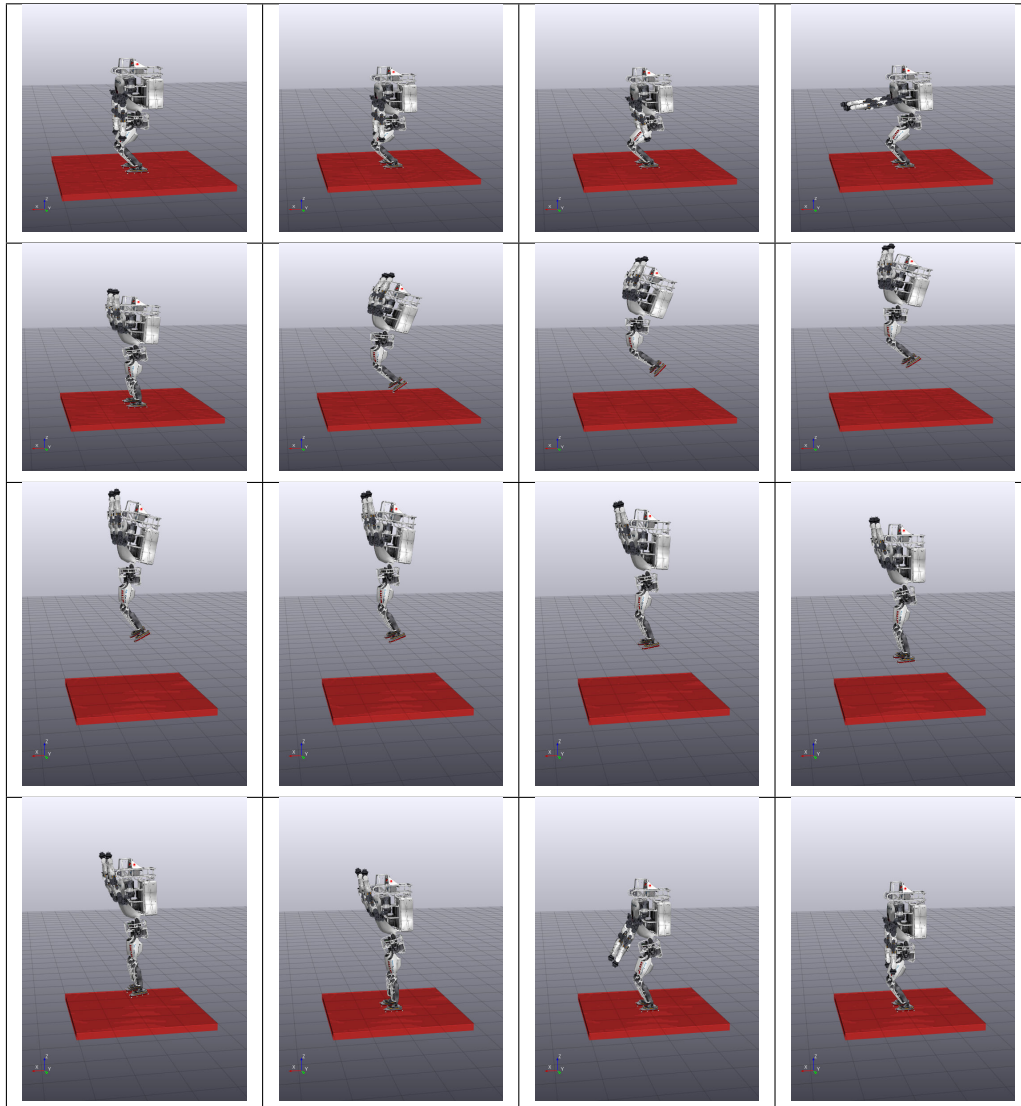
Figure 6: Dynamic Coupling ellipsoids between two consecutive instants during a vertical jump with arm swing.

the nature of the system and the motion limits the direction of the direct application of these torques. However, the vertical acceleration capacity is extended by exploiting the dynamic coupling in the bias term which includes the effect of the ground contact forces on the acceleration of the floating base. Figure (4) focuses on the dynamic coupling the first nine instants of the trajectories without showing the ellipsoid for the sake of clarity. We can observe that employing arms swings increases the capacity of the robot to accelerate in the vertical against gravity. Arms swings increase indirectly the ground reaction forces which by turn increase the capacity of vertical acceleration of the humanoid. This may confirm the conjecture of [Che+08] on the mechanism of jumping with arm swing from the biomechanics community.

3.5 CONCLUSION

In this chapter, we have introduced the Joint Space Dynamic Coupling Ellipsoid (JS-DCE) which describes the set of admissible accelerations of the passive subsystem in a graphical and intuitive manner, while taking into consideration the second-order nonholonomic constraint imposed by the underactuation, torque bounds on the active subsystem, inertial distribution over the manipulator, gravity effect, nonlinear velocity-dependent forces. We highlighted the role of the natural dynamics which can be interpreted as the bias vector responsible for displacing the center of the JS-DCE from the origin of the acceleration space. Thus inducing a drift and directly affecting the set of possible accelerations. In a dynamical trajectory, this relationship can be better grasped by employing the "Joint Space Dynamic Coupling Map (JS-DCM)," a novel analysis technique in the joint acceleration space based on JS-DCE, to help gain insight into a dynamic

Table 2: Snapshots of the vertical jump with arms swing trajectory: Instants are ordered from top left to bottom right



trajectory and analyze the dynamic coupling between the passive and active subsystems of an underactuated robot. More importantly, it allows analyzing the pivotal role of the natural dynamics of the system on the passive subsystem during a dynamic motion. This tool was developed with the floating-base system in mind. Floating-base systems dynamic modeling paradigm became prominent recently as it encompasses many-legged robots or any robotic system with intermittent contact or spatial mobile manipulators. The floating-base system is inherently underactuated by construction. It is important to understand how the developed forces in the active-subsystem along with its torque limits as well as the contact forces affect the motion of the floating-base. To this end, we have extended the JS-DCM analysis to floating-base systems and demonstrates its merits on a high-dimensional humanoid robot performing a vertical jump with the aid of arm swing. The motion planning and control of the vertical jump are generated using the state-of-the-art trajectory optimization tool, and the JS-DCM is used as a posteriori analysis tool of the resultant motion.

DYNAMIC COUPLING MAP IN THE TASK SPACE

4.1 DYNAMIC COUPLING MAP IN THE TASK SPACE

In certain applications, it is more natural to reason about the underactuated mechanical system in the task space acceleration space, when it is more relevant than the generalized accelerations space. We extend the previous analysis to describe the dynamic coupling between the active subsystem and the task space, while taking into consideration the unactuated nature of the mechanical system.

let $X = [x_1 \ x_2 \ \dots \ x_m]^T \in \mathbb{R}^m$ denote the m -dimensional task vector, which can represent the Cartesian position of the end effector of the manipulator or the center of mass of the underactuated system or any configuration dependent task can be formulated as $X = f(q)$. By taking the Taylor expansion of this mapping, we express the Jacobian that maps the task space velocities to the generalized velocities of the underactuated system

$$\dot{X} = J(q)\dot{q} \quad (110)$$

Where $J(q) \in \mathbb{R}^{(m \times n)}$ is the task space Jacobian matrix. The task space acceleration can be found by differentiating Eq.(110) with respect to time yielding

$$\ddot{X} = J(q)\ddot{q} + \dot{J}(q, \dot{q})\dot{q} \quad (111)$$

We drop the dependence on q and \dot{q} for clarity of presentation, and we partition further Eq.(111) into passive and active subsystems as follows

$$\ddot{X} = \begin{pmatrix} J_p & J_a \end{pmatrix} \begin{pmatrix} \ddot{q}_p \\ \ddot{q}_a \end{pmatrix} + \dot{J}\dot{q} \quad (112)$$

Where $J_p \in \mathbb{R}^{m \times n_p}$ is the Jacobian between the generalized coordinates of passive subsystem and the task space, while $J_a \in \mathbb{R}^{m \times n_a}$ is the Jacobian between the generalized coordinates of active subsystem and the task space.

Hence, we can express the relation between the acceleration of the end-effector of an underactuated manipulator \ddot{X} (or any point of interest in the task space) and the control input torques τ by substituting Eq.(61) in Eq.(112)

$$\ddot{\mathbf{X}} = \begin{pmatrix} \mathbf{J}_p & \mathbf{J}_a \end{pmatrix} \begin{pmatrix} \zeta_{pp} & \zeta_{pa} \\ \zeta_{ap} & \zeta_{aa} \end{pmatrix} \begin{pmatrix} -\mathcal{N}_p \\ \tau - \mathcal{N}_a \end{pmatrix} + \dot{\mathbf{J}}\dot{\mathbf{q}} \quad (113)$$

Following the same derivation of Eq.(62) for the passive joint-space acceleration, (113) can be rewritten in the following form

$$\ddot{\mathbf{X}} = \ddot{\mathbf{X}}_\tau + \ddot{\mathbf{X}}_{bias} \quad (114)$$

where

$$\ddot{\mathbf{X}}_\tau = (\mathbf{J}_p \zeta_{pa} + \mathbf{J}_a \zeta_{pp}) \tau \quad (115)$$

$$\ddot{\mathbf{X}}_{bias} = \dot{\mathbf{J}}\dot{\mathbf{q}} - (\mathbf{J}_p \zeta_{pp} \mathcal{N}_p + \mathbf{J}_p \zeta_{pa} \mathcal{N}_a + \mathbf{J}_a \zeta_{aa} \mathcal{N}_a + \mathbf{J}_a \zeta_{ap} \mathcal{N}_p) \quad (116)$$

Same interpretation as in Section 3.1.2 apply but for the task space acceleration instead of the joint space acceleration. $\ddot{\mathbf{X}}_\tau$ denotes the acceleration of the end effector due to the applied torque while $\ddot{\mathbf{X}}_{bias}$ represents the intrinsic motion of the end effector which was defined earlier as the behaviour due to the natural dynamics of the system. We note as well another important difference between Eq. (63) and Eq. (115). In the case of the task space Eq. (115), acceleration from the active input torque is transmitted to the end effector through two sources; direct transmission through the active subsystem $\mathbf{J}_a \zeta_{pp}$ and indirect transmission through the passive subsystem $\mathbf{J}_p \zeta_{pa}$ by the means of inertial coupling \mathbf{M}_{pa} . Eq. (115) can be written as

$$\ddot{\mathbf{X}}_\tau = \mathbf{J} \tilde{\mathbf{z}} \tau \quad (117)$$

where

$$\tilde{\mathbf{z}} = [\zeta_{pa} \ \zeta_{pp}]^T \quad (118)$$

4.1.1 Dynamic Coupling Ellipsoid in the Task Acceleration Space

As in Section 3.1.3, the torque bounds generate a polytope of dimension n_a in the torque space. The goal of the task space dynamic coupling ellipsoid is to represent geometrically, in the task acceleration space, the ensemble of the accelerations achievable by the end effector of the underactuated manipulator while taking into consideration the torque limits on the active subsystem and the natural dynamics affecting the acceleration limits such as gravity and gyroscopic forces.

Following the same procedure in 3.1.3 for deriving the dynamic coupling ellipsoid in the generalized acceleration space, we express the relation between the task space acceleration and the normalized torque vector by substituting Eq. (66) in Eq. (114) as

$$\ddot{\mathbf{X}} = \mathbf{J}\tilde{\mathbf{Z}}\mathbf{L}\tilde{\boldsymbol{\tau}} + \ddot{\mathbf{X}}_{\text{bias}} \quad (119)$$

Finally, the Dynamic Coupling Ellipsoid in the task acceleration space can be found by substituting Eq. (119) in Eq. (104)

$$(\ddot{\mathbf{X}} - \ddot{\mathbf{X}}_{\text{bias}})^{\top} (\mathbf{J}\tilde{\mathbf{Z}}\mathbf{L})^{-\top} (\mathbf{J}\tilde{\mathbf{Z}}\mathbf{L})^{-1} (\ddot{\mathbf{X}} - \ddot{\mathbf{X}}_{\text{bias}}) \leq 1 \quad (120)$$

Eq. (121) describes the equation of a n_m -dimensional ellipsoid in the task acceleration space. Note that this ellipsoid is the approximation of the acceleration polytope defined in Eq. (119) and Eq. (68), which maps the n_a -dimensional hypercube to a polytope of dimension n_m in the task space acceleration space that delimits the set of attainable accelerations by the end effector.

Since the torque bound matrix \mathbf{L} is a symmetric matrix, the previous result simplifies to

$$(\ddot{\mathbf{X}} - \ddot{\mathbf{X}}_{\text{bias}})^{\top} \mathcal{Z}^* (\ddot{\mathbf{X}} - \ddot{\mathbf{X}}_{\text{bias}}) \leq 1 \quad (121)$$

Where we define *the dynamic coupling factor in the task space* as

$$\mathcal{Z}^* = \tilde{\mathbf{Z}}^{\top} \mathbf{J}^{\top} \mathbf{L}^2 \mathbf{J} \tilde{\mathbf{Z}} \quad (122)$$

Definition 4.1.1. *The Dynamic Coupling Ellipsoid (DCE) of the task space of an underactuated manipulator is*

$$\mathcal{E}_{\ddot{\mathbf{X}}} = \{ \ddot{\mathbf{X}} \in \mathbb{R}^{n_m} \mid (\ddot{\mathbf{X}} - \ddot{\mathbf{X}}_{\text{bias}})^{\top} \mathcal{Z}^* (\ddot{\mathbf{X}} - \ddot{\mathbf{X}}_{\text{bias}}) \leq 1 \} \quad (123)$$

where $\ddot{\mathbf{X}}_{\text{bias}} \in \mathbb{R}^{n_m}$ is the center of the ellipsoid $\mathcal{E}_{\ddot{\mathbf{X}}}$ while the dynamic coupling factor $\mathcal{Z}^* \in \mathbb{S}_{++}^{n_m}$ determines the size and orientation of $\mathcal{E}_{\ddot{\mathbf{X}}}$

Note that from Eq.(122), the dynamic coupling factor in the task space \mathcal{Z}^* depends on the diagonal torque bounds matrix \mathbf{L} and the inertia distribution of the manipulator ζ_{p_a} which, in turn, crucially depends on the inertial coupling M_{p_a} as shown in Eq.(57) or Eq. (59). Moreover, unlike the joint space dynamic coupling factor $\tilde{\mathcal{Z}}$, defined in Eq. (73), the task space dynamic coupling factor \mathcal{Z}^* depends on the task space Jacobian as well, which makes it prone to kinematic singularities.

Let the singular-value decomposition of the dynamic coupling factor, $\tilde{\mathcal{Z}}$, be

$$\mathcal{Z}^* = \mathbf{U}\Sigma\mathbf{V}^T \quad (124)$$

where \mathcal{Z}^* is a rank r matrix, $\mathbf{U} \in \mathbb{R}^{n_m \times n_m}$ and $\mathbf{V} \in \mathbb{R}^{n_a \times n_a}$ are orthogonal matrices. The principal axes of the m_r -dimensional ellipsoid is determined by the eigenvectors $\mathbf{u}_1, \mathbf{u}_2, \dots, \mathbf{u}_r$. While the corresponding lengths of the semi-axes are given by $\sqrt{\sigma_1}, \sqrt{\sigma_2}, \dots, \sqrt{\sigma_r}$ where $\sqrt{\sigma_1} \geq \sqrt{\sigma_2} \geq \dots \geq \sqrt{\sigma_r}$. Thus, the principal axes of the task space DCE, $\mathcal{E}_{\ddot{\chi}}$, are

$$\sqrt{\sigma_1}\mathbf{u}_1, \sqrt{\sigma_2}\mathbf{u}_2, \dots, \sqrt{\sigma_r}\mathbf{u}_r$$

Similar to the dynamic manipulability ellipsoid, the volume of the ellipsoid dynamic coupling ellipsoid $\mathcal{E}_{\ddot{\chi}}$ is proportional to the determinant of the dynamic coupling factor $\det(\mathcal{Z}^*)$, or equivalently, the product of its singular values $\sigma_1 \sigma_2 \dots \sigma_r$.

However, unlike the dynamic manipulability ellipsoid which is defined only for fully actuated manipulators, as shown in Eq.(28), the dynamic coupling ellipsoid correctly accounts for the underactuation constraint and the influence of actuation distribution over the DoFs of the manipulator.

On the other hand, the term $\ddot{\mathbf{X}}_{bias}$ is responsible for translating the ellipsoid center from its origin. This term has been overlooked or neglected in all previous work except for few studies which studied special cases on a fully actuated manipulator. We introduce *the Task Space Dynamic Coupling Map (TS-DCM)*, which helps in analyzing the relationship between the task space DCE $\mathcal{E}_{\ddot{\chi}}$, its principal axis, and the vector $\ddot{\mathbf{X}}_{bias}$ in the task acceleration space, as shown in Figure 7. More importantly, it has a pivotal role in providing graphical and intuitive manner to analyze the evolution of this relationship in a dynamic trajectory, as demonstrated in Section 4.2.

The term $\ddot{\mathbf{X}}_{bias}$ groups all forces acting on the end-effector except the input control torque. Therefore, it represents the natural dynamics acting on the task space as defined in chapter 1. The term $\ddot{\mathbf{X}}_{bias}$ have strong implications on the behaviour of the underactuated manipulator which have not been considered in previous studies. For example, if the origin is not included in the task space DCE this implies that the end-effector (or any point of interest in the task space) is experiencing a considerable drift acceleration due to the natural dynamics and that the physical capacity of the actuators cannot bring the end-effector to a halt. Moreover, the ellipsoid's center displacement due to

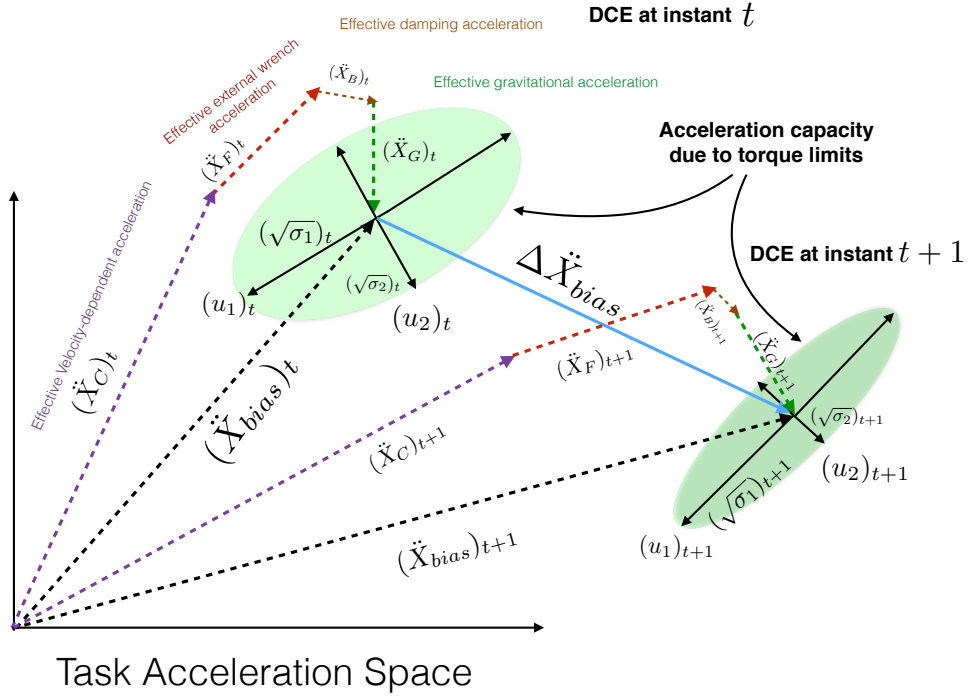


Figure 7: Illustration of the Task Space Dynamic Coupling Map (TS-DCM)

the term \ddot{X}_{bias} is a \mathbb{R}^{n_m} vector in the task acceleration space which can be decomposed to its original constituents.

Eq. (116) describes an affine relation the between the natural dynamics acting on the end-effector and the natural dynamics acting on all the manipulator itself, which can be decomposed further into the sum of the natural dynamics originating from the active subsystem \mathcal{N}_a and the passive subsystem itself \mathcal{N}_p projected appropriately using the task space Jacobian and the inverse of the inertia matrix. In addition, to the velocity-dependent acceleration $\dot{J}\dot{q}$ due to the nonlinear relationship between the reference frames. Recall that from Eqs.(47) and (48), \mathcal{N}_p and \mathcal{N}_a depend on gravity, velocity dependent forces, damping and external wrench, if exist. Hence, it is possible to find the direction and magnitude of influence of each force on the task acceleration space in a graphical and intuitive manner.

$$\ddot{X}_{bias} = \ddot{X}_G + \ddot{X}_C + \ddot{X}_B + \ddot{X}_{pF} \quad (125)$$

Where the gravitational effect on the acceleration of the passive subsystem on \ddot{X}_{bias} is represented by the displacement vector $\ddot{X}_G \in \mathbb{R}^{n_m}$ of the center of the ellipsoid $\mathcal{E}_{\ddot{X}}$. From Eqs. (116), (48), and (47) it can be expressed as

$$\ddot{X}_G = \ddot{X}_{G_a} + \ddot{X}_{G_p} \quad (126)$$

where

$$\ddot{X}_{G_a} = -J_p \zeta_{pa} G_a - J_a \zeta_{aa} G_a \quad (127)$$

$$\ddot{X}_{G_p} = -J_p \zeta_{pp} G_p - J_a \zeta_{ap} G_p \quad (128)$$

Note that the terms $J_p \zeta_{pa} G_a$ and $J_a \zeta_{ap} G_p$ represents the gravity forces transmitted to the end-effector through the inertial coupling while the terms $J_a \zeta_{aa} G_a$ and $J_p \zeta_{pp} G_p$ are the gravity terms of each subsystem transmitted directly to the end effector. Moreover, notice that from Eq.(122) and Eq.(127), \ddot{X}_{G_a} can be rewritten as $\ddot{X}_{G_a} = \mathcal{Z}^{*1/2} G_a$ this reinforces the notion of the task space dynamic coupling factor \mathcal{Z}^* as a transmission factor between all the forces acting on the active subsystem and the task space. Accordingly, the rest of the bias forces can be formulated in the same manner.

4.1.2 Natural Dynamic Index in the Task Acceleration Space

We propose three performance indices derived from the DCM analysis tool. These performance indices describe the relationship between the influence of the natural dynamics and the input torque along with its limits on the acceleration of a particular body part or a subsystem. Thus, the performance measure is aptly named as *Natural Dynamic Index (NDI)*, or in this particular case the task space Natural Dynamic Index.

The first index of the three variants is named *NDI-1*, and it describes the scalar ratio of the natural dynamics influence represented by the norm of $\|\ddot{X}_{bias}\|$ to the norm of the eigenvalues of DCE, $\|\sigma\|$, which is an approximation the maximum torque influence on the passive acceleration space.

$$NDI-1 = \frac{\|\ddot{X}_{bias}\|}{\|\sigma\|} \quad (129)$$

NDI-1 is important to understand the significance of the natural dynamics in a particular dynamic morion e.g.if $NDI-1 \gg 1$ then it would signify that the torque capacity of the underactuated robot cannot override the natural dynamics and vice versa.

The second natural dynamic index $NDI-2$ describes the absolute value of cosine the angle between the vector of the effective acceleration due to the natural dynamics on the passive acceleration, $\vec{q}_{p_{bias}}$, and the major axis of the DCE, \vec{u}_1 , which represents the direction of the maximum torque transmission in the passive acceleration space.

$$NDI2 = \left| \frac{(\vec{u}_1 \cdot \vec{X}_{bias})}{(\|\vec{u}_1\| \cdot \|\vec{X}_{bias}\|)} \right| \quad (130)$$

$NDI-2$ attempts to grasp the relationship between the natural dynamics and the ability of the system to exploit these forces. $NDI-2$ is a scalar value bounded between 0 and 1. $NDI-2 = 1$ signifies that the DCE's major axis is aligned with the effective natural dynamics, meaning that the direction corresponding to maximum torque transmission in the passive acceleration space is aligned with the direction of the effective natural dynamics in the same space.

The third natural dynamic index $NDI-3$ describes the value of cosine the angle between the vector of the actual torque transmission to the passive acceleration space \vec{q}_{p_τ} and the vector of the effective acceleration due to the natural dynamics on the passive acceleration, $\vec{q}_{p_{bias}}$.

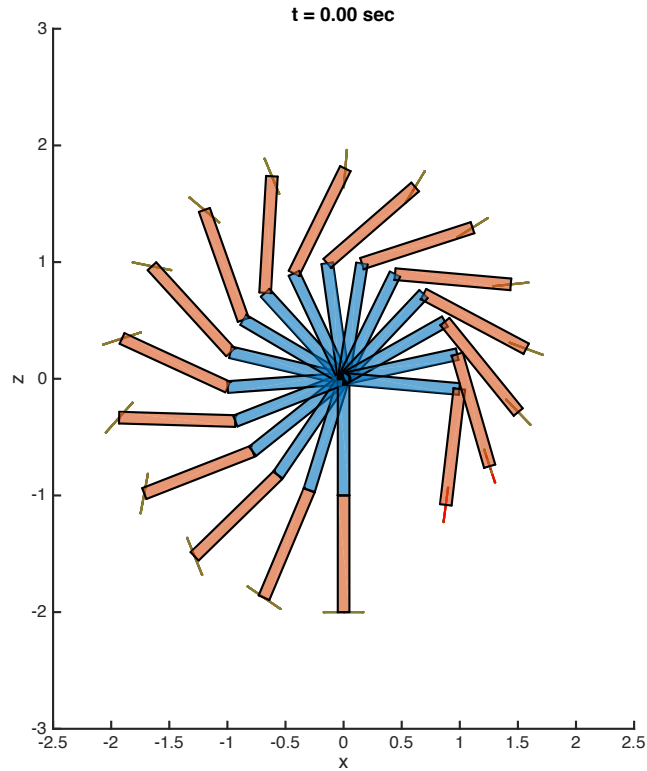
$$NDI3 = \frac{(\vec{X}_\tau \cdot \vec{X}_{bias})}{(\|\vec{X}_\tau\| \cdot \|\vec{X}_{bias}\|)} \quad (131)$$

$NDI-3$ is a performance measure crucial to understand the relationship between the actual input torques and the natural dynamics acting on the passive subsystem. $NDI-3$ is a signed scalar value bounded between -1 and 1 . $NDI-3 = 1$ signifies that the effective acceleration due the actual torque input vector is aligned and acting in the same direction of the effective natural dynamics acting on the acceleration of the passive subsystem, whereas $NDI-3 = -1$ signifies that the actual input torque acts against the influence of the natural dynamics on the passive subsystem.

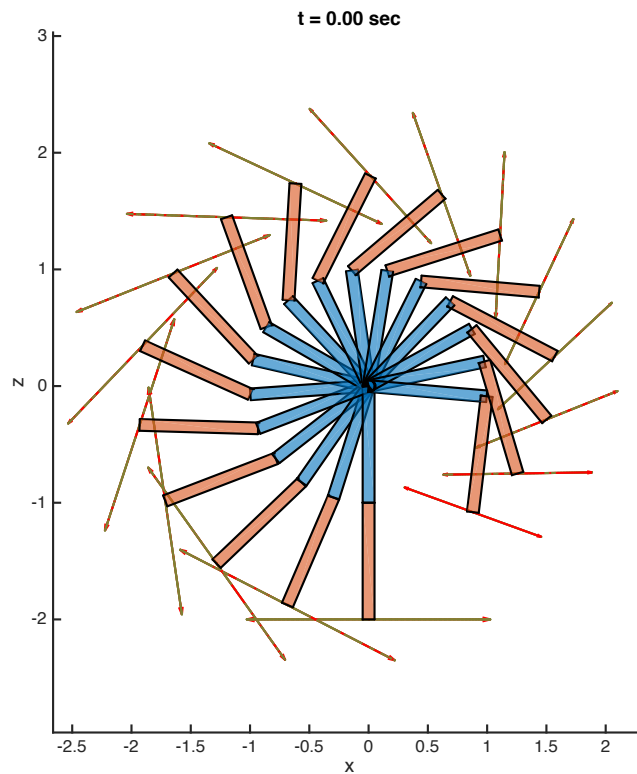
The significance of the proposed index is demonstrated in [Section 4.2](#). Note that the proposed natural dynamic index in the task space is applicable for any type of robotic system including fully actuated robotic systems.

4.1.3 Effect of Actuation Distribution on the DCE

The dynamic coupling ellipsoid DCE provides a graphical an intuitive way to analyze the acceleration capabilities of an underactuated ma-



(a) AP-type underactuated manipulator



(b) PA-type underactuated manipulator

Figure 8: Effect of actuation distribution on the Dynamic Coupling Ellipsoid in the task space for 2-Dof underactuated manipulator : (a) ActivePassive (AP)-type underactuated manipulator has a relatively limited capacity to accelerate the end effector compared to (b) PassiveActive (PA)-type underactuated manipulator

nipulator while taking into consideration all the related complexities. In this section we show the effect of actuation distribution on the capacity of several examples of underactuated manipulators to generate end-effector acceleration in the task space.

Consider a planar two-link underactuated manipulator with link lengths $l_1 = l_2 = 1$ m where l_1 and l_2 are the link lengths of the first and the second link, respectively. Assume that each link has the inertia of a cylinder where the center of mass of each link lies at the center of the link's length. In addition, assume equal masses for both links $m_1 = m_2 = 1$ kg and torque limit is set to $L = 1$ N.m. We study two types of planar 2-Dof underactuated manipulator; a Passive-Active (PA) underactuated manipulator, where the first joint near the base is passive and the actuator is installed on the second joint near the end effector, and an Active-Passive (AP) underactuated manipulator with the reverse actuation distribution. Moreover, to focus on the effect of actuation distribution, we neglect for the moment the gravity forces as well as other velocity dependent forces.

Figure 8 shows the task space DCE in the sagittal plane for two 2-DoF underactuated manipulators with different actuation distribution, namely, PA-type shown in Figure 8b and AP-type shown in Figure 8a. In both cases, the task space DCE ellipsoid degenerates to a single line. The reason is that, in both cases, we have $n_a = n_p = 1$; thus the rank of the dynamic coupling factor is always equal to 1 $\text{rank}(\mathcal{Z}^*) = 1$. Consequently, the SVD of \mathcal{Z}^* gives only a single eigenvector u_1 and a corresponding eigenvalue σ_1 .

It is also interesting to note that in Figure 8b the lengths of the degenerated ellipsoids are longer than that of Figure 8a. In other words, the eigenvalues of the dynamic coupling factor \mathcal{Z}^* of the PA-type underactuated manipulator are greater than that of the AP-type underactuated manipulator. This observation can be interpreted as the PA-type underactuated manipulator has a better capacity to accelerate the end-effector as the actuator is placed near to it. The AP-type underactuated manipulator has more difficulty in accelerating the end-effector due to the additional burden of the inertia of link 1 and link 2 which require more torque to achieve the same acceleration capacity of the PA-type.

Another important observation is to be made regarding the orientation of the eigenvector with respect to generalized coordinates. Figure 8b shows that DCE's axis is almost always perpendicular to the last link. This is understandable from the fact that the acceleration of the end-effector depends primarily on the actuation torque which rotates directly the second link. On the other hand, Figure 8a

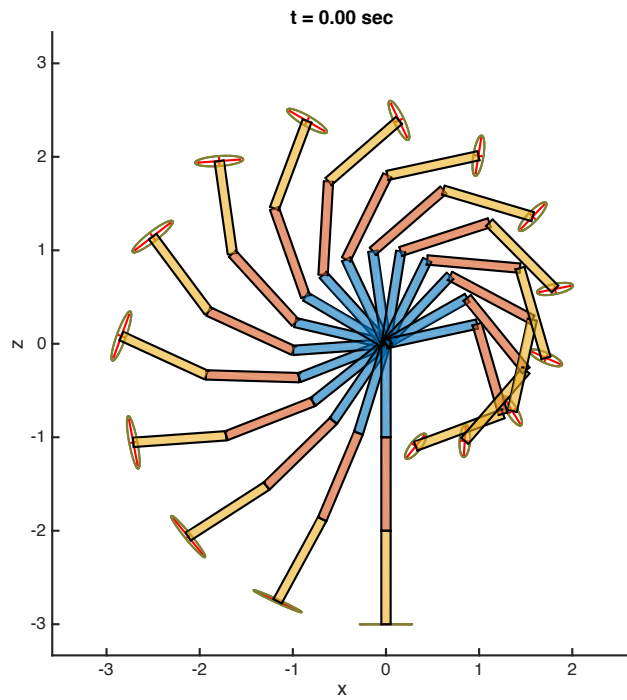
shows that the DCE's axis tends towards an alignment with the manipulator's second link, which is pronouncedly clear when $q_2 = \pi/2$ or when the second link is perpendicular to the first link. This can be explained by the fact that since the actuator rotates the first link and the second joint is passive and do not transmit torques, the torque is then transmitted along the direction of the second link.

Figure 9 shows the task space DCE for two types of 3-DoF underactuated manipulator: The first type is an Active-Active-Passive (AAP)-type where the first and second joints are active while the third joint is passive; the second type is a Passive-Active-Active (PAA)-type where the first joint is passive while the second and third joints are active. In case of 3-Dof underactuated manipulator the rank of the dynamic coupling factor is equal to two, $\text{rank}(\mathcal{Z}^*) = 2$, hence, \mathcal{Z}^* has two unique eigenvectors. Consequently DCE is a 2-D ellipse in the 2-dimensional acceleration space of the task space. This implies that increasing the number of actuators in a underactuated manipulator increases the isotropicity of the acceleration capabilities. Moreover, regarding the size and orientation of the ellipsoid, it is clear from Figure 9 that same conclusion made for the 2-D underactuated manipulator applies for the 3-DoF version. PAA-type underactuated manipulator has greater singular values of the dynamic coupling factor \mathcal{Z}^* than that of AAP-type. Consequently, Figure 9b shows that PAA-type has bigger ellipsoids than AAP-type shown in Figure 9a. Therefore, it is generally beneficial to place the actuators near the location of interest to increase its acceleration capacity. Conversely, as previously noted for the DME of fully-actuated manipulators, shorter axis implies that acceleration are more accurately controlled.

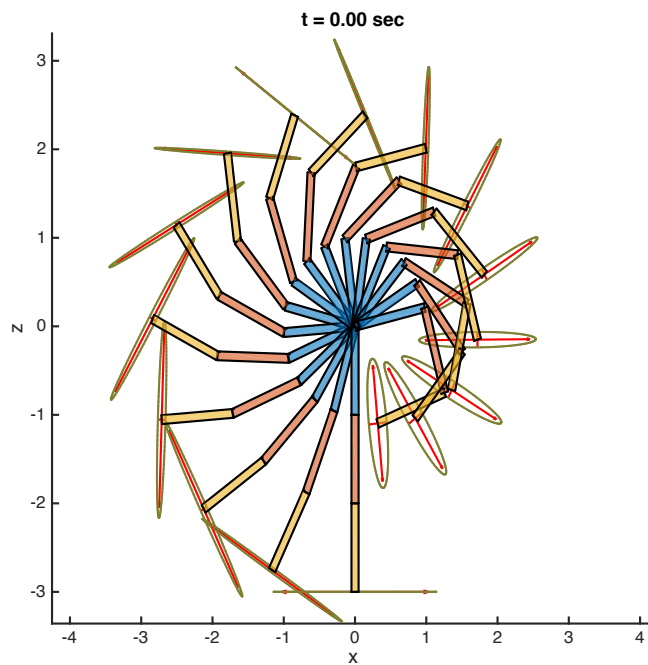
Figure 10 shows the task space DCE for two types of 4-DoF underactuated manipulator: The first type is an Active-Active-Passive-Passive (AAPP)-type where the first and second joints are active while the third and fourth joints are passive; the second type is a Passive-Passive-Active-Active (PPAA)-type where the first and the second joints are passive while the second and third joints are active. Same conclusion regarding the size and orientation of the DCE applies for the higher-dimensional underactuated manipulator. We also note that the DCE in Figure 10a is much smaller than Figure 10b and even smaller than in the AAP-type underactuated manipulator Figure 9a simply because AAPP has the same actuation capacity of AAP while having the burden of the inertia of an extra passive link.

4.1.4 Effect of Inertia Distribution on the DCE

One of the advantages of DCE is that it can easily provide a graphical intuition on the acceleration capacity of a general high-dimensional

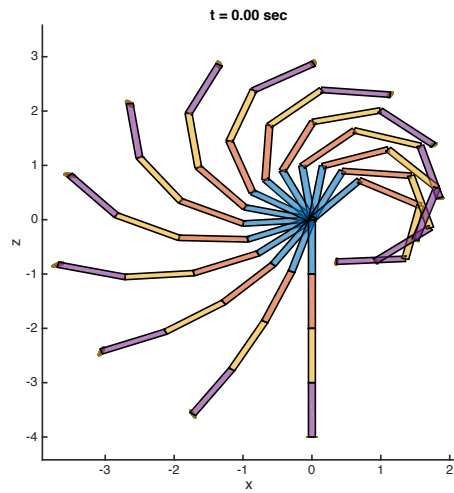


(a) AAP-type underactuated manipulator

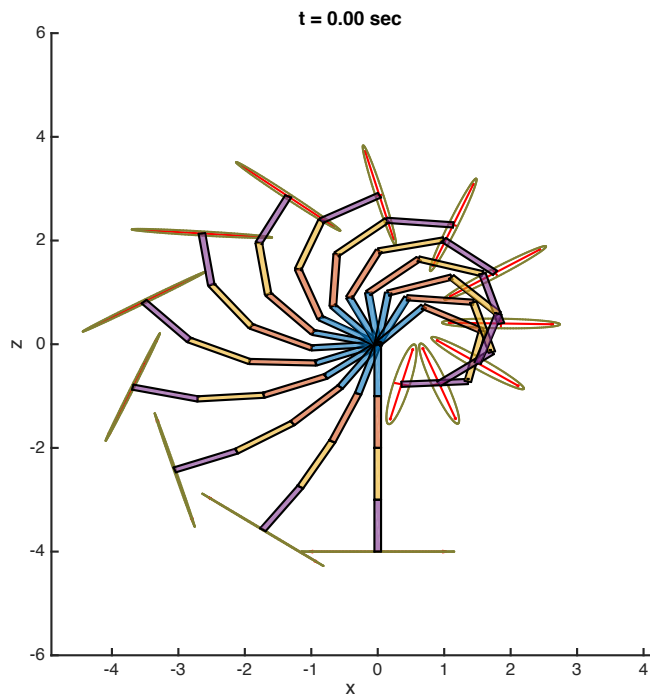


(b) PAA-type underactuated manipulator

Figure 9: Effect of actuation distribution on the Dynamic Coupling Ellipsoid in the task space for a 3-Dof underactuated manipulator : (a) (AAP)-type underactuated manipulator has a relatively limited capacity to accelerate the end effector compared to (b) PassiveActive (PAA)-type underactuated manipulator



(a) AAAP-type underactuated manipulator



(b) PPAA-type underactuated manipulator

Figure 10: Effect of actuation distribution on the Dynamic Coupling Ellipsoid in the task space for a 4-Dof underactuated manipulator : (a) (AAPP)-type underactuated manipulator has a relatively limited capacity to accelerate the end effector compared to (b) PassiveActive (PPAA)-type underactuated manipulator

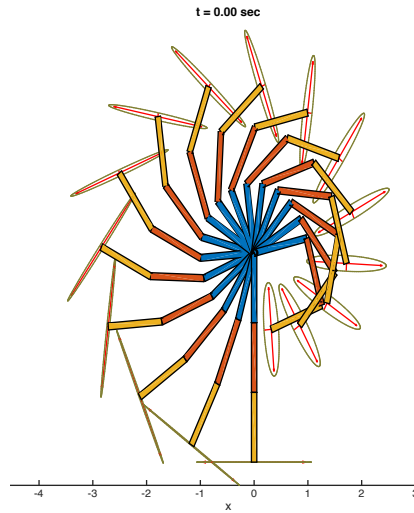
underactuated manipulator while taking into consideration the influence of the manipulator's variable inertia distribution. Figure 11 shows the task space DCE of a 3-DoF underactuated manipulator type PAA with three different inertia distribution.

Figure 11a shows the task space DCE of the manipulator's end-effector acceleration in various configurations as in Figure 9b but with a mass of the first link, which is attached to a passive joint, $m_1 = 10\text{kg}$ ten times larger than the PAA-type manipulator shown in Figure 9b. However, the DCE results are strikingly similar despite the augmented mass of the first link. The interpretation of this result is that the active joints transmit motion directly through the second and third link to the end-effector, the inertia of the first link doesn't influence the transmission factor between the input torques and the end-effector's acceleration. On the other hand, increasing the inertias of the second and the third links, shown in Figure 11b and Figure 11c, respectively, reduces greatly the acceleration capacity of the end-effector given the limited torque capacity.

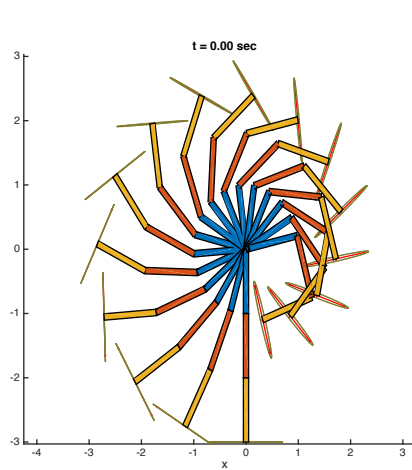
4.1.5 Effect of Torque Limits on the DCE

The task space DCE takes into consideration the effect of the torque limit of each actuator on the acceleration capability of the end effector. Recall that the task dynamic coupling factor \mathcal{Z}^* in Eq. (122) depends on the torque scaling matrix L^2 . Therefore, increasing the torque limits will generally result in higher singular values u_i of the task space dynamic coupling factor \mathcal{Z}^* . Consequently, higher torque limits will result in larger ellipsoids without affecting its orientation.

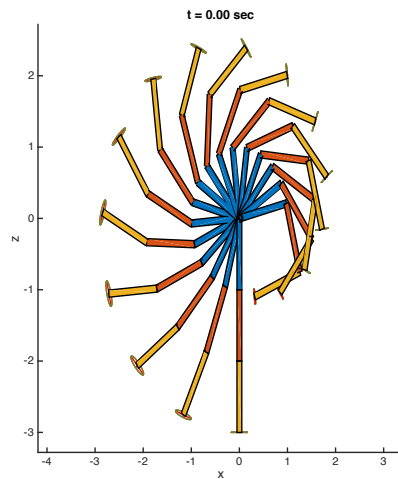
Figure 12 shows four different cases for the torque limits of a 4-DoF AAPP-type underactuated manipulator. Figure 12a shows the task space DCE results for the same manipulator example in Figure 10a with the torque scaling factor $L = \text{diag}(1, 1)$. The DCE results are barely visible in this case because the manipulator's inertia and actuation distribution diminish considerably the manipulator's ability to accelerate the end effector. Figure 12d shows the task space DCE after multiplying both torque limits by a factor of ten $L = \text{diag}(10, 10)$, this has the effect of magnifying the ellipsoid's size while preserving its shape (ratio of eigenvalues) and orientation (eigenvectors). Figure 12d confirms the hypothesis that increasing the actuation redundancy and actuation capacity increases the isotropicity of the manipulator's acceleration capacity. Figure 12c shows the task space of an AAPP-type underactuated manipulator with a torque scaling vector $L = \text{diag}(1, 10)$. We observe that multiplying the torque of the first joint only by a factor of ten renders a behaviour similar, and even more pronounced, to that of an AP-type underactuated manipulator



(a) PAA-type underactuated manipulator with link masses $m_1 = 10$ kg $m_2 = m_3 = 1$ kg



(b) PAA-type underactuated manipulator with link masses $m_1 = m_3 = 1$ kg $m_2 = 10$ kg



(c) PAA-type underactuated manipulator with link masses $m_1 = m_2 = 1$ kg $m_3 = 10$ kg

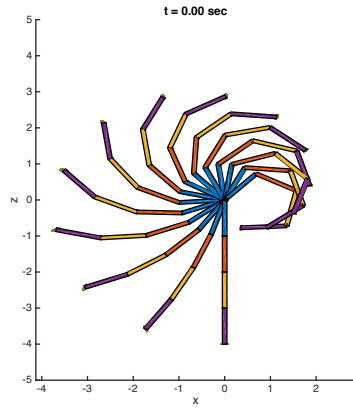
Figure 11: Effect of actuation distribution on the Dynamic Coupling Ellipsoid in the task space for a 3-Dof underactuated manipulator PAA-type : (a) (AAPP)-type underactuated manipulator has a relatively limited capacity to accelerate the end effector compared to (b) PassiveActive (PPAA)-type underactuated manipulator

Figure 8a where The ellipsoid's major axis align with the last passive link. This confirms the proposed hypothesis in Section 4.1.3 that if passive or weak actuators exist between the active actuators and the end-effector (or any point of interest) then the control input efforts will be transmitted through the principal axis of the links. Conversely, Figure 12b shows the task space DCE for an AAPP-type underactuated manipulator with a torque scaling vector of $L = \text{diag}(10,1)$; multiplying the torque of the second joint by a factor of ten renders a behaviour similar to that of an PA-type underactuated manipulator Figure 8b, where the ellipsoid's major axis tends to be more perpendicular to the last passive link.

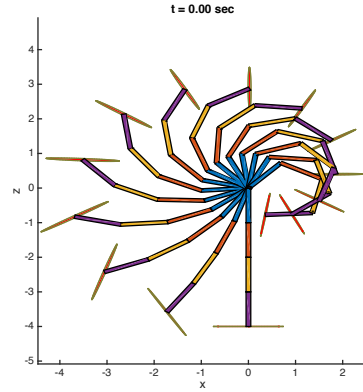
4.1.6 Effect of Gravity on the DCE

Gravity is one of the bias forces that is responsible of translating the DCE's center in the task acceleration space. Previous sections demonstrated that the effect of inertia distribution, actuation distribution or torque limits affected only the orientation, shape and size of the DCE with having any influence on the position of its center. Therefore, it was drawn appropriately with its center coinciding with the manipulator's end-effector to easily visualize the relationship between the ellipsoid's orientation and the manipulator's configuration. On the other hand, the ellipsoid's size was scaled arbitrarily to fit in the task space. However, it is important to note that DCE is an ellipsoid that demonstrates the underactuated manipulator ability to accelerate the end effector. Therefore, by introducing the bias acceleration \ddot{X}_{bias} , it is more appropriate to examine the DCE in the *Dynamic Coupling Map (DCM)*, which helps in visualizing the relation between several DCE in the task acceleration space to understand the effect of the bias forces on the achievable set of accelerations.

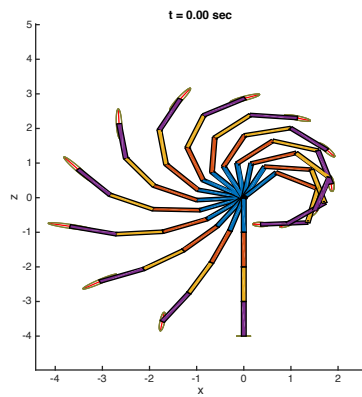
Figure 13 shows the effect of gravity on task space DCE demonstrated on a AAPP-type 4-DoF underactuated manipulator with a generalized coordinate $q = [2.1, 0.5, 0.9, 0.5]^T$ with torque scaling matrix $L = [10, 10]^T$ N.m. In the previous section, Figure 12d showed the DCE in various configuration without taking into consideration the effect of gravity. All ellipsoids were scaled arbitrarily and centered on the end-effector because the task space bias acceleration is null $\ddot{X}_{\text{bias}} = 0$. Figure 13a shows that by introducing gravity and assuming zero generalized velocity $\dot{q} = 0$, we get a non-zero bias acceleration and from Eq.(125) only on the bias acceleration due to gravity $\ddot{X}_{\text{bias}} = \ddot{X}_G$. Figure 13b shows that The bias vector due to gravity translates the center of DCE downwards in the vertical acceleration direction towards $-g = -9.8\text{m/s}^2$. The orientation and magnitude of the gravity bias vector depends on the posture of the robot q and



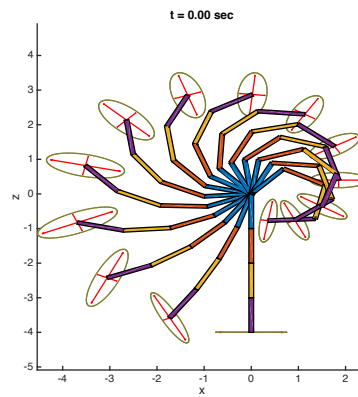
(a) AAPP-type underactuated manipulator with torque limits $\tau_1^{\text{limit}} = \tau_2^{\text{limit}} = 1 \text{ N.m}$



(b) AAPP-type underactuated manipulator with torque limits $\tau_1^{\text{limit}} = 1 \text{ N.m}$ $\tau_2^{\text{limit}} = 10 \text{ N.m}$



(c) AAPP-type underactuated manipulator with torque limits $\tau_1^{\text{limit}} = 10 \text{ N.m}$ $\tau_2^{\text{limit}} = 1 \text{ N.m}$



(d) AAPP-type underactuated manipulator with torque limits $\tau_1^{\text{limit}} = \tau_2^{\text{limit}} = 10 \text{ N.m}$

Figure 12: Effect of torque limits on the Dynamic Coupling Ellipsoid in the task space for a 4-DoF AAPP-type underactuated manipulator : (a) (AAPP)-type underactuated manipulator has a relatively limited capacity to accelerate the end effector compared to (b) PassiveActive (PPAA)-type underactuated manipulator

is determined from Eqs. (126)-(128). The exact decomposition \ddot{X}_{bias} and the contribution of each term is shown in Figure 14.

The interpretation of Figure 13b is that in the case of zero gravity and the given robot's posture, the shown 4-DoF AAPP-type underactuated manipulator is capable of accelerating the end-effector with an acceleration of $\ddot{X} = [-3.3, 2.28]^T \text{ m/s}^2$ which corresponds to $u_1 \sigma_1$. The underactuated manipulator cannot exceed this acceleration due to the physical limits on the actuator's torque capacity. The origin of DCE represents the acceleration of the end-effector if null torque vector is applied, therefore it represents the instantaneous acceleration of the end-effector due to natural dynamics. In case of zero gravity, the origin of the DCE coincides with the origin of the acceleration space, therefore the end-effector will remain still. Conversely, in the case of gravity, the origin of DCE coincides with the acceleration $\ddot{X} = [0; 9, -9.39]^T \text{ m/s}^2$ which represents the natural instantaneous acceleration of the end-effector at the given posture.

Another important conclusion can be drawn from the DCM regarding the relationship between the dynamic coupling factor and the bias acceleration. It is clear from Figure 13b that $\|\ddot{X}_{\text{bias}}\| > \|u\sigma\|$, this implies that the underactuated manipulator does not have enough torque to counter or compensate the natural dynamics of the system. This idea is reinforced in Figure 15, where the relationship between the effect torque limits and the end-effector acceleration bias due to gravity is explored. Figure 15 shows the DCE of the same underactuated manipulator, shown in Figure 13a, but with two different torque scaling factors $L = [80, 80]^T \text{ N.m}$ (shown in dotted line), and $L = [10, 10]^T \text{ N.m}$ (shown in solid line). The DCM, shown in Figure 15, gives a clear an intuitive picture of the interplay of the different parameters on dynamic behaviour of the underactuated manipulator. It is clear that the shown underactuated manipulator with torque limits $L = [10, 10]^T \text{ N.m}$ cannot overpower the natural dynamics. However, by paying the hefty price of increasing the torque limits to $L = [80, 80]^T \text{ N.m}$ while retaining the same inertia —or decreasing the inertia while retaining the same torque capacity, thus increasing the torque to mass ratio —the underactuated manipulator can be barely counter or compensate the natural dynamics (only gravity in this case). Thus, a given underactuated manipulator can compensate or override the natural dynamics if and only if the acceleration bias vector \ddot{X}_{bias} is encapsulated inside the DCE.

Another interesting case is that an underactuated manipulator can be *dynamically singular even though it is not kinematically singular*. Figure 16 shows the effect of gravity on DCE for the same 3-dof AAP-type underactuated manipulator previously discussed in Figure 9a

A robot can override the natural dynamics if and only if the acceleration bias vector \ddot{X}_{bias} is encapsulated inside the DCE.

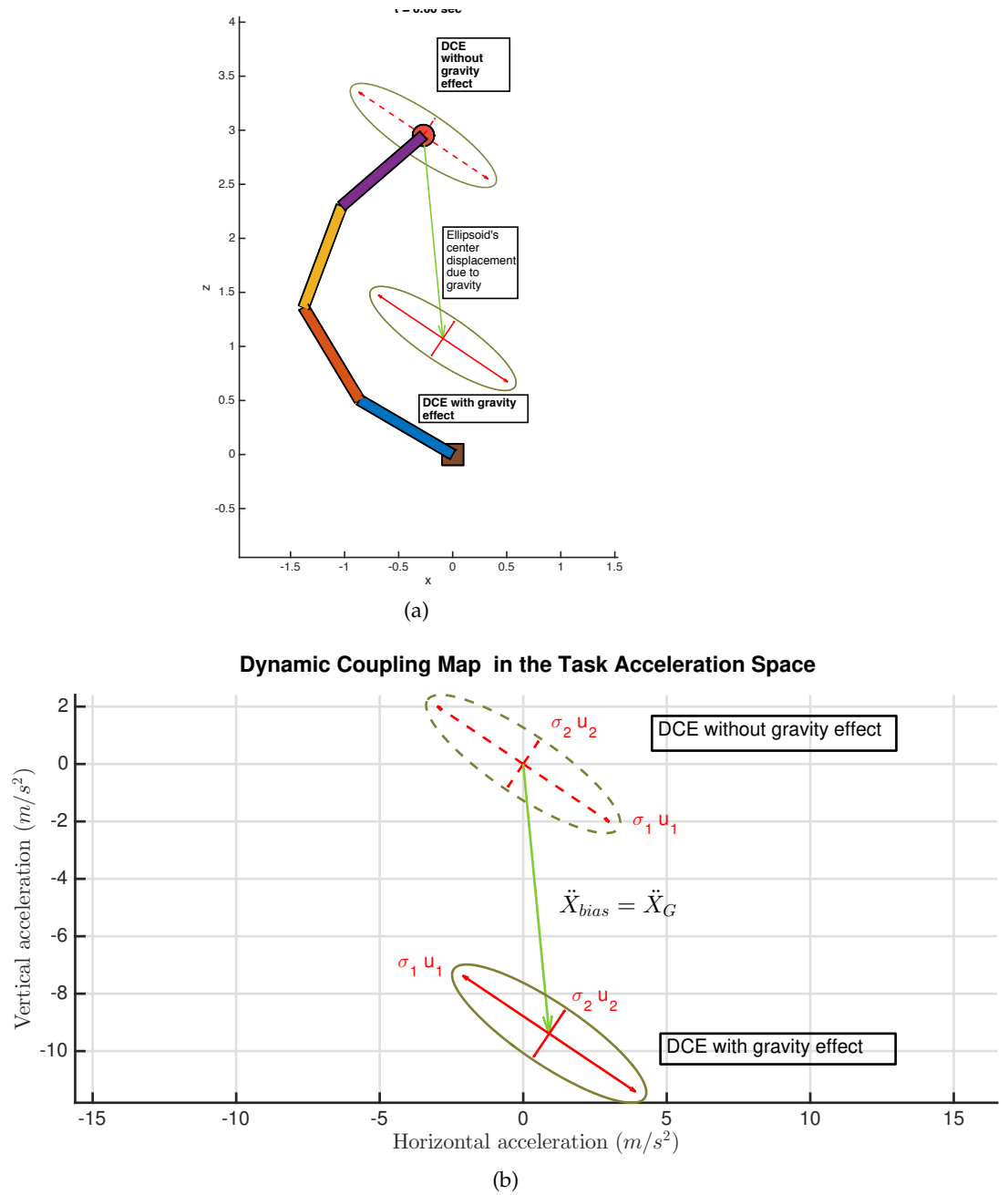
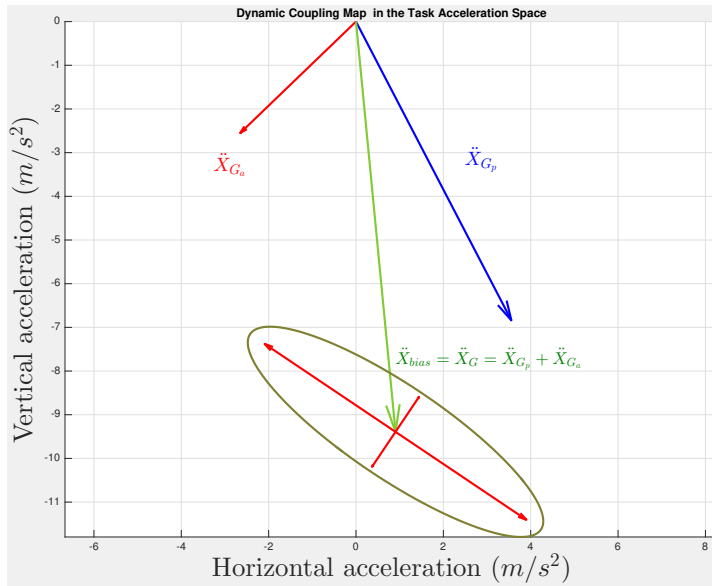
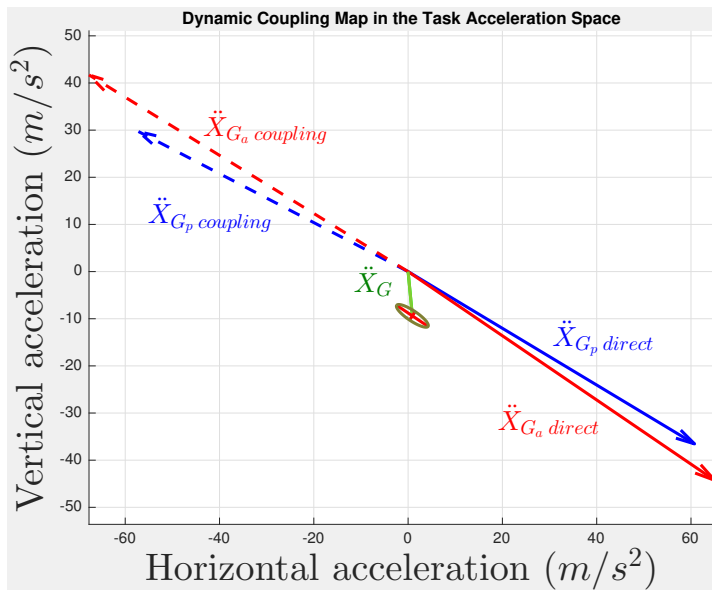


Figure 13: Effect of Gravity on task space DCE demonstrated on a AAPP-type 4-DoF underactuated manipulator with a generalized coordinate $q = [2.1, 0.5, 0.9, 0.5]^T$ (a) DCE without the effect of gravity (dotted line) in the task space with its origin coinciding with the end-effector while the DCE is displaced relatively (b) Dynamic coupling map showing the DCE in the task acceleration space



(a)



(b)

Figure 14: Decomposition of task acceleration bias due to gravity into its components (a) Task bias acceleration decomposition showing the effect of each the active and passive subsystems (b) the influence of each subsystem can be further decomposed into a component due to inertial coupling and another component representing direct influence.

with the generalized coordinates $q = [2.1, 0.5, 0.9, 0.5]^T$. Figure 16a shows the DCE with respect to robot's posture while Figure 16b shows the DCE in the acceleration space with a torque scaling factor $L = [1, 1]^T$ N.m. Note that the DCE is degenerated to a line because there is only one non-zero eigenvalue σ_1 of the dynamic coupling factor \mathcal{Z}^* . This case is called appropriately *dynamic singularity*; note as well that the 3-DoF manipulator is not in a kinematically singular configuration. Figure 16c and the DCM in Figure 16d show clearly that even after increasing the torque-to-mass ratio by a factor of ten $L = [10, 10]^T$ N.m the underactuated manipulator does not have the ability to compensate the natural dynamics because the eigenvector u_1 of the DCE does not pass through the origin. Therefore, any attempt to apply any combination of the torque vector τ will cause the system to accelerate in the direction of the principal axis of the DCE.

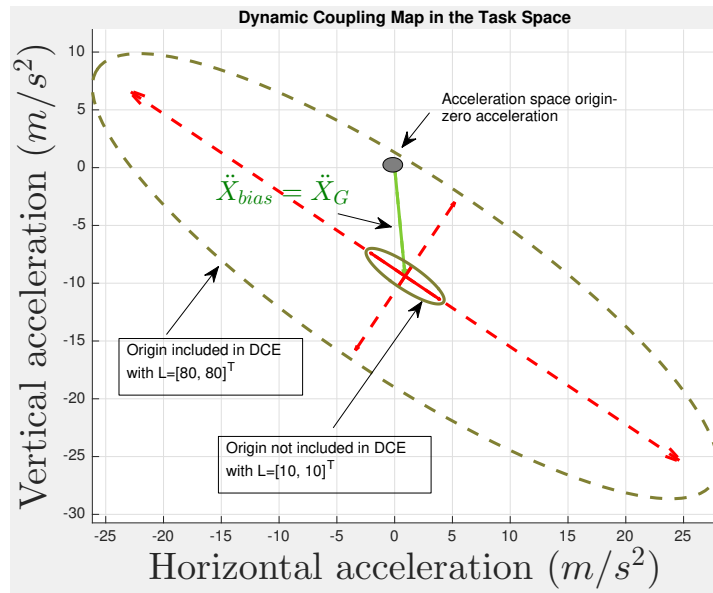


Figure 15: Relationship between torque limits and task acceleration bias due to gravity

4.2 CASE STUDY: GYMNAST SWING-UP DYNAMIC MANEUVER

In this section, we demonstrate the effectiveness of the Task-Space Dynamic Coupling Map (TS-DCM) and the associated Natural Dynamic Index (NDI) in analyzing a highly dynamic maneuver. In particular, we choose the swing-up motion of a gymnast on a high bar as a demonstrative case study. The dynamic motion is generated using a nonlinear optimization solver guided by data from the sports science and biomechanics community. Although the nonlinear optimization is becoming increasingly popular in the robotics community, it remains treated as a black-box which takes as input several constraints, objective function, and boundary conditions and output

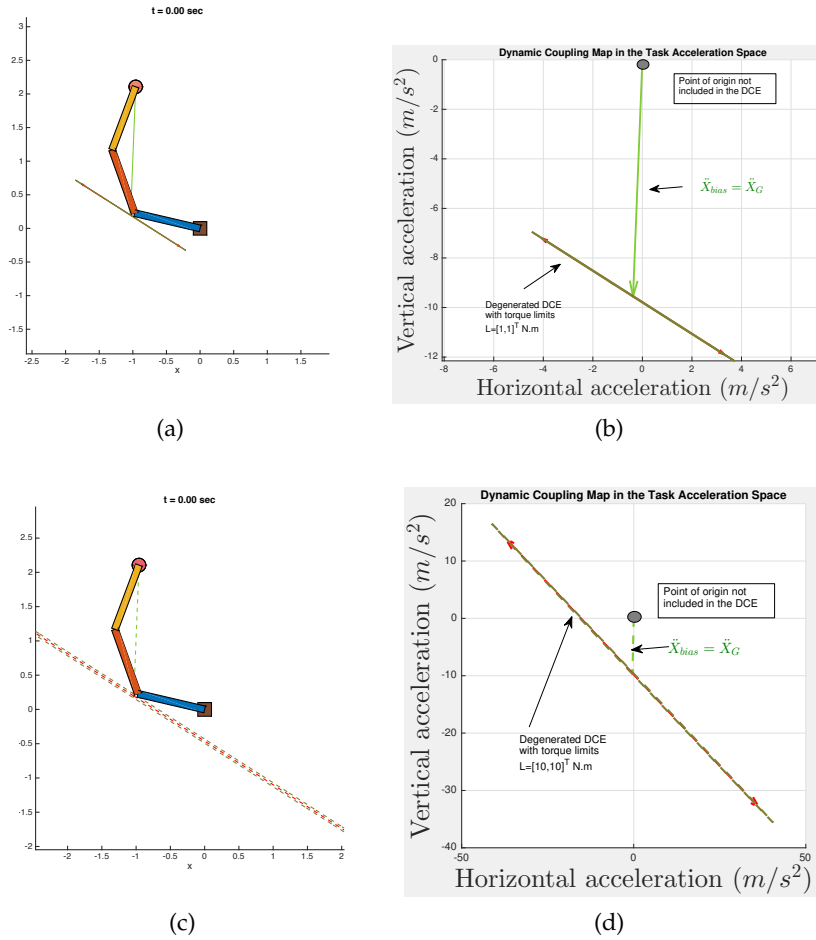


Figure 16: Relationship between torque limits and acceleration bias due to gravity effect highlighting the case of dynamic singularity on a AAP-type 3-DoF underactuated manipulator with a generalized coordinate $q = [1.8, 1.0, 0.7]^T$ (a) DCE is shown with respect to underactuated manipulator's posture demonstrating a dynamically degenerated DCE although the robot is not in a kinematically singular configuration (b) the corresponding DCM for the robot with low torque capacity $L = [1, 1]^T$ N.m shows a dynamically degenerated DCE which doesn't cover the acceleration space origin (c) DCE with respect to underactuated manipulator's posture after increasing the torque-to-mass ratio by a factor of ten $L = [10, 10]^T$ N.m (d) Corresponding DCM demonstrating that the DCE remains dynamically degenerated despite increasing the torque-to-mass ratio by a factor of ten

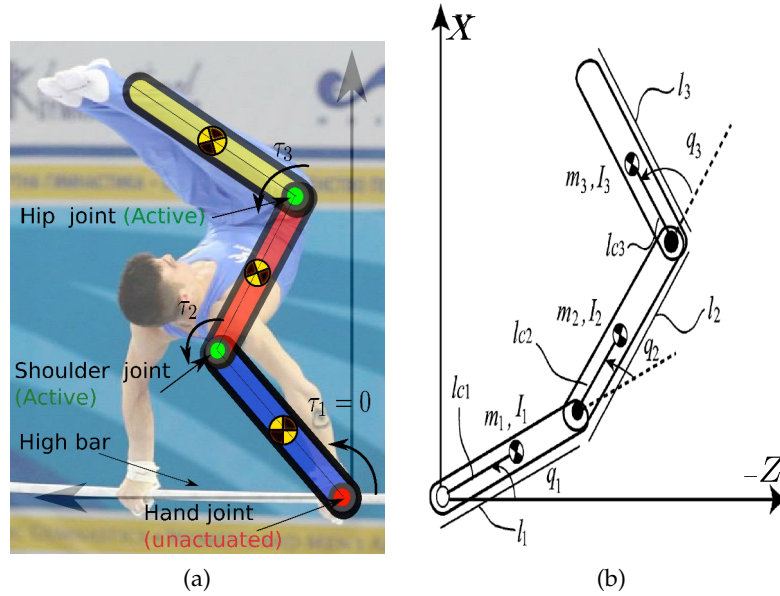


Figure 17: Approximation of a Gymnast on a high-bar as a three-link under-actuated manipulator

a local-optimal trajectory. It is difficult to understand how the optimization reached to this particular motion or to estimate the quality of the output motion by relying solely on the output motion. Notwithstanding this limitation, we propose the DCM and the associated NDI as a graphical and intuitive trajectory analysis tool that helps in providing a more intuitive insight into the mechanism of the resulting dynamic motion and its quality in terms of exploiting the robot's robot dynamic capabilities. NDI also demonstrates the pivotal role of exploiting the natural dynamics in highly dynamic manoeuvres.

4.2.1 Model Description

Swinging is a primordial movement primitive which is ubiquitous in the dynamic behaviour of many living organisms. Brachiation [GR05], or body swinging, is a principal movement element in arboreal locomotion in which primates, such as gibbons, swing from tree limb to tree limb by swinging their body while at least one hand is grasping a support at all times. This locomotion mode is also known as a continuous contact brachiating gait which can be regarded as an upside down walking. Other examples include the agile manoeuvres of animals that exploit the swinging dynamics of their tails to achieve a sudden acceleration, deceleration or extreme direction adjustments such as geckos and lizards, or even cheetahs [PB13; Lib+12]. However, [Ale03] stated that our understanding of these dynamic manoeuvres is still very limited. On the other hand, perhaps the epitome of human agile and graceful dynamic motions can be found in the sport of

artistic gymnastics. Prassas has stated that – *mastering of swinging*– is a critical motor skill for gymnasts to succeed in competition and to be treated as other essential attributes such as strength, flexibility, and stamina [PPK74]. Swinging requires complex dynamic coordination between various body parts and proper timing in order to achieve a desired movement while minimizing their muscular work [Aleo3][Yam+09][GR05].

Gymnasts use swings in various movements including kips, casts and giant swings on a high bar or rings. Gymnasts are in some routines required to do full circular movements followed by a flight phase with acrobatic movements such as somersaults and twists. Gymnast swing behaves as a pendular movement that may be composed of several sub-pendulums including the legs, the trunk, the arms and the rings (in case of rings routine). Therefore, the swing dynamics depends on the dynamic coupling between the subsystems, which if synchronized correctly could achieve synergy to deliver a high-performance movement otherwise the movement of subsystems can be counter-productive in which the resulting motion can be sub-optimal or not achieved at all.

Gymnastic maneuvers has been studied extensively in the sport science and biomechanics communities and has been a source of inspiration for many robotic advances. [HM90] introduced a canonical model of underactuated systems known as the Acrobot (for acrobatic robot). It can be considered as a highly simplified model of a human gymnast on a high bar, where the underactuated first joint models the gymnast’s hands on the bar, and the actuated second joint models the gymnast’s hips. The objective is to swing up the Acrobot from the downward stable equilibrium point to the upright unstable equilibrium point and balance it about the upright vertical. This motion control problem is usually decomposed into two sub-problems; first, the swing-up motion control [ÅF00] [Sp095] [Xin13], once the robot’s configuration is brought up to the neighborhood of the unstable equilibrium point, switching to a stabilization controller is necessary[OS01]. Several variants of the Acrobot have been proposed either by increasing the number of degrees of freedoms [KH06] [ST08] [Ibu+15] or by varying the placement of the actuators [LO02]. During the last two decades, many researchers have investigated the approach of passivity or energy-based control of underactuated mechanical systems. [LD06] showed that the dynamic coupling becomes more complex when the number of links increases, and its control problem becomes more challenging. [XKo7a] noted that energy based techniques are difficult to apply for higher dimension robots.

*mastering of
swinging is of
paramount
importance for
gymnasts desiring to
succeed in
competition*

For the purpose of illustration, we focus our attention on the swing-up dynamic motion of an extended version of the acrobat called *the 'Gymnast' robot* shown in Figure 17. [XK07b] argue the importance of the extra third active joint representing the shoulder joint. The gymnast robot is a simplified approximation of an athlete swinging his body on a high bar. Assuming symmetrical motion, we restrict our attention to the sagittal plane. This model has been widely used to study various gymnastic maneuvers on a high-bar. The model is composed of three links representing the arm, the trunk and the leg. All three links are connected by 1-DoF rotary joints. Assuming negligible elasticity in the high-bar, we can consider the arm to rotate freely around the high-bar, thus the arm is connected to the world through a passive joint. This joint imposes a non-integrable second-order nonholonomic constraint. On the other hand, the second and the third joints, representing the shoulder and the hip joint, respectively, are active and torque controlled. Therefore, a gymnast on a high-bar is an underactuated system where the first joint $q_p = q_1$ is passive $n_p = 1$, while the second and third joints $q_a = [q_2, q_3]^T$ are active $n_a = 2$. The system's generalized coordinates is $q = [q_1, q_2, q_3]^T$ rad, where the q_1 is the angle between the vertical axis and the arm, while the second and third coordinates are taken relative to the connected links. All angles are taken positive clockwise. The control input is the torque vector $\tau = [\tau_1, \tau_2]^T$ N.m acting on the second and third joints.

The inertial and kinematic parameters are loosely based on the actual anthropomorphic data from the biomechanics community as shown Table 3. The three parts of the body are approximated with cylindrical elements where the first link represents the arm with a mass denoted by m_1 and a cylinder length of l_1 and assuming its center of mass lies at lc_1 with a moment of inertia I_1 . Accordingly, the trunk and the legs are represented by with link 2 and link 3, respectively .

4.2.2 Approach

Trajectory optimization algorithms are a powerful class of methods for generating goal-directed behavior in dynamical systems by computing admissible state and control sequences that minimize a cost functional subject to a set of constraints. In this work, we employ nonlinear trajectory optimization for the swing-up motion generation and control. Second-order Nonholonomic and torque constraints fit naturally into the direct formulation of trajectory optimization. Furthermore, there exists strong evidence that humans solve task-level and motor-level challenges through optimization processes. A

PARAMETERS	VALUES
l_1 [m]	0.6
l_2 [m]	0.55
l_3 [m]	0.8
lc_1 [m]	0.3
lc_2 [m]	0.275
lc_3 [m]	0.4
m_1 [kg]	6
m_2 [kg]	33
m_3 [kg]	22
I_1 [kgm ²]	0.18
I_2 [kgm ²]	0.83
I_3 [kgm ²]	1.17

Table 3: Physical parameters of the Gymnast robot model

good overview of optimal control in sensorimotor systems is given by [Todo4].

Trajectory optimization approach is becoming increasingly attractive with the advent of computational power and the recent advances in nonlinear optimization [PCT13][Hau14]. Given an initial trajectory that may be non-optimal or even non-feasible, trajectory optimization methods can often quickly converge to a high-quality, locally-optimal solution. In this work, the system is modeled using MIT toolbox Drake [Ted16] in a Matlab environment. The Gymnast swing-up problem is formulated as a direct collocation Nonlinear Program (NP) which is solved using a non-linear optimization solver, Sparse Non-linear OPTimizer (SNOPT) [GMS02] based on Sequential Quadratic Program (SQP) algorithm. Reader is referred to Appendix B for a brief background on the optimization algorithm and a general overview of NP methods.

The Swing-up motion of a 3-link robot is thus formulated as a trajectory optimization problem where the objective function or the cost functional is given by

- Cost functional

$$J = \Phi(t_f, \mathbf{x}_f) + \int_0^{t_f} \phi(\mathbf{x}(t), \mathbf{u}(t), t) dt \quad (132)$$

where $\Phi(\cdot)$ and $\phi(\cdot)$ are the final cost and the running cost functions, respectively. The cost function Equation 132 is referred to as the *Bolza* form as it involves both integral term $\phi(\cdot)$ and a boundary term $\Phi(\cdot)$. In this work we choose to minimize the final time t_f as a boundary term, while minimizing the input torques and the generalized velocities as the running cost. Therefore, Equation 132 is implemented as

$$J = t_f + \int_0^{t_f} \tau^T R \tau + \mathbf{x}^T Q \mathbf{x} dt \quad (133)$$

where $R = \text{diag}(R_1, R_2)$ is a diagonal matrix with the weights for the torque input and $Q = \text{diag}(0, 0, 0, Q_1, Q_2, Q_3)$ is the weighting matrix for the state vector. The first three terms in the Q matrix are null because we penalize only the generalized velocities.

However, as we employ direct collocation method this continuous formulation is transcribed into a nonlinear

On the other hand, trajectory constraints can be categorized into three types :

- Boundary constraints

Boundary constraints are generally defined as

$$\mathbf{b}_{\min} \leq \mathbf{b}(t_0, \mathbf{x}_0, t_f, \mathbf{x}_f) \leq \mathbf{b}_{\max} \quad (134)$$

In our implementation, the boundary conditions are clearly defined by the starting state of the gymnast from rest at the vertical downward equilibrium position and the motion ends at the vertical upward unstable equilibrium position. Thus, the boundary constraints can be expressed as

$$\mathbf{x}_0 = [0, 0, 0, 0, 0, 0]^T \quad (135)$$

$$\mathbf{x}_f = [\pi, 0, 0, 0, 0, 0]^T \quad (136)$$

- Bounds on the state and control variables

Bounds on state and control variables during the motion can generally be expressed as

$$\mathbf{x}_{\min} \leq \mathbf{x}(t) \leq \mathbf{x}_{\max} \quad (137)$$

$$\tau_{\min} \leq \tau(t) \leq \tau_{\max} \quad (138)$$

In the case of the swing-up movement of the gymnast, in addition to the torque constraints, we impose bounds constraint on the generalized coordinates to prevent solutions with several turns.

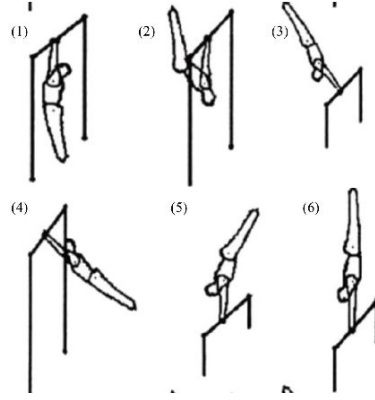


Figure 18: Six stages of gymnast swing-up movement

$$-\pi \leq \mathbf{q} \leq \pi \quad (139)$$

In order to test the influence of torque limits on the output motion of the trajectory optimization, two torque limits are evaluated. In one optimization problem, high torque limits are set to $-500 \text{ N.m} \leq \tau(t) \leq 500 \text{ N.m}$ in another optimization problem the low torque limits are set to $-80 \text{ N.m} \leq \tau(t) \leq 80 \text{ N.m}$.

- Path Constraints

Path constraints in trajectory optimization imposes constraints on the state and/or the input torques at certain instants during the trajectory and they are generally expressed as

$$\mathbf{c}_{\min} < \mathbf{c}(t, \mathbf{x}, \boldsymbol{\tau}) < \mathbf{c}_{\max} \quad (140)$$

The nonlinear optimization provides a local-optimal solution. Thus, in order to get a local-optimal solution which is similar to the actual movement of the gymnast, the nonlinear optimization problem is divided in two phases. In the first phase, we restrict the path of the gymnast motion to follow the six phases of motion of the actual gymnast swing-up motion as shown in [Figure 18](#). In each phase we define a bounding box constraint on the generalized coordinates of the gymnast robot as

$$\mathbf{q}_{i_{\min}} < \mathbf{q}_i < \mathbf{q}_{i_{\max}} \quad (141)$$

However the path constraints may not be dynamically consistent with the rest of the optimization problem and result in non-feasible trajectory. Therefore, these constraints are relaxed in a second phase and we feed the output solution of the first phase as the guess solution for the second phase which result in a dynamically feasible

local-optimal trajectory which is similar to the actual gymnast motion. the constraints relaxation and solution cascading scheme is a common practice in nonlinear optimization problems to converge to a feasible and high-quality solution.

Finally, we analyze the output trajectory using a novel graphical and quantitative technique "*Dynamic Coupling Map (DCM)*" along with the associated natural dynamic indexes that help gain insight into the dynamic motion of the underactuated system and the associated control strategy. In particular, we employ the task space formulation presented in [Section 4.1](#) to study the influence of different the dynamic constraints such as the torque limits and the second-order nonholonomic constraints due to the underactuation nature of the gymnast on the task-space acceleration of the terminal organ (foot) which is required to move from the down equilibrium position to the up-right unstable position. More interestingly, the DCM and the associated natural dynamic indexes help in understanding the relationship between the natural dynamics acting on the system and the input torques. Our ultimate goal for studying such systems is to understand problems of dynamic locomotion in both biological systems and in robotic systems which exploit its natural dynamics.

4.2.3 Results

For richer motion analysis, we study the effect of increasing the torque limits of the active subsystem (shoulder and hip joints) on the dynamic swing-up manoeuvre of the gymnast-robot. Therefore, two trajectory optimization problems are solved with two sets of torque limits while maintaining the same physical parameters values and optimization related settings. The low torque dynamic swing-up manoeuvre corresponds to a gymnast-robot with torque limits set to $|\tau_{\text{limit}}| = [50 \ 50]^T$ N.m while the high-torque case corresponds to a gymnast-robot with torque limits set to $|\tau_{\text{limit}}| = [500 \ 500]^T$ N.m.

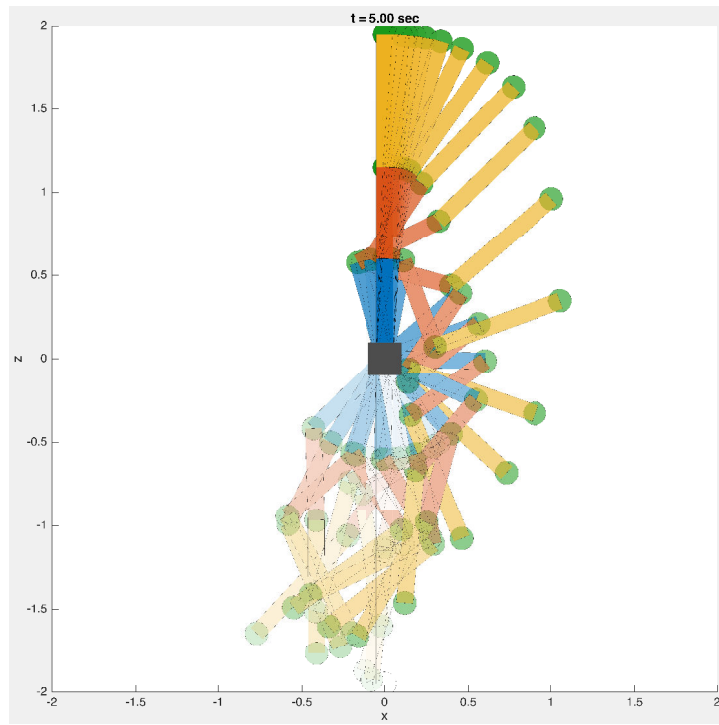
The nonlinear trajectory optimization solver outputs two different local-optimal trajectories demonstrating two different dynamic behaviours for the swing-up dynamic manoeuvre of the gymnast-robot for the two cases as depicted in [Figure 19](#). The first link which represents the arms is shown in blue and is connected to a rigid bar shown in black via a passive pivot joint. The second and third links representing the torso and the legs are shown in red and yellow, respectively. Both are connected via active pivot joints representing the shoulder and hip joint, respectively. The motion of the gymnast-robot with low torque limits exhibits a swinging phase before accelerating to the upright vertical configuration as shown in [Figure 19a](#), whereas the gymnast-robot in the high-torque case accelerates directly to the

goal configuration. Note that in [Figure 19b](#) the gymnast's motion exhibits oscillations or "a kicking motion" despite the high torque capacity which should permit a smooth motion towards the goal configuration. This phenomenon is exhibited due to the underactuation nature on the gymnast-robot which imposes a second order nonholonomic constraint, whereas a fully-actuated robot with sufficient torque can perform a linearly interpolated motion between the two configurations, for more details reader is referred to the discussion in [Section 4.2.4](#).

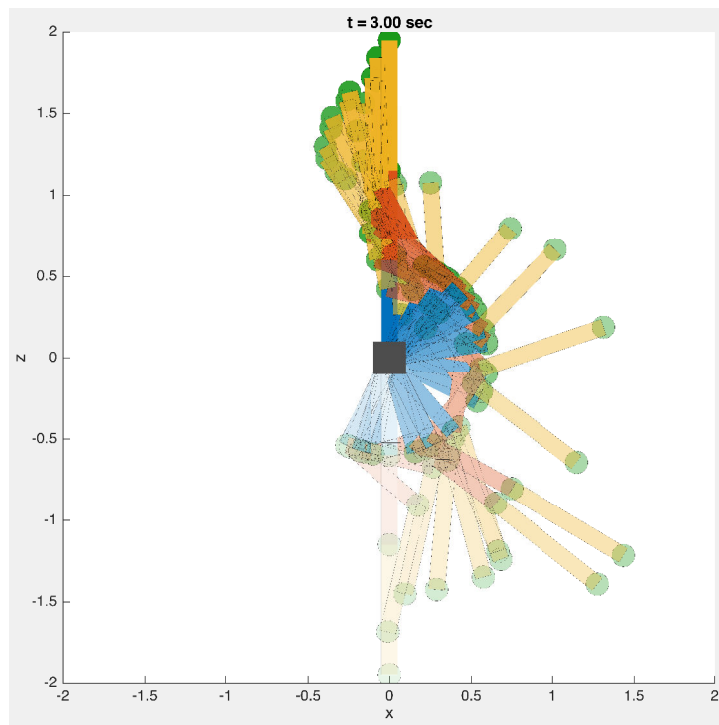
The resultant local-optimal trajectory for the low torque case is shown in [Figure 20](#). The evolution of the generalized coordinates and the generalized velocities during the swing-up motion are shown in [Figure 20b](#) and [Figure 20c](#), respectively. [Figure 20a](#) shows the local-optimal torque control profile, recall that τ_1 and τ_2 are the torque inputs for the active subsystems, corresponding to the shoulder and hip joints, respectively. Accordingly, the local optimal trajectory for the high torque case is shown in [Figure 21](#). Note that despite the nonlinear trajectory optimization requires an initial guess for the motion trajectory including, torque profile, generalized coordinates and generalized velocities in addition to the expected duration of the motion. The trajectory optimization solver finds a local optimal solution different than the initial guess. For example, although we have set an initial guess of the time span of the motion to be $t_0 = 6$ s in both cases the achieved the goal configuration with an optimal time of $t^* = 5$ s in the case of low torque capacity whereas the optimal time is reduced to $t^* \simeq 3$ s in the case of high torque capacity.

The output of the nonlinear trajectory optimization if further analyzed using the Task Space-Dynamic Coupling Map (TS-DCM) technique which provides a graphical and quantitative analysis tool to understand the influence of dynamic constraints (e.g. torque limits, underactuation) on the motion and the control strategy used to achieve the final optimal motion. The results are organized in tables with three rows, the first row shows the gymnast robot at a specific instant while the second and third rows show the corresponding TS-DCE and TS-DCM, respectively. The analysis results for the low-torque case are shown in [Table 4](#) to [Table 7](#) while the results for the high-torque case are shown in [Table 8](#) to [Table 10](#)

Furthermore, a comparison of the Natural Dynamic Index (NDI) during the swing-up dynamic manoeuvre for the gymnast robot between both cases: low-torque capacity (shown in blue) and high-torque capacity (shown in red) is given in [Figure 22](#). The evolution of NDI_1 with time is shown in [Figure 22a](#) while the evolution of NDI_2 and NDI_3 are shown in [Figure 22b](#) and [Figure 22c](#), respectively

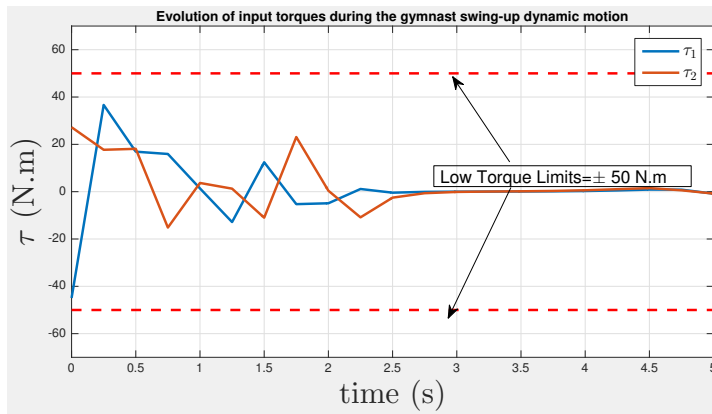


(a)

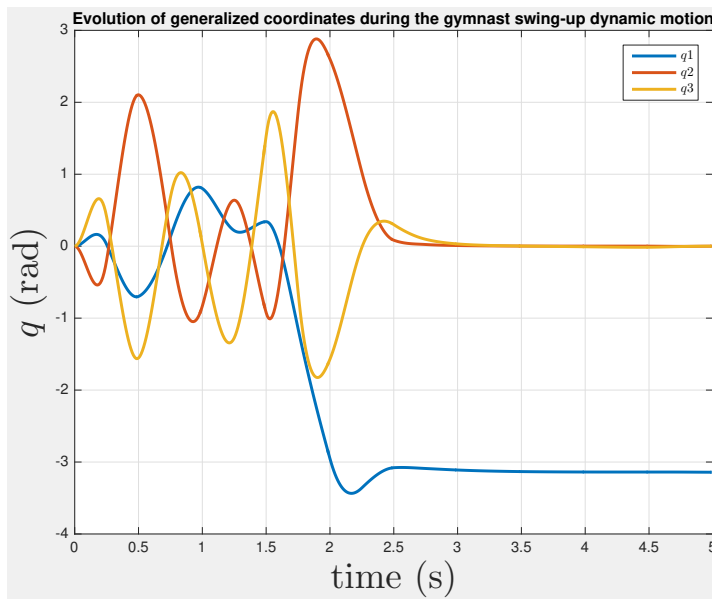


(b)

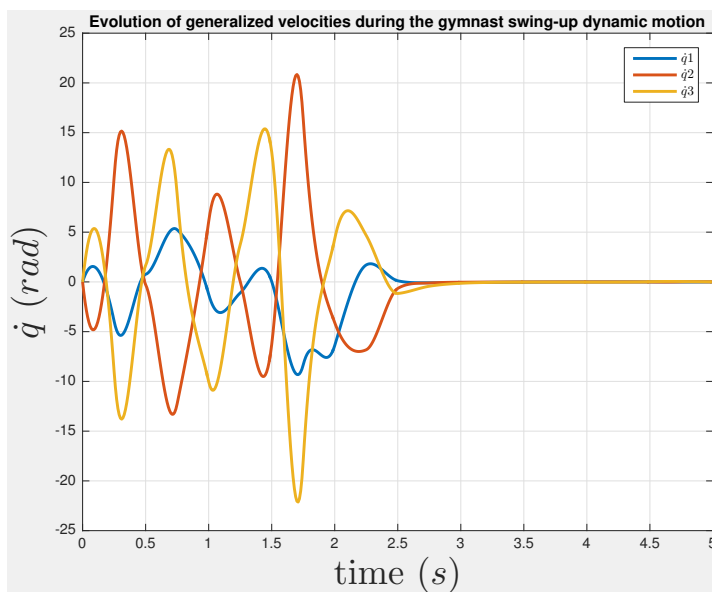
Figure 19: Local-optimal motion results for the gymnast-robot swing-up dynamic manoeuvre showing two different dynamic behaviours between low torque and high-torque constraints. (a) Swing-up motion compilation with low torque constraint $|\tau_{limit}| = [50, 50]^T$ N.m exhibits a swinging phase which is absent in (b) the swing-up motion with high torque constraints $|\tau_{limit}| = [500, 500]^T$ N.m



(a)



(b)



(c)

Figure 20: Nonlinear trajectory optimization results for the dynamic swingup manoeuvre of the gymnast-robot swing-up with low torque capacity. (a) Shows the local-optimal torque control profile, while (b) and (c) shows the local-optimal trajectory for the generalized coordinates and the generalized velocities, respectively.

Table 4: DCM analysis for the dynamic swing-up manoeuvre of the gymnast robot with low torque capacity

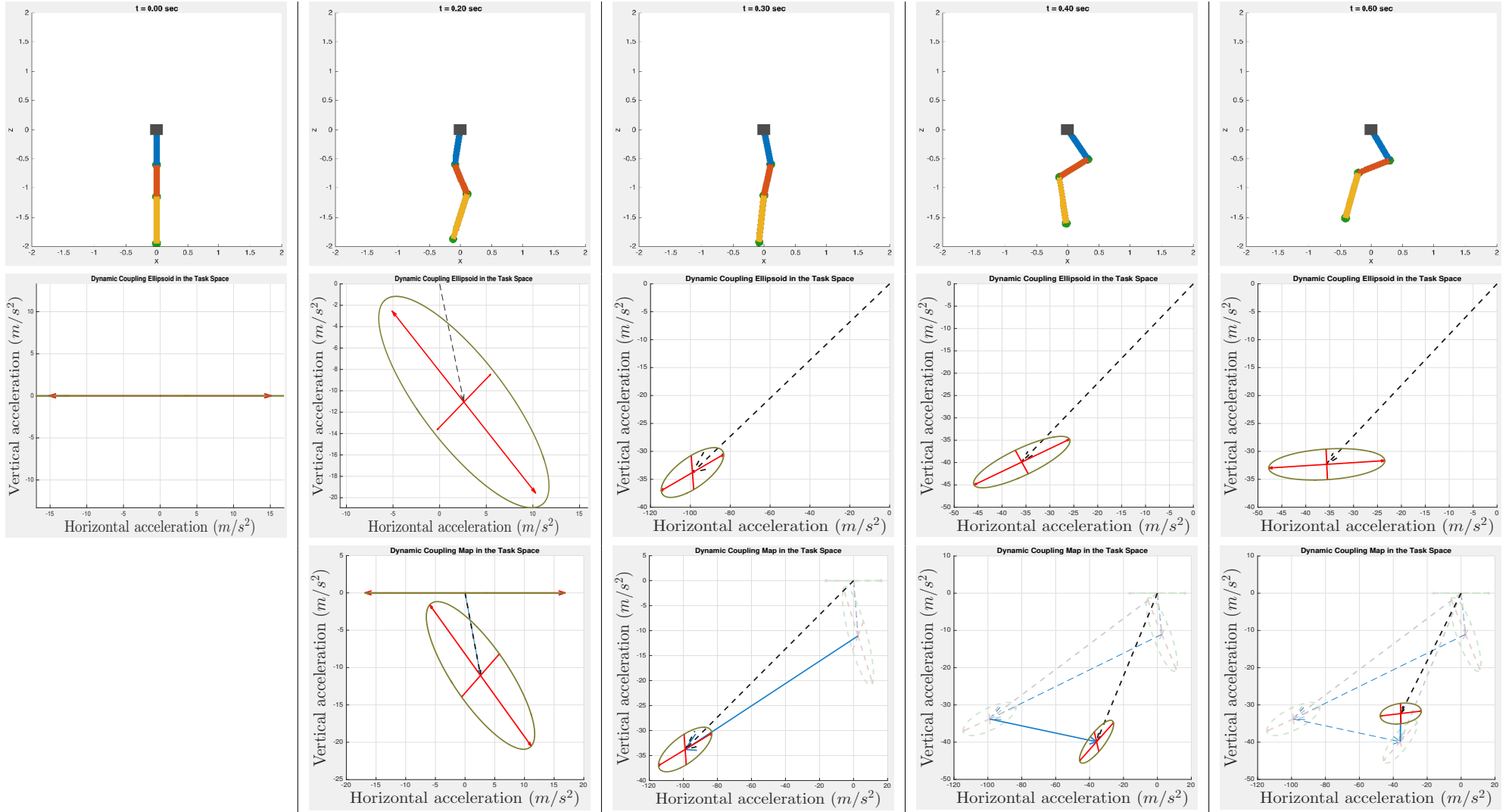


Table 5: Table 3 Continued: DCM analysis for the dynamic swing-up manoeuvre of the gymnast robot with low torque capacity

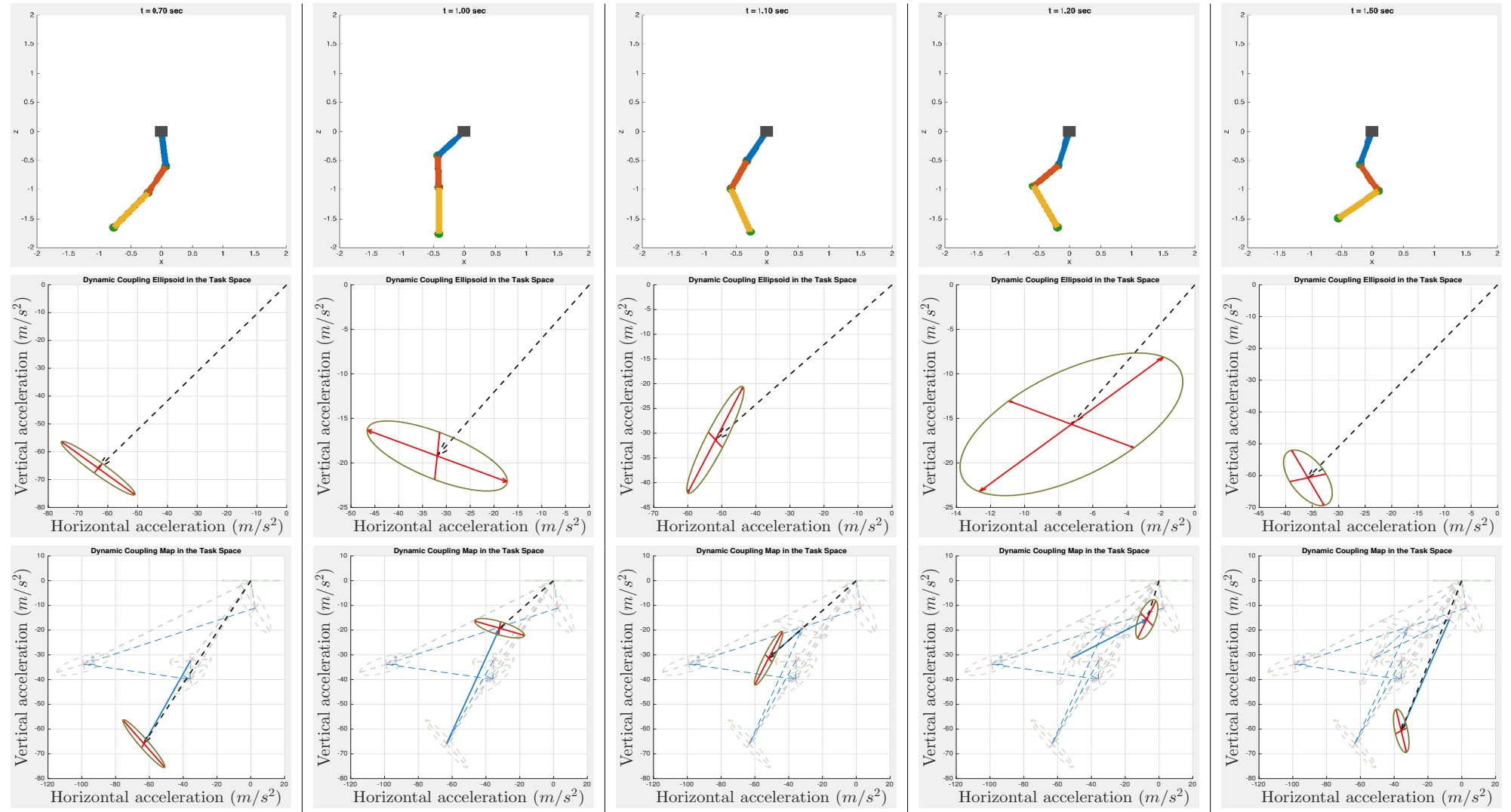


Table 6: Table 4 Continued: DCM analysis for the dynamic swing-up manoeuvre of the gymnast robot with low torque capacity

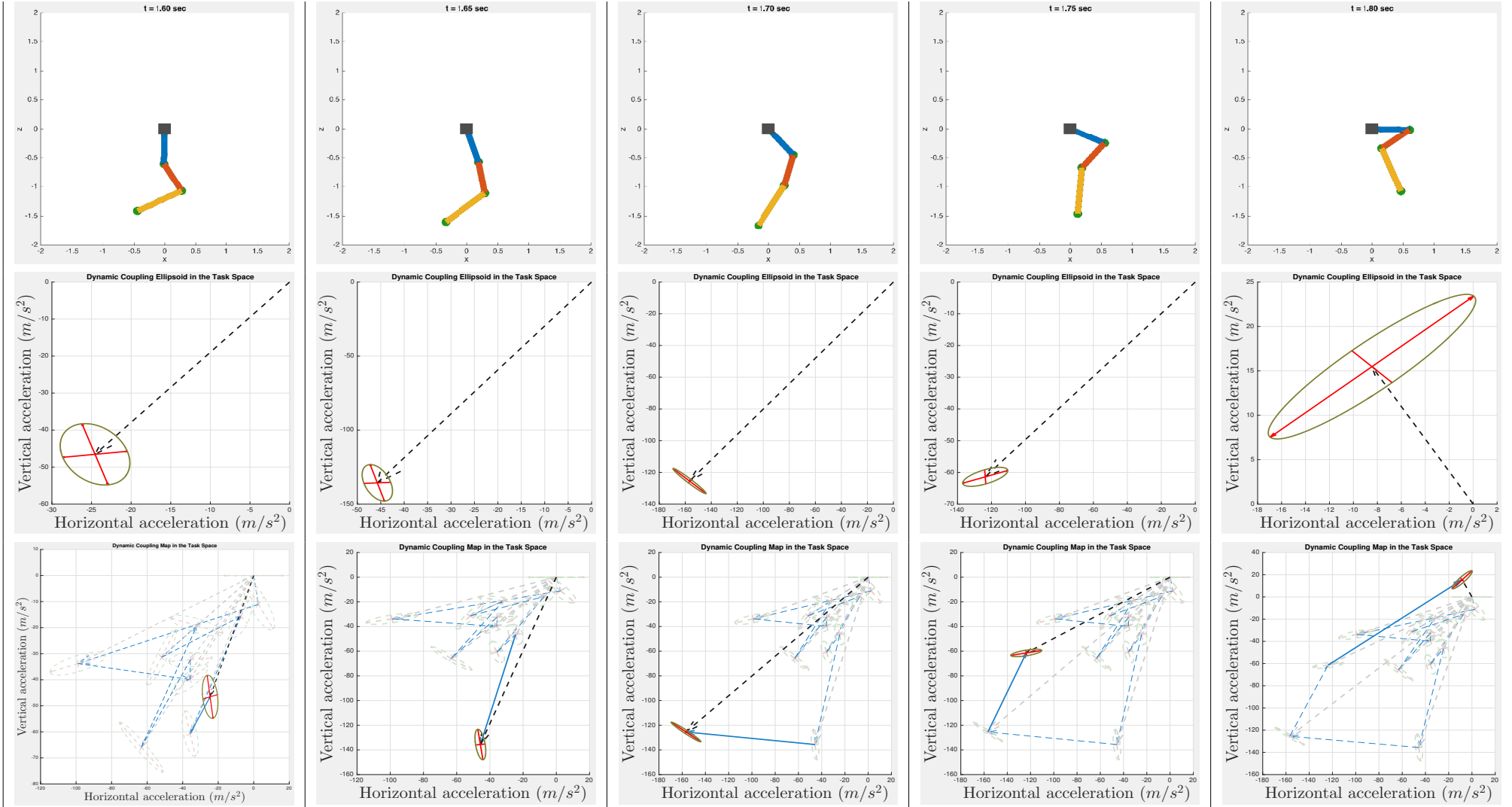
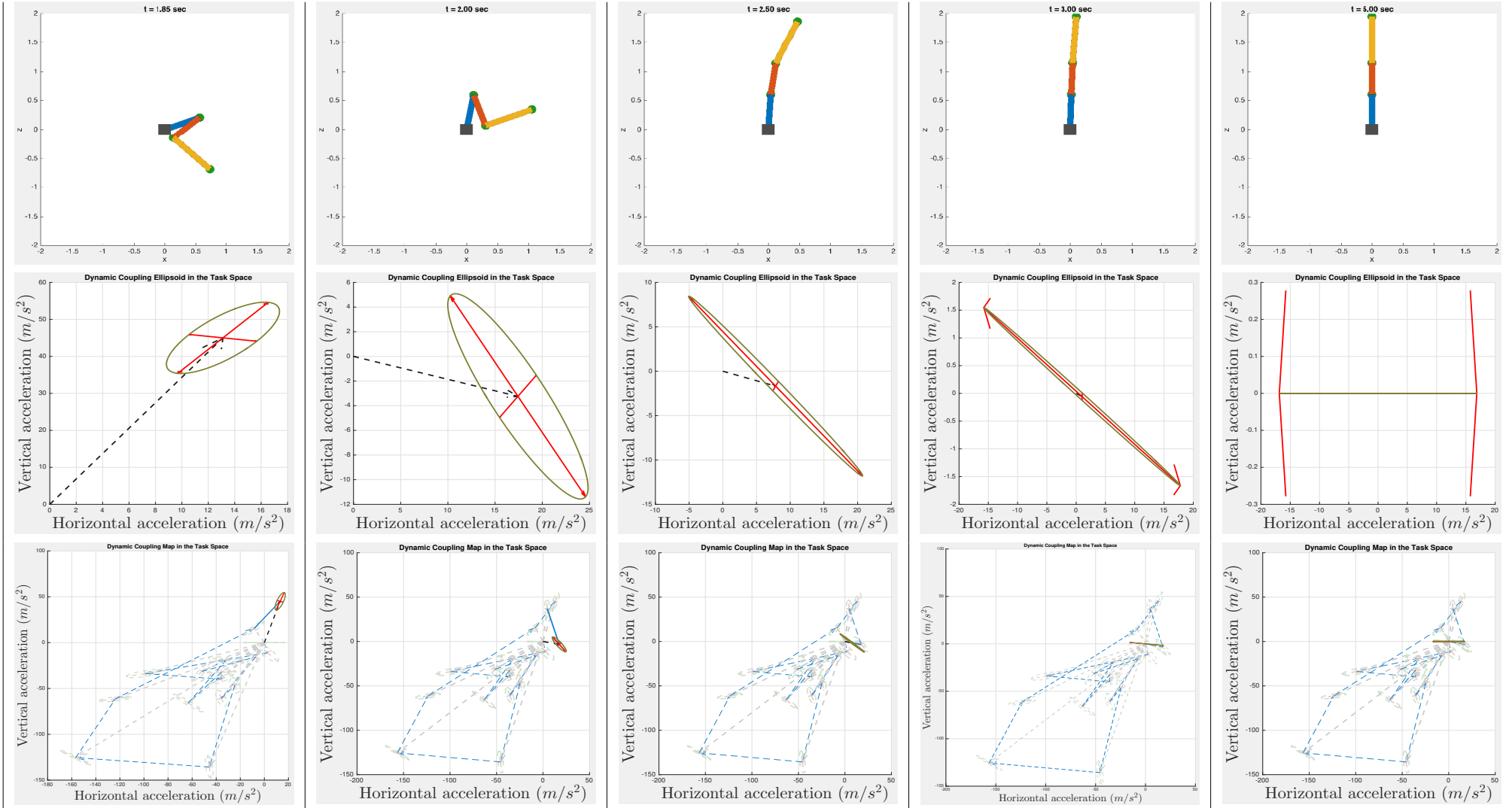
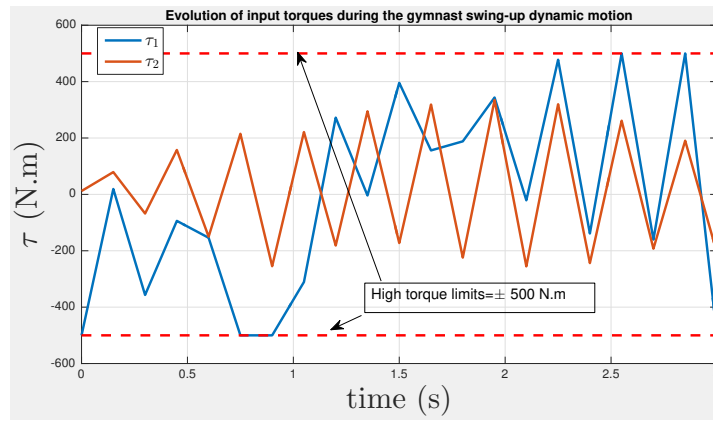
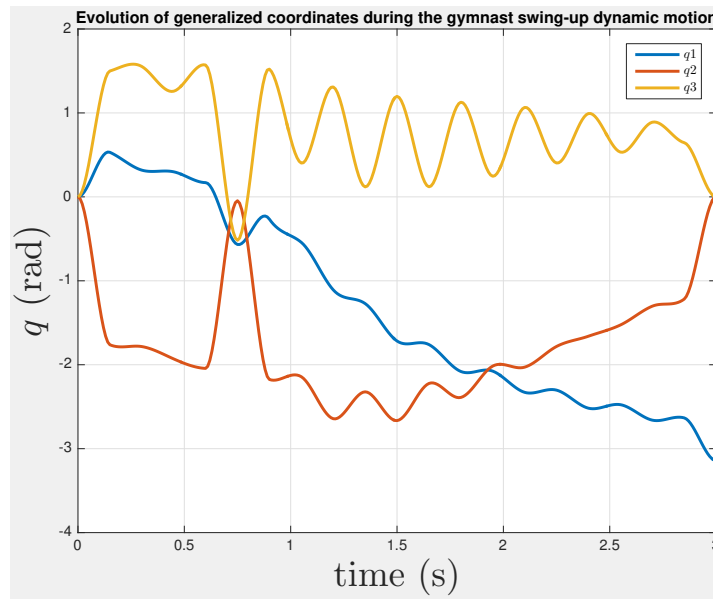


Table 7: Table 5 Continued: DCM analysis for the dynamic swing-up manoeuvre of the gymnast robot with low torque capacity

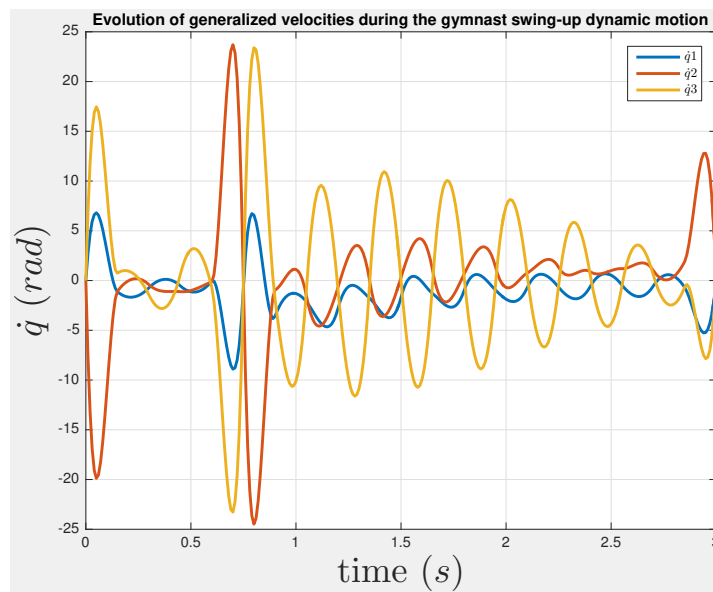




(a)



(b)



(c)

Figure 21: Nonlinear trajectory optimization results for the dynamic swingup manoeuvre of the gymnast-robot swing-up with high torque capacity. (a) Shows the local-optimal torque control profile, while (b) and (c) shows the local-optimal trajectory for the generalized coordinates and the generalized velocities, respectively.

Table 8: DCM analysis for the dynamic swing-up manoeuvre of the gymnast robot with high torque capacity

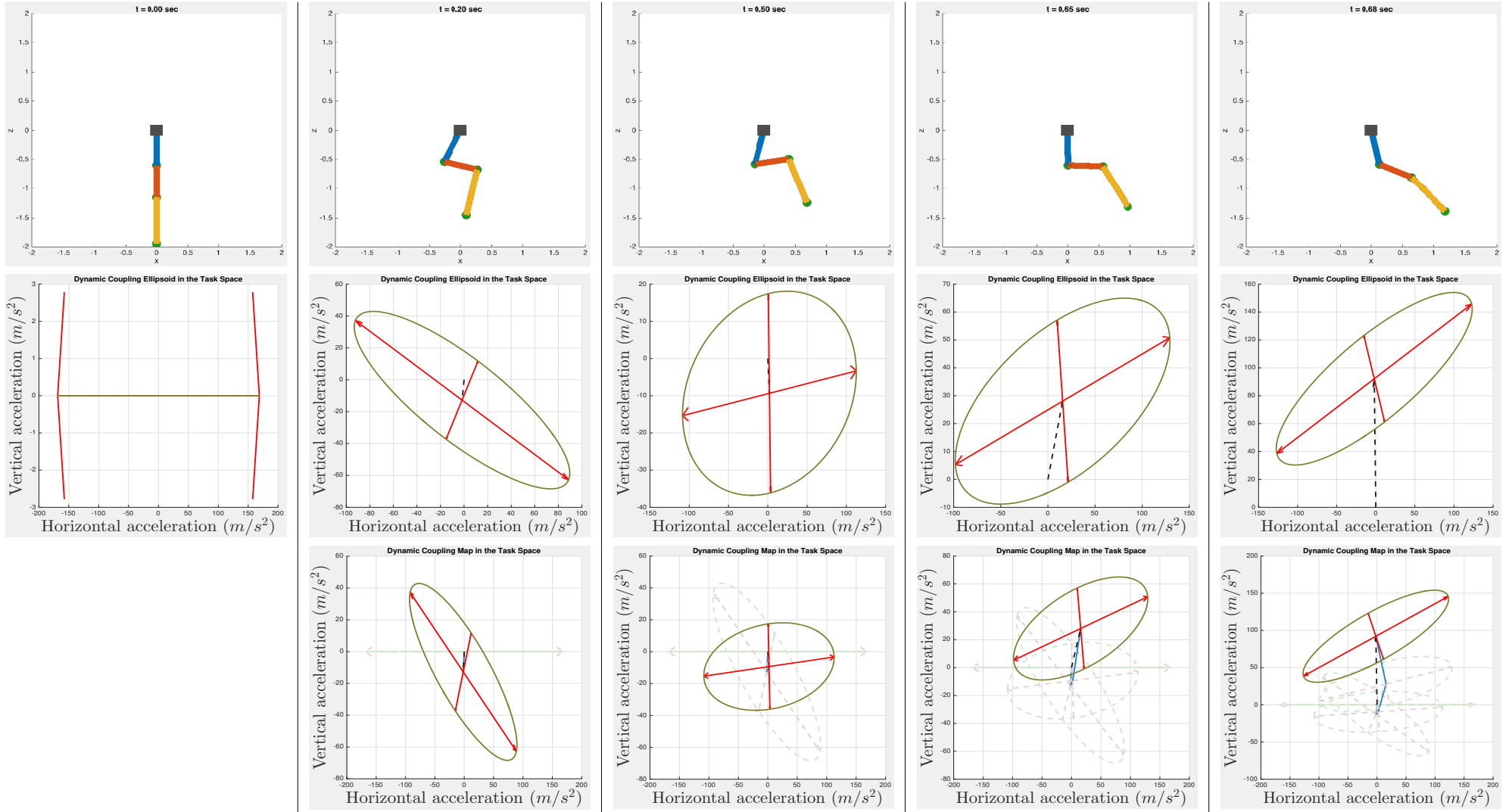


Table 9: table 7 continued: DCM analysis for the dynamic swing-up manoeuvre of the gymnast robot with high torque capacity

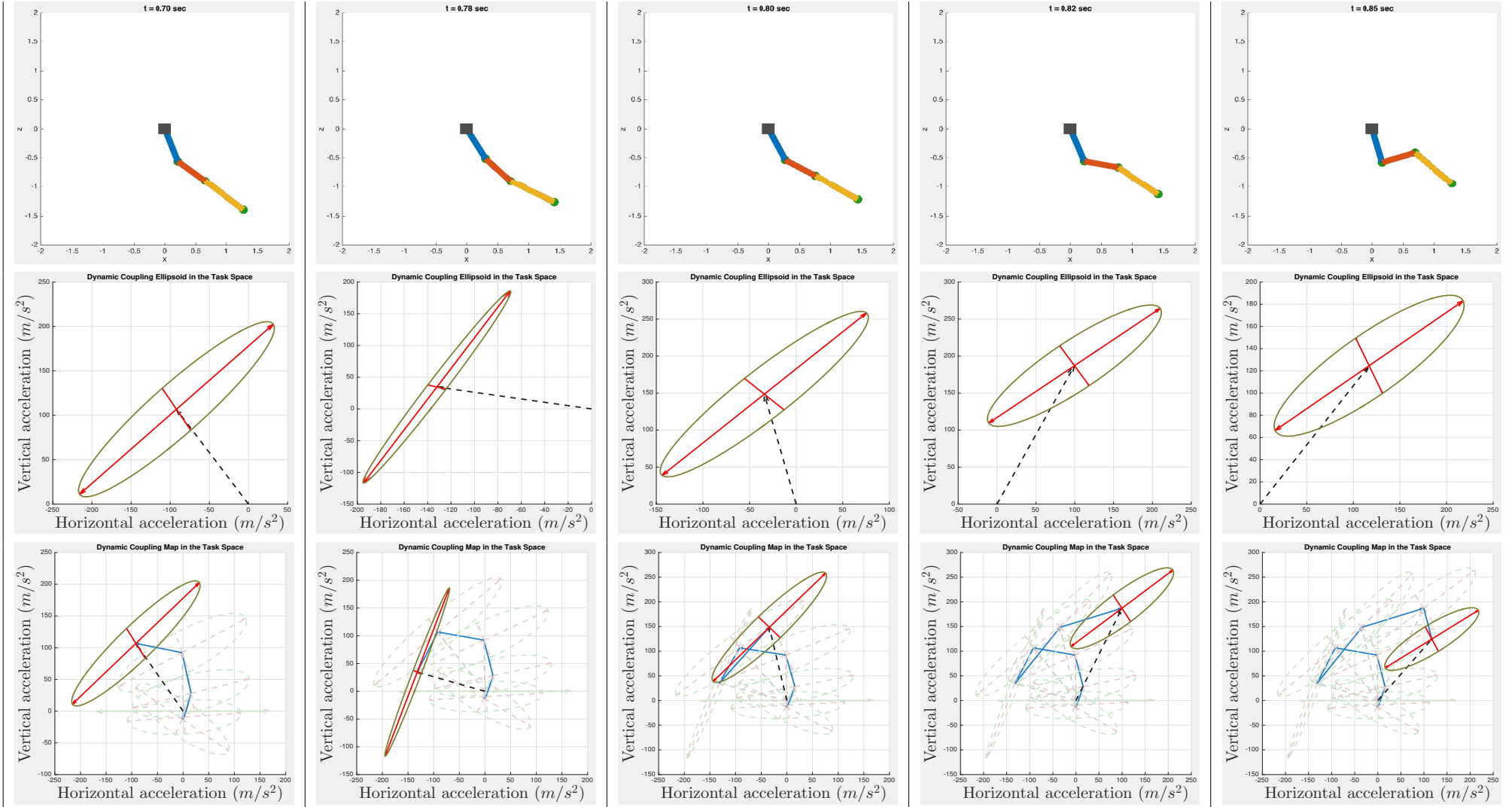
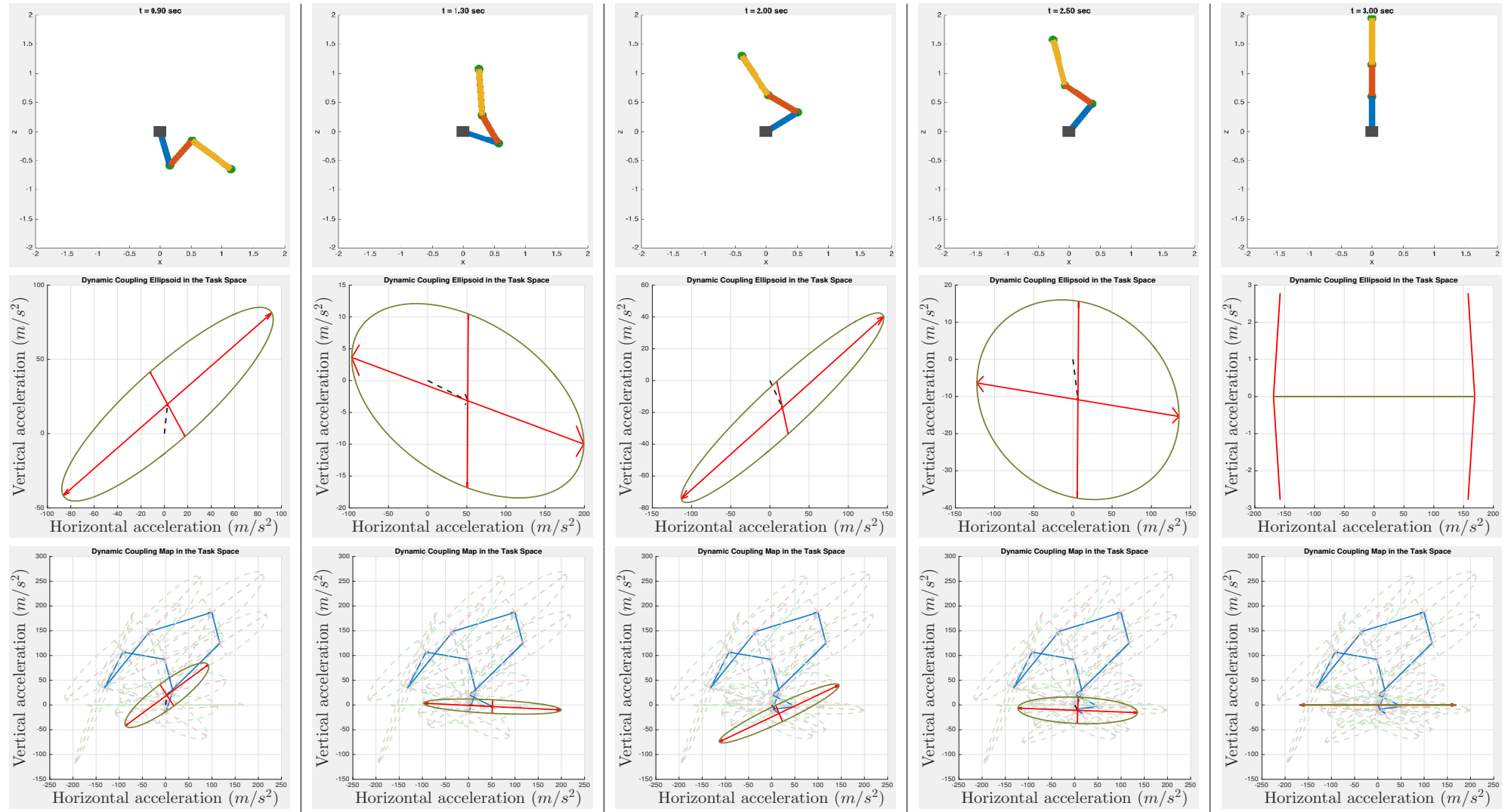


Table 10: table 8 continued: DCM analysis for the dynamic swing-up manoeuvre of the gymnast robot with High torque capacity

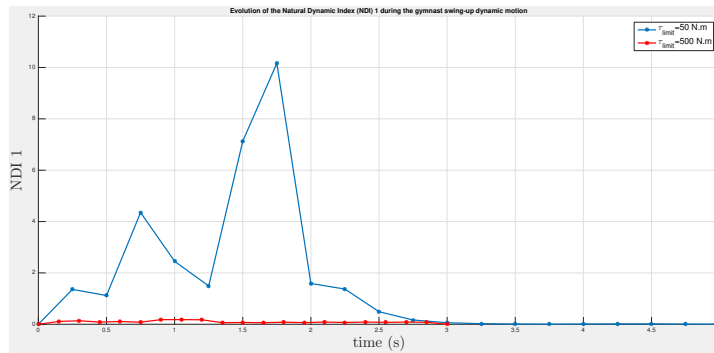


4.2.4 Discussion

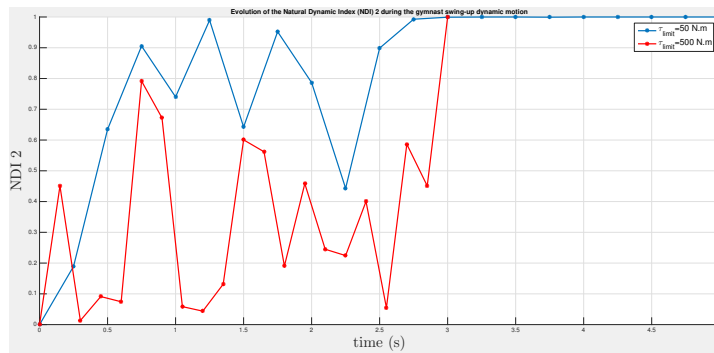
Trajectory optimization proved to be an interesting approach to generate high quality dynamic motion despite its local optimality aspect. Moreover, its natural capacity to integrate all types of constraints (linear, nonlinear, complementarity problems), objective functions and application-related heuristics allowed it to gain traction in the robotics community. However, after many iterations, the optimization solver outputs a single local optimal trajectory without any insight into the nature of the given trajectory. The swing up motion example illustrates the emergence of nontrivial solution to the torque control, velocity and position trajectory from simple core principles (time and torque minimization, boundary conditions, torque limits, dynamic model, etc.).

We demonstrate how to use the Dynamic Coupling map (DCM) and the associated Natural Dynamic Indexes to analyze the dynamic motion given by the optimization. For a richer analysis, we provide a comparative study of two different cases of the swing-up motion of a gymnast-robot. Both cases retain the same physical parameters values of the gymnast model and optimization settings except that in the first case severe torque limits were applied while in the second case high-torques were allowed. The resulting dynamic motions for both cases are drastically different. Qualitatively speaking, the first case, with low torque limits (50 N.m) demonstrates more swinging phases compared to the second case with high-torque limits (500 N.m).

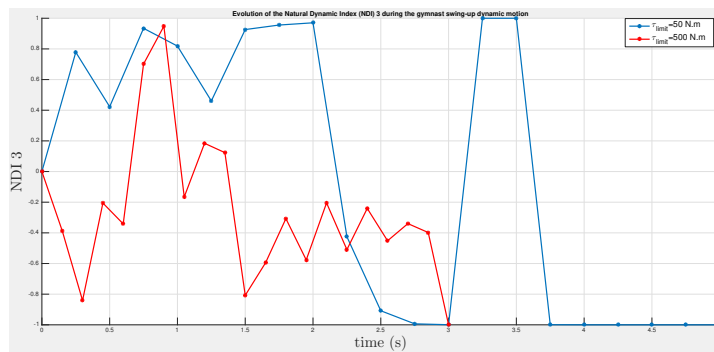
DCM and the associated indexes provide more in-depth dynamic analysis of the swing-up motion. To facilitate the navigation and explanation of the DCM, let the location of each cell in the tables [Table 4](#) to [Table 10](#) be referred to by the triplet (t, r, c) , where t , r and c corresponds to the number of table, row and column, respectively. The 'Gymnast-robot' starts from an equilibrium position depicted in cell $(1,1,1)$. Since the starting configuration is singular, the corresponding task space Dynamic Coupling Ellipsoid (DCE) in cell $(1,2,1)$, representing the acceleration capacity of the terminal organ or the foot (shown in green), is degenerated to a single line in the horizontal acceleration. The DCE shows that the torque limits impose horizontal acceleration limits to $\pm 15 \text{ m/s}^2$, however since the DCE is degenerated the gymnast robot cannot generate vertical acceleration in this configuration. Since the origin of the DCE coincides with the origin of the acceleration space then the initial state is stable. Meanwhile, [Figure 20a](#) shows that the robot applies the maximum torque on the hip joint and starts by quickly saturating. Consequently, at $t = 0.2$, the robot starts by retracting the legs. The corresponding DCM, depicted in cell $(1,3,2)$, shows that as the robot starts getting out of singularity



(a)



(b)



(c)

Figure 22: Comparison of the Natural Dynamic Index (NDI) during the swing-up dynamic manoeuvre for the gymnast robot between both cases: low-torque capacity (shown in blue) and high-torque capacity (shown in red). the evolution of NDI_1 with time is shown in (a) while the evolution of NDI_2 and NDI_3 are shown in (b) and (c), respectively

the DCE is no longer degenerated and has the capacity to generate a vertical acceleration which is limited to -1 m/s^2 and -20 m/s^2 due to torque limits as well as the drift vector \ddot{X}_{bias} (shown in black). The DCE shows that despite the non-degenerated ellipsoid in the task acceleration space, the robot is not capable to generate a positive vertical acceleration. This is mainly due to the drift vector \ddot{X}_{bias} which is dominated by the gravity term because the generalized velocity \dot{q} is still low and the velocity dependent forces has relatively little effect. Thus, the center of the DCE is shifted towards $-g \text{ m/s}^2$ as shown in [Section 4.1.6](#). Moreover, since the DCE does not contain the origin of the acceleration space it is clear that robot does not have the torque capacity to compensate the negative gravity acceleration. Therefore, it is impossible to achieve positive vertical acceleration by depending solely on the torque capability of the active subsystem of the under-actuated robot. Interestingly, it is possible to attain other areas in the acceleration space even it is initially not covered by the DCE due to the torque restrictions. This can be achieved by exploiting the \ddot{X}_{bias} vector to shift the origin of the DCE towards the positive vertical acceleration. This means that the only mean to achieve a considerable positive vertical acceleration is to exploit the natural dynamics acting on the system. *Equivalently, the DCM provides a graphical and a quantitative tool to analyze the qualitative idea of exploiting the natural dynamics by studying the evolution of \ddot{X}_{bias} vector and its relation with DCE and the input torques as demonstrated afterwards.* ‘

DCM analysis shows graphically and quantitatively how the gymnast robot exploit the natural dynamics as its actuators solely fails to achieve the swing-up dynamic manoeuvre

Indeed, the motion depicted in the following frames shows that as the gymnast-robot velocity increases the norm of the acceleration bias vector \ddot{X}_{bias} increases as well. Note that in cell(1,2,3), the DCE shows that the natural dynamics, represented by the bias vector (shown in black), is considerably greater than the ellipsoid itself which represents the influence of the input torques on the acceleration of the terminal organ. The evolution ratio of the influence of the natural dynamics (also called drift forces) to the actual torque capacity is reflected by the proposed index *NDI 1*, shown in [Figure 22a](#). This means that as the *NDI 1* becomes greater than 1 ($\text{NDI1} > 1$) the input torques can neither control the motion of the robot nor compensate the drift forces which arise due to the natural dynamics. However, it is possible to indirectly control or exploit the natural dynamics through the synchronised use of the input torques. We attempt to capture the synchronisation between the natural dynamics and the input torques through the proposed indexes *NDI 2* and *NDI 3* which are shown in [Figure 22b](#) and [Figure 22c](#), respectively. Recall from [Section 4.1.2](#) that *NDI 2* describes the absolute value of the angle between the acceleration bias vector \ddot{X}_{bias} and the major axis of the ellipsoid while *NDI 3* defines the angle between the acceleration bias vector \ddot{X}_{bias} and the acceleration due to the input torques \ddot{X}_{τ} . The blue curves in [Fig-](#)

ure 22b and Figure 22c corresponding to the evolution of NDI_2 and NDI_3 for the case of swing-up motion with low torque limits, show that they are generally above 0.5. This can be interpreted as the input torques act in generally in the direction of the natural dynamics in order to exploit it instead of trying to override it or to compensate for it.

The key challenge is to steer the natural dynamics, or equivalently the acceleration bias vector \ddot{X}_{bias} in the desired direction. In the case of the dynamic swing-up manoeuvre, the goal is to steer \ddot{X}_{bias} towards the positive vertical acceleration space. The analysis shown in Table 4 to Table 7 shows that there are two principal mechanisms to achieve this motion. *The first mechanism is to exploit the velocity-dependent inertial forces by the means of inertia redistribution.* The frames from $t = 0.2$ s to $t = 1.7$ s show that the gymnast-robot attempts several swings to increase its velocity. A closer inspection shows that the gymnast-robot reconfigure its inertia distribution by retracting and extending its center of mass which result in amplifying the angular oscillations. From the DCM perspective and by inspecting the trace of evolution of the natural dynamics \ddot{X}_{bias} (shown in blue) from cell(1,3,2) to cell(6,3,1), we can observe a discretized version of a swirl pattern. The high natural dynamic indexes in Figure 22b and Figure 22c demonstrate that the swirl pattern is a not a chaotic movement but rather a purposely planned trajectory in order to exploit the natural dynamics to achieve the desired swing-up movement. This confirms the results reported in [SS02], where they demonstrated on a variable length pendulum that by proper extension and retraction of the pendulum, hence redistributing the inertia, the Coriolis forces are exploited and steered to achieve attenuation/amplification of the angular oscillation. This model is used to explain a child on a playground swing. One explanation of the phenomenon of the swirl pattern is that it is not possible to steer to an arbitrary acceleration due to the second-order nonholonomic constraints imposed by the underactuation of the system. Therefore, it is not possible to steer directly towards the positive vertical acceleration, however it is possible to manoeuvre to any point in the acceleration space through a series of manoeuvres following the shown swirl pattern. The kinematic equivalent of this phenomenon is the car parallel parking problem which has a first-order nonholonomic constraint which make it possible to reach an arbitrary position only through a series of adequate manoeuvres.

The second principal mechanism is the acceleration channeling through singularity. This mechanism can be clearly observed by inspecting the DCM at cell(5,3,3) which corresponds to dynamic motion at $t = 1.7$ s. Note that the active subsystem of the gymnast robot is at a singu-

lar configuration. Also note that it is only at this moment that the gymnast robot starts to steer the acceleration bias vector \ddot{X}_{bias} considerably towards the positive vertical acceleration space. In the two following frames at $t = 1.75$ s and $t = 1.8$ s you can observe a surge in the vertical acceleration capacity from -130 m/s² to 20 m/s². Meanwhile, note that the surge in acceleration is not due to a surge in the input torques as shown in [Figure 20a](#) at $t = 1.7$ s. The surge in the vertical acceleration is rather due to the synchronization between the input torques and the natural dynamics. This conclusion is confirmed by the three natural dynamic indexes shown in [Figure 22](#); at $t = 1.7$ s $NDI_1 = 10$ which means that the influence of the natural dynamics on the terminal organ acceleration is 10 times more than the influence of input torques. Moreover, $NDI_2 > 0.9$ which means that the DCE's principal axis is oriented towards the acceleration bias vector \ddot{X}_{bias} and $NDI_3 > 0.9$ meaning that the input torques fully exploit the natural the dynamics to achieve a surge in the positive vertical acceleration. A similar result is reported by [\[RG02\]](#) for a fully actuated manipulator where the authors claim that *"singularity appears to offer an efficient means for "focusing" kinetic energy to produce movement in a particular direction"*. However, we show that in the case of underactuated manipulator only the active subsystem needs to be in a singular configuration. This demonstrates the coherence of the proposed DCM analysis technique with the literature.

In contrast to the swing-up motion of the gymnast-robot with low torque limits, the trajectory optimization solver outputs a completely different dynamic motion after increasing the torque limits 10 folds to 500/ : N.m. The output trajectory depicted in [Figure 21](#) and [Table 8](#) to [Table 10](#) shows that the gymnast-robot reaches the upward vertical goal configuration without the need to perform the swing-up manoeuvre. This result is demonstrated graphically and quantitatively using the DCM analysis technique and the associated natural dynamic indexes. In [Table 8](#) the DCE starts in a degenerated configuration similar to the case of the gymnast with low torque limits. However, a clear difference appears in the following frames, the DCE depicted in cell(7,2,2) to cell(7,2,4) demonstrate that the torque capability of the underactuated gymnast-robot is greater than the influence of the natural dynamics (shown in dotted black line), which is also demonstrated in [Figure 22a](#), where NDI_1 is near zero. The DCE occupies a large area of the acceleration space encompassing the origin of the acceleration space and part of the positive vertical acceleration. Consequently, the gymnast-robot has the physical capacity to compensate and override the natural dynamics. This demonstrated clearly in [Figure 22c](#) where NDI_3 is mostly negative, implying that the input torques counteract the natural dynamics.

4.3 CONCLUSION

In this chapter we extended the formulation of the aforementioned analysis technique for task-space acceleration analysis while highlighting the interpretation of TS-DCE and the TS-DCM of the robot dynamics by applying it on a variety of underactuated manipulators with different kinematic and dynamic parameters to demonstrate clearly the mechanism of the analysis technique. Finally, chapter 4 demonstrates the merits of the TS-DCM analysis tool is demonstrated by applying it to the dynamic swing-up maneuver of the gymnast-robot on a high bar. The dynamic motion is first generated using direct collocation trajectory optimization loosely based on the actual motion of a gymnast on a high-bar. However, since trajectory optimization is often treated as a black-box providing a local-optimal trajectory without any insight into the mechanism of the motion, the TS-DCM along with the associated natural dynamic indexes are employed to help gain insight into the dynamic motion of the underactuated system and the associated control strategy and highlight the pivotal role of exploiting the natural dynamics to achieve the dynamic motion.

In the previous chapters, we have presented the DCM as 'a posteriori' graphical analysis tool of the dynamic capability of underactuated manipulators. In this chapter, we take a step towards using DCM as a guiding heuristic tool that helps in synthesizing a motion which exploits the natural dynamic and minimizes energy expenditure. First, we start by presenting the kinodynamic problem formulation then we give an overview of the different approaches of the sampling-based motion planning highlighting the advantages and limitations of each approach. We follow by describing how can the DCM be employed as a control policy and we demonstrate the effectiveness of the Dynamic Coupling based heuristic in planning the famous swing up maneuver of the acrobot robot. We also show how can the proposed DC heuristic be integrated with kinodynamic sampling-based methods such as RRT and EST to improve their performance

5.1 A REVIEW ON KINODYNAMIC SAMPLING BASED MOTION PLANNING

The sampling-based approach has been shown to be a practical solution for quickly finding feasible path for relatively high-dimensional motion planning challenges. The success of "geometrical" path planning algorithms such as RRT and PRM has motivated researchers to further extend its scope to handle kinodynamic problems. Historically, the most common approach for such a problem is to solve it in a decoupled manner, whereby the problem is decomposed in steps of computing a collision-free path (neglecting the differential constraints), then add a dynamic filter which smoothes the path to satisfy the motion constraints, and finally consider "time" of motion by reparameterizing the trajectory so that the robot can execute it. However in principle, most dynamic robots controlled by the second-order derivative of their configuration (e.g., acceleration, torque) and which exhibit drift cannot be treated by a decoupled approach for trajectory planning given their controllability properties [Lau98]. Intuitively, systems with drift constraints are systems where from some states it is impossible to stop instantaneously (this is typically due to momentum). More rigorously, a system $\dot{x} = f(x, u)$ is a drift system if for some state x there does not exist any admissible control u such that $f(x, u) = 0$.

To solve such challenges, the idea of kinodynamic planning has been proposed [Don93], which involves directly searching for a collision-free and feasible trajectory in the underlying system’s state space. This is a harder problem than kinematic path planning, as it involves searching a higher-dimensional space and respecting the underlying flow that arises from the dynamics. Given its importance, however, it has attracted a lot of attention in the robotics community. Sampling-based kinodynamic planners can be divided into two broad categories: state sampling approaches such as RRT and control sampling approaches such as EST and SST. State sampling approaches requires a steering function. This function returns the optimum or at least a feasible path between two states in the absence of obstacles. In the case of a dynamical system, the steering function corresponds to the solution of a two-point boundary value problem (BVP). However, such function exists only for simple dynamics or linearized dynamics (e.g. LQR-RRT) which performs well only close to the linearization area. Furthermore, properties of path planners such as *probabilistic completeness* for RRT is not directly transferable to its kinodynamic version [CPN14]. Actually, Kunz [KS14] showed the incompleteness of the standard Kinodynamic RRT with best input and fixed time step. To avoid the use of steering function and linearization, one can sample the control space directly using forward propagation. Such planners were initially proposed by [Hsu+02]. EST finds an admissible trajectory, rather than the optimal one. Recently [PKP14a; LLB13] showed that expanding the node using random shooting, based on forward propagation of the dynamics can converge to a near-optimal or even an optimal solution under certain conditions. [PKP14b] concludes that for general non-linear systems where a steering function is not available or expensive to compute, a better strategy to directly sample the control space is a fruitful avenue for further improvement. *The focus in this work is to propose a new motion planning algorithm that can handle underactuated robots more efficiently by exploiting the natural dynamics of the system.*

5.1.1 Kinodynamic Planning Problem Formulation

This section develops the notation and mathematical objects necessary to understand sampling-based kinodynamic motion planning. We adopt a terminology similar to [HZ16] and [Jeo15] and we formalize the problem definition as following:

Definition 5.1.1 (Kinodynamic Planning Problem). *Given a state space S , an obstacle region S_{obs} , a feasible goal region S_{goal} , feasible states S_{feas} , feasible inputs $\mathcal{U}_{\text{feas}}$, an initial state $s_0 \in S_{\text{feas}} \setminus S_{\text{obs}}$ a dynamical system \mathcal{D} . A feasible kinodynamic planning problem $\mathcal{P} = (S, \mathcal{U}, s_0, S_{\text{goal}}, S_{\text{feas}}, S_{\text{feas}}, \mathcal{D})$ ask to produce a trajectory $\mathbf{s}(t) : [0, T] \rightarrow S$ and control $\tau(t) : [0, T] \rightarrow$*

\mathcal{U}_{feas} such that

$$\mathbf{S}(0) = \mathbf{s}_I \quad (\text{initial state}) \quad (142)$$

$$\mathbf{S}(T) \in \mathcal{S}_{goal} \subseteq \mathcal{S} \quad (\text{goal state}) \quad (143)$$

$$\mathbf{S}(t) \in \mathcal{S}_{feas} \subseteq \mathcal{S} \quad \forall t \in [0, T] \quad (\text{kinematic constraints}) \quad (144)$$

$$\mathbf{S}(t) \notin \mathcal{S}_{obs} \quad \forall t \in [0, T] \quad (\text{avoid collision}) \quad (145)$$

$$\mathbf{u}(t) \in \mathcal{U}_{feas} \subseteq \mathcal{U} \quad \forall t \in [0, T] \quad (\text{control constraints}) \quad (146)$$

$$\dot{\mathbf{s}}(t) = \mathbf{D}(\mathbf{s}(t), \mathbf{u}(t)) \quad \forall t \in [0, T] \quad (\text{dynamic equation}) \quad (147)$$

$$(148)$$

5.1.2 Taxonomy Of Kinodynamic Planners

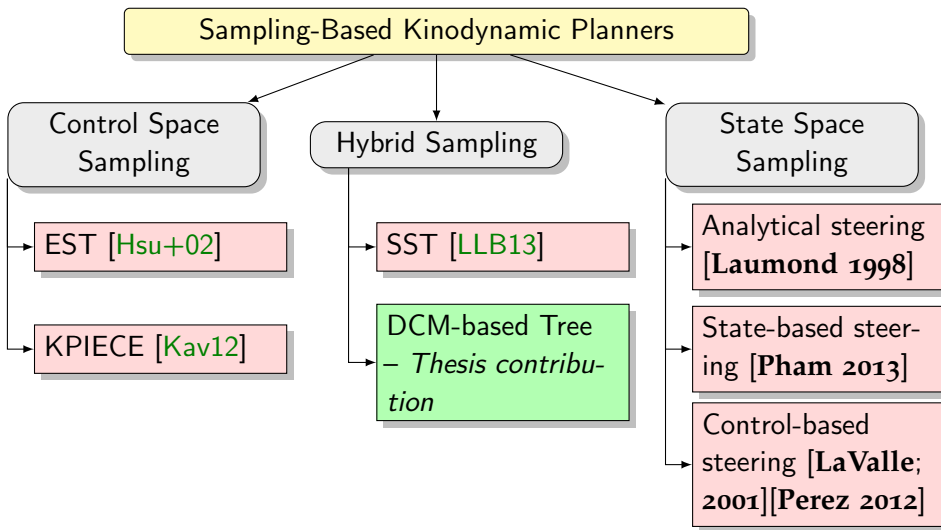


Figure 23: Taxonomy of kinodynamic planners

Extending SBP algorithms to kinodynamic problems is not trivial since states connections in the state-space cannot generally be achieved using direct straight-line interpolation as in the case of path planning in the configuration space. Thus, different approaches were proposed to comply with the kinodynamic constraints. They can be categorized into state-space sampling approach that has several steering methods and control space sampling approach that doesn't rely on a steering method. A simplified taxonomy of the different approaches is illustrated in [Figure 23](#)

State sampling approach depends on a steering method to create a feasible trajectory (edge) between two states (nodes) in the tree. Steering methods can be categorized into three categories:

- **Control-based steering:** compute a control function $\mathbf{u} : [0, T] \rightarrow \mathcal{U}_{adm}$ and generate the corresponding trajectory using forward dynamic. This approach does not guarantee that the desired

state is reached by the end of the trajectory. One of the known algorithms in this category is RRT [LaVo1], in which random functions u are sampled from a family of primitives (e.g., piecewise-constant functions), a number of them are tried and only the one bringing the system closest to the target (sampled state) is retained. Linear-Quadratic Regulation (LQR) [Per+12] is also control-based steering: in this case, u is computed as the optimal policy for a linear approximation of the system given a quadratic cost function.

- **State-based steering:** interpolate a trajectory $\gamma : [0, \Delta t] \rightarrow C$, for instance a Bezier curve matching the initial and target configurations and velocities, and compute a control that makes the system track it. For fully-actuated system, this is typically done using inverse dynamics. If no suitable control exists, the trajectory is rejected.
- **Analytical steering:** with control-based steering, it is easy to respect differential constraints but difficult to reach the desired state. Conversely, with state-based steering, it is easy to reach the desired state but difficult to enforce differential constraints (for instance, inverse dynamics cannot always be used with non-holonomic systems). For some systems, steering functions satisfying both requirements are known, like Reeds and Shepp curves for cars. When it is the case, the problem can be reduced to path planning.

5.2 THE PROPOSED DYNAMIC COUPLING BASED ALGORITHM

Motion planning and control of underactuated nonlinear mechanical systems is still a main concern for the robotics and control communities. Despite the various approaches and frameworks proposed to tackle this problem, they all boil down to finding a control policy which maps sensors to actions. A control policy is a function that generates the motor commands based on the state. The two main approaches for finding a control policy are optimal control theory and reinforcement learning. Optimal control theory [Kir12] answers the question by establishing a certain cost function ((e.g., minimum jerk, minimum torque)) over a predefined time frame. The control law automatically results as the solution of the associated optimization problem. Depending on the problem structure and the resolution method, the control law can be either a feedback control policy or quite often a pure open-loop trajectory, while the correction of errors during execution is left to simple PID controller. The principal limitations of the optimal control approach are:

- Computational requirements limited its application for systems with nonlinear dynamics and strong coupling.

- Optimal control approaches for non-linear systems suffer from the *local-minimum problem* and the sensitivity to the provided initial guess solution, which quickly leads to undesired behaviour or quite often a lot of tuning.
- Identifying the underlying optimality criteria for a certain task is a challenging problem by itself. Not to mention, the challenging complications that arise in the case of multiple criteria for a single task or when the task is decomposed into several sub-task. The sub-field of inverse optimal control is devoted entirely to solve this problem given the optimal solution. However, inverse optimal control problems are difficult from a mathematical point of view, since they require to solve a parameter identification problem inside an optimal control problem [MTL10].

On the other hand, reinforcement learning (RL) finds a control policy by exploiting the data collected through intensive interaction with the dynamical system, therefore, avoiding the classical and laborious analytical approach of optimal control theory. There are two principal paradigms for RL application in robotics, model-free and model-based approaches. Model-free policy search typically requires an expert demonstration to initialize the learning process, followed by many interactions with the actual robot. Model-based policy search attempts to improve the sampling efficiency by learning a simulator of the robot's dynamics from data. Subsequently, the simulator generates trajectories that are used for policy learning. However, both RL paradigms suffer from serious drawbacks:

- Model-free RL approaches often require a large amount of data from these interactions, which limits their applicability.
- While optimization of the initial demonstrated policy leads to improved task performance, in the most popular gradient-based approaches the resulting solution remains within the envelope of the initially demonstrated policy. This limits the method's ability to discover novel optimal control behaviors.
- Not well suited for high-dimensional problems with continuous action and state space leading to the known curse of dimensionality.

We propose to formulate the DCM and the natural dynamics as a feedback control policy that exploits the natural dynamics based on the actual state of the robot. The proposed control policy presents a new control paradigm that is based on a deep insight directly from the robot dynamics itself. The main advantage of the proposed feedback control policy is that can provide *instantly* the input torques that exploit the natural dynamics with direct calculations given the exact dynamic model. Furthermore, *we show that the proposed control policy if*

The famous DeepMind's paper [Mni+15] which applied RL to learn Atari pong game required 50 million frames or 38 days to find a control policy. However, if you just changed the ball color you have to repeat the learning process

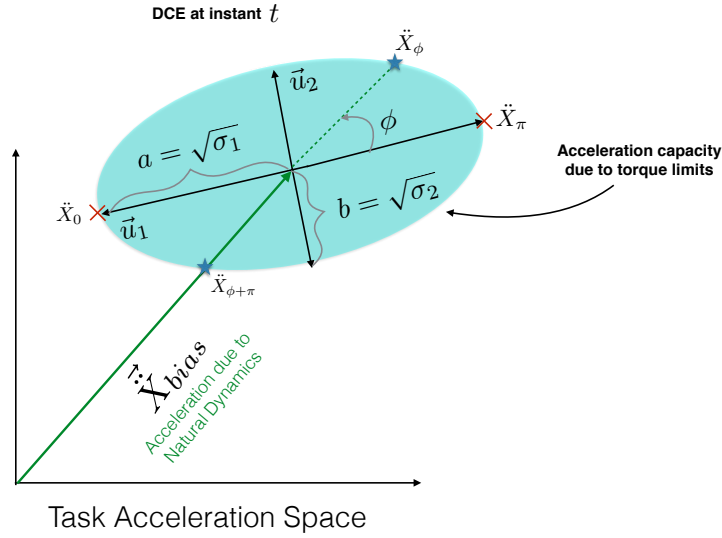


Figure 24: Illustration of DCM-based control policy

combined with sampling-based motion planning scheme can provide an efficient motion planning and control approach that doesn't need neither initial solution guess nor any time-consuming training phase nor laborious and computationally demanding calculations, thus avoiding the aforementioned limitations of the other motion planning paradigms.

5.2.1 Natural Dynamics based Control Policy

We have previously demonstrated in section [Section 4.2](#) that the DCM analysis tool in the task space and the associated natural dynamic indexes show *a posteriori* the mechanism of exploiting the natural dynamics during the dynamic swing-up maneuver of the gymnast-model. More precisely, given a dynamic model and a particular state, the TS-DCM provides the set of achievable accelerations in the task space, $\mathcal{E}_{\ddot{x}}$ from [Equation 74](#), given the torque limits on the active subsystem as well as the second-order nonholonomic constraints imposed by the underactuation. More importantly, it can provide the subset of task-space accelerations that exploit the natural dynamics of the system. These desired accelerations in the task space can be mapped back to the input torques using an adequate operational space control scheme for underactuated systems. Therefore, by following this briefly sketched derivation, we get a feedback control policy that exploits the natural dynamics of the system.

5.2.1.1 Natural Dynamics Based Control Inputs

We define the operational space accelerations that exploit the natural dynamics as the subset of accelerations from the set of the achievable accelerations, defined by the DCE $\mathcal{E}_{\ddot{x}}$, which are generally aligned with the acceleration bias vector $\vec{\ddot{X}}_{bias}$. In a m-d operational space, the intersection between the m-d $\vec{\ddot{X}}_{bias}$ vector and the m-d ellipse given by $\mathcal{E}_{\ddot{x}}$ result in two specific operational space accelerations; One acceleration that exploits the passive dynamics and the other which counteracts and compensate the effect of the passive dynamics within the limits of the torque constraints, as illustrated in [Figure 24](#).

For the sake of demonstration, let $m = 2$, thus the 2-d operational space has the coordinates $X = [X_1 \ X_2]^T$, and the operational acceleration space coordinates are $\ddot{X} = [\ddot{X}_1 \ \ddot{X}_2]^T$. Therefore, the 2-d dynamic coupling ellipse is described parametrically by the equations

$$\ddot{X}_1 = \ddot{X}_{bias_1} + a \cos(\alpha), \quad (149)$$

$$\ddot{X}_2 = \ddot{X}_{bias_2} + b \sin(\alpha), \quad (150)$$

$$0 \leq \alpha \leq 2\pi \quad (151)$$

where $a = \sqrt{\sigma_1}$ and $b = \sqrt{\sigma_2}$ are the semi-length of the ellipse's major and minor axes, respectively. σ_1 and σ_2 are the eigenvalues calculated from the singular value decomposition of the dynamic coupling factor \mathcal{Z}^* in [Equation 124](#). $(\ddot{X}_{bias_1}, \ddot{X}_{bias_2})$ are the coordinates of the center of dynamic coupling ellipse in the operational acceleration space. The ellipse is parameterized by the variable α with a value limited between the 0 and 2π .

The angle between the acceleration bias vector and the ellipse's major axis can be found by multiplying the vector $\vec{\ddot{X}}_{bias}$ with the ellipse's rotation matrix with respect to task acceleration frame U which is calculated from the singular value decomposition in [Equation 124](#)

$$\vec{\ddot{X}}'_{bias} = U \vec{\ddot{X}}_{bias} \quad (152)$$

Finally, the angle between the acceleration bias vector and the DCE's principal axis can be found by taking the multi-valued inverse tangent of the rotated acceleration bias vector $\vec{\ddot{X}}'_{bias}$ using the atan2 function

$$\phi = \text{atan2}(\ddot{X}'_{bias_2}, \ddot{X}'_{bias_1}) \quad (153)$$

By substituting ϕ back in the ellipse's parametric equations [Equation 149](#)- we get the achievable operational space acceleration that exploit the natural dynamics. On the other hand, $\phi + \pi$ is the opposite operational space acceleration

5.2.1.2 *Operational space control*

To compute the input torques needed to realise the calculated accelerations, we employ the operational space control scheme presented by Mistry et al. in [MR12]. However, we note two important contributions. First, we calculate a desired operational space acceleration based on the natural dynamics of the system while Mistry et al. calculate a desired acceleration based on a simple PD form that doesn't take into account the robot dynamics. Second, the operational space control scheme presented in [MR12] cannot handle torque constraints while we guarantee that torque limits are respected thanks to the calculated accelerations from DCM that implicitly take into consideration the inequality constraints on the control input of the active subsystem.

We briefly outline the operational space control. However, for further details reader is referred to [MR12]. Khatib [Kha87] has derived the dynamics in the operational space for unconstrained and fully actuated robot as

$$\Lambda \ddot{X} + (JM^{-1}N - \dot{J}\dot{q}) = F \quad (154)$$

where $\Lambda = (JM^{-1}J^T)^{-1}$ and F is an external force applied at the end-effector. Thus, the operational space control equation for fully-actuated and redundant manipulator is formulated as

$$\tau = J^T F + (I - J^T J^{\#}) \tau_0 \quad (155)$$

where F is calculated from Equation 154 using a desired task acceleration \ddot{X}_{des} in place of \ddot{X} , and $J^{\#}$ is the following generalized inverse of J^T

$$J^{\#} = (JM^{-1}J^T)^{-1} JM^{-1} \quad (156)$$

As discussed by Khatib, this generalized inverse is defined to be dynamically consistent with the task: it is the only generalized inverse that results in zero end-effector acceleration for any τ_0 . This inverse also solves the equation $\dot{x} = J\dot{q}$ for the joint velocities that minimize the instantaneous kinetic energy of the system. For a fully-actuated robot, Equation 155 provide the input torques that compensate for task space dynamics, such that $\ddot{X} = \ddot{X}_{des}$, while decoupling motion generated by τ_0 from the task-space dynamics. However, as noted by [MR12], such dynamic decoupling is not possible for underactuated robots. Note that in the case of underactuation constraints, the generated torques must satisfy

$$\tau = B\tau \quad (157)$$

$$B = \begin{bmatrix} 0 & 0 \\ I_{n_a} & 0 \end{bmatrix} \quad (158)$$

where B is the projector into the actuated joint space, and I_{n_a} is the n_a dimensional identity matrix. Since $J^T F \neq BJ^T F$, therefore, τ_0 has to compensate for the unactuated joints by adding a null space component with the control equation given as

$$\tau = J^T F + \mathbb{N} \tau_0 \quad (159)$$

where \mathbb{N} is defined as $\mathbb{N} = I - J^T J^{\dagger}$. Therefore, from [Equation 157](#) and [Equation 159](#) we have

$$J^T F + \mathbb{N} \tau_0 = BJ^T F + B \mathbb{N} \tau_0 \quad (160)$$

therefore, we can solve for τ_0

$$(I - B)J^T F = -(I - B)\mathbb{N}\tau_0 \quad (161)$$

$$\tau_0 = -[(I - B)\mathbb{N}]^\dagger (I - B)J^T F \quad (162)$$

where the Moore-Penrose pseudoinverse is denoted by the dagger symbol \dagger . Given that [Equation 161](#) has at least one valid solution for τ_0 , we can use [Equation 162](#) in [Equation 159](#) to write the operational space control equation as

$$\tau = \left(I - \mathbb{N}[(I - B)\mathbb{N}]^\dagger \right) J^T F \quad (163)$$

If the system has sufficient redundancy, there may be an infinite number of possible control solutions. However, by using the Moore-Penrose pseudoinverse in [Equation 162](#), we are computing the minimum possible $\|\tau_0\|$. Thus [Equation 163](#) represents the operational space control solution with the minimum possible null space effect. Note that [Equation 163](#) generates dynamically consistent torques for the active-subsystem that achieve the desired operational space acceleration with a null-space motion that compensate for the lost torque at the passive joints.

5.2.1.3 Demonstration of the natural dynamics-based policy on the Acrobot

The ND- control policy shown in the previous section is a general feedback control policy that is based on the natural dynamics analysis of the system, and it is applicable on any dynamical system given

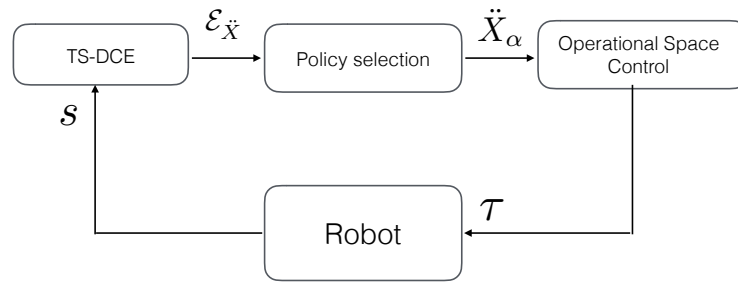


Figure 25: Block diagram of DCE-based control

its dynamical model. However, in order to better understand and appreciate the effect of applying the ND-control policy on a dynamical system, we test it on a canonical underactuated robot model, the acrobot, and study the emerging dynamical behaviour.

Each point in the state dependent DCE represents an achievable operation space acceleration that can be passed to the operational space controller as the desired acceleration (see [Section 5.2.1.2](#)). However, we identify four unique acceleration points, as shown in [Figure 24](#):

- \ddot{X}_0, \ddot{X}_π : are the two acceleration points on both ends of the ellipsoids major axis representing the task space accelerations with the maximum torque transmission efficiency. Using the parametric equation of the ellipsoid ([Equation 149](#)) we can find these accelerations using the parametric angle $\alpha = 0$ and $\alpha = \pi$, hence the notation of the operational space accelerations \ddot{X}_0, \ddot{X}_π with the subscripts 0 and π .
- $\ddot{X}_\phi, \ddot{X}_{\phi+\pi}$: are the natural dynamics based accelerations as defined in [Section 5.2.1.1](#). \ddot{X}_ϕ is the operational space acceleration that exploits the natural dynamics while $\ddot{X}_{\phi+\pi}$ is the acceleration which counteracts the natural dynamics, using the DCE's parametric angle $\alpha = \phi$ and $\alpha = \phi + \pi$, respectively.

The block diagram of the DCE based feedback policy, shown in [Figure 25](#), consists of calculating the task space dynamic coupling ellipsoid TS – DCE(s) at the given state s using the robot's dynamic model, as shown in [Section 4.1](#). TS – DCE(s) will provide the ellipsoid $\mathcal{E}_{\ddot{X}}$ which represents an approximation of the set of feasible task-space accelerations bounded by the physical limits of the input control. More importantly, TS – DCE(s) will provide the acceleration bias vector \ddot{X}_{bias} as shown in [Figure 24](#) which represents the direction and magnitude of the natural dynamics on the task space

acceleration. \ddot{X}_{bias} is a crucial information to calculate the natural dynamics based accelerations as defined in [Section 5.2.1.1](#). The policy selection module selects a particular task space acceleration from the acceleration ellipsoid $\mathcal{E}_{\ddot{X}}$. In particular, the task space acceleration \ddot{X}_{α} is determined based on a given policy using the parameter α from the ellipsoid's parametric equation. For example, to get a dynamical behaviour that exploits the natural dynamics, the acceleration \ddot{X}_{ϕ} is selected based on the angle of the acceleration bias vector \ddot{X}_{bias} , whereas for a motion that maximises the torque transmission efficiency \ddot{X}_0 is selected. The desired acceleration from the policy selection module is then passed to the operational space control to get the required control input τ to achieve the desired behaviour.

The presented control scheme is applied on the acrobot with a frequency of 100 Hz. The acrobot is a canonical underactuated robot with links lengths $l_1 = l_2 = 1$ m and masses $m_1 = m_2 = 1$ Kg the first joint θ_1 is unactuated while the second joint θ_2 has an input torque limit of $\|\tau\| = 5$ N.m.

First and foremost, it is interesting to know what does each policy produces in terms of input torque and how does it evolve in the state space, since for each state $s = (q, \dot{q})$ there is a unique input torque τ . [Figure 26](#) show the torque as function of the state for control policies \ddot{X}_0 and \ddot{X}_{π} . Both policies represent the maximum torque transmission efficiency from the active subsystem (joint 2) to the operational point (terminal organ). Several observations can be made:

- First, if we thought of this feedback control policy as a black box that takes the state as an input and produces a torque as an output, we observe that both control policies based on \ddot{X}_0 and \ddot{X}_{π} outputs a torque that is always at the limits of the torque bounds regardless of the state. This observation made clear by using the the colormap plots in [Figure 26c](#) and [Figure 26d](#), where the torque has a binary value either $\tau = \tau_{max} = +5$ N.m represented by yellow or $\tau = \tau_{min} = -5$ N.m represented by blue.
- The output torque varies with both angles q_1 and q_2 . However, the angular velocities does not influence the output torque of these policies. This made clear by comparing the torque given by the state $\{0 \leq q_1, q_2 \leq 2\pi \mid s = [q_1, q_2, 0, 0]^T\}$ with zero angular velocities as shown in [Figure 26c](#) and [Figure 26d](#), with the output torque for the states $\{0 \leq q_1, q_2 \leq 2\pi \mid s = [q_1, q_2, 10, 10]^T\}$ where the angular velocities is increased significantly to 10 rad/s.
- The torque from both control policies based on \ddot{X}_0 and \ddot{X}_{π} are exactly the same with opposite signs. However,

- Note that the proposed control policy provides a torque which is strictly within the torque limits.

On the other hand, [Figure 27](#) shows the control policy based on \ddot{X}_ϕ and $\ddot{X}_{\phi+\pi}$, which are dependants on the natural dynamics of the robot. Several observations to be made as well:

- Contrary to the previous control policy shown in [Figure 26](#), the natural dynamics based policy produces a torque manifold in the state space that is relatively smooth and has continuous spectrum between τ_{\max} and τ_{\min} .
- Contrary to the previous control policy shown in [Figure 26](#), the natural dynamics based policy varies with the angular velocities as well as the configuration. This made clear by comparing the torque given by the state $\{0 \leq q_1, q_2 \leq 2\pi \mid s = [q_1, q_2, 0, 0]^T\}$ with zero angular velocities as shown in [Figure 27a](#) and [Figure 27b](#), with the output torque for the states $\{0 \leq q_1, q_2 \leq 2\pi \mid s = [q_1, q_2, 10, 10]^T\}$, shown in [Figure 27e](#) and [Figure 27f](#) which represent the control policy based on \ddot{X}_ϕ and $\ddot{X}_{\phi+\pi}$, respectively, where where the angular velocities is increased significantly to 10 rad/s. It is interesting to note that, the control policy generally reduces the output torque as the velocity increases.
- The torque from both control policies based on \ddot{X}_ϕ and $\ddot{X}_{\phi+\pi}$ are exactly the same with opposite signs. However, it is important to note that both policies produce different motion behaviour, as shown in [Figure 28](#), even though they are the same with opposite signs.
- Note that the proposed control policy provides a torque which is strictly within the torque limits.

Finally, [Figure 28](#) and [Figure 29](#) show the resulting motion and the output trajectories after applying each of the four previous control policies with a frequency of 100 Hz. A couple of observations can be made at this point. First of all, each control policy produces a distinct dynamic behaviour. The first two rows in [Figure 28](#) show the resultant motion and torque input due to the control policies \ddot{X}_0 and \ddot{X}_π . The resulting torque inputs and motions are exactly the inverse of each other, since the control policy in both cases depends only on the configuration as shown in [Figure 26](#). Moreover, the input torques are strictly at the limits of torque bounds. On the other hand, the third and fourth rows in [Figure 28](#) show the motion of the natural dynamics based control policies. Both motions and input torque are completely different even though they share the same torque manifold with opposite signs, but as they depend on the velocity as well

as the configuration they interacts differently with the dynamics. The control policy based on \ddot{X}_ϕ exploits the natural dynamics to produce smooth swings while the control policy based on $\ddot{X}_{\phi+\pi}$ tends to counteracts the natural dynamics and produces a rotational motion for the second link.

Nevertheless, it is clear that none of the four control policies achieve the full swing-up manoeuvre by itself. Recall that these control policies is purely based on task space acceleration without taking into consideration a specific goal configuration or velocity. This limitation raises the need for a higher level motion planning algorithm that can explore the state space using a combination of these control policies in order to reach a specific goal state. In the next section we show how these limitations are alleviated using a sampling-based motion planning algorithm.

5.2.2 *Natural Dynamics based Motion Planning Algorithm*

The Natural Dynamics based control policy presented in the previous section can generate dynamic motions that exploit the inherent natural dynamics of the system. However, its main limitation is that it cannot reason about a specific desired goal position and velocity. In addition, for particular manoeuvres such as the swing-up, the dynamic motion is composed of several phases of accelerations and decelerations to reach a specific state. For a general system with complex dynamics, it is unknown a priori the conditions (state and/or time-dependent conditions) for switching between both behaviours. Therefore, we leverage the existing kinodynamic sampling-based motion planning techniques such as RRT and EST with our natural dynamics based control inputs. We demonstrate that the natural dynamics based control inputs improve their convergence rate as well as the resulting motion quality regarding energy expenditure and trajectory smoothness.

The proposed Natural Dynamics based Tree (NDT) is a tree-based search in the state space, similar to other kinodynamic planners such as RRT, EST, KPIECE, and SST. Although these planners are different in many aspects, they share a common feature; they assume no access to a BVP solver (or a steering function) that connects two arbitrary points in the state space with a feasible or an optimal solution. This feature enabled these approaches to be applicable to a wide range of systems with complex dynamics, since solving the BVP problem is as hard as the original motion planning problem and is only available for systems with simple dynamics. However, the major drawback of these approaches is that they resort to a Monte-Carlo propagation scheme, which means that these methods usually apply

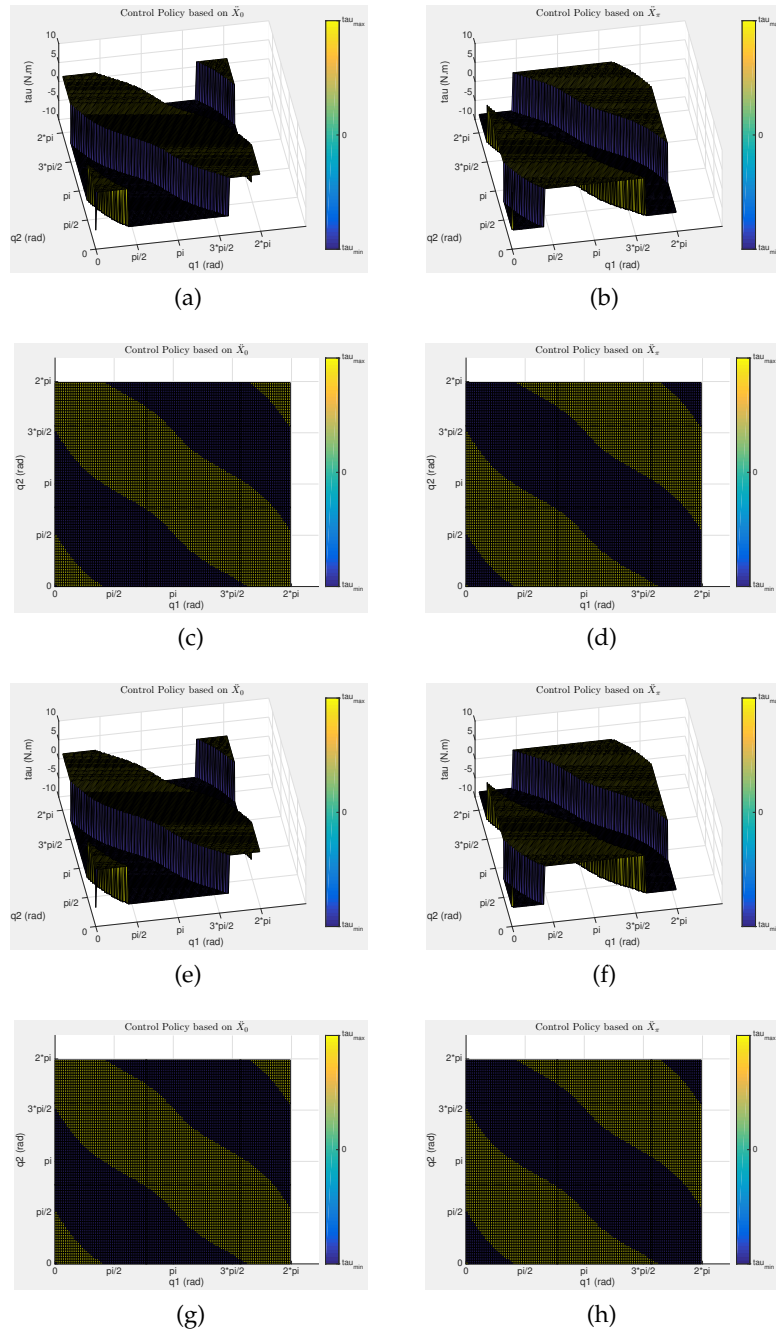


Figure 26: The feedback control policies for the acrobot based on \ddot{X}_0 and \ddot{X}_τ , showing in particular the torque evolution with the acrobot’s state. Figure 26a and Figure 26b show the 3-D plot of the torque τ as function of the configuration (q_1, q_2) while $\dot{q}_1 = \dot{q}_2 = 0$ for control policies based on \ddot{X}_0 and \ddot{X}_τ , respectively. Figure 26c and Figure 26d are their equivalent colormaps where the torque is represented by the colour spectrum within the torque bounds $\|\tau\| = 5$ N.m. Same plots are repeated in the four subsequent figures but with a velocity vector $\dot{q}_1 = \dot{q}_2 = 10$ to show the effect of velocity on the control policies.

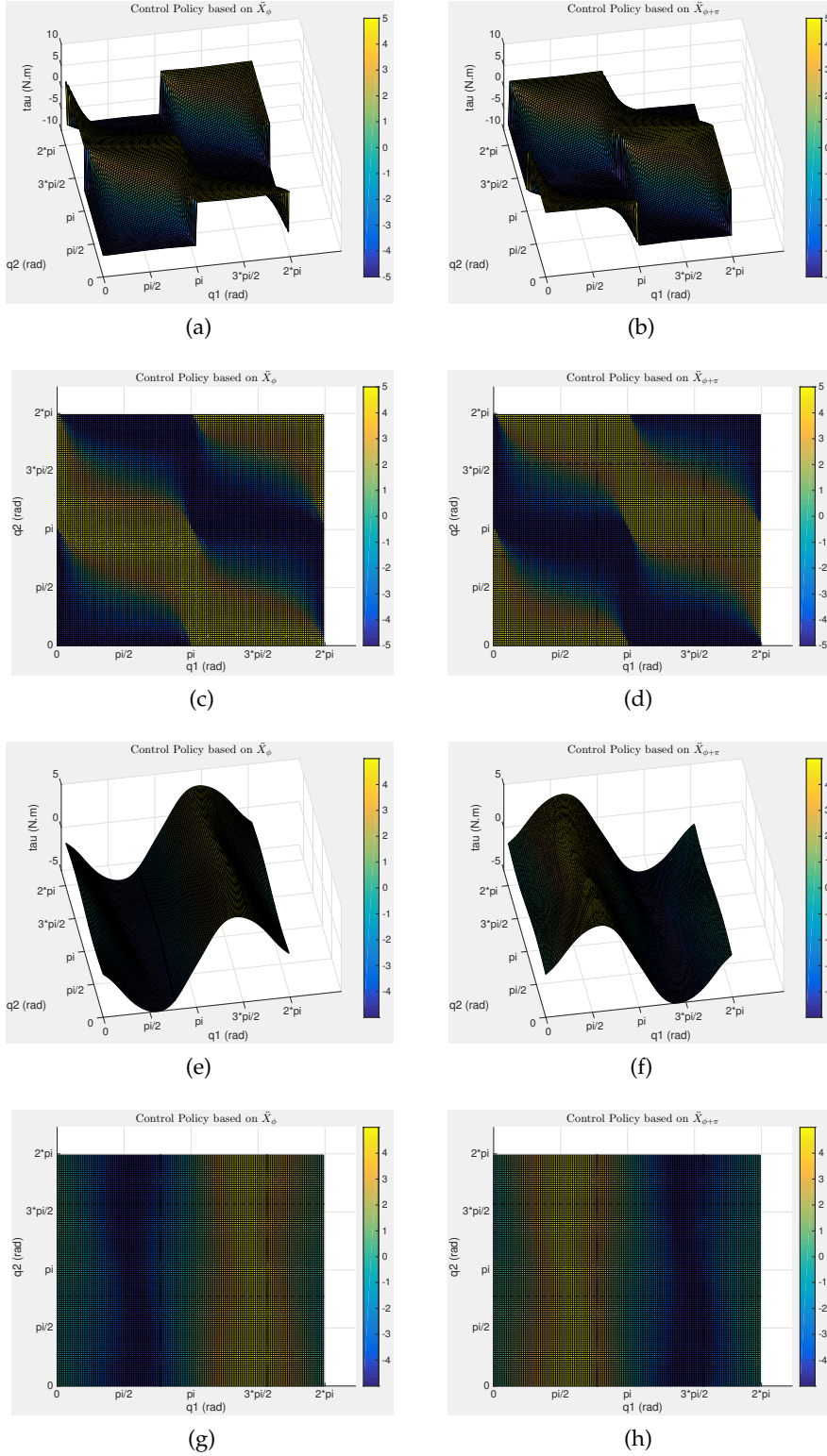


Figure 27: The feedback control policies for the acrobot based based on \ddot{X}_ϕ and $\ddot{X}_{\phi+\pi}$, showing in particular the torque evolution with the acrobot's state. Figure 27a and Figure 27a show the 3-D plot of the torque τ as function of the configuration (q_1, q_2) while $\dot{q}_1 = \dot{q}_2 = 0$ for control policies based on \ddot{X}_ϕ and $\ddot{X}_{\phi+\pi}$, respectively. Figure 27c and Figure 27d are their equivalent colormaps where the torque is represented by the colour spectrum within the torque bounds $\|\tau\| = 5$ N.m. Same plots are repeated in the four subsequent figures but with a velocity vector $\dot{q}_1 = \dot{q}_2 = 10$ to show the effect of velocity on the control policies.

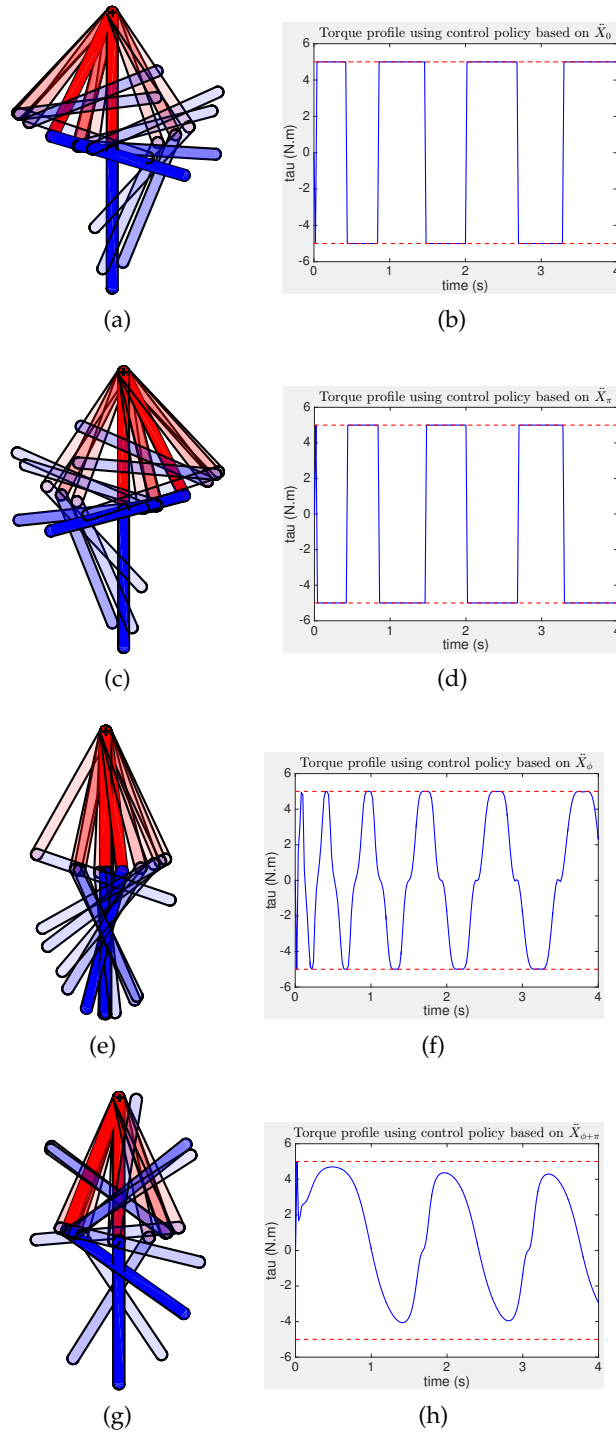


Figure 28: Resulting motion for the acrobot upon applying the four control policies for four seconds with a frequency of 100 Hz. Each row corresponds to the resulting motion for a particular control policy in the following order: \dot{X}_0 , \dot{X}_{π} , \dot{X}_{ϕ} and $\dot{X}_{\phi+\pi}$. The figures on the left column show the compilation of the resulting motion of each control policy. All motions starts in the vertical equilibrium position $s = [0, 0, 0, 0]^T$ with a dense colour and it gets brighter as time advances. The figures on the right column show the input torque profile produced by each control policy.

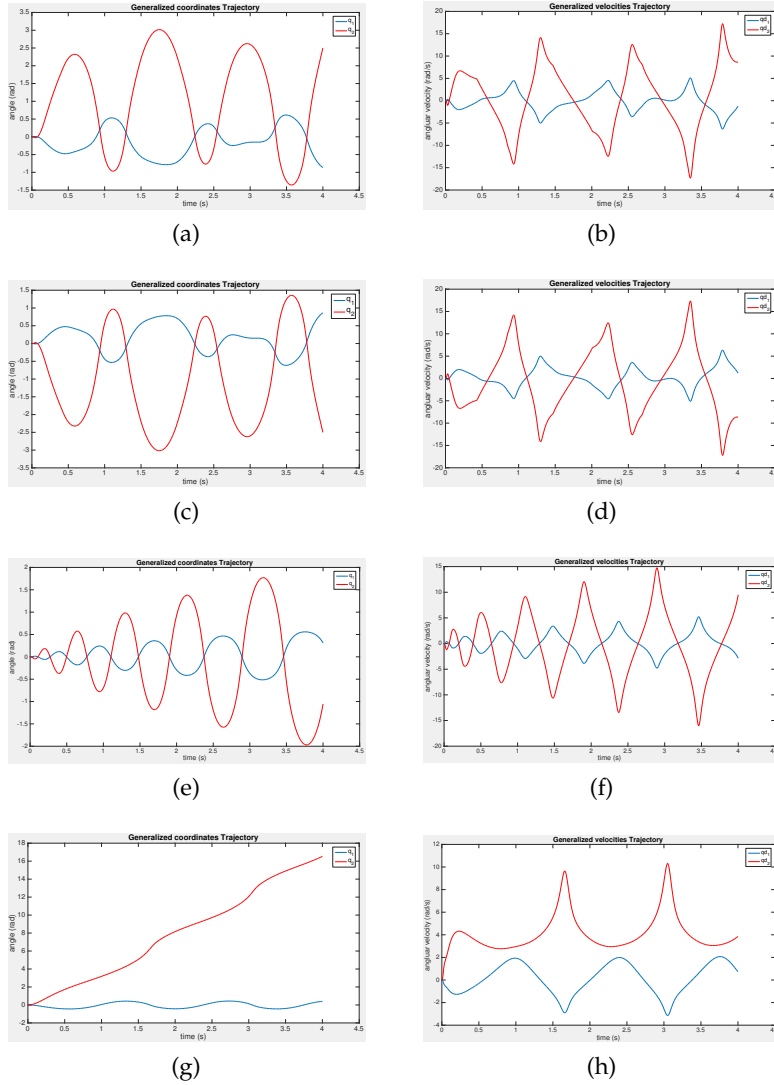


Figure 29: Configuration and velocity trajectories for the acrobot upon applying the four control policies for four seconds with a frequency of 100 Hz. Each row corresponds to the state trajectory for a particular control policy in the following order: \ddot{X}_0 , \ddot{X}_{pi} , \ddot{X}_ϕ and $\ddot{X}_{\phi+\pi}$. The figures on the left column show the generalised coordinates trajectory while the right column shows the generalized velocities trajectories.

a randomly sampled control input during a random sampled time in a black-boxed simulator of the system. Despite the generality of these approaches, they suffer from low convergence rate and jerky motion due to random nature of the control inputs. The main advantage of the proposed NDT algorithm is that we use the natural dynamics based input controls instead of randomly sampled input controls, which we demonstrate empirically that it is more efficient, more smooth, and leads to higher convergence rate.

The NDT Algorithm (1) builds a tree $\mathcal{T} = (\mathbb{V}, \mathbb{E})$ whose vertices and edges are the states $s \in \mathbb{R}^{2n}$, where n is the number of DOF (assuming that the state space is $2n$), and motions v . Each motion is defined as $v = (s(t), u(t), \Delta t)$, where $s(t)$ is the state trajectory between the two states on both ends of the edge and $u(t) \in \mathbb{R}^{n_a}$ is the applied input control trajectory during a duration $\Delta t \in \mathbb{R}^{\geq 0}$. Moreover, a distinguished feature of NDT is that the vertices in the motion tree \mathcal{T} are divided in two groups, *Explored vertices* and *Unexplored vertices* denoted by $\mathbb{V}_{\text{Explored}}$ and $\mathbb{V}_{\text{Unexplored}}$, respectively. We define $\mathbb{V}_{\text{Explored}}$ as the vertices that has motions (or edges) starting from these particular vertices, which means that all k control inputs have already been applied at these vertices therefore they will add not further information to the tree This means. This tree partition scheme is inspired by the *Interior and Exterior cells* scheme in the KPIECE algorithm [Kav12] to focus the exploration on states that have not been explored before, which allows the motion planner to cover the state space faster.

The algorithm begins in line by initializing the tree \mathcal{T} with an unexplored vertex $\mathbb{V}_{\text{Unexplored}}$ holding the initial state s_{init} which has no associated motion in the edge. From a high-level perspective, the NDT algorithm follows an RRT-like tree expansion strategy such that it samples a state S_{rand} uniformly at random from the state space S (line 4), then it searches for the *nearest neighbour* in the tree (line5). The *NearestNeighbor* routine find a candidate state s_{near} for further expansion which is explored by applying a control input. This expansion strategy is known as a *Voronoi biasing strategy* because the probability of choosing a node in \mathcal{T} is proportional to the volume of its Voronoi cell. The *Voronoi bias* stimulates the tree to extend outwards and explore new regions. It is a desirable property since it enables relatively rapid and efficient exploration of the state space.

However, contrary to the kinodynamic RRT, described in algorithm (4), the proposed NDT algorithm has two distinguishing features. The first and the most distinctive feature from RRT and other kinodynamic planners is the control sampling method. RRT and most general kinodynamic planners employ a Monte-Carlo approach where

the input control is sampled randomly from the input control space $u_k \in \mathcal{U}$ and applied for a sampled duration Δt , whereas the NDT algorithm computes control torques based on the natural dynamics of the system at the given state using the natural dynamics feedback control policy. The second feature different from RRT is the vertex selection for propagation routine. RRT selects the nearest neighbor to a sampled state from the tree \mathcal{T} whether it has been already explored or not while the NDT algorithm selects the nearest neighbor from the unexplored vertices $\mathbb{V}_{\text{Unexplored}}$ only and apply the calculated natural dynamics based control inputs.

The NDT algorithm 1 can be described in details as follows: Line 3

Algorithmus 1 : Natural Dynamics based Tree (NDT)

input : Kinodynamic problem (\mathcal{P}), State Space (\mathcal{S}), Initial state (s_{init}), Goal region (S_{goal}), Distance metric (d), Integration time limits ($\Delta t_{\text{max}}, \Delta t_{\text{min}}$), Number of sampled control trials (k), Maximum number of nodes N_{max}

output : State trajectory $\mathbf{s}(t) \in S_{\text{feas}}$ for $t \in [0, t_f]$ from s_I to $s_{\text{terminal}} \in S_{\text{goal}}$ and control trajectory $\mathbf{u}(t)$ for $t \in [0, t_f]$

```

1 Initialization:  $\mathbb{V}_{\text{Explored}} \leftarrow \emptyset, \mathbb{V}_{\text{Unexplored}} \leftarrow \{s_{\text{init}}\}$ 
2  $\mathcal{T} = \{\mathbb{V} \leftarrow (\mathbb{V}_{\text{Explored}} \cup \mathbb{V}_{\text{Unexplored}}), \mathbb{E} \leftarrow \emptyset\}$ 
3 while ( $i \leq N_{\text{max}} \vee (\mathcal{T} \cap S_{\text{goal}} = \emptyset)$ ) do
4    $s_{\text{rand}} \leftarrow \text{Sample}(\mathcal{S})$ 
5    $s_{\text{near}} \leftarrow \text{NearestNeighbor}(\mathbb{V}_{\text{Unexplored}}, s_{\text{sampled}})$ 
6    $(v_1 \dots v_k) \leftarrow \text{EXTEND} - \text{ND}(s_{\text{near}}, v_{\text{near}}, k)$ 
7   for  $j = 1$  to  $k$  do
8     if  $v_k(t) \in S_{\text{feas}}$  for  $t \in [0, \Delta t_k]$  then
9       Let  $s_{\text{new}_k} = \mathbf{s}_k(\Delta t_k)$  denote the end of the extension
10       $\mathbb{V}_{\text{Unexplored}} \leftarrow \mathbb{V}_{\text{Unexplored}} \setminus \{s_{\text{near}}\}$ 
11       $\mathbb{V}_{\text{Explored}} \leftarrow \mathbb{V}_{\text{Explored}} \cup \{s_{\text{near}}\}$ 
12       $\mathbb{V}_{\text{Unexplored}} \leftarrow \mathbb{V} \cup \{s_{\text{new}_k}\}$ 
13       $\mathbb{E} \leftarrow \mathbb{E} \cup \{v_k(t) : s_{\text{near}} \rightarrow s_{\text{new}_k}\}$ 
14      if  $s_{\text{new}_k} \in S_{\text{goal}}$  then
15        return State and control trajectory in  $\mathcal{T}$  from  $s_I$  to
16         $s_{\text{new}_k}$ 
17      end
18    end
19  end

```

Algorithmus 2 : ND-EXTEND

input : Dynamical system D , Starting state s_{start} , associated motion v_{start} , Integration time limits $(\Delta t_{max}, \Delta t_{min})$, Number of sampled control trials (k)

output : k Natural-Dynamic based motions $v_1 \dots v_k$ from s_{start} to $s_{k_{end}}$

// Calculate Natural Dynamics based input control

- 1 $u_1 \dots u_k \leftarrow \text{ND-Control}(D, s_{start})$
- 2 **for** $i = 1$ **to** k **do**
- 3 $\Delta t_k \leftarrow \text{Sample}([\Delta t_{min}, \Delta t_{max}])$
- 4 $u_k(t) = \text{PiecewiseControlProfile}(v_{start}, u_k, \Delta t_k)$
- 5 $s_k(t) \leftarrow \text{Integrate}(D, x_s, u_k(t), \Delta t_k)$
- 6 $v_k = \{s_k(t), u_k(t), \Delta t_k\}$
- 7 **end**
- 8 **return** $v_1 \dots v_k$

Algorithmus 3 : ND-Contol

input : Dynamical Model D , Control input Constraints L , state s , Number of sampled control inputs (k)

output : k Natural-Dynamic based control inputs $u_1 \dots u_k$

// Calculate the Task-Space Dynamic Coupling Ellipsoid (TS-DCE) at state s

- 1 $\mathcal{E}_{\ddot{x}}(s) = \text{TS-DCE}(D, L, s)$ from [Equation 123](#)
- // Sample k Task-space accelerations from $\mathcal{E}_{\ddot{x}}(s)$
- 2 **for** $i = 1$ **to** k **do**
- // Sample Natural Dynamics based acceleration as shown in [Section 5.2.1.1](#)
- 3 $\ddot{X}_i \leftarrow \text{ND-SampleAcceleration}(\mathcal{E}_{\ddot{x}}(s))$
- // Calculate the input torques for the desired task space acceleration \ddot{X}_i as shown in [Section 5.2.1.2](#)
- $u_i \leftarrow \text{OperationalSpaceControl}(D, s, \ddot{X}_i)$
- 4 **end**
- 5 **return** $u_1 \dots u_k$

5.3 EXPERIMENT RESULTS

In order to demonstrate the effectiveness of the proposed NDT motion planning algorithm, we compare its performance with the classical RRT kinodynamic algorithm on the swing-up motion planning problem of the acrobot robot.

The acrobot is a canonical model for an underactuated robot. The swing up motion planning problem consist of finding a trajectory in the state space as well as the required input control to move the acrobot from its stable downward position to its unstable inverted position. The final unstable position is usually stabilized by switching to an adequate linear controller (e.g., LQR). However, the stabilization of the final position is not considered as part of the motion planning. Despite the simplicity of the acrobot model, its dynamics are complex enough that it has attracted the attention of the community to consider it as a test bed for nonlinear control and motion planning problems.

5.3.1 Model Description

The term "Acrobot" was coined at Berkeley by Murray and Hauser as they studied its controllability properties. However, the swing-up problem was introduced by [Spo95], motivated by the study of brachiation and gymnast motions. The Acrobot model is a two-link planar robot, shown in Figure 30. The generalized coordinates vector is $\mathbf{q} = [q_1 \ q_2]^T$, where q_1 is the angle of the first link relative to the vertical and q_2 is the angle of the second link relative to the first link. The generalized velocities vector is $\dot{\mathbf{q}} = [\dot{q}_1 \ \dot{q}_2]^T$, thus the Acrobot has a four dimensional state vector $s = [q_1 \ q_2 \ \dot{q}_1 \ \dot{q}_2]^T$. A single actuator is place on the second joint with an input control τ , while the first joint is passive. The Acrobot's kinematic and inertial parameters are detailed in Table 11.

5.3.2 Results

The Acrobot swing-up motion planning problem is solved by the NDT and RRT kinodynamic motion planning algorithms with two different torque limits: $\|\tau_{limit}\| = 5 \text{ N.m}$ and $\|\tau_{limit}\| = 10 \text{ N.m}$. Each of the four motion planning is solved for 100 trials. Hence, RRT_tau5 and RRT_tau10 denote the results of the RRT algorithm for the acrobot's with torque limits $\|\tau_{limit}\| = 5 \text{ N.m}$ and $\|\tau_{limit}\| = 10 \text{ N.m}$, respectively, NDT_tau5 and NDT_tau10 denote the results for the NDT algorithm.

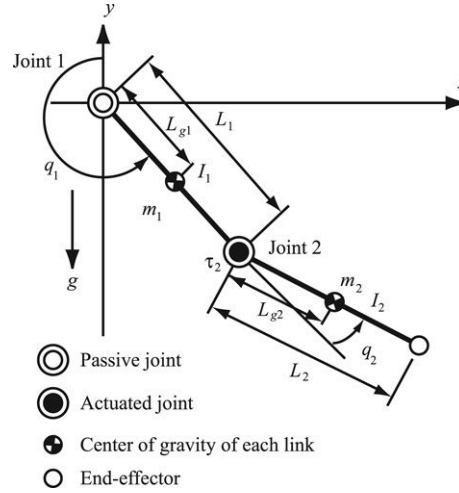


Figure 30: Model of the Acrobot robot

Table 11: Acrobot model parameters

Symbol	Description	Value
m_1	mass of link 1	1.0 kg
m_2	mass of link 2	1.0 kg
L_1	length of link 1	1.0 m
L_2	length of link 2	1.0 m
L_{g1}	center of mass of link 1	0.5 m
L_{g2}	center of mass of link 2	0.5 m
I_1	moment of inertia of link 1	0.083 kg.m ²
I_2	moment of inertia of link 2	0.083 kg.m ²

Comparative tables of the results of the NDT and RRT algorithms are shown in Table 12 and Table 13. Three metrics are used to measure the efficiency of the algorithms; the total calculation time, the total number of nodes and the number of iterations of the main loop before reaching a successful motion solution. The motion planning is declared successful if it has reached the tolerance region around the goal state $s_{goal} = [\pi 0 0 0]^T$ using the condition $|d(s, s_{goal})| \leq R_{goal}$, where the distance metric d defined as $d(s_1, s_2) = w_q \|q_1 - q_2\|^2 + w_v \|\dot{q}_1 - \dot{q}_2\|^2$. Table 13 compares the results regarding the quality of the final motion using two metrics: The duration of the final motion and the energy consumption which is defined as $E = \sum |\tau_k \cdot \dot{q}_{2k} \cdot \Delta t_k|$.

In the case of low torque limit $\|\tau_{limit}\| = 5 \text{ N.m}$, RRT has failed to find a feasible motion before reaching a termination condition on the total number of nodes $N = 20000$ nodes. Therefore, the results for RRT_tau5 is marked as N/A.

Table 12: Comparison of motion planning results

	Calculation Time (s)			Number of nodes			Number of iterations		
	min	mean	max	min	mean	max	min	mean	max
RRT_tau5	N/A	N/A	N/A	N/A	N/A	N/A	N/A	N/A	N/A
NDT_tau5	42.3	119.9	142.6	1043	2858	3425	174	476	571
RRT_tau10	37.5	408.2	1337	486	4051	9930	485	4050	9929
NDT_tau10	3.9	7.4	12.1	100	189	316	17	31	53

Table 13: Continued: Comparison of motion planning results

	Energy consumption (J)			Final motion duration (s)		
	min	mean	max	min	mean	max
RRT_tau5	N/A	N/A	N/A	N/A	N/A	N/A
NDT_tau5	67.1	67.1	67.1	4.9	4.9	4.9
RRT_tau10	117.2	245.9	411.6	3.6	7.0	11.7
NDT_tau10	110.9	110.9	110.9	3.7	3.8	3.8

The statistical results of the 100 trials for each of the four motion planning problems is also shown using a box-and-whisker diagram in [Figure 31](#) to [Figure 34](#). On each box, the central mark indicates the median, and the bottom and top edges of the box indicate the 25th and 75th percentiles, respectively. The whiskers extend to the most extreme data points not considered outliers, and the outliers are plotted individually using the '+' symbol.

Finally, for the sake of completeness, a sampled motion solution from each algorithm is shown in [Figure 36](#), [Figure 37](#) and [Figure 38](#).

5.3.3 Discussion

The results shown in the previous section for the motion planning problem of the swing-up maneuver of an acrobot model demonstrates clearly the superiority of the proposed NDT algorithm over a classical Monte-Carlo based kinodynamic motion planning algorithm such as RRT. This is demonstrated from both perspectives, the performance of the algorithm to reach a feasible solution and the quality of the output solution.

Regarding the algorithm's performance, the box-and-whiskers diagrams for the calculation time, number of nodes and number of iterations shown in [Figure 31](#), [Figure 32](#), and [Figure 33](#) respectively, show that the proposed NDT algorithm have significantly lower values with several order of magnitudes, and more importantly, with much

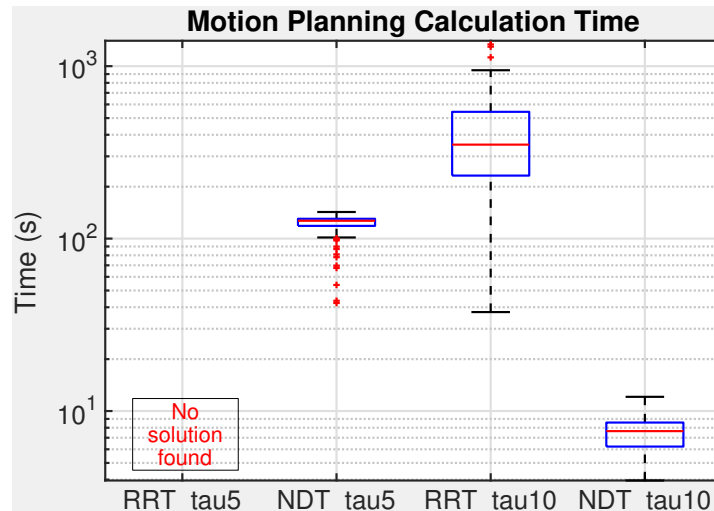


Figure 31: Comparison of calculation time between NDT and RRT motion planning algorithms to reach a successful solution for the acrobot swing-up manoeuvre in two cases with different torque limits using a box plot for 100 trials each. NDT_tau5 and NDT_tau10 denote the results for the NDT algorithm with torque limit $\|\tau\| = 5$ N.m and $\|\tau\| = 10$ N.m, respectively, whereas RRT_5 and RRT_10 are the results of the RRT algorithm with torque limits $\|\tau\| = 5$ N.m and $\|\tau\| = 10$ N.m, respectively. The calculation time in seconds is shown on a logarithmic scale

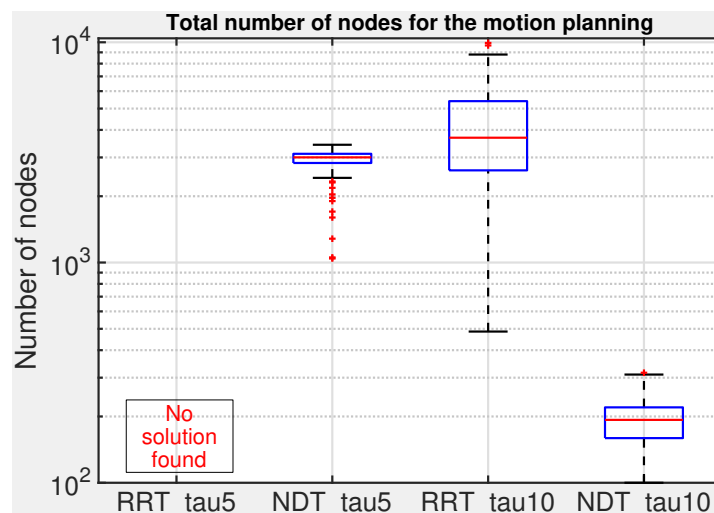


Figure 32: Comparison of number of nodes to reach a motion solution of the acrobot's swing-up by the NDT and RRT motion planning algorithms in two cases with different torque limits using a box plot for 100 trials each. NDT_tau5 and NDT_tau10 denote the results for the NDT algorithm with torque limit $\|\tau\| = 5$ N.m and $\|\tau\| = 10$ N.m, respectively, whereas RRT_5 and RRT_10 are the results of the RRT algorithm with torque limits $\|\tau\| = 5$ N.m and $\|\tau\| = 10$ N.m, respectively. Number of nodes are shown on a logarithmic scale

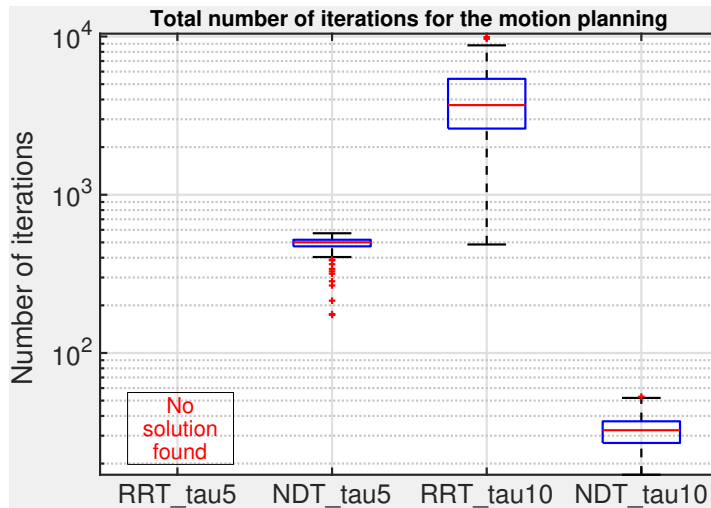


Figure 33: Comparison of number of iterations to reach a motion solution of the acrobot's swing-up by the NDT and RRT motion planning algorithms in two cases with different torque limits using a box plot for 100 trials each. NDT_tau5 and NDT_tau10 denote the results for the NDT algorithm with torque limit $\|\tau\| = 5$ N.m and $\|\tau\| = 10$ N.m, respectively, whereas RRT_5 and RRT_10 are the results of the RRT algorithm with torque limits $\|\tau\| = 5$ N.m and $\|\tau\| = 10$ N.m, respectively. Number of iterations are shown on a logarithmic scale

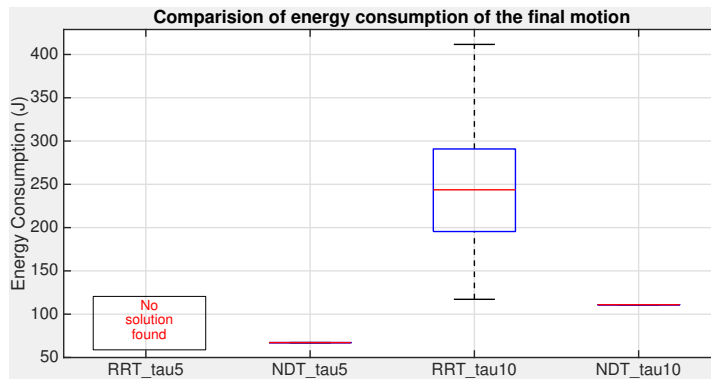


Figure 34: Comparison of energy consumption during the final motion solution of the acrobot's swing-up by the NDT and RRT motion planning algorithms in two cases with different torque limits using a box plot for 100 trials each. NDT_tau5 and NDT_tau10 denote the results for the NDT algorithm with torque limit $\|\tau\| = 5$ N.m and $\|\tau\| = 10$ N.m, respectively, whereas RRT_5 and RRT_10 are the results of the RRT algorithm with torque limits $\|\tau\| = 5$ N.m and $\|\tau\| = 10$ N.m, respectively.

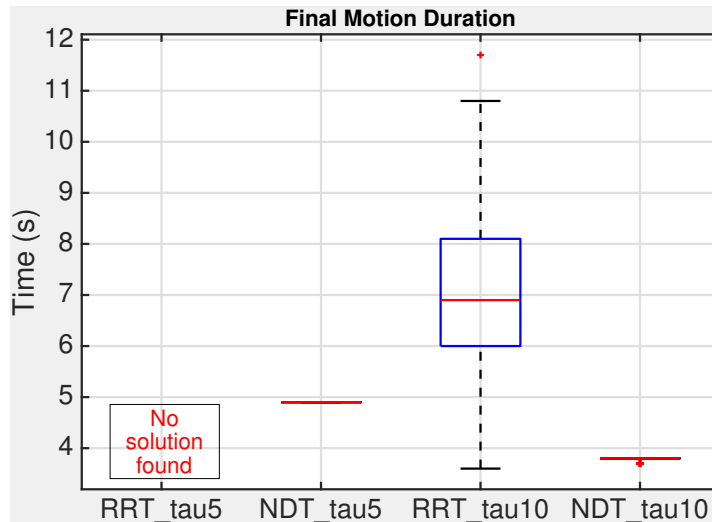
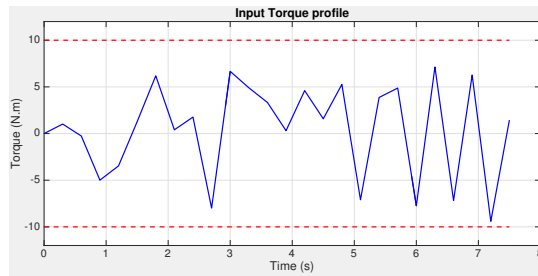


Figure 35: Comparison of the acrobot’s swing-up motion duration given by the NDT and RRT motion planning algorithms in two cases with different torque limits using a box plot for 100 trials each. NDT_tau5 and NDT_tau10 denote the results for the NDT algorithm with torque limit $\|\tau\| = 5$ N.m and $\|\tau\| = 10$ N.m, respectively, whereas RRT_5 and RRT_10 are the results of the RRT algorithm with torque limits $\|\tau\| = 5$ N.m and $\|\tau\| = 10$ N.m, respectively.

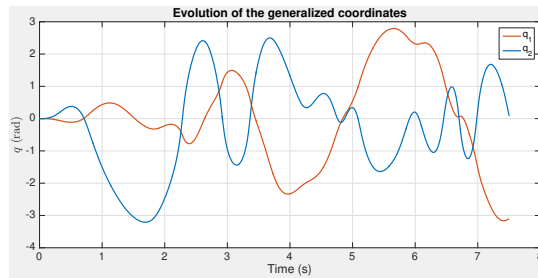
lower variability. This result is expected since the NDT algorithm depends on a particular control policy for the propagation phase, while the RRT randomly samples an input torque each iteration. It is worth noting that the NDT algorithm finds a motion solution successfully in the case of restricted torque limit while the RRT has failed to find a solution before reaching the maximum number of nodes.

Regarding the quality of the final motion solution, the box-and-whiskers diagrams for the energy consumption and the final motion duration shown in Figure 34 and Figure 35, respectively, reveal that the proposed NDT algorithm reaches a high-quality solution (i.e., low energy consumption and short motion duration) with respect to the RRT algorithm, although we do not claim that the NDT algorithm provides an optimal solution in terms of energy or motion duration.

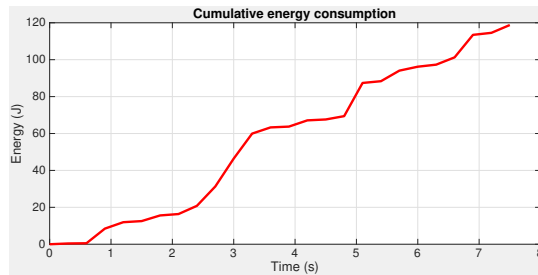
It is interesting to note that there is almost no variability in the final motion, meaning that it reaches nearly the same solution. This can be explained by the fact that in the current implementation the NDT algorithm employs a two particular natural dynamics based policies which provides two sets of input torques and the role of the NDT algorithm is to find the right combination of these policies to reach to the goal configuration. The variability that was shown earlier regarding the calculation time and the number of nodes is mainly due to



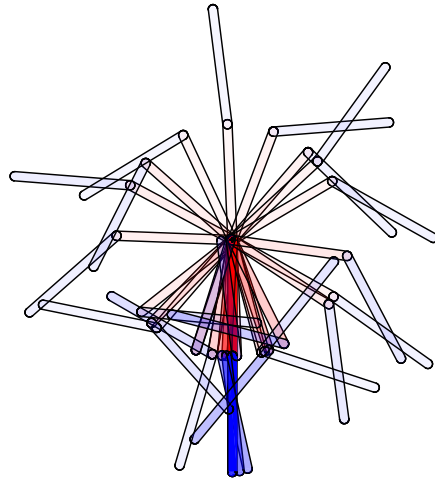
(a)



(b)

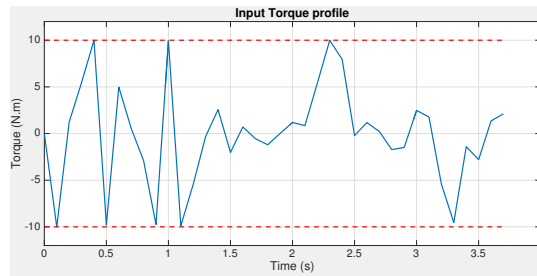


(c)

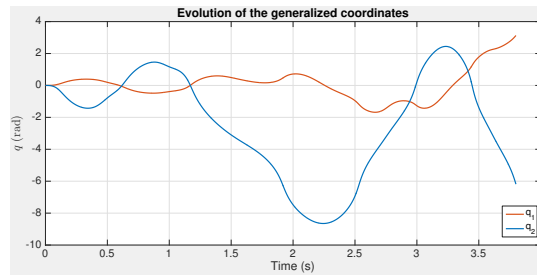


(d)

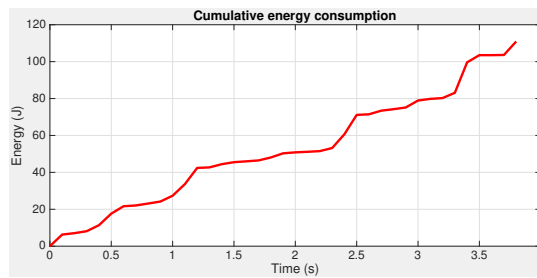
Figure 36: Output motion solution from RRT Kinodynamic algorithm for the acrobot swing-up manoeuvre with $\|\tau_{limit}\| = 10$ N.m (a) shows the torque profile in blue while the torque limits are shown in dotted red lines. (b) shows the evolution of the generalized coordinates during the motion; the angle of the first and the second joints are shown in red and blue, respectively. (c) shows the cumulative energy consumption during the motion. (d) shows a compilation of the resultant motion, the first and second links are shown in red and blue, respectively, and the colours get brighter as the motion advances in time



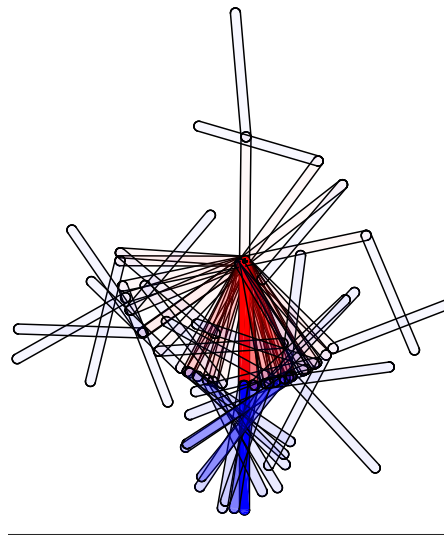
(a)



(b)

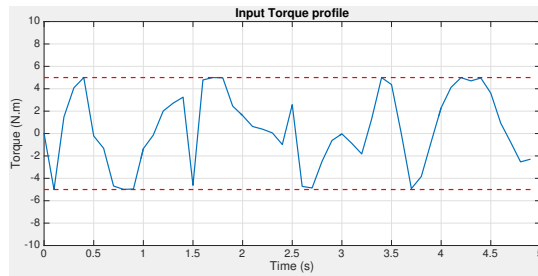


(c)

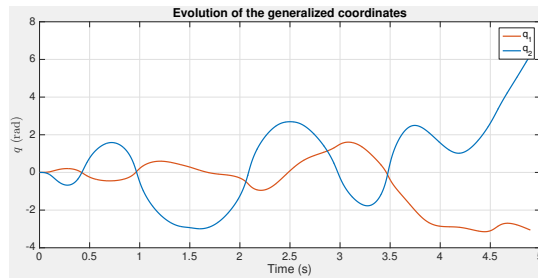


(d)

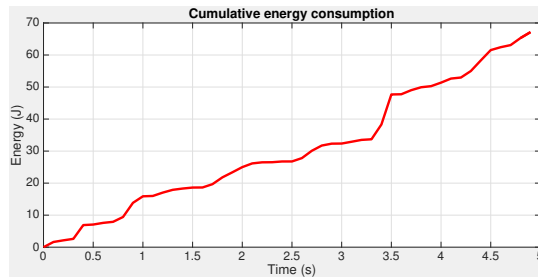
Figure 37: Output motion solution from the NDT motion planning algorithm for the acrobot swing-up manoeuvre with $\|\tau_{limit}\| = 10 \text{ N.m}$ (a) shows the torque profile in blue while the torque limits are shown in dotted red lines. (b) shows the evolution of the generalized coordinates during the motion; the angle of the first and the second joints are shown in red and blue, respectively. (c) shows the cumulative energy consumption during the motion. (d) shows a compilation of the resultant motion, the first and second links are shown in red and blue, respectively, the colours gets lighter as the motion advances in time



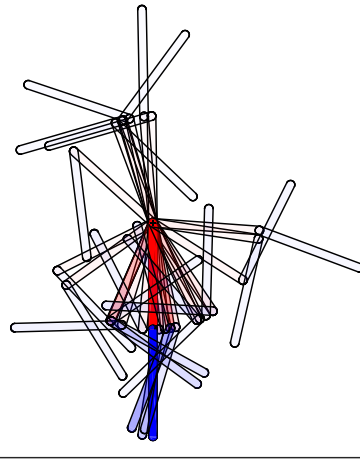
(a)



(b)



(c)



(d)

Figure 38: Output motion solution from the NDT motion planning algorithm for the acrobot swing-up manoeuvre with $\|\tau_{limit}\| = 5 \text{ N.m}$ (a) shows the torque profile in blue while the torque limits are shown in dotted red lines. (b) shows the evolution of the generalized coordinates during the motion; the angle of the first and the second joints are shown in red and blue, respectively. (c) shows the cumulative energy consumption during the motion. (d) shows a compilation of the resultant motion, the first and second links are shown in red and blue, respectively, the colours gets lighter as the motion advances in time

the random nature of sampling a state for propagation as in the RRT algorithm.

5.4 CONCLUSION

In this chapter, we aimed to leverage the proposed DCM and the associated NDI indexes from a posteriori motion analysis tools to a prior heuristic that can be employed to exploit the natural dynamics in a motion planning problem. The natural dynamics based control heuristic relies on the previous observation of the strong correlation between the natural dynamics, represented by the acceleration bias vector, and the input control during dynamic maneuvers. Several control policies were designed based on the TS-DCM, by identifying four main characteristic points in the task acceleration space. However, a single control policy is not sufficient to achieve a dynamic maneuver such as the swing-up of an acrobot with several phases of accelerations and decelerations. Thus, A novel sampling-based kinodynamic motion planning algorithm based on the natural dynamics of the system proposed. In addition, the effectiveness of the proposed NDT algorithm is demonstrated on planning the motion and control of the swing-up of the Acrobot along with a statistical comparison with RRT in terms of computation time and motion solution quality.

CONCLUSIONS & PERSPECTIVES

In this chapter, the thesis is concluded with a summary of the introduced contributions and an outlook on some lines of research identified as the consequent extension of the presented work.

6.1 CONCLUSION

In spite of the spectacular strides in science and technology and particularly in the fields of robotics, biomechanics, and neuroscience, there is still a significant discrepancy between robots and their biological counterparts (i.e., humans and animals) on several different levels. From the mechanical design and motion control perspective, there is a notable difference in motion's agility, smoothness, and energy efficiency. Sports performers coordinate their muscles actions to achieve a synergistic motion that surpasses their physical limits. Lizards and Cheetahs coordinate their tail swing to rapidly accelerate and maneuver during the pursuit of their prey. Gibbons coordinate their whole body's motion to swing gracefully between tree limbs. One of the key ingredients for such complex behaviors is motion coordination to exploit their natural dynamics. Yet there is a lack in the literature for a proper tool that analyzes and exploit the interlimb dynamic coordination for a robotic system with an arbitrary number of DOF and its relationship with the role of natural dynamics in shaping a synergistic motion.

To this end, we have developed an analysis technique in both the joint space and the task spaces and proposed three novel performance measures which allow quantifying the role of the natural dynamics during a dynamic motion and its significance with respect to the input control its physical bounds. Moreover, we leveraged the proposed analysis tools and the knowledge gained from the analysis studies by abstracting a hypothesis on the dynamic coordination to exploit the natural dynamics of the system and use it as a priori to develop a novel kinodynamic planning algorithm which plans a dynamic motion based on the natural dynamics of the system.

In this work, we have focused our attention on a particular class of robotic systems called underactuated robots. Unlike conventional fully-actuated robots where the natural dynamics can be suppressed by classical feedback control techniques, a large and diverse array of dynamical systems falls under the class of underactuated systems.

Synthesizing motion behavior for such underactuated systems is quite challenging. Underactuation imposes a second-order nonholonomic constraints on their dynamics that restrict the family of trajectories their accelerations can follow. A certain subclass of underactuated systems is composed of an active subsystem which can be directly controlled by the control input and a passive subsystem which can only be controlled indirectly through the dynamic coupling with the latter. This is one of the reasons that has compelled us to treat underactuated robots with torque limits. The fact that it is not feedback-linearizable, the non-negligible dynamic coupling and the severe torque limits remove the full control authority that one enjoyed in the fully-actuated robots, thus the class of underactuated robots forces you to handle the inherent nonlinear dynamics in an unconventional way.

In [Chapter 3](#), we have introduced the Joint Space Dynamic Coupling Ellipsoid (JS-DCE) which describes the set of admissible accelerations of the passive subsystem in a graphical and intuitive manner, while taking into consideration the second-order nonholonomic constraint imposed by the underactuation, torque bounds on the active subsystem, inertial distribution over the manipulator, gravity effect, nonlinear velocity-dependent forces. We highlighted the role of the natural dynamics which can be interpreted as the bias vector responsible for displacing the center of the JS-DCE from the origin of the acceleration space. Thus inducing a drift and directly affecting the set of possible accelerations. In a dynamical trajectory, this relationship can be better grasped by employing the "Joint Space Dynamic Coupling Map (JS-DCM)," a novel analysis technique in the joint acceleration space based on JS-DCE, to help gain insight into a dynamic trajectory and analyze the dynamic coupling between the passive and active subsystems of an underactuated robot. More importantly, it allows analyzing the pivotal role of the natural dynamics of the system on the passive subsystem during a dynamic motion. This tool was developed with the floating-base system in mind. Floating-base systems dynamic modeling paradigm became prominent recently as it encompasses many-legged robots or any robotic system with intermittent contact or spatial mobile manipulators. The floating-base system is inherently underactuated by construction. It is important to understand how the developed forces in the active-subsystem along with its torque limits as well as the contact forces affect the motion of the floating-base. To this end, we have extended the JS-DCM analysis to floating-base systems and demonstrates its merits on a high-dimensional humanoid robot performing a vertical jump with the aid of arm swing. The motion planning and control of the vertical jump are generated using the state-of-the-art trajectory optimization tool, and the JS-DCM is used as a posteriori analysis tool of the resultant motion.

In [Chapter 4](#), we extended the formulation of the aforementioned analysis technique for task-space acceleration analysis while highlighting the interpretation of TS-DCE and the TS-DCM of the robot dynamics by applying it on a variety of underactuated manipulators with different kinematic and dynamic parameters to demonstrate clearly the mechanism of the analysis technique. Finally, chapter 4 demonstrates the merits of the TS-DCM analysis tool is demonstrated by applying it to the dynamic swing-up maneuver of the gymnast-robot on a high bar. The dynamic motion is first generated using direct collocation trajectory optimization loosely based on the actual motion of a gymnast on a high-bar. However, since trajectory optimization is often treated as a black-box providing a local-optimal trajectory without any insight into the mechanism of the motion, the TS-DCM along with the associated natural dynamic indexes are employed to help gain insight into the dynamic motion of the underactuated system and the associated control strategy and highlight the pivotal role of exploiting the natural dynamics to achieve the dynamic motion.

In [Chapter 5](#), we leveraged the proposed DCM and the associated NDI indexes from a posteriori motion analysis tools to a prior heuristic that can be employed to exploit the natural dynamics in a motion planning problem. We presented a novel kinodynamic motion planning algorithm based on the natural dynamics of the system. The effectiveness of the proposed NDT algorithm is demonstrated on planning the motion and control of the swing-up of the Acrobot along with a statistical comparison with RRT in terms of computation time and motion solution quality.

6.2 PERSPECTIVES

The scope of the research topics tackled in this thesis leaves many unanswered questions and hence several directions for future research. They are hereby briefly discussed.

- **Validation of the proposed hypothesis of exploitation of natural dynamics based on natural systems performing highly dynamic motions** In this work we have depended on the state-of-the-art of nonlinear trajectory optimization to synthesize a dynamic trajectory which was analyzed subsequently with the proposed analysis technique. It will be very interesting to verify the proposed hypothesis by studying the actual trajectory of natural systems such as gymnast motion or brachiating gibbon using accurate motion capture systems. However, this is not an easy task as our analysis heavily depends on an accurate model identification and motion tracking data.

- **Extending the presented floating-base DCM analysis to other underactuated systems** In this work, we have studied a limited class of robotic systems. In particular, a subclass of underactuated robots where the input control of the active subsystem can only affect the passive subsystem through the dynamic coupling. However, other robotic systems such as quadrotors or even aerial mobile manipulators [Kon+14] are underactuated in the sense of the number of control inputs is less than the DoFs but the control inputs can directly influence all DoFs. The motivation is fueled by the recent interest in agile quadrotors maneuvers at high speed augmented with dynamic inertia such as cable suspended payload [Foe+17] or underactuated manipulators. Energy efficient motion planning can be facilitated by following the same methodology presented in this thesis. Applying the DCM analysis on the optimal trajectories will offer valuable insight on the mechanism of exploiting the inherent dynamic coupling between the manipulator or payload and the UAV base which could later be employed as a heuristic for energy efficient motion planning or a high-performance motion which exceeds the physical capacity of the onboard actuators.
- **Treatment of unit inhomogeneity:** A known problem which affects most of the performance measures and analysis with mixed units is unit inhomogeneity. When translational and rotational quantities are mixed, the results are not invariant to changes in units, which means that a simple scaling of units can produce different results which are not equivalent to each other. The unit-inhomogeneity issue can complicate a performance analysis, and thus, a careful treatment is required in order to obtain useful results. In this work, we have not encountered this problem because we have mainly focused on the translational cartesian accelerations. However, for more general motion analysis it is important to address this issue. Several previous works [BK05; Kha95] have already addressed this issue either by introducing a proper scaling factor or by projecting into a unified dimension or by separating the translational and rotational quantities.
- **Improvements for the NDT algorithm** The presented NDT kinodynamic motion planning algorithm is based on a vanilla version of RRT in its minimal form as a proof of concept. However, RRT and sampling-based motion planning algorithms, in general, have known several variants and tweaks to improve its performance and remedy some of its drawbacks. These ideas are also applicable to the NDT algorithm for performance improvement. Among those ideas are a Bi-directional tree search [LaV01], that alternatively grows two trees, one from the initial state and the other from the goal state. Other ideas treat

the planner's sensitivity to the distance metric by using offline learning [PA15; LB10] to automatically learn a distance metric close to the cost-to-go pseudo-metric instead of a simple Euclidean metric. Finally, the NDT algorithm can be extended to an asymptotically optimal motion planning algorithm by incorporating a cost function and following the same line of thought of SST* [LLB16] and the work in [HNTH10]. These are meta-algorithms that extend the search in state space of random-based motion planning, such as RRT and EST, to a search in State-Cost space.

- **Explore alternative motion planning approaches with the proposed natural dynamics based control heuristic** We have employed sampling-based planning approach as a test-vehicle for the proposed heuristic to exploit natural dynamics in motion planning. However, the performance and the quality of the output solution is highly sensitive to the limitations of the used motion planning approach. Therefore, it might be worthy to test the proposed heuristic with other motion planning approaches such as machine learning by rewarding the motion that maximizes the natural dynamic index thus maximizing the exploitation of the natural dynamics and producing more energy efficient and smoother trajectories.

PUBLICATIONS

- Zamzami, Z., Benamar, F., Sahbani, A., (2018). **Exploiting natural dynamics in motion planning.** (Manuscript In Preparation)
- Zamzami, Z., Benamar, F., (2018). **Dynamic Coupling Map: a tool to analyze highly dynamic motions for floating base robots.** International Conference on Humanoid Robots (Humanoids 2018), (To be submitted)
- Zamzami Z. and Benamar F. (2016). **Dynamic Coupling Map: Acceleration Space Analysis for Underactuated Robots.** In Proceedings of the 13th International Conference on Informatics in Control, Automation and Robotics ISBN 978-989-758-198-4, pages 548-557.
- Zamzami Z. and Benamar F. (2016). **Dynamic Coupling Map: Trajectory Analysis technique for Dynamic Motions of Underactuated Systems** Poster session presented at the workshop on Dynamic Locomotion and Manipulation with Complex Robots in the Real World (DLMC-2016). ETH Zurich, Switzerland
- Krid, M., Zamzami, Z., and Benamar, F. (2016). **Path Tracking Controllers for Fast Skidding Rover.** In Informatics in Control, Automation and Robotics 12th International Conference, ICINCO 2015 Colmar, France, July 21-23, 2015 Revised Selected Papers (pp. 29-47). Springer International Publishing.
- Krid, M., Benamar, F., and Zamzami, Z. (2016). **Design of an active device for controlling lateral stability of fast mobile robot.** *Robotica*, 34(11), 2629-2651.

Part I

APPENDIX

UNDERACTUATED ROBOTS DYNAMIC MODELLING

A.1 UNDERACTUATED MANIPULATOR DYNAMICS

A robotic manipulator is a collection of rigid bodies whose relative motion is constrained by the admissible velocities of the joints connecting two consecutive rigid bodies in the system. The rigid bodies are called the links of the robot. In this work, we assume that all links are rigid and all joints are ideal. An ideal joint constrains the motion between two links so that only certain relative velocities are allowed, independently of the torques and forces applied to the links. In this section, we address fixed-base underactuated manipulators with 1-DOF joints, i.e., revolute or prismatic joints with one degree of freedom. Fixed-base manipulators with conventional rotational and prismatic joints are most efficiently modeled using a Lagrangian framework because in this way the constraints are included in the dynamics by choosing the set of generalized coordinates as the joint variables.

The motion of a mechanical system is related via a set of dynamic equations to the forces and torques it is subject to. There are two main formalisms for deriving the dynamic equations for such mechanical systems: Newton-Euler equations that are directly based on Newton's laws; and Euler-Lagrange equations that have their root in the classical work of d'Alembert and Lagrange on analytical mechanics and the work of Euler and Hamilton on variational calculus. The main difference between the two approaches is in dealing with constraints. In robotics, Lagrangian dynamics formulation is a standard method to derive the equations of motions for simulation and control purposes because it doesn't include explicitly the non relevant constraint forces and other internal forces. we are mainly interested in how the input action on the actuators and external forces affect the accelerations of the rigid bodies.

Euler-Lagrange equations have its origins at the variational principles and the notion that the laws of nature act in such a way as to extremize some function, for more details the reader is referred to [GPS07; BL05]. As the Lagrangian approach originates from a principle in nature, it has the merit that it involves only physical quantities that can be defined without reference to a particular set of generalized coordinates, namely, the kinetic and potential energies. The formula-

tion is therefore automatically invariant with respect to the choice of coordinates for the system.

The Euler-Lagrange equations are derived directly from the energy expressed in the generalized coordinates. We first form the system Lagrangian as the difference between the kinetic and the potential energies of the system. The Lagrangian function is

$$L(\mathbf{q}, \dot{\mathbf{q}}) = \mathcal{K}(\mathbf{q}, \dot{\mathbf{q}}) - \mathcal{G}(\mathbf{q}) \quad (164)$$

where $\mathcal{K}(\mathbf{q}, \dot{\mathbf{q}})$ is the kinetic energy and $\mathcal{G}(\mathbf{q})$ is the potential energy of the system.

The total energy in a multibody mechanical system is found by adding the kinetic and potential energy of each rigid body with respect to some common inertial reference frame. An important difference compared to single rigid bodies is that the inertia matrix depends on the configuration of the multibody system. Thus, the partial derivatives of the inertia matrix will not vanish as for single rigid bodies.

A.1.1 Manipulator's Kinetic energy

The manipulator's kinetic energy is found in terms of the link velocities expressed in the link frame \mathcal{R}_i .

$$\mathcal{K}_i = \frac{1}{2} (\mathbf{V}_{0i}^B)^T \mathbf{I}_i \mathbf{V}_{0i}^B \quad (165)$$

where link velocity twist \mathbf{V}_{0i}^B denotes the linear and angular velocity of body i . The link velocity twist, represented with respect to an inertial frame \mathcal{R}_0 can be expressed in terms of the manipulator's generalized velocities by using the geometric Jacobian.

A.1.2 Manipulator's Kinematics using adjoint maps

let ξ_{ab}^c denotes the twist representing the velocity of \mathcal{R}_b with respect to \mathcal{R}_a as viewed/expressed from \mathcal{R}_c . Then ξ_i^i denotes the the body joint twist of joint i represented in \mathcal{R}_i . $\mathbf{V}_{ab}^c = \begin{bmatrix} \mathbf{v}_{ab}^c & \boldsymbol{\omega}_{ab}^c \end{bmatrix}^T \mathbb{R}^m$ denotes the twist variable describing the linear and angular velocities of frame \mathcal{R}_b with respect to \mathcal{R}_a as viewed from \mathcal{R}_c .

Given a joint i with axis \mathbf{p}_i^i represented in frame \mathcal{R}_i , then the joint body twist for a revolute joint is given by

$$\xi_i^i = \begin{bmatrix} 0 \\ p_i^{\hat{}} \end{bmatrix} \quad (166)$$

ξ_i^i describes the allowed motion of the joints as seen from the frame attached to the joints. Note that, ξ_i^i is always constant and independent of the manipulator configuration. The body Jacobian J_i^B for a frame \mathcal{R}_i attached to the center of gravity of link i is given by

$$J_i^B(q) = \begin{bmatrix} \text{Ad}_{g_{1i}^{-1}} \xi_1^1 & \text{Ad}_{g_{2i}^{-1}} \xi_2^2 & \dots & \text{Ad}_{g_{ii}^{-1}} \xi_i^i & 0_{(n-i) \times m} \end{bmatrix} \quad (167)$$

where the Adjoint map $\text{Ad}_{g_{ji}^{-1}}$ is used to transform the velocity of link j expressed in its body frame \mathcal{R}_j to the link frame \mathcal{R}_i . Then the mapping from the joint velocities to the velocity of frame \mathcal{R}_i attached to the center of gravity of link i is now given by

$$V_{0i}^B = J_i^B(q) \dot{q} \quad (168)$$

A.1.3 Joint Space Inertia Matrix (JSIM)

The Joint Space Inertia Matrix (JSIM) can be found from the kinetic energy as follows

$$\begin{aligned} \mathcal{K}_i &= \frac{1}{2} (V_{0i}^B)^T I_i V_{0i}^B \\ &= \frac{1}{2} (J_i(q) \dot{q}_i)^T I_i (J_i(q) \dot{q}_i) \\ &= \frac{1}{2} \dot{q}_i^T (J_i^T(q) I_i J_i(q)) \dot{q}_i \\ &= \frac{1}{2} \dot{q}^T M_i(q) \dot{q} \end{aligned} \quad (169)$$

which defines the JSIM of link i in terms of the body geometric jacobian as

$$M_i(q) = (J_i^B)^T I_i J_i^B \quad (170)$$

Using our definition, I_i is the generalized inertia matrix expressed in the reference frame \mathcal{R}_i attached to the center of gravity of link i and aligned with the principal axes of inertia and is therefore constant and defined as

$$I_i = \begin{bmatrix} m_{3 \times 3} & 0 \\ 0 & I_{3 \times 3} \end{bmatrix} \quad (171)$$

The JSIM of $M(q)$ of the total system is then given by

$$M(q) = \sum_{i=1}^n M_i(q) \quad (172)$$

A robotic manipulator with n 1-DoF prismatic or revolute joints is completely characterized by the configuration states $Q = q \in \mathbb{R}^n$ and $v = \dot{q} \in \mathbb{R}^n$ representing the joint positions and velocities, respectively. For an underactuated manipulator it is convenient to decompose the configuration vector into passive and active subsystems. Thus, for an underactuated manipulator with n_p passive joints and n_a active joints, where $n_a + n_p = n$. Thus, the generalized configuration vector is decomposed as $q = [q_p \ q_a]^T$. Accordingly, the JSIM can be decomposed into these two subsystems for the inertial coupling to appear as the cross diagonal terms in the matrix as

$$M(q) = \begin{bmatrix} M_{pp} & M_{pa} \\ M_{pa}^T & M_{aa} \end{bmatrix} \quad (173)$$

where $M_{pp} \in \mathbb{R}^{n_p \times n_p}$ represents the joint space inertia matrix for the system seen at the passive articulating subsystem with a dimension of. M_{aa} represents the inertia matrix of the active articulating subsystem. M_{pa} denotes the $p \times a$ inertial coupling matrix between the passive and the active articulating subsystems.

A.1.4 Potential energy

In this thesis we only consider the gravitational field as the only source of conservative force acting on the system. In that case, the potential energy of the linkage typically consists of the sum of the gravitational potential energies of each of the links. Let the wrench associated with the gravitational force of link i with respect to coordinate frame \mathcal{R}_b be given by

$$F_g^i = \begin{bmatrix} f_i \\ \hat{r}_i^g f_i \end{bmatrix} = -m_i g \begin{bmatrix} R_{bi} e_z \\ \hat{r}_i^g R_{bi} e_z \end{bmatrix} \quad (174)$$

where $e_z = [0 \ 0 \ 1]^T$ and \hat{r}_i^g is the center of gravity of link i expressed in \mathcal{R}_i . $f_i \in \mathbb{R}^3$ represents the forces that act on link i at the point r_i^g . In our case, \mathcal{R}_i is chosen so that r_i^g coincides with the origin so we have $r_i^g = 0$. The joint torque associated with the link i is given by

$$\tau_i^g = J_i^T(q) \text{Ad}_{g_{bi}}^T(q) F_g^i(q) \quad (175)$$

and the total effect of the gravitational forces is found by summing the effect of each link, which is given by

$$\mathcal{G}(\mathbf{q}) = \sum_{i=1}^n \tau_i^g \quad (176)$$

A.1.5 Lagrangian Dynamics

Now that we have found the kinetic and potential energy of the system, the dynamics can be found by the Lagrange equations in component form as

$$\frac{d}{dt} \left(\frac{\partial L}{\partial \dot{q}_i} \right) - \frac{\partial L}{\partial q_i} = \tau_i \quad (177)$$

$$\frac{dq_i}{dt} = \dot{q}_i \quad (178)$$

where τ_i are the joint torques and other generalized forces collocated with \dot{q}_i . However, note that for an underactuated manipulator, the torques for the passive subsystem are zero $\tau_i = 0 \quad \forall i \in n_p$. The dynamics can be written in matrix form as

$$\begin{aligned} & \begin{pmatrix} M_{pp}(\mathbf{q}) & M_{pa}(\mathbf{q}) \\ M_{pa}^T(\mathbf{q}) & M_{aa}(\mathbf{q}) \end{pmatrix} \begin{pmatrix} \ddot{\mathbf{q}}_p \\ \ddot{\mathbf{q}}_a \end{pmatrix} + \begin{pmatrix} C_{pp}(\mathbf{q}, \dot{\mathbf{q}}) & C_{pa}(\mathbf{q}, \dot{\mathbf{q}}) \\ C_{ap}(\mathbf{q}, \dot{\mathbf{q}}) & C_{aa}(\mathbf{q}, \dot{\mathbf{q}}) \end{pmatrix} \begin{pmatrix} \dot{\mathbf{q}}_p \\ \dot{\mathbf{q}}_a \end{pmatrix} \\ & + \begin{pmatrix} \mathbf{G}_p(\mathbf{q}) \\ \mathbf{G}_a(\mathbf{q}) \end{pmatrix} - \begin{pmatrix} \mathbf{J}_p^T(\mathbf{q})\mathbf{F} \\ \mathbf{J}_a^T(\mathbf{q})\mathbf{F} \end{pmatrix} = \begin{pmatrix} \mathbf{0}_{n_p \times 1} \\ \boldsymbol{\tau}_{n_a \times 1} \end{pmatrix} \quad (179) \end{aligned}$$

A.2 FLOATING-BASE RIGID BODY DYNAMICS

For robots whose root link can float freely in Cartesian space, e.g. humanoids, it is necessary to consider the pose of the root link with respect to (w.r.t.) the inertial reference frame. Differently from fixed-base manipulators, the inertial frame cannot be chosen at the base of the manipulator, but must be chosen at a fixed location. We will attach a reference frame \mathcal{R}_0 anchored to this ground and a reference frame \mathcal{R}_b to the floating base. \mathcal{R}_b also defines the base of the robot and is no longer inertial. n frames \mathcal{R}_i are assigned to each link so that the origins coincide with the axes of the joints or the center of gravity, respectively. We denote the configuration of the mobile platform with respect to the inertial frame by g_{0b} , while a vector $\mathbf{q} \in \mathbb{R}^n$ describes the configuration of the n euclidean joints including all Dofs of the active body limbs.

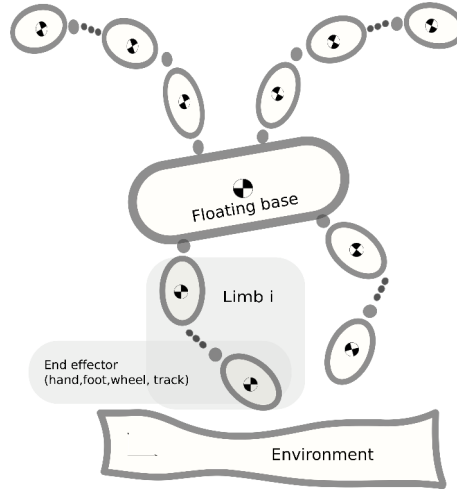


Figure 39: Illustration of a general floating-base system

A.2.1 Floating-base System's Configuration Space

We will adopt the notation presented in [MLS94; DS09]. Let Q_i describe the configuration of each rigid body in the system and v_i describe the velocity states. The configuration space of the floating base is denoted by the a matrix Q_b , where $Q_b \in SE(d)$ $d=2$ or $d=3$ for planar motion or spatial motion, respectively. The special Euclidean group is a lie group. An alternative way to express the configuration of the vehicle is as a vector q_b which gives $Q_b = q_b \in \mathbb{R}^d$. The location of a rigid body in space can be described by the position and orientation of a reference frame attached to the rigid body with respect to the inertial frame. The configuration space of a free floating rigid body has six degrees of freedom it is reasonable to represent the configuration as a vector in \mathbb{R}^6 . One way to do this is to first write the position of the rigid body as a vector $\mathbf{X} = [x_{0b} \ y_{0b} \ z_{0b}]^T$ and the orientation, also as a vector in \mathbb{R}^3 by the Euler angles $\Theta = [\phi_{0b} \ \theta_{0b} \ \psi_{0b}]^T$. The pose of the floating base in space is then given by a vector

$$q_b = g_{\check{0}b} = \begin{bmatrix} P_{0b} \\ \theta_b \end{bmatrix} = \begin{bmatrix} x_{0b} \\ y_{0b} \\ z_{0b} \\ \phi_{0b} \\ \theta_{0b} \\ \psi_{0b} \end{bmatrix} \quad (180)$$

The problem with this representation is that $SE(3)$ has a different topology than the Euclidean space \mathbb{R}^6 . It is thus not possible to cover $SE(3)$ continuously and globally using six coordinates in this way. To obtain a continuous and global covering of $SE(3)$ we need to use more than six real numbers. One representation that we can use is the unit quaternion, which requires four parameters to describe the orientation. We can also combine the rotation matrix and the position vector into one matrix, called the homogeneous transformation matrix, using 16 real numbers. In this way we choose a representation that allows us to describe the topology of $SE(3)$ globally and continuously at the expense of increasing the number of variables used to describe the configuration of the system to 7 (in case of quaternion representation) or 16. The velocity variables of the floating base can be described using body or spatial twists, or as the time derivative of the position variables q_b . In any case, the velocity vector is an element of \mathbb{R}^6 if the configuration space is the special Euclidean group, or a vector in \mathbb{R}^d if the configuration space is an d -dimensional subgroup of $SE(3)$.

We will assume that the active articulating body limbs consists only of 1-DoF joints with configuration space \mathbb{R} or S^1 . The configuration space of both prismatic and revolute joints can be described by the configuration states $Q_i \in \mathbb{R}$ for each joint $i = 1, \dots, n_a$. The configuration space of can therefore be written in terms of the joint positions as $Q_{a_i} = q_{a_i} \in \mathbb{R}$ with velocity variables $v_{a_i} = \dot{q}_{a_i} \in \mathbb{R}$ for both prismatic and revolute joints.

Using this approach the configuration space is written in terms of the configuration states Q_i which for a floating base system can be written as $Q = g_{0b}, q_a$ where $g_{0b} = g_{0b}(Q_b)$ is the floating base position and orientation and $q_a \in \mathbb{R}^n$ collects all limbs joints positions. The velocity variable are written as $\dot{q} = \dot{q}_b, \dot{q}_a$ where q_b is the time derivative of the position variables of the floating base and $\dot{q}_a \in \mathbb{R}^n$ collects the joint velocities of all limbs DOFs. Noting that the time derivative of the position variables q_b is different from the mobile base twist which has a geometrically meaningful representation of the velocities of the mobile base.

We can describe the pose of each frame \mathcal{R}_i relative to the inertial frame \mathcal{R}_0 as a homogeneous transformation matrix $g_{0i} \in SE(d)$ of the form

$$g_{0i} = \begin{bmatrix} R_{0i} & P_{0i} \\ 0 & 1 \end{bmatrix} \in \mathbb{R}^{4 \times 4} \quad (181)$$

with rotation matrix $R_{0i} \in SO(d)$ and translation vector $P_{0i} \in \mathbb{R}^d$. This pose can also be described using the vector of joint coordinates q and the floating base pose Q_b as

$$g_{0i} = g_{0b} g_{bi} = g_{0b}(Q_b) g_{bi}(q_a) \quad (182)$$

The floating base pose Q_b and the joint positions q_a thus fully determine the configuration state of the robot. We can then write the configuration of the floating base system as a vector

$$\mathbf{q} = \begin{bmatrix} q_b \\ q_a \end{bmatrix} \in \mathbb{R}^{d+n_a} \quad (183)$$

where

$$q_b = [x_{0b} \ y_{0b} \ z_{0b} \ \phi_{0b} \ \theta_{0b} \ \psi_{0b}]^T \quad (184)$$

and

$$q_a = [q_{a1} \ q_{a2} \ \dots \ q_{an_a}] \quad (185)$$

represents the configuration vector for the floating base, the n_a -links on-board limbs. The generalized velocities of the mobile manipulator system can be given in the inertial frame as

$$\dot{\mathbf{q}} = \begin{bmatrix} \dot{q}_b \\ \dot{q}_a \end{bmatrix} \in \mathbb{R}^{d+n_a} \quad (186)$$

This representation of the velocity variables has the apparent advantage that it can be integrated to find the position variables. It does not, however, give a geometrically meaningful representation of the floating base velocity in the same way as the velocity twists. We will therefore use the twist representation of the velocity variables for mobile manipulator systems to represent the velocities of the floating base and the robotic links.

A.2.2 Floating-base System Kinematics

The kinematics of the system can be naturally described in terms of the state variables g_{0b} for position/orientation and V^B or V^S for velocity. To allow for more general systems, and also multibody systems such as floating-base system, we will write the configuration of a rigid body as Q , where it is implicitly understood that $Q = q \in \mathbb{R}^m$ if the configuration space is Euclidean and where Q is a matrix Lie group if the configuration space is non-Euclidean. The velocity variable is written as a vector $v = \dot{q} \in \mathbb{R}^n$ for an Euclidean configuration space and as $v = V_{0b}^B \in \mathbb{R}^m$ if it is non-Euclidean. Using this formalism we obtain a global parameterization of a rigid idealized joint.

In this section we derive the for velocity twists in terms of adjoint maps for the n_a -links with respect to the inertial reference. In mobile robotics, it is generally preferred to use body coordinates for the robot velocities because these are the state variables that are normally measured by the sensors mounted on the robot (e.g. Inertial Measurement Unit (IMU)). Therefore, all Kinematic quantities expressed in body coordinates are denoted by superscript B. Let the link velocity twist V_{0i}^B denote the linear and angular velocity of body i , and $J_{g_i}^B(\mathbf{q}) \in \mathbb{R}^{m \times (m+n)}$ be the geometric Jacobian matrix of link i . The link geometric Jacobian provides a mapping from the mobile manipulator system velocity twists, which is the concatenation of the floating mobile base velocity twist and the joint velocities, to the velocity of link i in the robotic chain.

$$V_{0i}^B = J_{g_i}^B(\mathbf{q})\mathbf{V} \quad (187)$$

where

$$J_{g_i}^B(\mathbf{q}) = \frac{\partial V_{0i}^B}{\partial \mathbf{V}} \quad (188)$$

Alternatively link velocities can be expressed using adjoint maps as following

$$\widehat{V}_{0i}^B = \text{Ad}_{g_{bi}}^{-1} \widehat{V}_{0b}^B + \widehat{V}_{bi}^B \quad (189)$$

where the Adjoint map $\text{Ad}_{g_{bi}}^{-1}$ is used to transform the base velocity expressed in its body frame \mathcal{R}_b to the links frame \mathcal{R}_i . For a serial manipulator, the velocity of link i depends on all previous links in the chain (joints j , $i \leq j$ do not affect the motion of link i) where V_{bi}^B is the velocity of link i with respect to the mobile base \mathcal{R}_b expressed in the link frame \mathcal{R}_i .

$$\widehat{V}_{bi}^B = g_{bi}^{-1}(\mathbf{q})\dot{g}_{bi}(\mathbf{q}) \quad (190)$$

The time derivative of $g_{bi}(\mathbf{q})$ is given by the chain rule as

$$\dot{g}_{bi}(\mathbf{q}) = \sum_{j=1}^{n_a} \left(\frac{\partial g_{bi}}{\partial q_j} \dot{q}_j \right) \quad (191)$$

The twist coordinates V_{bi}^B can be extracted from the twist $\widehat{V} \in \mathfrak{se}(3)$ using the vee-map \vee .

$$\begin{aligned} V_{bi}^B &= \left(g_{bi}^{-1} \frac{\partial g_{bi}}{\partial q_j} \dot{q}_j \right)^\vee + \left(g_{bi}^{-1} \frac{\partial g_{bi}}{\partial q_j} \dot{q}_j \right)^\vee + \dots + \left(g_{bi}^{-1} \frac{\partial g_{bi}}{\partial q_j} \dot{q}_j \right)^\vee \\ &= \left[\left(g_{bi}^{-1} \frac{\partial g_{bi}}{\partial q_1} \dot{q}_1 \right)^\vee \quad \left(g_{bi}^{-1} \frac{\partial g_{bi}}{\partial q_2} \dot{q}_2 \right)^\vee \quad \dots \quad \left(g_{bi}^{-1} \frac{\partial g_{bi}}{\partial q_j} \dot{q}_j \right)^\vee \quad \mathbf{0}_{(n_a-i) \times m} \right] \begin{bmatrix} \dot{q}_1 \\ \dot{q}_2 \\ \vdots \\ \dot{q}_{n_a} \end{bmatrix} \quad (192) \\ &= J_{m,i} \dot{\mathbf{q}}_a \end{aligned}$$

where J_m is the body manipulator's link i Jacobian. The columns of the body Jacobian has an intuitive geometrical interpretation. They correspond to the joint twists written with respect to the joint twists $\xi_i(q)$ as observed from the link i at configuration q [MLS94].

$$J_{m,i}(q_a) = \begin{bmatrix} \xi_1 & \xi_2 & \dots & \xi_i & \mathbf{0}_{(n_a-i) \times m} \end{bmatrix} \quad (193)$$

A.2.3 Kinetic energy

The total energy in a multibody mechanical system is found by adding the kinetic and potential energy of each rigid body with respect to some common inertial reference frame.

A.2.3.1 Articulating links kinetic energy

The articulating link's kinetic energy is found in terms of the link velocities expressed in the link frame \mathcal{R}_i .

$$\begin{aligned} \mathcal{K}_i &= \frac{1}{2} (\mathbf{V}_{0i}^B)^T I_i \mathbf{V}_{0i}^B \\ &= \frac{1}{2} (\text{Ad}_{g_{bi}}^{-T} \mathbf{V}_{0b}^B + J_i(q_a) \dot{q}_a)^T I_i (\text{Ad}_{g_{bi}}^{-1} \mathbf{V}_{0b}^B + J_i(q_a) \dot{q}_a) \\ &= \frac{1}{2} (\text{Ad}_{g_{ib}}^T \mathbf{V}_{0b}^B + J_i(q_a) \dot{q}_a)^T I_i (\text{Ad}_{g_{ib}} \mathbf{V}_{0b}^B + J_i(q_a) \dot{q}_a) \quad (194) \\ &= \frac{1}{2} \begin{bmatrix} (\mathbf{V}_{0b}^B)^T & \dot{q}_a^T \end{bmatrix} M_i(q) \begin{bmatrix} \mathbf{V}_{0b}^B \\ \dot{q}_a \end{bmatrix} \\ &= \frac{1}{2} \mathbf{V}^T M_i(q) \mathbf{V} \end{aligned}$$

for $i = 1, \dots, n_a$ We see that the inertia matrix of the manipulator can be written in terms of the Adjoint map $\text{Ad}_{g_{ib}}(q)$ and the link body jacobian $J_i(q)$ as

$$M_i(q) = \begin{bmatrix} \text{Ad}_{g_{bi}}^T I_i \text{Ad}_{g_{bi}} & \text{Ad}_{g_{bi}}^T I_i J_i \\ J_i^T I_i \text{Ad}_{g_{bi}} & J_i^T I_i J_i \end{bmatrix} \in \mathbb{R}^{(m+n_a) \times (m+n_a)} \quad (195)$$

Note that the inertia matrix $M_i(q)$ can be written in a compact form using the body geometric jacobian J_{gi}^B as

$$M_i(q) = (J_{gi}^B)^T I_i J_{gi}^B \quad (196)$$

where

$$J_{gi}^B(q_a) = \frac{\partial \mathbf{V}_{0i}^B}{\partial \mathbf{V}} = \begin{bmatrix} \text{Ad}_{g_{ib}} & J_i \end{bmatrix} \in \mathbb{R}^{m \times (m+n_a)} \quad (197)$$

A.2.3.2 floating-base kinetic energy

The kinetic energy for the floating base can simply be expressed as

$$\mathcal{K}_b = \frac{1}{2} (\mathbf{V}_{0b}^B)^T \mathbf{I}_b \mathbf{V}_{0b}^B \quad (198)$$

or in the standard form using the same factorization for the floating base system as

$$\mathcal{K}_b = \frac{1}{2} \begin{bmatrix} (\mathbf{V}_{0b}^B)^T & \dot{\mathbf{q}}_a^T \end{bmatrix} \mathbf{M}_b \begin{bmatrix} \mathbf{V}_{0b}^B \\ \dot{\mathbf{q}}_a \end{bmatrix} = \frac{1}{2} \begin{bmatrix} (\mathbf{V}_{0b}^B)^T & \dot{\mathbf{q}}_a^T \end{bmatrix} \begin{bmatrix} \mathbf{I}_b & 0 \\ 0 & 0 \end{bmatrix} \begin{bmatrix} \mathbf{V}_{0b}^B \\ \dot{\mathbf{q}}_a \end{bmatrix} \quad (199)$$

We observe that the inertia matrix of the floating base is constant because we choose to represent the velocities in the floating base frame \mathcal{R}_b

A.2.3.3 Total Kinetic energy

The inertia matrix of the mobile manipulator system can be written in terms of the body geometric Jacobian

$$\mathbf{M}_i(\mathbf{q}) = (\mathbf{J}_{gi}^B)^T \mathbf{I}_i \mathbf{J}_{gi}^B \quad (200)$$

where

$$\mathbf{J}_{gi}^B(\mathbf{q}_a) = \frac{\partial \mathbf{V}_{0i}^B}{\partial \mathbf{V}} = \begin{bmatrix} \text{Ad}_{g_{ib}} & \mathbf{J}_i \end{bmatrix} \in \mathbb{R}^{m \times (m+n_a)} \quad (201)$$

The total kinetic energy of the floating-base system is given by the sum of the kinetic energies of the floating-base and all attached articulating links, that is,

$$\mathcal{K}(\mathbf{V}, \mathbf{q}_a) = \frac{1}{2} \mathbf{V}^T \left(\sum_{i=b}^n \mathbf{M}_i(\mathbf{q}_a) \right) \mathbf{V} = \frac{1}{2} \mathbf{V}^T \left(\begin{bmatrix} \mathbf{I}_b & 0 \\ 0 & 0 \end{bmatrix} + \sum_{i=1}^n \mathbf{M}_i(\mathbf{q}_a) \right) \mathbf{V} \quad (202)$$

where $\mathbf{M}(\mathbf{q}_a)$ is the inertia matrix of the attached articulating system. Note that neither $\mathcal{K}(\mathbf{q}_a, \mathbf{V})$ nor $\mathbf{M}(\mathbf{q}_a)$ depend on the pose g_{0b} nor the choice of inertial reference frame \mathcal{R}_0 .

A.2.4 Free-floating base Dynamics

The free-floating base system with generalized coordinates vector $\mathbf{q} = \begin{bmatrix} \mathbf{q}_b^T & \mathbf{q}_a^T \end{bmatrix}^T$ and quasi-velocity vector $\mathbf{V} = \begin{bmatrix} (\mathbf{V}_{0b}^B)^T & \dot{\mathbf{q}}_a^T \end{bmatrix}^T$. The velocity twist \mathbf{V} is called a quasi-velocity because \mathbf{V} itself has a clear geometric representation as velocity but its integral $\int \mathbf{V}$ has no physical interpretation. The lagrangian can be written in terms of the generalized coordinates \mathbf{q} and the body velocity twist \mathbf{V} as

$$\mathcal{L}(\mathbf{q}, \mathbf{V}) = \frac{1}{2} \mathbf{V}^T \mathbf{M}(\mathbf{q}) \mathbf{V} - \mathcal{G}(\mathbf{q}) \quad (203)$$

the partial derivatives of the Lagrangian then become

$$\frac{\partial L}{\partial \mathbf{V}} = M\mathbf{V} \quad (204)$$

$$\frac{d}{dt} \left(\frac{\partial L}{\partial \mathbf{V}} \right) = M(\mathbf{q})\dot{\mathbf{V}} + \dot{M}(\mathbf{q})\mathbf{V} \quad (205)$$

$$\frac{\partial L}{\partial \mathbf{q}} = \frac{1}{2} \frac{\partial^T (M(\mathbf{q})\mathbf{V})}{\partial \mathbf{q}} \mathbf{V} - \frac{\partial \mathcal{G}(\mathbf{q})}{\partial \mathbf{q}} \quad (206)$$

$$M(\mathbf{q}_a)\dot{\mathbf{V}} + C(\mathbf{q}, \mathbf{V})\mathbf{V} + G(\mathbf{q}) = S^T \boldsymbol{\tau} + {}^e J^T(\mathbf{q})\mathbf{w} \quad (207)$$

where S is a selection matrix indicating the actuated degrees of freedom, \mathbf{w} S is a selection matrix indicating the actuated degrees of freedom $S = [0_{6 \times n} \ I_{n \times n}]$, \mathbf{w} is the concatenation of the external contact wrenches, and J_e is their concatenated Jacobians.

A.2.5 Contact dynamics as complementarity problem

Many of the complexities of rigid body contact dynamics can be avoided by discretizing the system dynamics in time and reasoning about the integral of contact forces acting over a time step. In particular, no distinction is made between impulses and finite contact forces over a time step. By conservatively approximating the friction cone as a polyhedron, forward dynamics can be cast as a linear complementarity problem (LCP), for which efficient solvers exist. This has become a popular formulation for simulation of rigid bodies in frictional contact and it has recently seen applications to control design for legged systems.

This section will summarize existing theory of modeling non-impacting rigid contact. Let us define a set of gap functions $\phi_j(\mathbf{q})$ (for $j = 1, \dots, n$), where gap function j gives the signed distance between a link of the robot and another rigid body (part of the environment, another link of the robot, an object manipulated, etc.)

The gap functions return a positive real value if the bodies are separated, a negative real value if the bodies are geometrically intersecting, and zero if the bodies are in a 'kissing' configuration. The rigid contact model specifies that bodies never overlap, i.e.:

$$\phi_j(\mathbf{q}) \geq 0 \quad (208)$$

In the absence of friction, the constraints on the gap functions are enforced by forces that act along the contact normal. Projecting these forces along the contact normal yields scalars $\lambda_z^1, \dots, \lambda_z^N$. The forces should be compressive (i.e., forces that can not pull bodies together), which is denoted by restricting the sign of these scalars to be non-negative:

$$\lambda_z \geq 0 \quad (209)$$

A complementarity constraint keeps frictional contacts from doing work: when the constraint is inactive ($\phi_j > 0$) no force is applied and when force is applied the constraint must be active ($\phi_j = 0$). This constraint is expressed mathematically as $\phi_j \cdot \lambda_j = 0$. All three constraints can be combined into one equation

$$0 \leq \lambda_j \perp \phi_j(q) \geq 0 \quad (210)$$

B.1 BACKGROUND

Optimal control had its origins in the calculus of variations in the 17th century (Fermat, Newton, Leibnitz, and the Bernoullis). The calculus of variations was developed further in the 18th century by Euler and Lagrange and in the 19th century by Legendre, Jacobi, Hamilton, and Weierstrass. In the early 20th century, Bozza and Bliss put the final touches of rigor on the subject. In 1957, Bellman gave a new view of Hamilton-Jacobi theory which he called dynamic programming, essentially a nonlinear feedback control scheme. McShane and Pontryagin extended the calculus of variations to handle control variable inequality constraints, the latter enunciating his elegant maximum principle. The truly enabling element for use of optimal control theory was the digital computer, which became available commercially in the 1950s.

Optimal control has roots in linear and nonlinear programming (NLP), i.e., parameter optimization with inequality and/or equality constraints, which were developed shortly after WWII[KT51]. In particular, Kuhn and Tucker [KT51] gave a simple necessary condition for the system to be on a constraint boundary, namely that the gradient of the performance index must lie inside the "cone" of the constraint gradients. Efficient solvers have since been developed that solve NLP problems with thousands of parameters [WB06; GMS02]. For numerical solutions of optimal trajectory problems the control history must be approximated by values at a finite number of time points, so collocation methods using NLP can be used to solve such problems [Hargraves1987].

B.2 OPTIMAL CONTROL OVERVIEW

There are three types of algorithms for solving optimal control problems; Dynamic programming is an excellent solution to the optimal control problem for unconstrained low-dimensional systems, but it does not scale well to high-dimensional systems, since it requires a discretization of the full state space. Indirect methods tend to be numerically unstable and are difficult to implement and initialize. We will employ direct method for transcribing and solving the optimal control problem. The solution to an optimal control problem via transcription scales well to high-dimensional systems, but yields a single

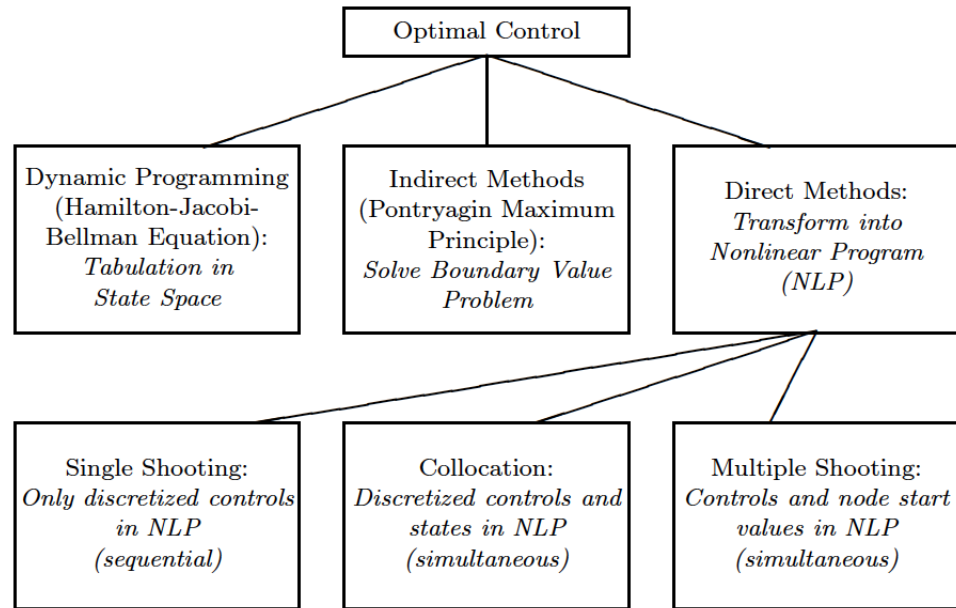


Figure 40: Overview of numerical methods for optimal control

trajectory through state and control space, rather than a global policy like dynamic programming. We give a broad description of the first two methods and discuss direct methods more deeply, as they are heavily used in robotics and computer graphics nowadays.

B.2.1 *Dynamic Programming*

In the late 1950's Richard Bellman introduced a generalization of the classical Hamilton-Jacobi theory [Bel71]. The key notion of these so-called extremal field methods, is described by a system of first-order nonlinear partial differential equations, known as the Hamilton-Jacobi-Bellman or HJB equation. Essentially these PDE's describe the optimal control functions $u^*[x, t]$ as well as the optimal objective for all possible initial conditions $[x(t_0), t_0]$. From a control theory perspective, this could be seen as optimal feedback control. Hamilton-Jacobi-Bellman theory has played a major role in the development of necessary and sufficient conditions, and has provided a unified theoretical basis for the field of optimal control. Despite its theoretical importance, the utility of dynamic programming is limited to unconstrained low-dimensional systems and does not scale well to high-dimensional systems [Bry75]. The great drawback of dynamic programming is, as Bellman himself calls it, the "*curse of dimensionality*." Even recording the solution to a moderately complicated problem involves an enormous amount of storage.

B.2.2 *Indirect Methods*

Indirect approach utilizes the optimize then discretize philosophy, that is, write the continuous optimality conditions first and then discretize them. The indirect approach solves the problem indirectly by converting the optimal control problem to a boundary-value problem. As a result, in an indirect method the optimal solution is found by solving a system of differential equations that satisfies endpoint and/or interior point conditions. The indirect approach leads to a multiple-point boundary-value problem that is solved to determine candidate optimal trajectories called extremals. Each of the computed extremals is then examined to see if it is a local minimum, maximum, or a saddle point. Of the locally optimizing solutions, the particular extremal with the lowest cost is chosen. In essence, an indirect method attempts to locate a root of the necessary conditions the transcription problem has small number of variables. the number of iteration variables is equal to the number of differential equations.

Advantages:

- generally more accurate than direct methods since it attempts to solve HJB partial differential equation equation by transforming into 2n-dimensional ODE
- The problem size doesn't grow since no discretization is performed before resolving the optimality conditions

Disadvantages:

- Sensitivity to initial guess is the major disadvantage of the indirect approach: In particular, a small change in the initial condition can produce a very large change in the final conditions.
- Not suitable for hybrid dynamics with multiple phases since it is extremely difficult to determine this information a priori, and failure to do so will cause the indirect method to fail.

B.2.3 *Direct Methods*

The direct transcription method utilizes a discretize then optimize philosophy. Specifically the dynamic differential equation and the objective function are replaced by discrete approximations leading to a large, sparse NLP problem. A direct method attempts to find a minimum of the objective (or Lagrangian) function.

Advantages:

- In contrast the direct method works because the underlying NLP algorithm determines the number, location, and correct active grid points for a linearly independent active set

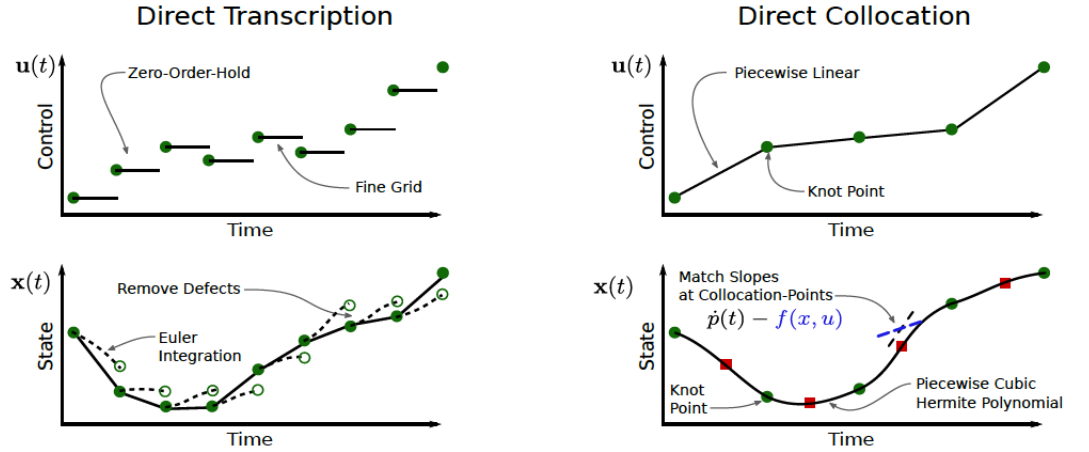


Figure 41: Illustration of direct methods for trajectory optimization

Disadvantages:

- The major drawback of direct methods comes from the fact that we only obtain an approximate solution of the OCP and prone to numerical errors, as the dynamics of the robot are approximated in between the nodes but a proper choice of discretization gives good results in practice.
- Transcribing the continuous OCP into a finite dimensional increase the size of the subsequent NLP, making its solution computationally expensive (can take several minutes or even hours to find a solution). However, specialized solvers can take advantage of the high sparsity of the NLP, i.e. the fact that the associated gradients contain a large number of zeros.

Nowadays direct method are the most commonly used methods due to their easy applicability to large-scale problems and their robustness.

B.3 TRAJECTORY OPTIMIZATION BY DIRECT COLLOCATION

A trajectory optimization problem seeks to find a trajectory for some dynamical system that satisfies some set of equality and inequality constraints while minimizing some cost functional. An abstraction of the Lagrangian dynamics, it can be written as a set of differential equations

$$\dot{x}(t) = f(x(t), u(t)) \quad (211)$$

where $x = \begin{bmatrix} q \\ \dot{q} \end{bmatrix} \in \mathbb{R}^{2n}$ represent the system states, assuming the number of generalized coordinates equal to the number of generalized

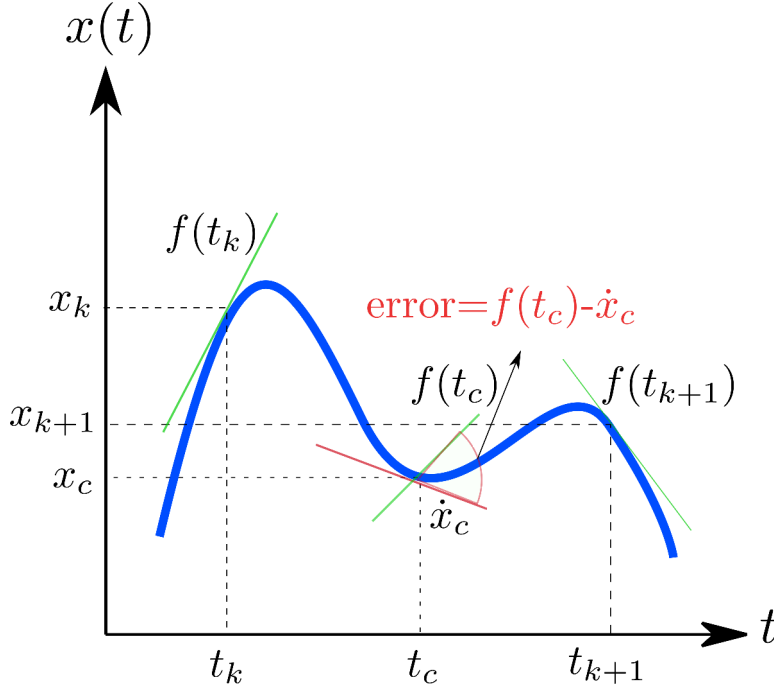


Figure 42: Illustration of the state trajectory discretization occurring in direct collocation optimization. System dynamics $f(t_c)$ are enforced to match the slope of the cubic \dot{x}_c at the collocation point x_c .

velocities. The input control vector $\mathbf{u} \in \mathbb{R}^m$ and the transition function $f(\cdot)$ defines the system evolution in time. Trajectory optimization problem seeks to find a finite-time input trajectory $\mathbf{u}(t), \forall t \in [0, t_f]$, such that a given criteria is minimized,

$$G = \phi(t_0, \mathbf{x}_0, t_f, \mathbf{x}_f) + \int_{t_0}^{t_f} g(t, \mathbf{x}, \mathbf{u}) dt \quad (212)$$

where $\phi(\cdot)$ and $g(\cdot)$ are the intermediate and final cost function. The objective function can be written in terms of quantities evaluated at the ends of the phases only, in that case it is referred to as the Mayer form. If the objective function only involves an integral it is referred to as a problem of Lagrange, and when both terms are present it is called a problem of Bolza.

The optimization may be subject to a set of boundary constraints

$$\mathbf{b}_{\min} < \mathbf{b}(t_0, \mathbf{x}_0) < \mathbf{b}_{\max} \quad (213)$$

$$\mathbf{b}_{\min} < \mathbf{b}(t_f, \mathbf{x}_f) < \mathbf{b}_{\max} \quad (214)$$

In addition, Dynamic constraints, including the second order non-holonomic constraints, can be added as path constraints

$$\mathbf{c}_{\min} < \mathbf{c}(t, \mathbf{x}(t), \mathbf{u}(t)) < \mathbf{c}_{\max} \quad (215)$$

Bounds on state variables and input control limits are added as

$$x_{\min} \leq x(t) \leq x_{\max} \quad (216)$$

$$u_{\min} \leq u(t) \leq u_{\max} \quad (217)$$

The result of the optimization is an optimal trajectory given by $[x^*(t), u^*(t)]$

To compute a feasible motion plan we transcribe the differential equation of the robot dynamics to algebraic equations and solve them through NonLinear Optimisation (NLP). [Bet10] showed that that NLP could be interpreted as discrete approximations of the continuous optimal control problem. There are mature NLP solvers used in robotics; SNOPT [GMS02] which is based on Sequential Quadratic Programming (SQP). The second solver is IPOPT [WBo6] using the Interior Point Method. However, The complete description of the solvers and the algorithms used lies outside of the scope of this work.

In this work, we employ direct method for transcribing and solving the optimal control problem. In direct collocation, the optimization searches over a set of decision variables z , comprised by a vector of the states and control trajectories discretized over time at certain points or nodes, i.e., $z = [x_k, u_k]$, for $k = 1, \dots, N$, where N represents the total number of nodes. Finally The NLP can be formulated as.

$$\underset{z}{\text{minimize}} \quad G(z) \quad (218)$$

$$\text{subject to :} \quad l \leq \begin{pmatrix} z \\ c(z) \\ Az \end{pmatrix} \leq u \quad (219)$$

In, direct collocation the input is represented as a piecewise-linear function of time, and the state is piecewise-cubic. The values of the state and control at each knot point are the decision variables. The slope of state is prescribed by the dynamics at each knot point. The collocation points are the mid-points of each cubic segment. The slope of the cubic at the collocation point is constrained to match the system dynamics at that point, as illustrated in figure. For more details the reader is referred to [Bet10][Bet98].

B.3.1 NLP Solvers

Nonlinear programming solvers are in a mature state of development given the vast experience of the field of mathematical optimization. Such solvers have been used and tested for numerical trajectory optimization during many years, primarily in the field of aircraft and

spacecraft trajectory planning. The most popular NLP solvers are SNOPT and IPOPT. This section presents some features aiming to describe the main differences between them and to identify the nature of any difference in their performances. A complete comparison between these classes of solvers can be found in [BG02].

- *SNOPT (Sparse Nonlinear OPTimizer)*[GMS02]: The basic structure of this implementation of the SQP algorithm involves major and minor iterations. Major iterations advance along a sequence of points z_h that satisfy the set of linear constraints. These iterations converge to a point that satisfies the remaining nonlinear constraints and the first-order conditions of optimality. The direction towards which the major iterations move is produced by solving a QP subproblem. Solving this subproblem is an iterative procedure by itself (i.e. the minor iterations), based on a Newton-type minimization approach. An important characteristic of all SQP algorithms is that they are 'active set algorithms'. Roughly speaking, this means that during the iterative procedure all the inequality constraints play a very explicit role during the search as the QP subproblem must estimate the active set of constraints in order to decide the search direction. A convenient feature of SNOPT is the possibility of using information about the gradient of the cost function and the constraints. It also uses information about the structure of the problem if it is provided, i.e. separating linear and nonlinear components of objective function and constraints.
- *iPOPT*[WB06]: This algorithm also depends on a Newton type subproblem. Nevertheless, inequalities are handled in a different manner. A barrier function is used to keep the search as far as possible from the bounds of the feasible set. The barrier parameters change along iterations, allowing proximity to the adequate constraint.

C.1 RAPIDL-EXPLORING RANDOM TREES (RRT)

The algorithm that constructs a kinodynamic RRT is shown in Algorithm (4). A tree based search where each vertex and edge represent a state and a trajectory, respectively. The tree $\mathcal{T} = (V, E)$ starts with an initial vertex as the initial state s_I and with no associated trajectory in the edge. RRT's strategy expands \mathcal{T} toward sparsely sampled regions by sampling a random state in S and extending the tree toward it using a steering function. This is known as a Voronoi biasing strategy because the probability of choosing a node in \mathcal{T} is proportional to the volume of its Voronoi cell.

Line (3) provides s_{rand} by randomly selecting a state within a given state bounds. In Line 4, the "nearest" vertex to x_{rand} is chosen according to the metric d . The EXTEND function attempts to grow the tree by adding a new vertex that is biased by the randomly selected state s_{rand} . This is also known as the steering problem which is required to compute an open-loop trajectory that brings a non-holonomic system from an initial state to a goal state without the presence of obstacles. Given the general difficulty of this problem for dynamic systems with drift or momentum, a Monte Carlo method is usually applied by applying a random control input $u_k \in U$ for a random or some fixed time Δt .

Algorithm (5) describes the EXTEND function which takes as input a start state s_s , a goal or terminal state s_t , a metric d , and an integration time interval Δt while k represents the number of trials. The EXTEND function consists of a simple iteration in which each step attempts to apply a randomly selected control $u_k \in U$ (line 3) for a randomly selected integration time $\Delta t \in [\delta_{\text{min}}, \delta_{\text{max}}]$ then proceeds by integrating the system dynamic D from s_s as the initial value. Consequently, the integration provides a trajectory $\mathbf{s}(t)$. If the number of trials $k > 1$ then k random control inputs u_k are applied for Δt_k producing k different trajectories $\mathbf{s}_k(t)$ after each trial the distance between the final state in the trajectory $s_{k_{\text{new}}} = \mathbf{s}_k(\Delta t_k)$ and s_t is evaluated and the trajectory \mathbf{s}_{best} that gets closest to s_t is retained.

Back to the main RRT loop in Algorithm (1), the trajectory $\mathbf{s}_{\text{best}}(t)$ is verified in line (6) if it is kinematically feasible and does not collide with an obstacle along the whole trajectory if one exists. Upon

success in the verification phase, the final state s_{new} of the trajectory $\mathbf{y}_{best}(\Delta t)$ we added to the tree as a new vertex and its associated trajectory as a new edge. In line (9), s_{new} is checked if it is an element of the predefined goal region S_{goal} . If true then we can trace the final trajectory in the search tree \mathcal{T} back to the initial state s_I .

Algorithmus 4 : Rapidly-exploring Random Tree (RRT)

input : Kinodynamic problem (\mathcal{P}), State Space (S), Initial state (s_I), Goal region (S_{goal}), Control space (U), Distance metric (d), Integration time limits ($\Delta t_{\text{max}}, \Delta t_{\text{min}}$), Number of sampled control trials (k), Maximum number of nodes N_{max}

output : State trajectory $\mathbf{s}(t) \in S_{\text{feas}}$ for $t \in [0, t_f]$ from s_I to $s_{\text{terminal}} \in S_{\text{goal}}$ and control trajectory $\mathbf{u}(t)$ for $t \in [0, t_f]$

```

1 Initialization:  $\mathcal{T} = \{V \leftarrow \{s_I\}, E \leftarrow \emptyset\}$ 
2 while ( $i \leq N_{\text{max}} \vee (\mathcal{T} \cap S_{\text{goal}} = \emptyset)$ ) do
3    $s_{\text{rand}} \leftarrow \text{Sample}(S)$ 
4    $s_{\text{near}} \leftarrow \text{NearestNeighbor}(\mathcal{T}, s_{\text{sampld}})$ 
5    $\mathbf{s}(t) \leftarrow \text{EXTEND}(s_{\text{near}}, s_{\text{rand}}, d, \Delta t, k)$ 
6   if  $\mathbf{s}(t) \in S_{\text{feas}}$  for  $t \in [0, \Delta t]$  then
7     Let  $s_{\text{new}} = \mathbf{s}(\Delta t)$  denote the end of the extension
8      $V \leftarrow V \cup \{s_{\text{new}}\}, E \leftarrow E \cup \{\mathbf{s}(t) : s_{\text{near}} \rightarrow s_{\text{new}}\}$ 
9     if  $s_{\text{new}} \in S_{\text{goal}}$  then
10      | return Trajectory in  $\mathcal{T}$  from  $s_I$  to  $s_{\text{new}}$ 
11      | end
12   end
13 end

```

Algorithmus 5 : RRT-EXTEND

input : Control space (U), Distance metric (d), Integration time limits ($\Delta t_{\text{max}}, \Delta t_{\text{min}}$), Number of sampled control trials (k)

output : State trajectory $\mathbf{s}(t)$ for $t \in [0, \Delta t_{\text{best}}]$ from s_s to s_t and control trajectory $\mathbf{u}_{\text{best}}(t)$ for $t \in [0, \Delta t_{\text{best}}]$

```

1 Initialization:  $d_{\text{best}} \leftarrow \infty, s_{\text{best}} \leftarrow \emptyset, \Delta t_{\text{best}} \leftarrow \emptyset$ 
2 for  $i = 1$  to  $k$  do
3    $\mathbf{u} \leftarrow \text{Sample}(U)$ 
4    $\Delta t \leftarrow \text{Sample}([\Delta t_{\text{min}}, \Delta t_{\text{max}}])$ 
5    $\mathbf{s}(t) \leftarrow \text{Integrate}(x_s, \mathbf{u}, D, \Delta t)$ 
6    $x_t \leftarrow \mathbf{s}(\Delta t)$ 
7   if  $d(\mathbf{s}(\Delta t), s_t) < d_{\text{best}}$  then
8     |  $d_{\text{best}} \leftarrow d(\mathbf{y}(\Delta t), x_t)$ 
9     |  $s_{\text{best}} \leftarrow \mathbf{s}$ 
10    |  $\Delta t_{\text{best}} \leftarrow \Delta t$ 
11    | end
12 end

```

C.2 EXPANSIVE SPACE TREE (EST)

EST is also a tree-based search like RRT however, EST's strategy differs in that it explicitly maintains an estimate of how densely \mathcal{T} covers the state space and employs random shooting instead of a steering approach. The density estimator is a function $\rho_r(s)$, where $r > 0$ is a kernel width parameter. Unlike RRT that relies on expanding \mathcal{T} towards a randomly sampled state, EST expansion strategy attempts to explore uniformly by sampling extensions inversely proportional to the nodes density then sample the control space randomly and apply it for a sampled duration. Pseudocode is given in Algorithm (3).

Line 3-9 sample a set of krandom extensions $\{(s_1, \Delta t_1), \dots, (s_k, \Delta t_k)\}$. The process samples a node from the tree with a probability inversely proportional to its density, draws a random control sample from \mathbf{U} , and integrates the dynamics over a duration Δt sampled from the range $[\Delta t_{\min}, \Delta t_{\max}]$. Then, it assigns a sampling weight to each candidate extension, inversely proportional to the density of its end state. As in RRT, in line 10-12, we check the feasibility of a candidate end state $s_j(\Delta t_j) \in S_{\text{feas}}$ before adding it to the list of candidate extensions.

To estimate density, several methods may be used. A kernel density estimator $\rho_r(s) = \sum_{s_r \in \mathcal{T}} \exp(-\|s - s_r\|^2 / r^2)$ is straightforward but requires $O(|\mathcal{T}|)$ time to evaluate. An alternate method stores a hash grid with a resolution over space and counts the number of existing nodes in \mathcal{T} in the same cell as s . However, grids do not scale well to high-dimensional spaces, providing poorer density estimates.

Algorithmus 6 : Expansive Space Tree (EST)

input : Kinodynamic problem (\mathcal{P}), State Space (S), Initial state (s_I), Goal region (S_{goal}), Control space (U), Distance metric (d), Integration time limits ($\Delta t_{\text{max}}, \Delta t_{\text{min}}$), Number of sampled control trials (k), Maximum number of nodes N_{max}

output : State trajectory $\mathbf{s}(t) \in S_{\text{feas}}$ for $t \in [0, t_f]$ from s_I to $s_{\text{terminal}} \in S_{\text{goal}}$ and control trajectory $\mathbf{u}(t)$ for $t \in [0, t_f]$

- 1 Initialization: $\mathcal{T} = \{V \leftarrow \{s_I\}, E \leftarrow \emptyset\}$
- 2 **while** ($i \leq N_{\text{max}} \vee (\mathcal{T} \cap S_{\text{goal}} = \emptyset)$) **do**
- 3 **for** $j = 1$ **to** k **do**
- 4 $s_{\text{rand}} \leftarrow \text{Sample}(\mathcal{T})$
- 5 $\mathbf{u} \leftarrow \text{Sample}(U)$
- 6 $\Delta t_j \leftarrow \text{Sample}([\delta_{\text{min}}, \delta_{\text{max}}])$
- 7 $\mathbf{s}(t) \leftarrow \text{Integrate}(s_j, \mathbf{u}, D, \Delta t_j)$
- 8 $w_j \leftarrow \frac{1}{(1 + \rho_r(y_j(\Delta t_j))^2)}$
- 9 $(\mathbf{y}, \Delta t) \leftarrow \text{Weighted random sample from } ((\mathbf{y}_1, \Delta t_1), \dots, (\mathbf{y}_k, \Delta t_k))$ with weights (w_1, \dots, w_k)
- 10 **if** $\mathbf{s}(t) \in S_{\text{feas}}$ for $t \in [0, \Delta t]$ **then**
- 11 Let $s_{\text{new}} = \mathbf{s}(\Delta t)$ denote the end of the extension
- 12 $V \leftarrow V \cup \{s_{\text{new}}\}, E \leftarrow E \cup \{\mathbf{s}(t) : s_{\text{near}} \rightarrow s_{\text{new}}\}$
- 13 **if** $s_{\text{new}} \in S_{\text{goal}}$ **then**
- 14 **return** Trajectory in \mathcal{T} from s_I to s_{new}
- 15 **end**
- 16 **end**
- 17 **end**
- 18 **end**

BIBLIOGRAPHY

- [AHH15] A Abate, R L Hatton, and J Hurst. "Passive-dynamic leg design for agile robots." In: *Robot. Autom. (ICRA), 2015 IEEE Int. Conf.* (2015), pp. 4519–4524. DOI: [10.1109/ICRA.2015.7139825](https://doi.org/10.1109/ICRA.2015.7139825).
- [ACN10] Pieter Abbeel, Adam Coates, and Andrew Y. Ng. "Autonomous helicopter aerobatics through apprenticeship learning." In: *Int. J. Rob. Res.* 29.13 (2010), pp. 1608–1639. ISSN: 02783649. DOI: [10.1177/0278364910371999](https://doi.org/10.1177/0278364910371999). arXiv: [0911.4714](https://arxiv.org/abs/0911.4714) [astro-ph.HE].
- [Ale90] R. Mcn Alexander. "Three Uses for Springs in Legged Locomotion." In: *Int. J. Rob. Res.* 9.2 (1990), pp. 53–61. ISSN: 17413176. DOI: [10.1177/027836499000900205](https://doi.org/10.1177/027836499000900205).
- [Ale03] R. Mcneill Alexander. *Principles of Animal Locomotion*. Princeton University Press, 2003.
- [ALC92] Jorge Angeles and Carlos S. López-Cajún. "Kinematic Isotropy and the Conditioning Index of Serial Robotic Manipulators." In: *Int. J. Rob. Res.* 11.6 (1992), pp. 560–571. ISSN: 17413176. DOI: [10.1177/027836499201100605](https://doi.org/10.1177/027836499201100605).
- [AF13] Yannick Aoustin and Alexander Formalskii. "Upward Jump of a Biped." In: *Int. J. Humanoid Robot.* 10.04 (2013), p. 1350032. ISSN: 0219-8436. DOI: [10.1142/S0219843613500321](https://doi.org/10.1142/S0219843613500321). URL: <http://www.worldscientific.com/doi/abs/10.1142/S0219843613500321>.
- [Arm+07] Rhodri Armour, Keith Paskins, Adrian Bowyer, Julian Vincent, William Megill, and Richard Bomphrey. "Jumping robots: a biomimetic solution to locomotion across rough terrain." In: *Bioinspir. Biomim.* 2.3 (2007), S65–82. ISSN: 1748-3190. DOI: [10.1088/1748-3182/2/3/S01](https://doi.org/10.1088/1748-3182/2/3/S01). URL: <http://www.ncbi.nlm.nih.gov/pubmed/17848786>.
- [Asa83] Haruhiko Asada. "A geometrical representation of manipulator dynamics and its application to arm design." In: *J. Dyn. Syst. Meas. Control. ASME* 105.3 (1983), pp. 131–135, 142. ISSN: 00220434. DOI: [10.1115/1.3140644](https://doi.org/10.1115/1.3140644).
- [AH02] Blake M. Ashby and Jean H. Heegaard. "Role of arm motion in the standing long jump." In: *J. Biomech.* 35.12 (2002), pp. 1631–1637. ISSN: 00219290. DOI: [10.1016/S0021-9290\(02\)00239-7](https://doi.org/10.1016/S0021-9290(02)00239-7).

- [ÅFoo] K. J. Åström and K. Furuta. “Swinging up a pendulum by energy control.” In: *Automatica* 36.2 (2000), pp. 287–295. ISSN: 00051098. DOI: [10.1016/S0005-1098\(99\)00140-5](https://doi.org/10.1016/S0005-1098(99)00140-5).
- [ABM17] Morteza Azad, Jan Babic, and Michael Mistry. “Dynamic manipulability of the center of mass: A tool to study, analyse and measure physical ability of robots.” In: *Proc. - IEEE Int. Conf. Robot. Autom.* 2017, pp. 3484–3490. ISBN: 9781509046331. DOI: [10.1109/ICRA.2017.7989398](https://doi.org/10.1109/ICRA.2017.7989398).
- [BPS95] P J Beek, C Peper, and D Stegeman. “Dynamical models of movement coordination.” In: *Hum. Mov. Sci.* 14 (1995), pp. 573–608.
- [BTB] Guillaume Bellegarda, Nihar Talele, and Katie Byl. “Exploring Nonintuitive Optima for Dynamic Locomotion.” In: ().
- [Bel+18] C. Dario Bellicoso, Fabian Jenelten, Christian Gehring, and Marco Hutter. “Dynamic Locomotion through Online Nonlinear Motion Optimization for Quadrupedal Robots.” In: *IEEE Robot. Autom. Lett.* 3766.c (2018), pp. 1–1. ISSN: 2377-3766. DOI: [10.1109/LRA.2018.2794620](https://doi.org/10.1109/LRA.2018.2794620). URL: <http://ieeexplore.ieee.org/document/8260889/>.
- [Bel71] Richard Bellman. *Introduction to the mathematical theory of control processes (Vol. 2)*. New York: Academic Press, 1971. ISBN: 9782881240775.
- [BLX95] Marcel Bergerman, Christopher Lee, and Yangsheng Xu. “A dynamic coupling index for underactuated manipulators.” In: *J. Robot. Syst.* 12.10 (1995), pp. 693–707. ISSN: 07412223. DOI: [10.1002/rob.4620121006](https://doi.org/10.1002/rob.4620121006). URL: <http://doi.wiley.com/10.1002/rob.4620121006>.
- [Ber+09] M. Berniker, A. Jarc, E. Bizzi, and M. C. Tresch. “Simplified and effective motor control based on muscle synergies to exploit musculoskeletal dynamics.” In: *Proc. Natl. Acad. Sci.* 106.18 (2009), pp. 7601–7606. ISSN: 0027-8424. DOI: [10.1073/pnas.0901512106](https://doi.org/10.1073/pnas.0901512106). URL: <http://www.pnas.org/cgi/doi/10.1073/pnas.0901512106>.
- [Ber67] N. A. Bernstein. *The Co-ordination and Regulation of Movements*. Oxford, England: Pergamon Press, 1967.
- [Bet98] John T. Betts. “Survey of Numerical Methods for Trajectory Optimization.” In: *J. Guid. Control. Dyn.* 21.2 (1998), pp. 193–207. ISSN: 0731-5090. DOI: [10.2514/2.4231](https://doi.org/10.2514/2.4231).
- [Bet10] John T. Betts. *Practical Methods for Optimal Control and Estimation Using Nonlinear Programming*. 2010, p. 434. ISBN: 9780898716887. DOI: [10.1137/1.9780898718577](https://doi.org/10.1137/1.9780898718577).

- [BG02] John T Betts and Joerg M Gablonsky. "A Comparison of Interior Point and SQP Methods on Optimal Control Problems." In: *Science (80-.)*. March (2002).
- [Bv88] Maarten F. Bobbert and Gerrit Jan van Ingen Schenau. "Coordination in vertical jumping." In: *J. Biomech.* 21.3 (1988), pp. 249–262. ISSN: 00219290. DOI: [10.1016/0021-9290\(88\)90175-3](https://doi.org/10.1016/0021-9290(88)90175-3). arXiv: 178.
- [BK00] A Bowling and O Khatib. "Robot acceleration capability: the actuation efficiency measure." In: *Robot. Autom. 2000. Proceedings. ICRA '00. IEEE Int. Conf.* 4. April (2000), 3970–3975 vol.4. ISSN: 0-7803-5886-4. DOI: [10.1109/ROBOT.2000.845350](https://doi.org/10.1109/ROBOT.2000.845350).
- [Bow05] Alan Bowling. "Mobility and dynamic performance of legged robots." In: *Proc. - IEEE Int. Conf. Robot. Autom.* 2005. April (2005), pp. 4100–4107. ISSN: 10504729. DOI: [10.1109/ROBOT.2005.1570749](https://doi.org/10.1109/ROBOT.2005.1570749).
- [BK95] Alan Bowling and Oussama Khatib. "Analysis of the acceleration of non-redundant manipulators." In: *Intell. Robot. Syst. 95. 'Human Robot Interact. Coop. Robot. Proceedings. 1995 IEEE/RSJ Int. Conf.* Vol. 2. 1995, 323–328 vol.2. ISBN: 0818671084. DOI: [10.1109/IR0S.1995.526236](https://doi.org/10.1109/IR0S.1995.526236).
- [BK98] Alan Bowling and Oussama Khatib. "Modular Redundant Manipulator Design for Dynamic Performance." In: *Courses Lect. Cent. Mech. Sci.* (1998), pp. 297–308. URL: <http://pdf.aminer.org/000/351/212/dynamic{performance}{analysis}{for}{non}{redundant}{robotic}{manipulators}{in}{contact}.pdf>.
- [BK03] Alan Bowling and Oussama Khatib. "Dynamic loading criteria in actuator selection for desired dynamic performance." In: *Adv. Robot.* 17.7 (2003), pp. 641–656. ISSN: 01691864. DOI: [10.1163/156855303769156992](https://doi.org/10.1163/156855303769156992).
- [BK05] Alan Bowling and Oussama Khatib. "The dynamic capability equations: a new tool for analyzing robotic manipulator performance." In: *IEEE Trans. Robot.* 21.1 (2005), pp. 115–123. ISSN: 1552-3098. DOI: [10.1109/TR0.2004.837243](https://doi.org/10.1109/TR0.2004.837243). URL: <http://ieeexplore.ieee.org/lpdocs/epic03/wrapper.htm?arnumber=1391020>.
- [Bry75] Arthur Earl Bryson. *Applied optimal control: optimization, estimation and control*. New York, 1975.
- [BII06] Jonas Buchli, Fumiya Iida, and Auke Jan Ijspeert. "Finding resonance: Adaptive frequency oscillators for dynamic legged locomotion." In: *IEEE Int. Conf. Intell. Robot. Syst.* (2006), pp. 3903–3909. DOI: [10.1109/IR0S.2006.281802](https://doi.org/10.1109/IR0S.2006.281802).

- [BL05] Francesco Bullo and Andrew D. Lewis. *Geometric Control of Mechanical Systems*. Springer New York, 2005, p. 727.
- [BB18] David Busson and Richard Bearee. "A Pragmatic Approach to Exploiting Full Force Capacity for Serial Redundant Manipulators." In: *IEEE Robot. Autom. Lett.* 3.2 (2018), pp. 888–894. ISSN: 2377-3766. DOI: [10.1109/LRA.2018.2792541](https://doi.org/10.1109/LRA.2018.2792541). URL: <http://ieeexplore.ieee.org/document/8255624/>.
- [CI06] G Cappellini and Yp Ivanenko. "Motor patterns in human walking and running." In: *J. Neurophysiol.* (2006), pp. 3426–3437. ISSN: 0022-3077. DOI: [10.1152/jn.00081.2006](https://doi.org/10.1152/jn.00081.2006). URL: <http://jn.physiology.org/content/95/6/3426.short>.
- [CPN14] Stephane Caron, Quang Cuong Pham, and Yoshihiko Nakamura. "Completeness of randomized kinodynamic planners with state-based steering." In: *Proc. - IEEE Int. Conf. Robot. Autom.* (2014), pp. 5818–5823. ISSN: 10504729. DOI: [10.1109/ICRA.2014.6907714](https://doi.org/10.1109/ICRA.2014.6907714).
- [Chao0] J.H. Challis. *Biomechanics in Sport*. Ed. by Vladimir M. Zatsiorsky. October. Oxford, UK: Blackwell Science Ltd, 2000, pp. 33–55. ISBN: 9780470693797. DOI: [10.1002/9780470693797](https://doi.org/10.1002/9780470693797). URL: <http://doi.wiley.com/10.1002/9780470693797.ch3><http://doi.wiley.com/10.1002/9780470693797>.
- [Che+08] Kuangyou B. Cheng, Chih Hung Wang, Hui Chuan Chen, Chin Dai Wu, and Hung Ta Chiu. "The mechanisms that enable arm motion to enhance vertical jump performance—A simulation study." In: *J. Biomech.* 41.9 (2008), pp. 1847–1854. ISSN: 00219290. DOI: [10.1016/j.jbiomech.2008.04.004](https://doi.org/10.1016/j.jbiomech.2008.04.004).
- [Chi+91] P. Chiacchio, S. Chiaverini, L. Sciavicco, and B. Siciliano. "Reformulation of dynamic manipulability ellipsoid for robotic manipulators." In: *Proceedings. 1991 IEEE Int. Conf. Robot. Autom.* IEEE Comput. Soc. Press, 1991, pp. 2192–2197. ISBN: 0-8186-2163-X. DOI: [10.1109/ROBOT.1991.131955](https://doi.org/10.1109/ROBOT.1991.131955). URL: <http://ieeexplore.ieee.org/document/131955/>.
- [CBVP97] Pasquale Chiacchio, Yann Bouffard-Vercelli, and François Pierrot. "Force polytope and force ellipsoid for redundant manipulators." In: *J. Robot. Syst.* 14.8 (1997), pp. 613–620. ISSN: 07412223. DOI: [10.1002/\(SICI\)1097-4563\(199708\)14:8<613::AID-ROB3>3.0.CO;2-P](https://doi.org/10.1002/(SICI)1097-4563(199708)14:8<613::AID-ROB3>3.0.CO;2-P).
- [Chi88] Stephen L. Chiu. "Task compatibility of manipulator postures." In: *Int. J. Rob. Res.* 7.5 (1988), pp. 13–21. ISSN: 02783649. DOI: [10.1177/027836498800700502](https://doi.org/10.1177/027836498800700502).

- [Colo5] Steve Collins. "Efficient Bipedal Robots Based on Passive-Dynamic Walkers." In: *Science* (80-.). 307.5712 (2005), pp. 1082–1085. ISSN: 0036-8075. DOI: [10.1126/science.1107799](https://doi.org/10.1126/science.1107799). URL: <http://www.sciencemag.org/cgi/doi/10.1126/science.1107799>.
- [CAK09] Steven H Collins, Peter G Adamczyk, and Arthur D Kuo. "Dynamic arm swinging in human walking." In: *Proc. R. Soc. B Biol. Sci.* 276.1673 (2009), pp. 3679–3688. ISSN: 0962-8452. DOI: [10.1098/rspb.2009.0664](https://doi.org/10.1098/rspb.2009.0664). arXiv: [1010.2247](https://arxiv.org/abs/1010.2247). URL: <http://rspb.royalsocietypublishing.org/cgi/doi/10.1098/rspb.2009.0664>.
- [CFM10] Sebastien Cotton, Philippe Fraisse, and Andrew P. Murray. "On the Manipulability of the Center of Mass of Humanoid Robots: Application to Design." In: *Proc. ASME 2010 Int. Des. Eng. Tech. Conf. Comput. Inf. Eng. Conf.* (2010), pp. 1259–1267. DOI: [10.1115/DETC2010-28162](https://doi.org/10.1115/DETC2010-28162).
- [DVT14] Hongkai Dai, Andres Valenzuela, and Russ Tedrake. "Whole-body Motion Planning with Simple Dynamics and Full Kinematics." In: *Int. Conf. Humanoid Robot.* (2014), pp. 295–302. DOI: [10.1109/HUMANOIDS.2014.7041375](https://doi.org/10.1109/HUMANOIDS.2014.7041375).
- [Dicoo] M. H. Dickinson. "How Animals Move: An Integrative View." In: *Science* (80-.). 288.5463 (2000), pp. 100–106. ISSN: 00368075. DOI: [10.1126/science.288.5463.100](https://doi.org/10.1126/science.288.5463.100). URL: <http://www.sciencemag.org/cgi/doi/10.1126/science.288.5463.100>.
- [DP96] K van den Doel and D K Pai. "Performances Measures for Robot Manipulators: A Unified Approach." In: *Int. J. Rob. Res.* 15.1 (1996), pp. 91–111.
- [DDK05] Jiro Doke, J Maxwell Donelan, and Arthur D Kuo. "Mechanics and energetics of swinging the human leg." In: *J. Exp. Biol.* 208.Pt 3 (2005), pp. 439–445. ISSN: 0022-0949. DOI: [10.1242/jeb.01408](https://doi.org/10.1242/jeb.01408).
- [Don93] P. Donald, B. and Xavier. "Kinodynamic Motion Planning." In: *IEEE Robot. Autom. Mag.* 17.1 (1993), pp. 1048–1066. ISSN: 1070-9932. DOI: [10.1109/MRA.2010.935794](https://doi.org/10.1109/MRA.2010.935794).
- [DS09] Vincent Duindam and Stefano Stramigioli. *Modeling and Control for Efficient Bipedal Walking Robots*. 2009. ISBN: 9783540899174. DOI: [10.1007/978-3-540-89918-1](https://doi.org/10.1007/978-3-540-89918-1). URL: <http://www.springer.com/engineering/robotics/book/978-3-540-89917-4>.
- [FH85] T Flash and N Hogan. "The coordination of arm movements: an experimentally confirmed mathematical model." In: *J. Neurosci.* 5.7 (1985), pp. 1688–1703. ISSN: 0270-6474.

- DOI: 4020415. URL: <http://www.ncbi.nlm.nih.gov/pubmed/4020415>.
- [Foe+17] Philipp Foehn, Davide Falanga, Naveen Kuppaswamy, Russ Tedrake, and Davide Scaramuzza. "Fast Trajectory Optimization for Agile Quadrotor Maneuvers with a Cable-Suspended Payload." In: *Robot. Sci. Syst. XIII* i (2017). DOI: 10.15607/RSS.2017.XIII.030. URL: <http://www.roboticsproceedings.org/rss13/p30.pdf>.
- [FKCo3] Yasuhiro Fukuoka, Hiroshi Kimura, and Avis H. Cohen. "Adaptive Dynamic Walking of a Quadruped Robot on Irregular Terrain Based on Biological Concepts." In: *Int. J. Rob. Res.* 22.3-4 (2003), pp. 187–202. ISSN: 0278-3649. DOI: 10.1177/0278364903022003004. URL: <http://journals.sagepub.com/doi/10.1177/0278364903022003004>.
- [GMS02] Philip E. Gill, Walter Murray, and Michael A. Saunders. "SNOPT: An SQP Algorithm for Large-Scale Constrained Optimization." In: *SIAM J. Optim.* 12.4 (2002), pp. 979–1006. ISSN: 1052-6234. DOI: 10.1137/S1052623499350013. arXiv: 17444372724. URL: <http://epubs.siam.org/doi/abs/10.1137/S1052623499350013>.
- [GPS07] H Goldstein, C Poole, and J Safko. *Classical Mechanics*. 2007. URL: <papers://6d732309-80c9-4f91-90fd-4ffdb7258f93/Paper/p6006>.
- [GR05] Mario W. Gomes and Andy L. Ruina. "A five-link 2D brachiating ape model with life-like zero-energy-cost motions." In: *J. Theor. Biol.* 237.3 (2005), pp. 265–278. ISSN: 00225193. DOI: 10.1016/j.jtbi.2005.04.014.
- [Gos+14] Ambarish Goswami, Seung Kook Yun, Umashankar Nagarajan, Sung Hee Lee, Kangkang Yin, and Shivaram Kalyanakrishnan. "Direction-changing fall control of humanoid robots: Theory and experiments." In: *Auton. Robots* 36.3 (2014), pp. 199–223. ISSN: 09295593. DOI: 10.1007/s10514-013-9343-2.
- [GK88] Timothy J. Graettinger and Bruce H. Krogh. "The Acceleration Radius: A Global Performance Measure for Robotic Manipulators." In: *IEEE J. Robot. Autom.* 4.1 (1988), pp. 60–69. ISSN: 08824967. DOI: 10.1109/56.772.
- [Hal+16] Duncan W. Haldane, M. M. Plecnik, J. K. Yim, and R. S. Fearing. "Robotic vertical jumping agility via series-elastic power modulation." In: *Sci. Robot.* 1.1 (2016), eaag2048. ISSN: 2470-9476. DOI: 10.1126/scirobotics.aag2048. URL: <http://robotics.sciencemag.org/lookup/doi/10.1126/scirobotics.aag2048>.

- [HM90] John Hauser and Richard M. Murray. “Nonlinear controllers for non-integrable systems: the Acrobot example.” In: *1990 Am. Control Conf.* 1 (1990), pp. 669–671. ISSN: 07431619.
- [Hau14] Kris Hauser. “Fast interpolation and time-optimization with contact.” In: *Int. J. Rob. Res.* 33.9 (2014), pp. 1231–1250. ISSN: 0278-3649. DOI: [10.1177/0278364914527855](https://doi.org/10.1177/0278364914527855). URL: <http://ijr.sagepub.com/content/33/9/1231.abstract>.
- [HNTH10] Kris Hauser and Victor Ng-Thow-Hing. “Fast smoothing of manipulator trajectories using optimal bounded-acceleration shortcuts.” In: *Proc. - IEEE Int. Conf. Robot. Autom.* (2010), pp. 2493–2498. ISSN: 10504729. DOI: [10.1109/ROBOT.2010.5509683](https://doi.org/10.1109/ROBOT.2010.5509683).
- [HZ16] Kris Hauser and Yilun Zhou. “Asymptotically Optimal Planning by Feasible Kinodynamic Planning in a State-Cost Space.” In: *IEEE Trans. Robot.* (2016), pp. 1–13. ISSN: 15523098. DOI: [10.1109/TR0.2016.2602363](https://doi.org/10.1109/TR0.2016.2602363). arXiv: [1505.04098](https://arxiv.org/abs/1505.04098).
- [Hee+17] Nicolas Heess et al. “Emergence of Locomotion Behaviours in Rich Environments.” In: (2017). arXiv: [1707.02286](https://arxiv.org/abs/1707.02286). URL: <http://arxiv.org/abs/1707.02286>.
- [Her+16] Alexander Herzog, Nicholas Rotella, Sean Mason, Felix Grimminger, Stefan Schaal, and Ludovic Righetti. “Momentum control with hierarchical inverse dynamics on a torque-controlled humanoid.” In: *Auton. Robots* 40.3 (2016), pp. 473–491. ISSN: 15737527. DOI: [10.1007/s10514-015-9476-6](https://doi.org/10.1007/s10514-015-9476-6). arXiv: [1410.7284](https://arxiv.org/abs/1410.7284).
- [HY16] Michael J. Hiley and Maurice R. Yeadon. “What governs successful performance of a complex whole body movement: The Kovacs release-regrasp on horizontal bar?” In: *J. Biomech.* 49.16 (2016), pp. 3971–3976. ISSN: 18732380. DOI: [10.1016/j.jbiomech.2016.11.048](https://doi.org/10.1016/j.jbiomech.2016.11.048).
- [Hsu+02] D. Hsu, R. Kindel, J.-C. Latombe, and S. Rock. “Randomized Kinodynamic Motion Planning with Moving Obstacles.” In: *Int. J. Rob. Res.* 21.3 (2002), pp. 233–255. ISSN: 0278-3649. DOI: [10.1177/027836402320556421](https://doi.org/10.1177/027836402320556421).
- [Hub+16] Christian M Hubicki, Ayonga Hereid, Michael X Grey, Andrea L Thomaz, and Aaron D Ames. “Work those arms: Toward dynamic and stable humanoid walking that optimizes full-body motion.” In: *2016 IEEE Int. Conf. Robot. Autom.* IEEE, 2016, pp. 1552–1559. ISBN: 978-1-4673-8026-3. DOI: [10.1109/ICRA.2016.7487293](https://doi.org/10.1109/ICRA.2016.7487293). URL: <http://ieeexplore.ieee.org/document/7487293/>.

- [Ibu+15] T Ibuki, M Sampei, A Ishikawa, and S Nakaura. "Jumping Motion Control for 4-Link Robot Based on Virtual Constraint on Underactuated Joint." In: *Sc.Ctrl.Titech.Ac.Jp* (2015), pp. 1–6. URL: http://www.sc.ctrl.titech.ac.jp/~ibuki/paper/IINS__ASCC15.pdf.
- [Ijs08] Auke Jan Ijspeert. "Central pattern generators for locomotion control in animals and robots: A review." In: *Neural Networks* 21.4 (2008), pp. 642–653. ISSN: 08936080. DOI: [10.1016/j.neunet.2008.03.014](https://doi.org/10.1016/j.neunet.2008.03.014). arXiv: [NIHMS150003](https://arxiv.org/abs/NIHMS150003).
- [Ijs+07] Auke Jan Ijspeert, Alessandro Crespi, Dimitri Ryczko, and J.-M. Cabelguen. "From Swimming to Walking with a Salamander Robot Driven by a Spinal Cord Model." In: *Science (80-.)*. 315.5817 (2007), pp. 1416–1420. ISSN: 0036-8075. DOI: [10.1126/science.1138353](https://doi.org/10.1126/science.1138353). URL: <http://www.sciencemag.org/cgi/doi/10.1126/science.1138353>.
- [Iva05] Y. P. Ivanenko. "Coordination of Locomotion with Voluntary Movements in Humans." In: *J. Neurosci.* 25.31 (2005), pp. 7238–7253. ISSN: 0270-6474. DOI: [10.1523/JNEUROSCI.1327-05.2005](https://doi.org/10.1523/JNEUROSCI.1327-05.2005). URL: <http://www.jneurosci.org/cgi/doi/10.1523/JNEUROSCI.1327-05.2005>.
- [Jeo15] Jeong hwan Jeon. "Sampling-Based Motion Planning Algorithms for Dynamical Systems." Ph. D. Thesis. Massachusetts Institute of Technology, 2015.
- [Kaj+03] S. Kajita, F. Kanehiro, K. Kaneko, K. Fujiwara, K. Harada, K. Yokoi, and H. Hirukawa. "Resolved momentum control: humanoid motion planning based on the linear and angular momentum." In: *Proc. 2003 IEEE/RSJ Int. Conf. Intell. Robot. Syst. (IROS 2003) (Cat. No.03CH37453)*. Vol. 2. October. IEEE, 2003, pp. 1644–1650. ISBN: 0-7803-7860-1. DOI: [10.1109/IROS.2003.1248880](https://doi.org/10.1109/IROS.2003.1248880). URL: <http://ieeexplore.ieee.org/document/1248880/>.
- [Kav12] Lydia E Kavraki. "A Sampling-Based Tree Planner for Systems with Complex Dynamics." In: 131 (2012), pp. 116–131.
- [Kha87] Oussama Khatib. *A unified approach for motion and force control of robot manipulators: The operational space formulation*. 1987. DOI: [10.1109/JRA.1987.1087068](https://doi.org/10.1109/JRA.1987.1087068). URL: http://ieeexplore.ieee.org/ielx5/56/23635/01087068.pdf?tp=*&arnumber=1087068*&isnumber=23635*\%5Cnhttp://ieeexplore.ieee.org/xpls/abs__all.jsp?arnumber=1087068.
- [Kha95] Oussama Khatib. "Inertial Properties in Robotic Manipulation: An Object Level Framework." In: *Int. J. Rob. Res.* 13.1 (1995), pp. 19–36.

- [Kir12] Donald E. Kirk. *Optimal control theory: An introduction*. Courier Corporation, 2012.
- [Kob+15] Taisuke Kobayashi, Kosuke Sekiyama, Tadayoshi Aoyama, Yasuhisa Hasegawa, and Toshio Fukuda. “Optimal use of arm-swing for bipedal walking control.” In: *Proc. - IEEE Int. Conf. Robot. Autom.* Vol. 2015-June. June. 2015, pp. 5698–5703. ISBN: VO -. DOI: [10.1109/ICRA.2015.7139997](https://doi.org/10.1109/ICRA.2015.7139997).
- [KBo8] Tamara G. Kolda and Brett W. Bader. “Tensor Decompositions and Applications.” In: *SIAM Rev.* 51.3 (2008), pp. 455–500. ISSN: 0036-1445. DOI: [10.1137/07070111X](https://doi.org/10.1137/07070111X). URL: <http://epubs.siam.org/doi/abs/10.1137/07070111X>.
- [KANo8] J Zico Kolter, Pieter Abbeel, and Andrew Y Ng. “Hierarchical Apprenticeship Learning , with Application to Quadruped Locomotion.” In: *Science (80-.)*. 1 (2008), pp. 1–8. URL: <http://www.robotics.stanford.edu/~ang/papers/nips07-hierarchicalapprenticeshiplearning.pdf>.
- [Kon+14] K. Kondak, F. Huber, M. Schwarzbach, M. Laiacker, D. Sommer, M. Bejar, and A. Ollero. “Aerial manipulation robot composed of an autonomous helicopter and a 7 degrees of freedom industrial manipulator.” In: *Proc. - IEEE Int. Conf. Robot. Autom.* (2014), pp. 2107–2112. ISSN: 10504729. DOI: [10.1109/ICRA.2014.6907148](https://doi.org/10.1109/ICRA.2014.6907148).
- [Kov+08] Mirko Kovač, Martin Fuchs, André Guignard, Jean Christophe Zufferey, and Dario Floreano. “A miniature 7g jumping robot.” In: *Proc. - IEEE Int. Conf. Robot. Autom.* c (2008), pp. 373–378. ISSN: 10504729. DOI: [10.1109/ROBOT.2008.4543236](https://doi.org/10.1109/ROBOT.2008.4543236).
- [Kre89] Kenneth Kreutz. “On manipulator control by exact linearization.” In: *IEEE Trans. Automat. Contr.* 34.7 (1989), pp. 763–767. ISSN: 00189286. DOI: [10.1109/9.29408](https://doi.org/10.1109/9.29408). URL: <http://ieeexplore.ieee.org/document/29408/>.
- [KT51] H. W. Kuhn and A.W Tucker. “Nonlinear Programming.” In: *Proc. Second Symp. Math. Stat. Probab.* x (1951), pp. 481–492. ISSN: 01605682. DOI: [10.1007/BF01582292](https://doi.org/10.1007/BF01582292). URL: <http://projecteuclid.org/euclid.bsm/1200500249>.
- [KS14] Tobias Kunz and Mike Stilman. “Probabilistically complete kinodynamic planning for robot manipulators with acceleration limits.” In: *IEEE Int. Conf. Intell. Robot. Syst.* (2014), pp. 3713–3719. ISSN: 21530866. DOI: [10.1109/IRoS.2014.6943083](https://doi.org/10.1109/IRoS.2014.6943083).

- [KH06] Ryo Kurazume and Tsutomu Hasegawa. "A new index of serial-link manipulator performance combining dynamic manipulability and manipulating force ellisoids." In: *IEEE Trans. Robot.* 22.5 (2006), pp. 1022–1028. ISSN: 15523098. DOI: [10.1109/TR0.2006.878949](https://doi.org/10.1109/TR0.2006.878949).
- [LaVo1] Steven M. LaValle. "Randomized Kinodynamic Planning." In: *Int. J. Rob. Res.* 20.5 (2001), pp. 378–400. ISSN: 0278-3649. DOI: [10.1177/02783640122067453](https://doi.org/10.1177/02783640122067453). arXiv: [arXiv: 1011.1669v3](https://arxiv.org/abs/1011.1669v3). URL: <http://ijr.sagepub.com/cgi/content/abstract/20/5/378><http://ijr.sagepub.com/cgi/doi/10.1177/02783640122067453>.
- [LDo6] Simon. Lam and E.J. Davison. "The real stabilizability radius of the multi-link inverted pendulum." In: *Am. Control Conf. 2006* 2 (2006), pp. 1814–1819. ISSN: 07431619. DOI: [10.1109/ACC.2006.1656483](https://doi.org/10.1109/ACC.2006.1656483). URL: <http://ieeexplore.ieee.org/stamp/stamp.jsp?tp={\&}arnumber=1656483{\%}5Cnhttp://ieeexplore.ieee.org/lpdocs/epic03/wrapper.htm?arnumber=1656483>.
- [LMH10] Martin de Lasa, Igor Mordatch, and Aaron Hertzmann. "Feature-based locomotion controllers." In: *ACM Trans. Graph.* 29.4 (2010), p. 1. ISSN: 07300301. DOI: [10.1145/1833351.1781157](https://doi.org/10.1145/1833351.1781157).
- [Lau98] Jean-Paul P. Laumond. *Robot Motion Planning and Control*. Springer-Verlag New York, Inc., 1998. ISBN: 3540762191.
- [LGo7] Sung Hee Lee and Ambarish Goswami. "Reaction Mass Pendulum (RMP): An explicit model for centroidal angular momentum of humanoid robots." In: *Proc. - IEEE Int. Conf. Robot. Autom.* April (2007), pp. 4667–4672. ISSN: 10504729. DOI: [10.1109/ROBOT.2007.364198](https://doi.org/10.1109/ROBOT.2007.364198).
- [LB10] Yanbo Li and Kostas E. Bekris. "Balancing state-space coverage in planning with dynamics." In: *Proc. - IEEE Int. Conf. Robot. Autom.* (2010), pp. 3246–3253. ISSN: 10504729. DOI: [10.1109/ROBOT.2010.5509481](https://doi.org/10.1109/ROBOT.2010.5509481).
- [LLB16] Yanbo Li, Zakary Littlefield, and Kostas E Bekris. "Asymptotically optimal sampling-based kinodynamic planning." In: *Int. J. Rob. Res.* 35.5 (2016), pp. 528–564. ISSN: 0278-3649. DOI: [10.1177/0278364915614386](https://doi.org/10.1177/0278364915614386). arXiv: [1407.2896](https://arxiv.org/abs/1407.2896). URL: <http://mms.sagepub.comhttp://journals.sagepub.com/doi/10.1177/0278364915614386>.
- [Lib+12] Thomas Libby, Talia Y. Moore, Evan Chang-Siu, Deborah Li, Daniel J. Cohen, Ardian Jusufi, and Robert J. Full. "Tail-assisted pitch control in lizards, robots and dinosaurs." In: *Nature* 481.7380 (2012), pp. 181–184. ISSN: 0028-0836. DOI: [10.1038/nature10710](https://doi.org/10.1038/nature10710). URL: <http://>

- www.nature.com/nature/journal/v481/n7380/abs/nature10710.html{\%}5Cnhttp://www.nature.com/nature/journal/v481/n7380/pdf/nature10710.pdf.
- [Lil+15] Timothy P. Lillicrap, Jonathan J. Hunt, Alexander Pritzel, Nicolas Heess, Tom Erez, Yuval Tassa, David Silver, and Daan Wierstra. “Continuous control with deep reinforcement learning.” In: *Found. Trends® Mach. Learn.* 2.1 (2015), pp. 1–127. ISSN: 1935-8237. DOI: [arXiv:1509.02971](https://doi.org/10.1109/IROS.2013.6696590). arXiv: [1509.02971](https://arxiv.org/abs/1509.02971). URL: <http://www.nowpublishers.com/article/Details/MAL-006><http://arxiv.org/abs/1509.02971>.
- [LLB13] Zakary Littlefield, Yanbo Li, and Kostas E Bekris. “Efficient Sampling-based Motion Planning with Asymptotic Near-Optimality Guarantees for Systems with Dynamics.” In: (2013), pp. 1779–1785. DOI: [10.1109/IROS.2013.6696590](https://doi.org/10.1109/IROS.2013.6696590).
- [LS02] Tzon-Tzer Lu and Sheng-Hua Shiou. “Inverses of 2×2 block matrices.” In: *Comput. Math. with Appl.* 43.1-2 (2002), pp. 119–129. ISSN: 08981221. DOI: [10.1016/S0898-1221\(01\)00278-4](https://doi.org/10.1016/S0898-1221(01)00278-4). URL: <http://linkinghub.elsevier.com/retrieve/pii/S0898122101002784>.
- [LO02] Alessandro De Luca and Giuseppe Oriolo. “Trajectory Planning and Control for Planar Robots with Passive Last Joint.” In: *Int. J. Rob. Res.* 21.5-6 (2002), pp. 575–590. ISSN: 0278-3649. DOI: [10.1177/027836402321261940](https://doi.org/10.1177/027836402321261940).
- [MZS09] Adriano Macchietto, Victor Zordan, and Christian R. Shelton. “Momentum control for balance.” In: *ACM SIGGRAPH 2009 Pap. - SIGGRAPH '09* (2009), p. 1. ISSN: 07300301. DOI: [10.1145/1576246.1531386](https://doi.org/10.1145/1576246.1531386). arXiv: [arXiv:1011.1669v3](https://arxiv.org/abs/1011.1669v3). URL: <http://portal.acm.org/citation.cfm?doid=1576246.1531386>.
- [McG90] T McGeer. *Passive Dynamic Walking*. 1990. DOI: [10.1177/027836499000900206](https://doi.org/10.1177/027836499000900206). URL: <http://dx.doi.org/10.1177/027836499000900206>.
- [MBD13] Pieter Meyns, Sjoerd M. Bruijn, and Jacques Duysens. “The how and why of arm swing during human walking.” In: *Gait Posture* 38.4 (2013), pp. 555–562. ISSN: 09666362. DOI: [10.1016/j.gaitpost.2013.02.006](https://doi.org/10.1016/j.gaitpost.2013.02.006). URL: <http://dx.doi.org/10.1016/j.gaitpost.2013.02.006>.
- [MR12] Michael Mistry and Ludovic Righetti. “Operational Space Control of Constrained and Underactuated Systems.” In: *Robot. Sci. Syst. VII* (2012), pp. 225–232. URL: <http://www.roboticsproceedings.org/rss07/p31.pdf>{\%}5Cnhttp:

- [//ieeexplore.ieee.org/xpl/bkabstractplus.jsp?bkn=6276859](http://ieeexplore.ieee.org/xpl/bkabstractplus.jsp?bkn=6276859).
- [Mni+15] Volodymyr Mnih et al. "Human-level control through deep reinforcement learning." In: *Nature* 518.7540 (2015), pp. 529–533. ISSN: 0028-0836. DOI: [10.1038/nature14236](https://doi.org/10.1038/nature14236). arXiv: [1312.5602](https://arxiv.org/abs/1312.5602). URL: <http://www.nature.com/articles/nature14236>.
- [MTL10] Katja Mombaur, Anh Truong, and Jean Paul Laumond. "From human to humanoid locomotion-an inverse optimal control approach." In: *Auton. Robots* 28.3 (2010), pp. 369–383. ISSN: 09295593. DOI: [10.1007/s10514-009-9170-7](https://doi.org/10.1007/s10514-009-9170-7).
- [MLS94] Richard M Murray, Zexiang Li, and S Shankar Sastry. *A Mathematical Introduction to Robotic Manipulation*. Vol. 29. 2. CRC Press, 1994, p. 480. ISBN: 9780849379819. DOI: [10.1.1.169.3957](https://doi.org/10.1.1.169.3957). URL: <http://scholar.google.com/scholar?hl=en&btnG=Search&q=intitle:A+Mathematical+Introduction+to+Robotic+Manipulation>{\#}0.
- [NLo6] Nirut Naksuk and C. S. George Lee. "Zero moment point manipulability ellipsoid." In: *Proc. - IEEE Int. Conf. Robot. Autom.* 2006.May (2006), pp. 1970–1975. ISSN: 10504729. DOI: [10.1109/ROBOT.2006.1641994](https://doi.org/10.1109/ROBOT.2006.1641994).
- [Nis+12] Jumpei Nishiguchi, Mamoru Minami, Akira Yanou, Takayuki Matsuno, and Tomohide Maeba. "Analyses of Jumping Motion of Humanoid Robot Using Arms ' Swinging." In: (2012), pp. 496–501.
- [NNGo6] Victor Nunez and Nelly Nadjar-Gauthier. "Humanoid vertical jump with compliant contact." In: *Proc. 8th Int. Conf. Climbing Walk. Robot. Support Technol. Mob. Mach. CLAWAR 2005*. 2006, pp. 457–464. ISBN: 3540264132. DOI: [10.1007/3-540-26415-9-55](https://doi.org/10.1007/3-540-26415-9-55).
- [OSo1] Reza Olfati-Saber. "Nonlinear Control of Underactuated Mechanical Systems with Application to Robotics and Aerospace Vehicles." In: (2001), p. 307.
- [OGO8] David E Orin and Ambarish Goswami. "Centroidal momentum matrix of a humanoid robot: Structure and properties." In: *2008 IEEE/RSJ Int. Conf. Intell. Robot. Syst. IROS*. 2008, pp. 653–659. ISBN: 9781424420582. DOI: [10.1109/IROS.2008.4650772](https://doi.org/10.1109/IROS.2008.4650772).
- [OGL13] David E. Orin, Ambarish Goswami, and Sung-Hee Lee. "Centroidal dynamics of a humanoid robot." In: *Auton. Robots* 35.2-3 (2013), pp. 161–176. ISSN: 0929-5593. DOI: [10.1007/s10514-013-9170-7](https://doi.org/10.1007/s10514-013-9170-7).

- 1007/s10514-013-9341-4. URL: <http://link.springer.com/10.1007/s10514-013-9341-4>.
- [ON91] Giuseppe Oriolo and Y. Nakamura. "Control of mechanical systems with second-order nonholonomic constraints: underactuated manipulators." In: [1991] *Proc. 30th IEEE Conf. Decis. Control*. IEEE, 1991, pp. 2398–2403. ISBN: 0-7803-0450-0. DOI: 10.1109/CDC.1991.261620. URL: <http://ieeexplore.ieee.org/document/261620/>.
- [OT15] Satomi Oshima and Motoko Taguchi. "Sports Performance." In: *Sport. Perform.* (2015), pp. 139–150. DOI: 10.1007/978-4-431-55315-1. URL: <http://www.scopus.com/inward/record.url?eid=2-s2.0-84955729802{\&}partnerID=tZ0tx3y1>.
- [PA15] Luigi Palmieri and Kai O Arras. "Distance Metric Learning for RRT-Based Motion Planning for Wheeled Mobile Robots." In: *Int. Conf. Robot. Autom.* 2015, pp. 637–643. ISBN: 9781479969234. DOI: 10.1109/ICRA.2015.7139246.
- [PKP14a] Georgios Papadopoulos, Hanna Kurniawati, and Nicholas M. Patrikalakis. "Analysis of Asymptotically Optimal Sampling-based Motion Planning Algorithms for Lipschitz Continuous Dynamical Systems." In: (2014). arXiv: 1405.2872. URL: <http://arxiv.org/abs/1405.2872>.
- [PKP14b] Georgios Papadopoulos, Hanna Kurniawati, and Nicolas M. Patrikalakis. "Analysis of Asymptotically Optimal Sampling-based Motion Planning Algorithms for Lipschitz Continuous Dynamical Systems." In: *arXiv Prepr. arXiv1405.2872* (2014). arXiv: arXiv:1405.2872v1.
- [PB15] Amir Patel and Edward Boje. "On the Conical Motion of a Two-Degree-of-Freedom Tail Inspired by the Cheetah." In: *IEEE Trans. Robot.* 31.6 (2015), pp. 1555–1560. ISSN: 1552-3098. DOI: 10.1109/TR0.2015.2495004. URL: <http://ieeexplore.ieee.org/document/7339741/>.
- [PB13] Amir Patel and M. Braae. "Rapid turning at high-speed: Inspirations from the cheetah's tail." In: *IEEE Int. Conf. Intell. Robot. Syst.* (2013), pp. 5506–5511. ISSN: 21530858. DOI: 10.1109/IR0S.2013.6697154.
- [PB14] Amir Patel and M Braae. "Rapid acceleration and braking: Inspirations from the cheetah's tail." In: *Proc. - IEEE Int. Conf. Robot. Autom.* IEEE, 2014, pp. 793–799. ISBN: 978-1-4799-3685-4. DOI: 10.1109/ICRA.2014.6906945. URL: <http://ieeexplore.ieee.org/lpdocs/epic03/wrapper.htm?arnumber=6906945>.

- [PS15] Sarosh Patel and Tarek Sobh. "Manipulator Performance Measures - A Comprehensive Literature Survey." In: *J. Intell. Robot. Syst.* 77.3-4 (2015), pp. 547–570. ISSN: 0921-0296. DOI: [10.1007/s10846-014-0024-y](https://doi.org/10.1007/s10846-014-0024-y). URL: <http://link.springer.com/10.1007/s10846-014-0024-y>.
- [Per+12] Alejandro Perez, Robert Platt, George Konidaris, Leslie Kaelbling, and Tomas Lozano-Perez. "LQR-RRT*: Optimal sampling-based motion planning with automatically derived extension heuristics." In: *2012 IEEE Int. Conf. Robot. Autom.* IEEE, 2012, pp. 2537–2542. ISBN: 978-1-4673-1405-3. DOI: [10.1109/ICRA.2012.6225177](https://doi.org/10.1109/ICRA.2012.6225177). URL: <http://ieeexplore.ieee.org/document/6225177/>.
- [Pla95] Robert R Playter. "Passive Dynamics in the Control of Gymnastic Maneuvers." PhD thesis. MASSACHUSETTS INSTITUTE OF TECHNOLOGY, 1995.
- [PHH04] Marko Popovic, Andreas Hofmann, and Hugh Herr. "Angular momentum regulation during human walking: biomechanics and control." In: *IEEE Int. Conf. Robot. Autom. 2004. Proceedings. ICRA '04. 2004.* IEEE, 2004, 2405–2411 Vol.3. ISBN: 0-7803-8232-3. DOI: [10.1109/ROBOT.2004.1307421](https://doi.org/10.1109/ROBOT.2004.1307421). URL: <https://pdfs.semanticscholar.org/9330/f59ea89ea0831accb40b049a28f477331dbe.pdf><http://ieeexplore.ieee.org/document/1307421/>.
- [PCT13] M. Posa, C. Cantu, and R. Tedrake. "A direct method for trajectory optimization of rigid bodies through contact." In: *Int. J. Rob. Res.* 33.1 (2013), pp. 69–81. ISSN: 0278-3649. DOI: [10.1177/0278364913506757](https://doi.org/10.1177/0278364913506757). URL: <http://ijr.sagepub.com/content/33/1/69.short>.
- [PPK74] Spiros G Prassas, College Park, and David L Kelley. "Mechanical Analysis of the Inverted Giant Swing." In: *Biomech. Sport II* (1974), pp. 218–226.
- [Pra00] Je Pratt. "Exploiting inherent robustness and natural dynamics in the control of bipedal walking robots." PhD thesis. Massachusetts Institute of Technology, 2000, pp. 1–157. ISBN: 0018-9286 VO - 48. DOI: [10.1109/TAC.2002.808489](https://doi.org/10.1109/TAC.2002.808489). URL: <http://oai.dtic.mil/oai/oai?verb=getRecord&metadataPrefix=html&identifier=ADA475455>.
- [Rai86] Marc H. Raibert. *Legged robots that balance*. Cambridge, MA, USA: Massachusetts Institute of Technology, 1986.
- [Rem11] C David Remy. "Optimal Exploitation of Natural Dynamics in Legged Locomotion." In: *PhD Diss., ETH Zurich* 19831 (2011). DOI: [10.3929/ethz-a-6665065](https://doi.org/10.3929/ethz-a-6665065).

- [Ren+15] Daniel Renjewski, Alexander Sprowitz, Andrew Peekema, Mikhail Jones, and Jonathan Hurst. "Exciting Engineered Passive Dynamics in a Bipedal Robot." In: *IEEE Trans. Robot.* 31.5 (2015), pp. 1244–1251. ISSN: 15523098. DOI: [10.1109/TR0.2015.2473456](https://doi.org/10.1109/TR0.2015.2473456).
- [RIo6] L Righetti and a J Ijspeert. "Programmable central pattern generators: an application to biped locomotion control." In: *Robot. Autom. 2006. ICRA 2006. Proc. 2006 IEEE Int. Conf.* May (2006), pp. 1585–1590. ISSN: 1050-4729. DOI: [10.1109/ROBOT.2006.1641933](https://doi.org/10.1109/ROBOT.2006.1641933).
- [RGo2] M T Rosenstein and R a Grupen. "Velocity-dependent dynamic manipulability." In: *Robot. Autom. 2002. Proceedings. ICRA '02. IEEE Int. Conf.* 3.2 (2002), pp. 2424–2429. DOI: [10.1109/ROBOT.2002.1013595](https://doi.org/10.1109/ROBOT.2002.1013595).
- [SYo5] Sophie Sakka and Kazuhito Yokoi. "Humanoid vertical jumping based on force feedback and inertial forces optimization." In: *Proc. - IEEE Int. Conf. Robot. Autom.* 2005 (2005), pp. 3752–3757. ISSN: 10504729. DOI: [10.1109/ROBOT.2005.1570692](https://doi.org/10.1109/ROBOT.2005.1570692).
- [SC82] J. Kenneth Salisbury and John J. Craig. "Articulated Hands: Force Control and Kinematic Issues." In: *Int. J. Rob. Res.* 1.1 (1982), pp. 4–17. ISSN: 17413176. DOI: [10.1177/027836498200100102](https://doi.org/10.1177/027836498200100102).
- [SSDo7] Umberto Scarfogliero, Cesare Stefanini, and Paolo Dario. "Design and Development of the Long-Jumping "Grillo" Mini Robot." In: *Proc. 2007 IEEE Int. Conf. Robot. Autom.* April. IEEE, 2007, pp. 467–472. ISBN: 1-4244-0602-1. DOI: [10.1109/ROBOT.2007.363830](https://doi.org/10.1109/ROBOT.2007.363830). URL: <http://ieeexplore.ieee.org/document/4209135/>.
- [SSo5] Stefan Schaal and Nicolas Schweighofer. "Computational motor control in humans and robots." In: *Curr. Opin. Neurobiol.* 15.6 (2005), pp. 675–682. ISSN: 09594388. DOI: [10.1016/j.conb.2005.10.009](https://doi.org/10.1016/j.conb.2005.10.009).
- [STo8] Alexander Shkolnik and Russ Tedrake. "High-dimensional underactuated motion planning via task space control." In: *2008 IEEE/RSJ Int. Conf. Intell. Robot. Syst. IROS (2008)*, pp. 3762–3768. DOI: [10.1109/IROS.2008.4651150](https://doi.org/10.1109/IROS.2008.4651150).
- [Spo95] Mark W. Spong. "Swing up control problem for the acrobot." In: *IEEE Control Syst. Mag.* 15.1 (1995), pp. 49–55. ISSN: 02721708. DOI: [10.1109/37.341864](https://doi.org/10.1109/37.341864).
- [Spo98] Mark W Spong. "Underactuated mechanical systems." In: *Control Probl. Robot. Autom. Springer (1998)*, pp. 135–150. DOI: [10.1007/BFb0015081](https://doi.org/10.1007/BFb0015081). URL: <http://www.springerlink.com/index/m3npk47uk3341510.pdf>.

- [SSo2] D. S.D. Stilling and W. Szyszkowski. "Controlling angular oscillations through mass reconfiguration: A variable length pendulum case." In: *Int. J. Non. Linear. Mech.* 37.1 (2002), pp. 89–99. ISSN: 00207462. DOI: [10.1016/S0020-7462\(00\)00099-8](https://doi.org/10.1016/S0020-7462(00)00099-8).
- [Swi+94] Stephan P. Swinnen, Jean MAssion, H. Heuer, and P. Casaer. "Interlimb Coordination: Neural, Dynamical, and Cognitive Constraints." In: (1994), p. 637.
- [TET12] Yuval Tassa, Tom Erez, and Emanuel Todorov. "Synthesis and stabilization of complex behaviors through on-line trajectory optimization." In: *IEEE Int. Conf. Intell. Robot. Syst.* (2012), pp. 4906–4913. ISSN: 21530858. DOI: [10.1109/IRoS.2012.6386025](https://doi.org/10.1109/IRoS.2012.6386025).
- [Ted16] Russ Tedrake. *Drake: A planning, control, and analysis toolbox for nonlinear dynamical systems*. 2016. URL: <http://drake.mit.edu>.
- [TBS10] Evangelos Theodorou, Jonas Buchli, and Stefan Schaal. "Reinforcement learning of motor skills in high dimensions: A path integral approach." In: *2010 IEEE Int. Conf. Robot. Autom.* 1.3 (2010), pp. 2397–2403. ISSN: 1050-4729. DOI: [10.1109/ROBOT.2010.5509336](https://doi.org/10.1109/ROBOT.2010.5509336). URL: <http://ieeexplore.ieee.org/document/5509336/>.
- [Todo4] Emanuel Todorov. "Optimality principles in sensorimotor control." In: *Nat. Neurosci.* 7.9 (2004), pp. 907–15. ISSN: 1097-6256. DOI: [10.1038/nn1309](https://doi.org/10.1038/nn1309). arXiv: [NIHMS150003](https://arxiv.org/abs/NIHMS150003). URL: <http://www.pubmedcentral.nih.gov/articlerender.fcgi?artid=1488877&tool=pmcentrez&rendertype=abstract>.
- [Tol+14] Michael T. Tolley, Robert F. Shepherd, Michael Karpelson, Nicholas W. Bartlett, Kevin C. Galloway, Michael Wehner, Rui Nunes, George M. Whitesides, and Robert J. Wood. "An untethered jumping soft robot." In: *IEEE Int. Conf. Intell. Robot. Syst. Iros* (2014), pp. 561–566. ISSN: 21530866. DOI: [10.1109/IRoS.2014.6942615](https://doi.org/10.1109/IRoS.2014.6942615).
- [TJ09] Matthew C. Tresch and Anthony Jarc. "The case for and against muscle synergies." In: *Curr. Opin. Neurobiol.* 19.6 (2009), pp. 601–607. ISSN: 09594388. DOI: [10.1016/j.conb.2009.09.002](https://doi.org/10.1016/j.conb.2009.09.002). arXiv: [NIHMS150003](https://arxiv.org/abs/NIHMS150003).
- [Tur90] Michael T. Turvey. "Coordination." In: *Am. Psychol.* 45.8 (1990), pp. 938–953. ISSN: 1935-990X. DOI: [10.1037/0003-066X.45.8.938](https://doi.org/10.1037/0003-066X.45.8.938). URL: <http://doi.apa.org/getdoi.cfm?doi=10.1037/0003-066X.45.8.938>.

- [Ugu+12] Barkan Ugurlu, Jody A Saglia, Nikos G Tsagarakis, and Darwin G Caldwell. "Hopping at the Resonance Frequency : A Trajectory Generation Technique for Bipedal Robots with Elastic Joints." In: (2012), pp. 1436–1443.
- [Ulz+08] Niek R. van Ulzen, Claudine J C Lamoth, Andreas Daffertshofer, Gün R. Semin, and Peter J. Beek. "Characteristics of instructed and uninstructed interpersonal coordination while walking side-by-side." In: *Neurosci. Lett.* 432.2 (2008), pp. 88–93. ISSN: 03043940. DOI: [10.1016/j.neulet.2007.11.070](https://doi.org/10.1016/j.neulet.2007.11.070).
- [Van+06] Bram Vanderborght, Björn Verrelst, Ronald Van Ham, Michaël Van Damme, Dirk Lefeber, Bruno Meira Y Duran, and Pieter Beyl. "Exploiting Natural Dynamics to Reduce Energy Consumption by Controlling the Compliance of Soft Actuators." In: *Int. J. Rob. Res.* 25.4 (2006), pp. 343–358. ISSN: 0278-3649. DOI: [10.1177/0278364906064566](https://doi.org/10.1177/0278364906064566). URL: <http://journals.sagepub.com/doi/10.1177/0278364906064566>.
- [VKHo9] B. W. Verdaasdonk, H. F. J. M. Koopman, and F. C. T. van der Helm. "Energy efficient walking with central pattern generators: from passive dynamic walking to biologically inspired control." In: *Biol. Cybern.* 101.1 (2009), pp. 49–61. ISSN: 0340-1200. DOI: [10.1007/s00422-009-0316-7](https://doi.org/10.1007/s00422-009-0316-7). URL: <http://link.springer.com/10.1007/s00422-009-0316-7>.
- [WBo6] Andreas Wachter and Lorenz T. Biegler. *On the implementation of an interior-point filter line-search algorithm for large-scale nonlinear programming*. Vol. 106. 1. 2006, pp. 25–57. ISBN: 1010700405. DOI: [10.1007/s10107-004-0559-y](https://doi.org/10.1007/s10107-004-0559-y).
- [Wan+01] T. Wannier, C. Bastiaanse, G. Colombo, and V. Dietz. "Arm to leg coordination in humans during walking, creeping and swimming activities." In: *Exp. Brain Res.* 141.3 (2001), pp. 375–379. ISSN: 00144819. DOI: [10.1007/s002210100875](https://doi.org/10.1007/s002210100875).
- [WO16] Patrick M Wensing and David E Orin. "Improved Computation of the Humanoid Centroidal Dynamics and Application for Whole-Body Control." In: *Int. J. Humanoid Robot.* 13.01 (2016), p. 1550039. ISSN: 0219-8436. DOI: [10.1142/S0219843615500395](https://doi.org/10.1142/S0219843615500395). URL: <http://www.worldscientific.com/doi/abs/10.1142/S0219843615500395>.
- [Wil99] Matthew M Williamson. "Robot Arm Control Exploiting Natural Dynamics." Phd thesis. Massachusetts Institute of Technology, 1999.

- [Win+18] Alexander Wayne Winkler, C. Dario Bellicoso, Marco Hutter, and Jonas Buchli. "Gait and Trajectory Optimization for Legged Systems through Phase-based End-Effector Parameterization." In: *IEEE Robot. Autom. Lett.* 3766.c (2018), pp. 1–1. ISSN: 2377-3766. DOI: [10.1109/LRA.2018.2798285](https://doi.org/10.1109/LRA.2018.2798285). URL: <http://ieeexplore.ieee.org/document/8283570/>.
- [WHo8] Sebastian Wolf and Gerd Hirzinger. "A new variable stiffness design: Matching requirements of the next robot generation." In: *Proc. - IEEE Int. Conf. Robot. Autom.* 2008, pp. 1741–1746. ISBN: 9781424416479. DOI: [10.1109/ROBOT.2008.4543452](https://doi.org/10.1109/ROBOT.2008.4543452).
- [Xin13] X Xin. "On simultaneous control of the energy and actuated variables of underactuated mechanical systems-example of the acrobot with counterweight." In: *Adv. Robot.* 27.12 (2013), pp. 959–969. ISSN: 01691864. DOI: [10.1080/01691864.2013.797145](https://doi.org/10.1080/01691864.2013.797145). URL: <http://www.scopus.com/inward/record.url?eid=2-s2.0-84879693363{\&}partnerID=40{\&}md5=b7aeac1bf2a324024375eb217767b4d>.
- [XKo7a] X. Xin and M. Kaneda. "Analysis of the energy-based swing-up control of the Acrobot." In: *Int. J. Robust Non-linear Control* 17.16 (2007), pp. 1503–1524. ISSN: 10498923. DOI: [10.1002/rnc.1184](https://doi.org/10.1002/rnc.1184). URL: <http://onlinelibrary.wiley.com/doi/10.1002/rnc.1553/abstracthttp://doi.wiley.com/10.1002/rnc.1184>.
- [XKo7b] Xin Xin and Masahiro Kaneda. "Design and analysis of swing-up control for a 3-link gymnastic robot with passive first joint." In: *Proc. IEEE Conf. Decis. Control* 23.6 (2007), pp. 1923–1928. ISSN: 01912216. DOI: [10.1109/CDC.2007.4434298](https://doi.org/10.1109/CDC.2007.4434298).
- [Xu93] Yangsheng Xu. "The measure of dynamic coupling of space robot systems." In: *IEEE Int. Conf. Robot. Autom.* Vol. 3. 1993, pp. 615–620. DOI: [10.1109/ROBOT.1993.291837](https://doi.org/10.1109/ROBOT.1993.291837). URL: http://ieeexplore.ieee.org/xpls/abs{_}all.jsp?arnumber=291837.
- [Yam+09] Taiga Yamasaki, Miyo Takeuchi, Kiyoshi Gotoh, and Xin Xin. "Criteria for Explaining a High Bar Movement." In: *Trans. Inst. Syst. Control Inf. Eng.* 22.12 (2009), pp. 399–406. ISSN: 1342-5668. DOI: [10.5687/iscie.22.399](https://doi.org/10.5687/iscie.22.399). URL: <http://joi.jlc.jst.go.jp/JST.JSTAGE/iscie/22.399?from=CrossRef>.
- [Yos85a] T. Yoshikawa. "Dynamic manipulability of robot manipulators." In: *Proceedings. 1985 IEEE Int. Conf. Robot. Autom.* 2 (1985), pp. 1033–1038. ISSN: 0741-2223. DOI: [10.1109/ROBOT.1985.1087277](https://doi.org/10.1109/ROBOT.1985.1087277).

- [Yos85b] Tsuneo Yoshikawa. "Manipulability of Robotic Mechanisms." In: *Int. J. Rob. Res.* 4.2 (1985), pp. 3–9. ISSN: 0278-3649. DOI: [10.1177/027836498500400201](https://doi.org/10.1177/027836498500400201).
- [YGS09] Seung-kook Yun, Ambarish Goswami, and Yoshiaki Sakagami. "Safe fall: Humanoid robot fall direction change through intelligent stepping and inertia shaping." In: *2009 IEEE Int. Conf. Robot. Autom.* (2009), pp. 781–787. ISSN: 1050-4729. DOI: [10.1109/ROBOT.2009.5152755](https://doi.org/10.1109/ROBOT.2009.5152755).
- [Zaj93] Felix E. Zajac. "Muscle coordination of movement: A perspective." In: *J. Biomech.* 26.SUPPL. 1 (1993), pp. 109–124. ISSN: 00219290. DOI: [10.1016/0021-9290\(93\)90083-Q](https://doi.org/10.1016/0021-9290(93)90083-Q).
- [Zor10] Victor Zordan. "Angular momentum control in coordinated behaviors." In: *Lect. Notes Comput. Sci. (including Subser. Lect. Notes Artif. Intell. Lect. Notes Bioinformatics)* 6459 LNCS (2010), pp. 109–120. ISSN: 03029743. DOI: [10.1007/978-3-642-16958-8_12](https://doi.org/10.1007/978-3-642-16958-8_12).